

ISOTHERMAL MICROCALORIMETRY AS A TOOL TO PROBE PARASITIC
REACTIONS IN LITHIUM-ION CELLS

by

Stephen Laurence Glazier

Submitted in partial fulfillment of the requirements
for the degree of Doctor of Philosophy

at

Dalhousie University
Halifax, Nova Scotia
July 2018

© Copyright by Stephen Laurence Glazier, 2018

DEDICATION

To Katie

TABLE OF CONTENTS

LIST OF TABLES	vii
LIST OF FIGURES	viii
ABSTRACT	xvii
LIST OF ABBREVIATIONS USED	xviii
ACKNOWLEDGEMENTS	xxi
CHAPTER 1 INTRODUCTION	1
1.1 MOTIVATION	1
1.2 OVERVIEW OF LITHIUM-ION CELLS	2
1.3 POSITIVE ELECTRODE MATERIALS	7
1.3.1 NMC	9
1.3.2 NCA	11
1.3.3 Coatings	11
1.4 NEGATIVE ELECTRODE MATERIALS	12
1.4.1 Graphite	12
1.4.2 Silicon-containing Materials	14
1.5 ELECTROLYTES	15
1.5.1 Salts	15
1.5.2 Solvents	16
1.5.3 The Solid Electrolyte Interphase	19
1.5.4 Additives	20
1.6 PARASITIC REACTIONS AND CELL FAILURE	23
1.6.1 Electrolyte Oxidation	26
1.6.2 Charge Endpoint Capacity Slippage	27
1.6.3 Self-Discharge	29
1.6.4 Electrolyte Reduction	30
1.6.5 Capacity Fade	31
1.6.6 Cross-talk and Shuttle Reactions	34
1.6.7 Coulombic Efficiency	36
1.6.8 Impedance	37
1.7 SCOPE OF THESIS	39

CHAPTER 2	LITHIUM-ION ISOTHERMAL MICROCALORIMETRY ...	42
2.1	HEAT FLOW OF A LITHIUM-ION CELL	42
2.1.1	Derivation of Measured Heat Flow.....	42
2.1.2	Overpotential.....	45
2.1.3	Entropy.....	46
2.1.4	Heat Flow of an NMC/graphite cell.....	47
2.2	PARASITIC HEAT FLOW.....	48
2.3	PAST STUDIES OF LITHIUM-ION ISOTHERMAL MICROCALORIMETRY	50
CHAPTER 3	EXPERIMENTAL TECHNIQUES	56
3.1	POUCH CELLS	56
3.2	ELECTROLYTES	59
3.3	CELL FORMATION CYCLE	59
3.4	LONG-TERM CYCLING	61
3.5	ULTRA-HIGH PRECISION COULOMETRY.....	62
3.6	GAS MEASUREMENTS	63
3.6.1	<i>Ex-situ</i> gas measurements.....	63
3.6.2	<i>In-situ</i> gas measurements.....	64
3.7	ELECTROCHEMICAL IMPEDANCE SPECTROSCOPY	65
3.8	STORAGE EXPERIMENTS	67
3.9	ISOTHERMAL MICROCALORIMETRY	67
3.9.1	Heat Flow Measurements	68
3.9.2	Experimental Setup.....	71
3.9.3	Baseline and Calibration.....	72
3.9.4	Experimental Notes and Uncertainty	73
3.10	GENERAL NOTES ON UNCERTAINTY	74
CHAPTER 4	USING HEAT FLOW TO PROBE SOLID ELECTROLYTE INTERPHASE FORMATION REACTIONS.....	75
4.1	EXPERIMENTAL.....	76
4.2	HEAT FLOW OF FORMATION	76
4.3	PYRIDINE BORON TRIFLUORIDE.....	81
4.4	PROP-1-ENE-1,3-SULTONE	85
4.5	CONCLUSIONS.....	88

CHAPTER 5	CHARGE-DISCHARGE METHOD OF EXTRACTING PARASITIC HEAT FLOW	90
5.1	MOTIVATION.....	90
5.2	METHOD	91
5.2.1	General Derivation.....	91
5.2.2	Overpotential Treatment	92
5.2.3	Parasitic Heat Flow and Consistency.....	94
5.3	STUDY: THE EFFECT OF ADDITIVES IN EC-FREE ELECTROLYTES	96
5.3.1	Motivation.....	96
5.3.2	Experimental	97
5.3.3	Results and Discussion	98
5.3.4	Conclusions.....	106
5.4	STUDY: THE EFFECT OF ADDITIVE CONTENT AND GRAPHITE TYPES ON PARASITIC REACTIONS.....	107
5.4.1	Motivation.....	108
5.4.2	Experimental	109
5.4.3	Results and Discussion	112
5.4.4	Conclusions.....	130
5.5	CHAPTER CONCLUSIONS	132
CHAPTER 6	IMPROVING THE CHARGE-DISCHARGE METHOD	133
6.1	CHARGE AND DISCHARGE PARASITIC HEAT FLOW	134
6.2	STUDY: THE EFFECT OF DIFFERENT NMC COMPOSITIONS AND POSITIVE ELECTRODE COATINGS ON THE PARASITIC HEAT FLOW OF LITHIUM-ION POUCH CELLS	140
6.2.1	Motivation.....	140
6.2.2	Experimental	141
6.2.3	Results and Discussion	142
6.2.4	Conclusions.....	153
6.3	FURTHER TREATMENT OF OVERPOTENTIAL	154
6.4	STUDY: THE EFFECT OF METHYL ACETATE IN NCA/SiO-GRAPHITE AND NMC/GRAPHITE POUCH CELLS.....	160
6.4.1	Motivation and Background	160
6.4.2	Experimental	161
6.4.3	Results and Discussion	163

6.4.4	Conclusions.....	179
6.5	CHAPTER CONCLUSIONS	180
CHAPTER 7	MEASURING PARASITIC REACTION ENTHALPY WITH ISOTHERMAL MICROCALORIMETRY AND HIGH-PRECISION COULOMETRY	182
7.1	MOTIVATION.....	182
7.2	EXPERIMENTAL.....	183
7.3	REVERSIBLE REDOX SHUTTLES	184
7.4	CHARGE-DISCHARGE METHOD.....	188
7.5	PARASITIC REACTION ENTHALPY	192
7.6	VOLTAGE-HOLD EXPERIMENTS	195
7.7	CONCLUSIONS.....	206
CHAPTER 8	CONCLUSIONS	208
8.1	CONCLUSIONS.....	208
8.2	FUTURE WORK	213
8.2.1	Future Studies to Improve Lithium-ion Cells.....	213
8.2.2	Development of parasitic heat flow methods.....	215
APPENDIX A:	COPYRIGHT PERMISSIONS.....	219
BIBLIOGRAPHY	221

LIST OF TABLES

Table 1: Properties of solvents used in this work.	17
Table 2: Cell builds used in this work	58
Table 3: Electrolyte chemicals used in this work	59
Table 4: Electrolyte compositions (1.0 M LiPF ₆).....	97
Table 5: Physical properties of AG and NG used in this study (provided by suppliers).....	110
Table 6: dV/dQ fitting results for AG and NG cells.....	125

LIST OF FIGURES

Figure 1.1: A schematic of lithium-ion cell components.....	3
Figure 1.2: The basic functions of a lithium-ion cell during charge (red arrows) and discharge (blue arrows).....	4
Figure 1.3: Voltage of a full cell (black), the $\text{LiNi}_{0.5}\text{Mn}_{0.3}\text{Co}_{0.2}\text{O}_2$ positive electrode (blue) and the graphite negative electrode (red) plotted vs. capacity. As capacity increases, Li is removed from the positive electrode and inserted into the negative electrode.	6
Figure 1.4: Voltage vs. specific capacity of common commercialized positive electrode materials during lithiation. Selected data digitized from Reference 14.....	9
Figure 1.5: $R\bar{3}m$ space-group a) trigonal unit cell (111 projection) and b) extended boundaries illustrating a layered structure.	10
Figure 1.6: a) Charge voltage curve of graphite during constant current discharge with labelled two-phase and single-phase regions. b) Cartoon representation of graphite stages. Lithium atoms are shown as green circles between graphite layers (black lines).	13
Figure 1.7: Chemical structures and abbreviations of additives used in this work.....	21
Figure 1.8: Energy level diagram of the kinetic electrolyte stability window with respect to the chemical potential of the positive and negative electrodes.	24
Figure 1.9: a) Charge and b) discharge processes of a lithium-ion cell. The positive and negative electrodes are denoted by a white '+' and a '-', respectively.	26
Figure 1.10: Electrolyte oxidation during a) charge, b) discharge, or c) open circuit.	26

Figure 1.11: Voltage vs capacity of an NMC532/graphite cell during 8 cycles between 3.0 V and 4.3 V. a) shows the full voltage range, b) shows a blown-up view of the discharge endpoint slippage, and c) shows a blown-up view of the charge endpoint capacity slippage.	28
Figure 1.12: Charge endpoint capacity vs cycle number for two cells under identical cycling conditions. Cell A has less electrolyte oxidation.	29
Figure 1.13: Open circuit storage test at 60°C and a starting voltage of 4.2 V.	30
Figure 1.14: Electrolyte reduction at the negative electrode.	31
Figure 1.15: Relative electrode shift due to electrolyte reduction in an NMC/graphite cell cycled between 3.0 V and 4.2 V.	32
Figure 1.16: Fractional capacity fade for two cells under identical cycling conditions. Cell A may experience less electrolyte reduction causing capacity loss than Cell B.	33
Figure 1.17: Cross-talk between electrodes.	34
Figure 1.18: A reversible electrolyte shuttle reaction.	35
Figure 1.19: Coulombic efficiency vs cycle number for two cells under identical cycling conditions.	37
Figure 1.20: a) Voltage vs capacity of a charge discharge cycle of an NMC532/graphite cell at a C/20 rate from 3.0 V to 4.3 V. b) ΔV vs. cycle for two cells cycled under identical conditions.	39
Figure 2.1: Heat flow profile of an NMC532/graphite cell during charge to 4.2 V (solid line) and discharge to 3.0 V (dashed line) at 10 mA and 40°C.	48
Figure 2.2: Figures from Downie and Dahn. ¹⁵³	53
Figure 3.1: The two cell geometries used in this thesis.	56

Figure 3.2: a) A simple circuit component model of an electrode-electrolyte interface. b) A Nyquist plot of the circuit section shown in a) when an AC response is measured	66
Figure 3.3: A labelled schematic of the interior of a TAM III calorimeter. Figure adapted from Reference 184.	69
Figure 3.4: a) The TAM III isothermal microcalorimeter (TA Instruments) used in this work. b) One of 12 lifters (one for each channel) with labelled components. c) A close-up view of the cell connections inside the ampoule, and the ampoule components.....	72
Figure 4.1: The heat flow (black) and voltage (red) of an NMC442/AG cell with control electrolyte containing EC during a formation cycle at 2 mA (~C/100).....	77
Figure 4.2: a) Measured cell voltage and b) heat flow during cell formation at 2 mA (~C/100) from NMC442/AG cells.....	79
Figure 4.3: The heat flow and differential capacity of a) control electrolyte (EC reduction), b) 2% VC, c) 2% FEC, d) 2% PBF, e) 4% PBF, and f) 2% PES.	80
Figure 4.4: The measured heat flow of formation for a) 2% PBF and b) 4% PBF (black) and calculated values (orange). The cell voltage is shown in blue.....	84
Figure 4.5: Heat flow of formation for 2% PES.	87
Figure 5.1: a) Cell voltage during charge (solid line) and discharge (dashed line) plotted vs. cumulative capacity for an NMC442/AG cell. b) Cell voltage vs. SOC (fractional capacity)	93
Figure 5.2: Calculated overpotential (left axis) and overpotential heat flow (right axis) during charge (solid line) and discharge (dashed line) of the cell in Figure 5.1 assuming a 1 mA current.	93

Figure 5.3: Parasitic heat flow (red) calculated as the average of the measured charge (solid black) and discharge (dashed black) heat flow	94
Figure 5.4: Parasitic heat flow of pair cells (SC-NMC532/AG) cycled from 4.0 V to 4.4 V at 1 mA found using the charge-discharge method with three different additive blends (A, B, and C).....	95
Figure 5.5: UHPC results for the barn cycling protocol from 2.8 V to 4.5 V at 40°C. a) Coulombic efficiency, b) relative charge endpoint, and c) discharge capacity.	99
Figure 5.6: Calculated parasitic heat flow during cycles between 3.9 V and a) 4.2 V and b) 4.3 V at 1 mA and 40°C.....	100
Figure 5.7: Calculated parasitic heat flow during cycles between 3.9 V and a,b) 4.4 V, c) 4.5 V, and d) 4.6V at 1 mA and 40°C.....	101
Figure 5.8: Calculated parasitic heat flow during cycles between 3.9 V and a) 4.6 V and b) the first (solid lines) and last (dashed lines) cycles to 4.2 V at 1 mA and 40°C.	103
Figure 5.9: Average calculated parasitic heat flow over each cycle between 3.9 V and the labelled voltage limits 1 mA and 40°C. Each point represents the average of the pair cells used.	104
Figure 5.10: a) EIS spectra for each cell after cell formation. b) Average R_{ct} of pair cells after formation. c) Average gas volumes of pair cells after formation (grey) and after calorimetry experiments (red). d) Photograph of the separators of each electrolyte after calorimeter experiments.....	106
Figure 5.11: SEM images of a,b) AG electrode surface c,d) NG electrode surface.....	112
Figure 5.12: UHPC results of additive blend loadings of 0.25, 0.5, and 1.0 in AG cells (left column) and NG (right column – only 0.25 NG is represented on the right y-axis).	113

Figure 5.13: Differential capacity dQ/dV plotted against cell voltage for a) AG cells and b) NG cells.	115
Figure 5.14: Extracted parasitic heat flow of each cell and electrolyte type during 3 cycles between 3.65 V and 3.85 V at 1mA and 40°C.....	118
Figure 5.15: Extracted parasitic heat flow for two cycles from 4.0 V to 4.3 V and 4.0 V to 4.4 V at 40°C.	119
Figure 5.16: Summary of all microcalorimetry cycles. The mean parasitic heat flow over each cycle is shown for all cells in a), and b) shows a zoomed in view of cells excluding the 0.25 NG cells.	120
Figure 5.17: <i>In-situ</i> volume measurements during 4.4 V and 4.5 V holds at 40°C for 100 hours each.....	121
Figure 5.18: <i>In-situ</i> pressure measurements of a) 1.0 AG and 1.0 NG cells, b) 0.25 AG and 0.25 NG cells vs. time cycled from 3.0 V to 4.2 V at a rate of C/6 at 40°C. c) The averaged pressure over each cycle. d) The change in pressure at top of charge.	123
Figure 5.19: Long term cycling results for NMC532/AG and NMC532/NG cells from 3.0 V to 4.3 V during C/3 CCCV cycling at 40°C.....	124
Figure 5.20: dV/dQ fitting results of 1.0 AG cells before (a) and after 550 cycles (b), and 1.0 NG cells before (c) and after (b) 586 cycles.....	126
Figure 5.21: dV/dQ fitting of the first cycle of a) 1.0 AG and b) 1.0 NG cells.....	127
Figure 5.22: The proposed mechanism responsible for the observed UHPC performance of natural graphite.....	128
Figure 5.23: Long term cycling results for coated NMC622/AG and NMC622/NG cells with 1.0 PES211 electrolyte cycled at C/3 CCCV at 40°C.	130

Figure 6.1: a) Heat flow during charge (solid lines) and discharge (dashed lines) NMC532B/NG (orange) and NMC622B/NG (blue) cells during a cycle between 3.9 V and 4.4 V at 1 mA after a previous cycle to 4.4 V at 40°C. b) The calculated entropic heat flow during charge (solid lines) and discharge (dashed lines).....	136
Figure 6.2: Voltage vs. capacity for an NMC532B/NG full cell (black), positive electrode (blue), and negative electrode (red).....	138
Figure 6.3: Charge (solid lines) and discharge (dashed lines) parasitic heat flow during a cycle between 3.9 V and 4.4 V at 1 mA and 40°C prior to the cycle in which the entropic heat flow was calculated.	139
Figure 6.4: Parasitic heat flow of different cell types: 442 (black), 532 A (red), 532 B (orange), 622 A (blue), and 622 B (light blue) calculated using the charge-discharge method.	143
Figure 6.5: Extracted theoretical entropic heat flow during each protocol step using the entropic method.....	145
Figure 6.6: The calculated charge (solid lines) and discharge (dashed lines) parasitic heat flows of each cell type during the first cycle to each voltage range	147
Figure 6.7: a) The mean parasitic heat flow during each cycle using the charge-discharge method for coated NMC grades between 3.9 V and the labelled UCV. b) <i>In-situ</i> gas measurements of cells during voltage-holds at 4.4 V and 4.5 V at 40°C. c) <i>Ex-situ</i> gas measurements and d) charge transfer resistance (R_{ct}) values	149
Figure 6.8: UHPC results for each cell type cycled from 3.0 V to a) 4.1 V, b) 4.2 V, and c) 4.3 V at C/20 and 40°C.	151
Figure 6.9: Long term cycling (C/3 CCCV at 40°C) from 3.0 V to 4.1 V, 4.2 V, and 4.3 V. Discharge capacity is shown in a), fractional discharge capacity in b), and ΔV in c).....	152

Figure 6.10: The overpotential heat flow calculated using the voltage vs. SOC (black). A linear fit to the overpotential heat flow at 33% and 67% SOC (red).....	155
Figure 6.11: A demonstration of the fitted overpotential and equilibrium correction in an SC-NMC532/AG cell during a cycle from 4.0 V to 4.4 V at 1 mA.	157
Figure 6.12: Parasitic heat flow of six pairs of cells with different electrolytes	158
Figure 6.13: The uncorrected measured heat flow during charge (solid grey) and discharge (dashed grey) of an NCA/SiO-graphite cell cycled from 3.9 V to 4.2 V at 3.7 mA at 40°C. The corrected measured heat flow is shown in black, and the corrected parasitic heat flow is shown in red.	159
Figure 6.14: Summarized UHPC results plotted vs. MA content during cycling between 3.0 V and 4.3 V at C/20 and 40°C.....	165
Figure 6.15: Parasitic heat flow calculated using the charge discharge method with the equilibrium correction and fitted overpotential at 1 mA and 40°C for cells with 0, 20 and 40 MA.....	167
Figure 6.16: The mean parasitic heat flow per cycle to the labelled UCV.....	168
Figure 6.17: a) Cell voltage vs. time and b) Gas volume vs. time during <i>in-situ</i> gas measurements with voltage-holds to 4.2 V, 4.3 V, and 4.4 V for 100 hours each at 40°C.	169
Figure 6.18: High rate (1C) CCCV cycling of cells from 3.0 V to 4.2 V at 20°C (left) and 40°C (right).	171
Figure 6.19: Normalized capacity during the first rate map after 100 1C cycles at a) 20°C and b) 40°C (from Figure 6.18).	172
Figure 6.20: Ultra high precision results for cells with 0 MA (black) and 20 MA (blue) cycled at C/20 from 3.0 V to 4.2 V at 40°C.	173

Figure 6.21: a) Voltage and b) gas volume from in-situ gas measurements.....	174
Figure 6.22: Parasitic heat flow of pouch cells cycled at C/100 between 3.9 V and 4.1 V at 40°C.	175
Figure 6.23: Parasitic heat flow of pouch cells cycled at C/100 between 3.9 V and 4.2 V at 40°C.	176
Figure 6.24: Mean parasitic heat flow per cycle of all cells cycled at C/100 between 3.9 V and the labeled upper cut off voltages at 40°C.	177
Figure 6.25: Long term cycling of cells after calorimetry experiments. Cells were cycled at 40°C at a rate of C/3 with a CCCV protocol.	178
Figure 7.1: A redox shuttle process in a) open circuit voltage conditions b) closed circuit with electrode equilibrium, and c) closed circuit charge.	185
Figure 7.2: i) Voltage versus time during a 2 mA (C/200) charge for cells containing shuttle molecules ii) Calculated IV , measured heat flow, and $I_{sh}V$. iii) Calculated reaction enthalpy change per mole of electrons supplied to the shuttle.	187
Figure 7.3: Calculated parasitic heat flow of cells with EC:EMC:DMC-based electrolytes (black), EC:EMC:DMC:MA-based electrolytes (red), and FEC:TFEC-based electrolytes (blue).....	191
Figure 7.4: Mean parasitic heat flow per cycle for cells containing EC:EMC:DMC-based electrolytes (black), EC:EMC:DMC:MA-based electrolytes (red), and FEC:TFEC-based electrolytes (blue).	192
Figure 7.5: Simplified parasitic reaction schemes	193
Figure 7.6: IV (black) and measured heat flow (red) in cells with coated NMC532 with EC:EMC:DMC-based electrolytes (left column) and cells with EC:EMC:DMC:MA-based electrolytes (right column).....	196

Figure 7.7: Integrated a) cumulative parasitic energy, b) cumulative IV energy, c) cumulative reaction energy, d) net enthalpy change per mole of electrons at different upper cutoff voltages.....	198
Figure 7.8: Total integrated results from the final 50 hours of voltage-holds.	200
Figure 7.9: <i>IV</i> (black) and measured heat flow (red) from cells with coated NMC532 with an EC:EMC:DMC:MA-based electrolyte during a 4.4 V voltage-hold at 40°C on a) a Keithley 2602B source-meter and b) a Novonix charger.....	204
Figure 7.10: Integrated total parasitic energy (a,b), <i>IV</i> energy (c,d), reaction energy (e,f), and enthalpy change per mole of electrons (g,h) during 4.4 V holds on a Keithley 2602B source-meter (left column), and a Novonix system (right column)	205

ABSTRACT

Understanding the mechanisms affecting the lifetime of lithium-ion cells is critical to extend cell lifetime and increase the energy density for applications such as grid energy storage and electric vehicles. Unwanted, or parasitic, reactions between the electrode materials and the electrolyte can consume the available lithium and electrolyte components, limiting cell lifetime. This work developed methods of probing parasitic reactions *in-situ* and non-destructively in short experiments using isothermal microcalorimetry. The effect of different electrode materials, electrolyte additives, and solvents on cell lifetime was investigated by isolating the heat flow due to parasitic reactions – the parasitic heat flow.

Three methods were developed in this work. The first method probed the reactions occurring during the formation of the solid electrolyte interphase, which occurs the first time a cell is charged. The measured heat flow was compared to theoretical estimates of the heat flow of proposed reaction pathways using computed values in the literature.

The second method used the measured heat flow during slow charge-discharge cycles to isolate the parasitic heat flow as a function of cell voltage. The method was used in multiple studies to explore the effects of electrolyte additives, solvents, positive electrode coatings, positive electrode composition, and negative electrode materials on the parasitic heat flow. The technique correlated with cell performance in almost all cases, but the results suggested that differences between electrode or electrolyte components could introduce different types of parasitic reactions, affecting the parasitic heat flow.

Finally, a method was introduced to probe the reaction enthalpies of parasitic reactions using high-precision voltage-holds. The study found that different solvents and positive electrode coatings played a large role in determining the types of parasitic reactions occurring in cells. Additionally, the rates and types of parasitic reactions were found to change significantly with the cell voltage.

The methods developed in this work provided insight into the mechanisms responsible for limited lifetime in the cells studied and contributed to a better understanding of parasitic reactions in lithium-ion cells. New measurement techniques found that changes in parasitic processes could be quantified, and depend on cell voltage, electrode materials, electrode coatings, and electrolyte chemistries.

LIST OF ABBREVIATIONS USED

°C	degree Celsius
A	amp
AC	alternating current
AG	artificial graphite
Ah	amp hour
BET	Brunauer–Emmett–Teller
C	coulomb
#C	number (#) of full capacity charges per hour
C/##	a full charge in ## hours
CB	carbon black
CCCV	constant-current constant-voltage
CE	coulombic efficiency
CIE	coulombic inefficiency
cm	centimeter
CMC	carboxymethyl cellulose
cP	centipoise
C_s	heat capacity of sample
DBDB	3,5-di-tert-butyl-1,4-dimethoxybenzene
DDB	2,5-di-tert-butyl-1,4-dimethoxybenzene
DFT	density functional theory
DMB	2,5-dimethyl-1,4-dimethoxybenzene
DMC	dimethyl carbonate
DTD	ethylene sulfate
e	electronic charge
EA	ethyl acetate
EC	ethylene carbonate
EIS	electrochemical impedance spectroscopy
EIV	IV energy
EMC	ethyl methyl carbonate
E_p	parasitic energy
E_r	reaction energy
ETIS	electrothermal impedance spectroscopy
EV	electric vehicle
eV	electron volts
F	Faraday's constant
FEC	fluoroethylene carbonate
FRA	frequency response analysis
g	gram
G	Gibbs energy
GC	gas chromatography
H	enthalpy

I	current
I_p	parasitic current
j	sqrt(-1)
k	reaction rate
K	Kelvin
kg	kilogram
k_s	sample heat conductance
L	liters
LCO	LiCoO ₂
LTO	Li ₄ Ti ₅ O ₁₂
m	meters
MA	methyl acetate
mAh	milliamp hour
m_{cell}	mass of a cell
MMDS	methylene methyldisulfonate
N	total number of sites in a host
n	number of filled sites
NCA	LiNi _x Co _y Al _(1-x-y) O ₂
NG	natural graphite
NMC	LiNi _x Mn _y Co _(1-x-y) O ₂
OCV	open circuit voltage
PBF	pyridine boron trifluoride
PC	propylene carbonate
PE	polyethylene
PES	prop-1-ene-1,3-sultone
PES211	additive blend containing 2% PES, 1% DTD, 1% TTSPi
PPF	pyridine boron pentafluoride
PVDF	polyvinylidene fluoride
q	heat
Q_c	charge capacity
Q_d	discharge capacity
\dot{q}	heat flow
\dot{q}_{ch}	heat flow during charge
\dot{q}_{dis}	heat flow during discharge
\dot{q}_p	parasitic heat flow
$\dot{q}_{p\ average}$	average parasitic heat flow
$\dot{q}_{p\ ch}$	parasitic heat flow during charge
$\dot{q}_{p\ dis}$	parasitic heat flow during discharge
Q_p	parasitic capacity
R_{cell}	cell resistance
R_{ct}	charge transfer resistance
S	entropy
s	entropy per site

S_b	Seebeck coefficient
SBR	styrene butadiene rubber
SEI	solid electrolyte interphase
t	time
TAP	triallyl phosphate
T_b	boiling temperature
TFEC	bis(2,2,2-trifluoroethyl) carbonate
T_m	melting temperature
TTSPi	tris(trimethylsilyl)phosphite
TTSP	tris(trimethylsilyl)phosphate
U	internal energy
UCV	upper cut off voltage
v	volume
V_{bar}	average voltage
VC	vinylene carbonate
V_{cell}	cell voltage
v_{cell}	cell volume
V_{ch}	cell voltage during charge
V_{dis}	cell voltage during discharge
V_{eq}	equilibrium cell voltage
V_{hyst}	voltage hysteresis
W	watt
Wh	watt hour
wt.	by weight
x	ratio of filled sites to total number of sites (n/N)
XPS	x-ray photoelectron spectroscopy
Z	impedance
ΔH	enthalpy of reaction
ΔH_e	enthalpy of reaction per mole of electrons
ΔQ_c	charge endpoint capacity slippage
ΔQ_d	discharge endpoint capacity slippage
ΔV	difference in charge and discharge average voltages
ϵ	dielectric constant
η	overpotential
η_v	viscosity
μ_-	negative electrode chemical potential
μ_+	positive electrode chemical potential
ρ	density
τ	time constant
ω	frequency

ACKNOWLEDGEMENTS

I would like to acknowledge my supervisor, Dr. Jeff Dahn for his unwavering dedication to every member of the Lab. Without his constant support, motivation, and excitement surrounding our research, this degree would not have been such an engaging, energizing experience.

I would like to acknowledge Tesla, 3M Company, Dalhousie University, NSERC, and the Walter Sumner Foundation for financial support through various portions of this work.

I would like to acknowledge every member of the Dahn Lab over the last few years. It has been a privilege to work with such a diverse group of researchers from numerous scientific fields from around the globe. You have all taught me a great deal about research, collaboration, community, and friendship. I would especially like to thank Dr. Jing Li for being a constant source of inspiration and mentorship, as well as a great friend.

Finally, I would like to acknowledge the people closest to me. Mom and Dad: Your support has been unparalleled. Though distance separates us, you are always with me. Sean, Christie, Jon, Alex, and Lauren: Thank-you for providing me with much needed breaks from my work through physical labour, Skype chats, and making time for me even though I have little to give to you. Drew: Honk. Katie: Thank-you for being there every step of the way. Thank-you for learning and growing with me, and for being my rock. I cannot wait for our next adventure and all the adventures to follow.

CHAPTER 1 INTRODUCTION

1.1 MOTIVATION

Lithium-ion cells are used as energy storage devices in portable electronics, electric vehicles (EVs), and more recently grid energy storage. Lithium-ion cells for applications such as grid storage and EVs must have lifetimes on the order of ten years or more, have high energy density and specific energy, perform well in a wide range of temperatures, charge and discharge quickly, be safe, and low in cost.

Many commercialized lithium-ion chemistries have a desirable theoretical energy density due to large charge storage capacity and high operating potentials.^{1,2} However, many commonly used chemistries operate at potentials which cause reactions between the electrode surfaces and the liquid electrolyte, consuming electrolyte and lithium, decreasing the lifetime of cells.^{3,4} Increasing the stability of the electrolyte and the electrolyte-electrode interfaces would allow for higher energy density lithium-ion cells, and in turn lower cost, can improve safety, and increase lifetime.

The development of high energy density lithium-ion cells requires a deeper understanding of the mechanisms responsible for decreased lifetime. Ideally, methods which predict the lifetime of cells would take weeks or months, rather than charging and discharging cells for years or decades. Therefore, high-precision measurements which directly probe unwanted reaction processes in cells are desired. Techniques which allow for sensitive measurements of parasitic reactions will help guide the advancement of materials and electrolytes for high energy density lithium-ion cells with long lifetime.

1.2 OVERVIEW OF LITHIUM-ION CELLS

A secondary (rechargeable) lithium-ion cell is an electrochemical ‘rocking-chair’ device which utilizes a difference in chemical potential between two materials that can reversibly store lithium to store energy or do work in a circuit. A lithium-ion cell typically contains a positive electrode and a negative electrode on metallic current collectors, a porous, insulating separator, and a non-aqueous liquid electrolyte.

Electrode materials are typically layered materials in which lithium atoms can be reversibly inserted (intercalation) or removed (deintercalation) between layers. For example, LiCoO_2 is an example of a positive electrode material with alternating layers of lithium, oxygen, cobalt, oxygen, lithium, etc., and graphite (which will be referred to as C_6 in this thesis) is a common layered negative electrode material. Electrode materials are typically blended with a polymeric binder to bond particles together and to the current collector. A conductive carbon is also usually mixed into the electrode to provide electronic connection between particles. More details about positive and negative electrode materials will be discussed in Sections 1.3 and 1.4, respectively. The separator is a microporous polymer film which allows for electrolyte and Li^+ ions to pass between electrodes while maintaining electrical isolation. The separator will not be discussed in detail in this work. The liquid electrolyte acts as the means of ion transport between electrodes and typically contains a lithium salt such as lithium hexafluorophosphate (LiPF_6) dissolved in a blend of carbonate solvents such as ethylene carbonate (EC) and ethyl methyl carbonate (EMC). Electrolytes will be discussed in detail in Section 1.5.

To maximize energy density, electrodes are typically coated on both sides of the current collectors. In most cells the current collectors are aluminum foil for the positive

electrode and copper foil for the negative electrode. The electrodes and separator are assembled in one of many configurations such as stacked, folded, or wound. The bulk shape of the cell interior is often referred to as the jelly-roll. A schematic of the basic interior components of a wound, cylindrical lithium-ion cell is shown in Figure 1.1. The jelly-roll is contained in either a flexible pouch or a hard metal enclosure, which is filled with electrolyte when assembled. The negative electrode is usually designed to be wider than the positive electrode for safety reasons, creating an ‘overhang’ region, as seen in Figure 1.1. The overhang prevents Li^+ ions from the positive electrode from plating as Li metal on the edge of the negative electrode current collector when a cell is charging.



Figure 1.1: A schematic of lithium-ion cell components.

The basic operation of a lithium-ion cell is outlined in Figure 1.2. When charging a cell, current is applied through an external circuit, driving electrons from the positive electrode to the negative electrode. To maintain charge balance in the cell, lithium ions deintercalate from the positive electrode structure (LiMO_2 in Figure 1.2, where M is a transition metal) and intercalate into the graphite negative electrode. The lithium atoms in the negative electrode have a higher chemical potential (μ_-) than the lithium atoms in the positive electrode (μ_+). Thus, when the cell is charged, work is done on the

electrochemical system and energy is stored in the cell. When a load is placed in the external circuit, the reverse happens spontaneously: electrons flow through the circuit from the negative electrode to the positive electrode, releasing the stored energy as work in the circuit while lithium atoms deintercalate from the negative electrode and intercalate into the positive electrode.

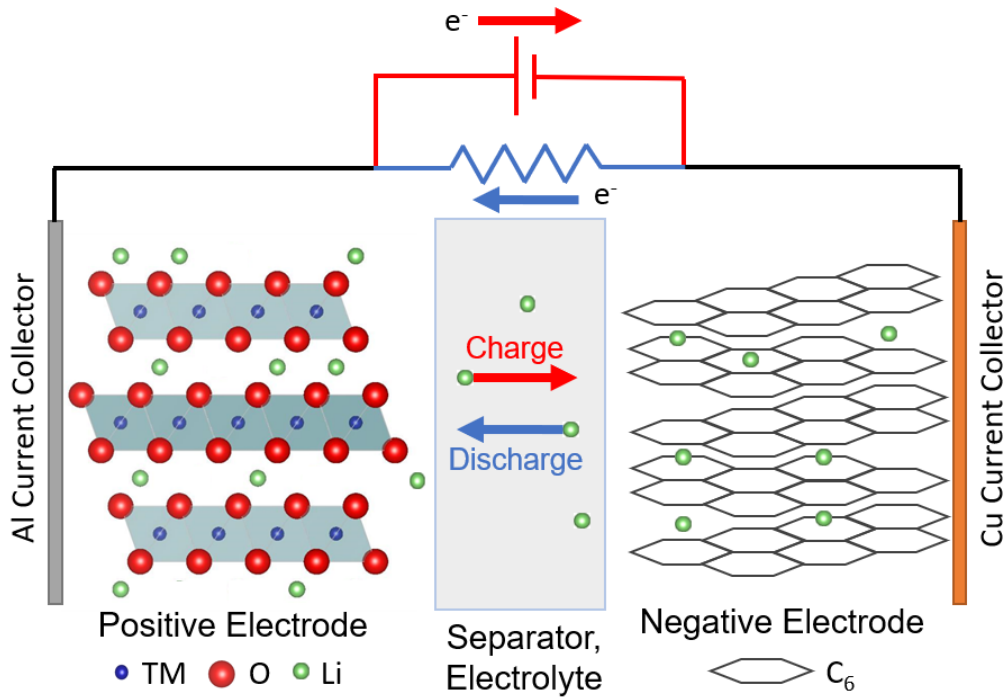
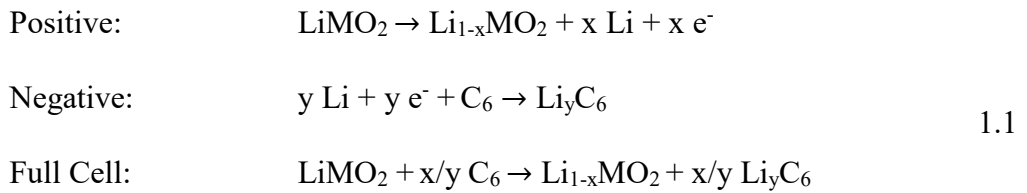


Figure 1.2: The basic functions of a lithium-ion cell during charge (red arrows) and discharge (blue arrows).

The half-cell intercalation reaction of each electrode and the full cell reaction can be expressed by



The equilibrium voltage of the cell is given in volts (V) by

$$V_{eq} = \frac{\mu_-(y) - \mu_+(1-x)}{e} \quad 1.2$$

where e is the electronic charge and $(1-x)$ and y are the lithium contents of the positive and negative electrode half-cell reactions shown above. The cell capacity is defined as the total amount of charge transferred in the external circuit during the total time of a charge or discharge between two fixed voltage limits and is typically given in amp hours (Ah) or milliamp hours (mAh). For example, using a constant current (I in amps, A) the capacity of a charge cycle over a time t (in hours, h) would be

$$Q_{charge} = \int_0^t I dt = It. \quad 1.3$$

Specific capacity refers to the capacity per unit mass, typically expressed in mAh/g. The energy of a cell is simply the capacity multiplied by the average voltage of the cell and is usually expressed in Watt hours (Wh). Specific energy density and volumetric energy density refer to the energy per unit mass or volume, respectively, given in Wh kg⁻¹ or Wh L⁻¹.

Figure 1.3 shows the voltage of a full cell (black) with an LiNi_{0.5}Mn_{0.3}Co_{0.2}O₂ positive electrode and a graphite negative electrode plotted against the cell capacity. Also shown are the constituent positive (blue) and negative (red, right axis) electrode voltage measured vs. a lithium metal reference (Li/Li⁺). The electrode material voltage curves are aligned such that the ‘balance’ of the cell is shown, (i.e., the relative capacities of each material in the cell) and demonstrate where the features in the full cell voltage-capacity curve come from. Cells are balanced for operation between specific voltage ranges. As

depicted in Figure 1.3 (the cell is balanced for 4.5 V operation) the positive electrode is always designed to have less capacity than the negative electrode before the full cell reaches the designed upper cut off voltage. A larger negative electrode capacity ensures that when charging the cell (moving towards the right in Figure 1.3), the negative electrode does not become fully lithiated and begin to plate Li metal on the surface of the electrode.

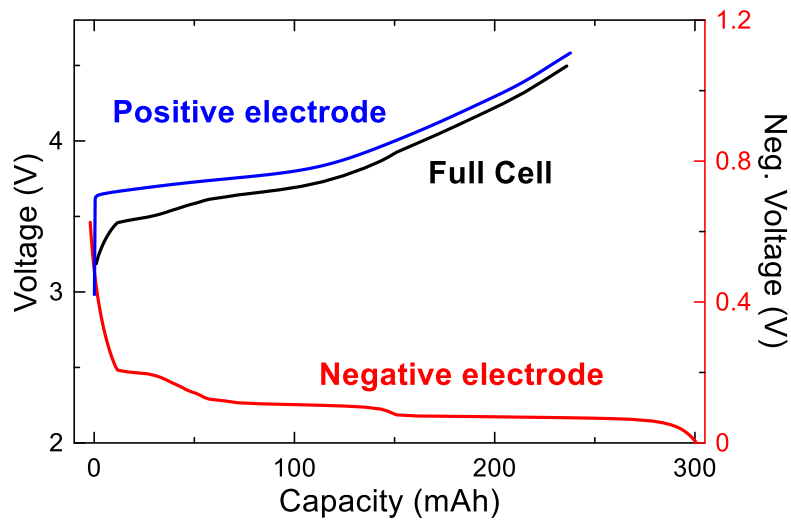


Figure 1.3: Voltage of a full cell (black), the $\text{LiNi}_{0.5}\text{Mn}_{0.3}\text{Co}_{0.2}\text{O}_2$ positive electrode (blue) and the graphite negative electrode (red) plotted vs. capacity. As capacity increases, Li is removed from the positive electrode and inserted into the negative electrode.

The choice of electrode materials governs many properties of a cell, such as the operating cell voltage, specific capacity, and the energy density. The choice of electrode materials and electrolyte influences the rate capabilities (whether the cell can charge/discharge quickly), lifetime, and cost. Lifetime can refer to either calendar lifetime (measured in hours, years, etc.) or charge-discharge cycle lifetime (measured in number of cycles). Processes which contribute to decreased lifetime can be physical degradation of cell components (particle cracking, electrical disconnection, lithium metal formation, etc.), or chemical degradation (reactions between the electrolyte and electrodes, oxygen

loss and transition metal dissolution from the positive electrode, thermal decomposition of electrolyte or salt, etc.).⁵⁻⁹ The rate and severity of these failure mechanisms depend on the materials used and the conditions cells are exposed to such as temperature, voltage, and rate. Understanding the root cause of failure mechanisms in cells is critical to improve the lifetime of lithium-ion cells.

In this work, the physical degradation of cell materials is considered, but the majority of failure analysis focuses on chemical degradation involving reactions at the electrolyte-electrode interfaces. The term ‘parasitic reactions’ is typically used to describe these chemical processes and covers a wide variety of mechanisms. Due to the complexity of the electrochemical system inside a lithium-ion cell, the exact processes that occur during parasitic reactions are not well understood. Parasitic reactions will be discussed in detail in Section 1.6.

This section provided a basic, qualitative overview of lithium-ion cell operation and cell failure. The following three sections will go into further detail describing the positive and negative electrodes, as well as components of the electrolyte. Details regarding parasitic reactions and the effects of parasitic reactions on cell performance will then be discussed. Background will be given with an emphasis on materials and techniques used in this thesis.

1.3 POSITIVE ELECTRODE MATERIALS

To achieve cells with high energy density, positive electrode materials with high operating potential vs. Li/Li^+ and/or high specific capacity are required. This work only considers commercialized (functional) positive electrode materials which operate at high

average voltage (>3.8 V) and yield high specific capacities. Figure 1.4 shows the voltage vs. specific capacity curves of five commercialized positive electrode materials. According to Figure 1.4, layered metal oxides with the chemical formula LiMO_2 (where M is a blend of transition metals) are materials of interest to this work. In order to use the full theoretical capacity of layered metal oxides, the positive electrode material must be charged to potentials upwards of 4.7 V. Typical electrolytes are not stable at these high potentials, leading to parasitic reactions (specifically electrolyte oxidation). Some materials such as $\text{LiNi}_{0.5}\text{Mn}_{1.5}\text{O}_4$ (LNMO) operate at a very high average voltage of ~ 4.75 V with a theoretical capacity of 146 mAh g^{-1} .¹⁰⁻¹² However, due to operating potentials of up to 5.0 V, LNMO suffers from challenges due to electrolyte stability which are out of the scope of the current work.^{10,11,13} Section 1.6 discusses the impact of high voltage operation on parasitic reactions in lithium-ion cells. This work uses two types of layered transition metal oxides which will be discussed in Section 1.3.1 and 1.3.2. Electrode surface coatings will be introduced in Section 1.3.3.

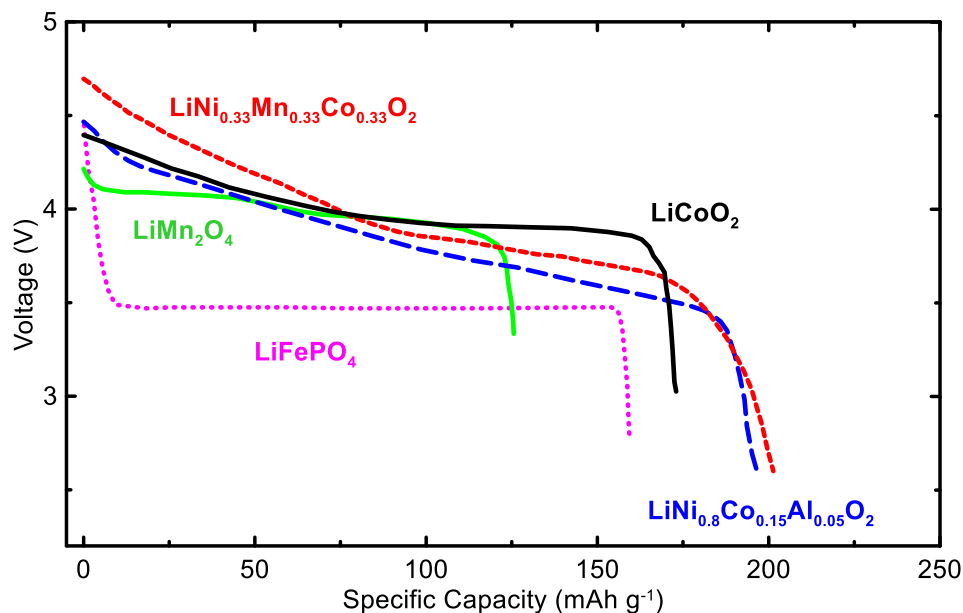


Figure 1.4: Voltage vs. specific capacity of common commercialized positive electrode materials during lithiation. Selected data digitized from Reference 14.

1.3.1 NMC

A common positive electrode material is based on the formula $\text{LiNi}_x\text{Mn}_y\text{Co}_{1-x-y}\text{O}_2$. The shorthand name for this material is NMC and is commonly referred to by its ratio of nickel, manganese, and cobalt. For example, $\text{LiNi}_{0.33}\text{Mn}_{0.33}\text{Co}_{0.33}\text{O}_2$ is called NMC111, $\text{LiNi}_{0.5}\text{Mn}_{0.3}\text{Co}_{0.2}\text{O}_2$ is called NMC532, etc. NMC is based on the first commercialized lithium-ion positive electrode material LiCoO_2 (LCO), identified in 1980.¹⁵ In recent years NMC has replaced LCO in many applications due to its superior thermal and structural stability, high useful specific capacity (160 – 200 mAh g^{-1} vs. 145-180 mAh g^{-1}), significantly lower cost, and high rate capabilities.^{14,16–19} The layered structure of the LiMO_2 family is described by the $R\bar{3}m$ space group and is shown in Figure 1.5, where M is either Ni, Mn, or Co in NMC. Transition metal atoms occupy the 3a sites and while lithium occupies 3b sites, forming alternating layers of lithium and transition metal atoms octahedrally coordinated by oxygen atoms.

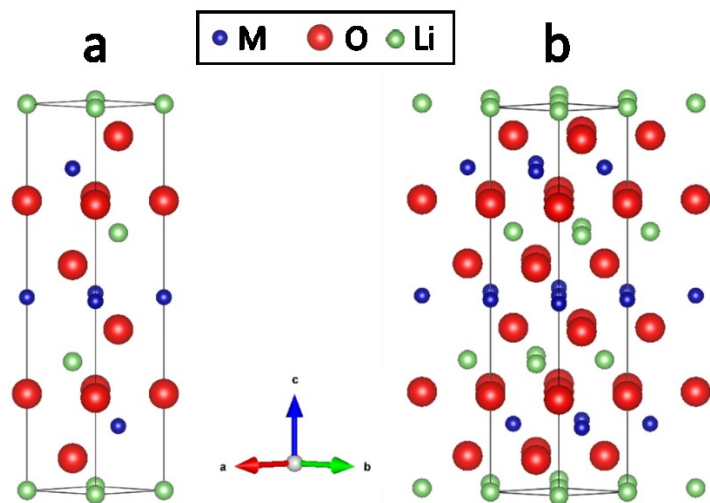


Figure 1.5: $R\bar{3}m$ space-group a) trigonal unit cell (111 projection) and b) extended boundaries illustrating a layered structure.

Many types of NMC have been investigated to achieve optimal combinations of properties from each transition metal. Increasing the amount of Ni relative to Co in NMC reduces the cost due to lower Co content, but yields lower thermal stability²⁰⁻²² and can increase the number of Ni^{2+} ions preferentially occupying Li sites.²³ High Ni content in NMC also can lead to more electrolyte oxidation, but is necessary to decrease Co content.^{24,25} Fortunately, developments in electrolyte chemistries and positive electrode surface coatings have allowed for the use of some high Ni-containing NMC chemistries, and will be discussed shortly. Adding Co to $LiNiO_2$ was found to mitigate the degree of cationic disorder between layers in materials using low cost synthesis.²⁶ Manganese is much cheaper and less toxic than Ni and Co, but contributes to a phase transition to a spinel structure,²⁷ and Mn^{2+} dissolution into electrolyte when high ratios of Mn are used.^{5,28} A few types of NMC have become quite popular which achieve a balance of cost, energy density, and structural and chemical stability, namely NMC111, NMC442, NMC532, and

NMC622.^{14,25} NMC811 is a promising material which significantly decreases Co content compared to other chemistries and is being adopted by some manufacturers.^{22,25,29}

Most of this work involves three different chemistries of NMC: NMC442, NMC532, and NMC622. The details of the materials will be noted in the text where applicable.

1.3.2 NCA

$\text{LiNi}_x\text{Co}_y\text{Al}_{1-x-y}\text{O}_2$ (NCA) is another common positive electrode material based on the layered structure of LCO and NMC. Al has been found to improve overall structural and thermal stability, as well as the electrochemical performance compared to materials without Al.³⁰ However, since Al^{3+} is electrochemically inactive, NCA must contain low concentrations of Al in order to maintain its high specific capacity of $\sim 200 \text{ mAh g}^{-1}$.¹⁴ Therefore NCA materials typically contain high ratios of Ni:(Co+Al) of 4:1.^{31,32} NCA has also been reported to show structural degradation at particle grain boundaries during long-term use.³³

Some portions of this work involve a proprietary NCA material in cells provided by one of Tesla's suppliers.

1.3.3 Coatings

Positive electrode coatings have become a popular way of mitigating reactions with electrolyte, particularly in high-nickel NMC materials. Coatings such as Al_2O_3 have been found to protect against electrolyte oxidation and damage from hydrofluoric acid, HF, increasing the lifetime of cells.^{34,35} TiO_2 has also been found to help create a protective coating which allows for high rate capabilities.³⁶ LaPO_4 has been found to increase lifetime at moderate potentials and increase surface structural stability of Mn-containing positive

electrode materials such as LiMn_2O_4 ,³⁷ but was found to decrease performance in NMC cells operated above 4.4 V.³⁸

Some of the materials in this work have positive electrode coatings: either Al_2O_3 or proprietary materials. Some comparisons between coatings will be made, and the presence of coatings will be indicated in the text when applicable.

1.4 NEGATIVE ELECTRODE MATERIALS

Like the positive electrode materials introduced in Section 1.3, this work uses commercialized materials which yield high cell potentials (low negative electrode potential vs. Li/Li^+) and have high specific capacity. The ideal candidate based on these metrics alone would be to use Li metal. Lithium can be plated and stripped from a Li metal negative electrode instead of using an intercalation material. However, Li metal electrodes have been found to cause issues due to heterogeneous stripping and plating of Li, leading to lithium dendrites.³⁹ These imperfections can cause capacity loss and safety issues due to lithium loss and short circuits in cells, leading to self-discharge or catastrophic failure.^{39,40} The use of Li metal electrodes is a topic of interest in the field, but is not applicable to this body of work. Some commercialized negative electrode materials such as $\text{Li}_4\text{Ti}_5\text{O}_{12}$ (LTO) yield cells which have very long lifetime, good safety and structural stability, but have low specific capacity and high negative electrode operating voltages (175 mAh g^{-1} and 1.55 V vs Li/Li^+ respectively for LTO).⁴¹

1.4.1 Graphite

Graphite is the most widely used negative electrode due to its low potential vs. Li/Li^+ (average voltage of ~ 0.15 V), relatively high theoretical specific capacity of ~ 370

mAh g^{-1} , low volume expansion ($\sim 10\%$ along the stacking axis during lithiation), and compatibility with long lifetime cells.^{14,42} Figure 1.6a shows the voltage *vs.* specific capacity of graphite during charge. Figure 1.6a depicts the multiple labelled plateau regions during charge. These voltage plateaus are due to two coexisting phases of Li_xC_6 , and the sloped regions are due to the presence of a single phase.^{43,44} This multi-stage intercalation process is commonly referred to as staging. In Figure 1.6, stage 1 is labelled ‘1’, and multi-phase regions are labeled by the two coexisting phases (eg. 1-2). An ‘L’ indicates a ‘liquid’-like state in which no preferential ordering within lithium layers occurs. Figure 1.6b illustrates the stages of Li_xC_6 as lithium is inserted ($0 < x < 1$). The stage number represents the number of graphene sheets between layers of intercalated lithium.

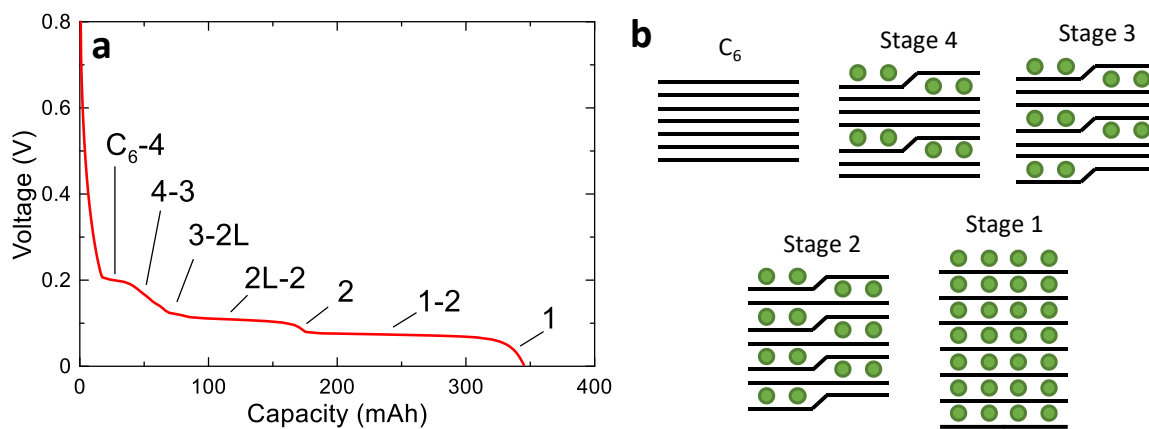


Figure 1.6: a) Charge voltage curve of graphite during constant current discharge with labelled two-phase and single-phase regions. b) Cartoon representation of graphite stages. Lithium atoms are shown as green circles between graphene layers (black lines).

Though safe, non-toxic, and inexpensive, graphite has some limitations. The low operating potential of graphite *vs.* Li/Li^+ means that electrolyte species can be reduced at the surface, creating reactions which can form gas or a solid layer over the surface of the graphite. This layer can increase impedance in the cell and consumes some of the available lithium in the cell. However, this layer called the solid electrolyte interphase (SEI) has

also been found to mitigate further reduction and protect the graphite surface when certain chemicals are used.⁴⁵⁻⁴⁷ This protective SEI layer will be discussed further in Section 1.5. Another issue that can arise is the intercalation of electrolyte solvent species into the graphite layers, causing exfoliation, increased surface area, and subsequently more reaction products.^{48,49} Finely tuned protective layers or surface coatings can prevent solvent intercalation.^{45,48,49}

Graphite materials for lithium-ion cells can be manufactured from natural graphite sources or synthesized from petroleum products. In this work, the source of the graphite type used in each chapter will be distinguished by the terms natural graphite (NG) and synthetic, aka artificial graphite (AG). A comparative study between NG and AG is discussed in Chapter 5 of this thesis.

Most cells used in this thesis contain graphite alone as the negative electrode material. Some cells use a blend of graphite and silicon oxide (SiO).

1.4.2 Silicon-containing Materials

Although graphite has a high specific capacity compared to most positive electrode materials, it is not comparable to that of silicon. Lithium can reversibly alloy with Si up to a composition of $\text{Li}_{15}\text{Si}_4$ with a low operational voltage vs. Li/Li^+ , and a large specific capacity of 3500 mAh g^{-1} , but a volume expansion of $\sim 300\%$.⁵⁰⁻⁵² The large volume expansion occurs in every direction, and can cause particle strain and cracking during charge, leading to loss of material during discharge (contraction).⁵³ Particle cracking also leads to newly exposed surface area for parasitic reactions to take place, consuming electrolyte and Li.^{54,55} To mitigate some of this volume expansion, materials such as SiO and SiO-C nanocomposites have been investigated and show improved performance

compared to Si.^{56–59} Combining graphite and Si-containing materials is one way to trade off higher capacity with shorter lifetime. Using combinations of low expansion materials such as graphite with Si/SiO may also decrease the impact of lithiation on structural damage to the entire electrode during cycling.

Parts of this work use cells containing a blend of graphite and SiO as the negative electrode and will be noted in the text where applicable.

1.5 ELECTROLYTES

Electrolytes provide the means of ion transport in lithium-ion cells. This work uses non-aqueous, liquid electrolytes composed of a lithium salt dissolved in solvent. In almost every case there is one or more chemical additive(s) in the electrolyte. Electrolytes should ideally have good lithium diffusion kinetics (high ionic conductivity and low viscosity) to allow for fast charging and discharging rates, high temperature stability, and electrochemical stability suitable for the electrode chemistries. This section will introduce the components of electrolytes, and Section 1.6 will discuss the limitations of electrolytes in high energy density systems with respect to parasitic reactions.

1.5.1 Salts

The most common lithium salt is lithium hexafluorophosphate (LiPF₆). LiPF₆ has a high solution conductivity when dissolved in typical solvents, and good electrochemical stability.⁶⁰ LiPF₆ has been found to decompose electrochemically to form lithium fluoride (LiF) which can help to protect electrodes from parasitic reactions. However, products of thermal decomposition of LiPF₆ such as PF₅ have been found to contribute to the production of CO₂, fluorophosphates, esters, and hydrofluoric acid (HF) above 55°C.^{9,60,61}

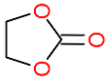
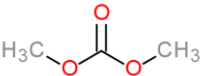
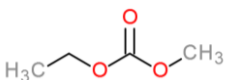
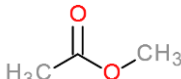
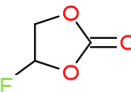
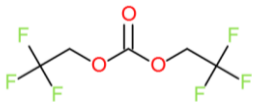
Alternatives to LiPF_6 have been investigated including lithium tetrafluoroborate (LiBF_4), which yields electrolytes with better thermal stability than LiPF_6 , but lower conductivity and poor synergy with graphite electrodes.^{62,63} Lithium bis(oxolato)borate (LiBOB) has been shown to increase thermal stability and cycling performance in NCA/graphite cells at 55°C , but also increases the impedance of the cells, leading to poor rate performance.^{64–66} Blends of LiPF_6 and LiBF_4 ⁶³ or LiBOB ⁶⁶ have shown compromises between the above advantages and disadvantages.

Although many salts have been investigated, LiPF_6 remains the most popular choice for academic and commercial use. This work only uses LiPF_6 .

1.5.2 Solvents

Solvents in lithium-ion cells present some of the largest issues facing the advancement of high energy density, long lifetime cells. Solvents have a strong impact on the performance of cells at different temperatures, the temperature stability of the electrolyte, and the voltage stability of the electrolyte. Typically, a blend of cyclic and linear carbonates is used as the solvent in a lithium-ion cell. Some fluorinated carbonates are also used as solvents. Table 1 shows the chemical structures and some chemical properties of the solvents used in this work: melting point (T_m), boiling point (T_b), viscosity (η_v), and dielectric constant (ϵ).

Table 1: Properties of solvents used in this work.

Solvent name (short form)	Chemical Structure	T _m (°C)	T _b (°C)	η _v (cP 25°C)	ε (25°C)	Ref.
Ethylene Carbonate (EC)		36.4	248	1.90 (40°C)	89.78 (40°C)	3
Dimethyl Carbonate (DMC)		4.6	91	0.59	3.11	3
Ethyl Methyl Carbonate (EMC)		-53	110	0.65	2.95	3
Methyl Acetate (MA)		-98	57	0.4	6.68	67,68
Fluoroethylene Carbonate (FEC)		~20	212	3.5	108	69,70
Bis(2,2,2- trifluoroethyl) Carbonate (TFEC)		-43*	118	Not found	Not found	71

* Measured in the Dahn Lab with a TA DSC q2000 (±1°C)

The rate performance of cells is largely affected by the ionic transport properties of the electrolyte. The viscosity and dielectric constant play a large role in transport properties. Cyclic carbonates such as EC are used to increase the salt dissociation (larger number of charge carriers) due to a higher dielectric constant. However, cyclic carbonates tend to have high viscosity and tend to be solid at room temperature. Propylene carbonate (PC) is another cyclic carbonate with similar properties to EC, but has been found to co-intercalate into graphite, causing exfoliation and active material loss.^{48,49,72} Linear carbonates such as EMC and DMC have a low dielectric constant, but a lower viscosity and melting point than cyclic carbonates, leading to better ion mobility and performance at low temperatures.⁷³ Blends of carbonates such as EC:EMC:DMC (1:1:1 wt.) are typically used in cells because of the balance of physical properties between solvents.³ Other co-

solvents have been investigated to yield good lithium mobility during low temperature performance.

Esters such as methyl acetate (MA) and ethyl acetate (EA) have low viscosities, low melting points, and the ability to impart high ionic conductivity to the electrolyte. MA was first investigated by NASA as a solvent for lithium-ion cells for very low temperature applications due to a melting point of $-98\text{ }^{\circ}\text{C}$.⁶⁷ MA can improve conductivity by 18% and viscosity by 30% at room temperature compared a blend of EC:EMC:DMC (25:5:70 wt.) when 20% wt. of MA is added as a co-solvent.⁶⁸ Studies have found that that MA can significantly increase the high-rate performance of NMC/graphite cells.^{74,75} However, MA has also been found to contribute to decreased cell lifetime due to unwanted reactions with electrodes.^{75,76} Some of the work in this thesis investigated the effect of MA on high rate performance and cell lifetime, and will be discussed in Chapter 6. MA has the potential to allow for very high rate performance in cells and allow for lower temperature applications compared to traditional electrolytes.

Lithium mobility is not the only consideration for electrolyte solvents. The electrochemical stability of the electrolyte plays a major role in determining if a lithium-ion cell will have a long lifetime. If the electrochemical stability window of the electrolyte encompasses the potential ranges of both the positive and negative electrode at all states of lithiation ($\sim 0.1\text{ V} - 4.7\text{ V vs Li/Li}^+$), then unwanted electrochemical side reactions would be less likely. However, most electrolytes made with carbonate solvents tend to oxidize over 4.0 V vs. Li/Li^+ .^{3,77-79} Some solvents such as FEC have been found to oxidize at potentials around 4.5 V .^{80,81} However, FEC also tends to reduce at higher potentials than most other solvents, leading to electrolyte reduction at the negative electrode.^{82,83} EC is

also known to reduce on graphite (low voltage) negative electrodes, forming products such as ethylene, lithium carbonate (Li_2CO_3), and lithium ethylene dicarbonate ($((\text{CH}_2\text{OCO}_2\text{Li})_2)$).^{77,84–86} The instability of electrolytes provides a challenge to the adaptation of high energy density cells due to the broad potential range. Fortunately, the study of electrolyte decomposition has led to the realization that some reaction products actually help prevent further reactions and will be discussed in the next section.

1.5.3 The Solid Electrolyte Interphase

Some reaction products from electrolyte oxidation and reduction form an electrically insulating and ionically permeable (passivating) layer on electrodes known as the solid electrolyte interphase (SEI).^{4,46,46,72,77,86,87} The operational voltage of graphite is much lower than the reduction potential of most solvent molecules, so during the first charge of a lithium-ion cell a significant amount of electrolyte reduction occurs, forming the negative electrode SEI. The first cycle of a lithium-ion cell is known as the ‘formation cycle’. Similar processes can happen at the positive electrode due to oxidation products. The SEI layers can then mitigate further oxidation and reduction.

Many past studies have focused on the negative electrode SEI due to the widespread adaptation of low-voltage graphite negative electrodes.^{47,82,83,88} More recently, similar films have been found on the positive electrode due to oxidation reactions.^{89–91} The SEI has been found to contain not only products of solvent reactions, but is also influenced by salt and transition metals leached from the positive electrode.^{5,92,93} Products from reactions at one electrode have also been found to influence the composition of the other electrode SEI.⁹⁴ This chemical interaction between electrodes is termed ‘cross-talk’.

1.5.4 Additives

Although the SEI layers formed by solvent reactions can help to slow reactions in cells, most solvents do not form completely passivating SEIs. For example, FEC and EC have been found to form slightly passivating SEIs, but the continual growth of SEI leads to shorter lifetime and limits lithium kinetics.^{46,77,95} Some chemicals with much higher reduction potentials than typical solvents have been found to create very robust SEIs, and reduce before the solvent during the formation cycle. When added in controlled amounts, these chemicals can be used to create SEI layers with good passivation and lithium kinetics. The SEIs created by these chemical ‘additives’ then help prevent further parasitic reactions.^{4,83,95–98}

Electrolyte additives allow for a simple, cost effective way of hindering parasitic reactions in lithium-ion cells. A chemical is usually described as an additive when it is used in concentrations of less than 5% by weight (wt.) of the total electrolyte solution. Additive concentrations and blends can be adjusted to tune properties of the SEI during cell manufacturing with little change to the production process. Hundreds of additives have been studied in the literature. Figure 1.7 shows the additives used in this thesis and the abbreviations.

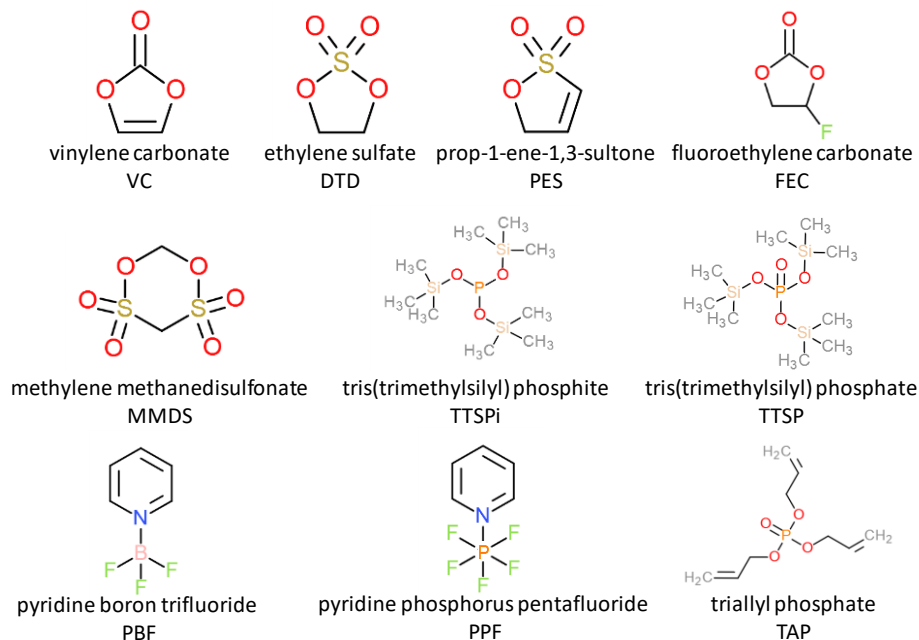


Figure 1.7: Chemical structures and abbreviations of additives used in this work.

Vinylene carbonate (VC) is perhaps the most well-known electrolyte additive. The reduction potential of VC is higher than that of EC, and the products of VC reduction form a very stable, passivating SEI on graphite electrodes compared to that of EC.^{87,99,100} Products of VC reduction include lithium alkyl carbonates (ROCO₂Li), lithium oxalate (Li₂C₂O₄), Li₂CO₃, and polymerized VC.^{83,87} Similar to VC, FEC has been found to form similar SEI products, but also forms LiF which contributes to the protective properties of both positive and negative electrode SEIs.^{61,83,101,102}

Sulfur containing additives such as ethylene sulfate (DTD), methyl methanedisulfonate (MMDS), and prop-1-ene-1,3-sultone (PES) have been found to lead to a very homogeneous, passivating negative electrode SEI containing ROCO₂Li, ROSO₂Li, Li₂CO₃, and lithium sulfite (Li₂SO₃).^{103–106} These additives tend to form SEIs with good lithium mobility, allowing for fast ion transfer when used in small amounts.^{105,106}

Sulfur containing additives such as DTD and MMDS have also been found to contribute to positive electrode SEI layers which also impede electrolyte oxidation.^{105,107}

Many works have investigated combining additives to blend desired SEI properties.^{108–113} One such combination is composed of 2% wt. PES, 1% wt. DTD (or MMDS) and 1% wt. TTSPi. This additive blend is called PES211 and has been found to create very protective SEI layers and yield very long lifetimes compared to almost every other additive combination in the literature in NMC/graphite cells.^{35,113–115} However, due to thick SEI layers on the negative electrode, cells containing PES211 cannot facilitate fast lithium diffusion through the SEI, leading to lithium plating on the negative electrode during high-rate charging.¹¹⁶

Although studied for decades, the exact composition of the SEI, and the chemical pathways leading to its formation are not well understood. The above references typically use surface or gas analysis after SEI formation to probe the SEI composition. The number of parameters present in a lithium-ion cell electrochemical system makes it difficult to determine preferential reaction pathways leading to SEI formation, even with modern computational techniques. *In-situ* analysis techniques are needed to probe SEI formation mechanisms and compare results with other post-mortem analyses and computational studies. Chapter 4 will introduce a technique that could probe formation reactions *in-situ* and non-destructively.

The development of additive systems is extremely important for high-energy density lithium-ion cells. Understanding, or at least quantifying the parasitic reaction processes that are responsible for cell failure is critical to design interphases between the electrodes and electrolytes which prevent or dramatically hinder the decomposition of

electrolyte. The next section will give an overview on different types of parasitic reactions and the impact of each on cell lifetime.

1.6 PARASITIC REACTIONS AND CELL FAILURE

A parasitic reaction in a lithium-ion cell refers to any chemical reaction other than reversible lithium intercalation between electrodes. This work is primarily concerned with the electrochemical decomposition of the electrolyte *via* oxidation or reduction, which are assumed to be the dominant types of parasitic reactions occurring in cells. Other types of parasitic reactions include (but are not limited to): thermal decomposition,^{9,60,117,118} oxidation or alloying of the negative and positive electrode current collectors, respectively,^{119,120} transition metal dissolution from the positive electrode,^{5,6,93,121} and oxygen release^{61,122} from the positive electrode.

Electrolyte species can readily oxidize at the positive electrode when the chemical potential of the positive electrode is lower than the kinetic stability window of the electrolyte species. Similarly, a molecule can reduce when the chemical potential of the negative electrode is higher than the kinetic stability window of the electrolyte species. Passivating SEI layers can effectively raise and lower the upper and lower stability limits of the electrolyte with respect to the electrodes. Figure 1.8 demonstrates a schematic of the kinetic stability window of an electrolyte species with respect to the electrode potentials at a high state of charge (SOC), and the effect of the SEI layers. As the cell is charged (moving to the right in Figure 1.8), the chemical potential of the negative electrode increases rapidly at first, then begins to plateau as graphite staging occurs. Since the operational potential of graphite is outside the stability limit of most solvents, electrolyte

reduction can readily occur if the negative electrode SEI layer is not sufficiently passivating. While a cell is charging the chemical potential of the positive electrode decreases, especially after ~50% delithiation. If the stability limit of electrolyte species is not sufficient for operation at these potentials, species will readily oxidize at the surface.

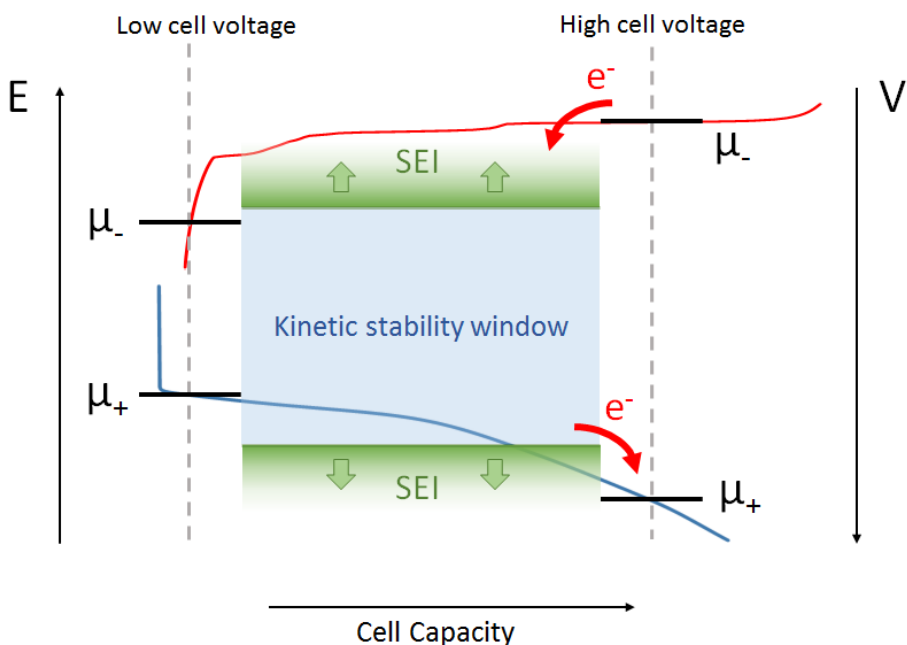


Figure 1.8: Energy level diagram of the kinetic electrolyte stability window with respect to the chemical potential of the positive and negative electrodes. Voltage-capacity curves of a graphite negative electrode (red) and NMC positive electrode (blue) have been added for conceptual aid. When a cell is at low voltage the electrolyte tends to be stable with respect to the electrodes. When the cell is at high voltage the electrolyte can be unstable at the electrodes and oxidize or reduce. The SEI effectively widens the stability window on the positive electrode and negative electrode, preventing further oxidation and reduction at high cell voltage, respectively.

Figure 1.8 demonstrates the issues surrounding high energy density lie in the voltage stability of electrolytes. If the graphite negative electrode is sufficiently passivated, minimal electrolyte reduction will occur. However, the potential of the positive electrode continually increases during charge. If all the theoretical capacity of the positive electrode is to be used, either electrolytes with very high oxidation potentials or very robust positive

electrode SEI layers are needed. Leaving lithium-ion cells at a fully charged or fully discharged state for long periods of time causes higher rates of parasitic reactions to occur. For technologies such as grid storage for renewable energy and EVs long storage times are ideal, and therefore require more stable electrolyte systems.

In addition to the kinetic stability window of the electrolyte, the composition of the electrode materials and temperature have been found to influence the rate and products of parasitic reactions, which further complicates the study of cell failure.^{4,93,121,123} Computational studies have attempted to predict parasitic reaction pathways using quantum chemistry, but rely on simplified models which do not replicate the chemical environment in a real cell.^{84,124–129} Computational techniques tend to overestimate the stability of electrolytes, although the observed trends tend to agree with experimental findings.^{124,129}

This section will introduce the general mechanisms of electrolyte oxidation, reduction, cross-talk, and reversible redox shuttles in lithium-ion cells. The impact of these reactions on various performance metrics and cell lifetime will also be discussed.

Schematics of the active charge and discharge processes in a cell are shown in Figure 1.9. This section contains similar diagrams depicting parasitic reaction processes during charge and discharge. Figure 1.9 can be used to compare parasitic processes to the ideal case.

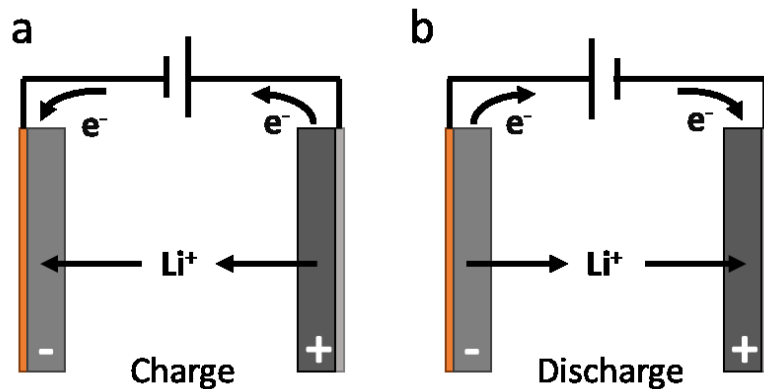


Figure 1.9: a) Charge and b) discharge processes of a lithium-ion cell. The positive and negative electrodes are denoted by a white '+' and a '-', respectively.

1.6.1 Electrolyte Oxidation

If a solvent species denoted S oxidizes at the positive electrode, it loses an electron, creating a charge imbalance in the cell. Thus, to maintain charge balance in the electrodes and the electrolyte, a lithium-ion must be removed from the electrolyte and intercalated into an electrode. Figure 1.10a demonstrates an oxidation process during charge and Figure 1.10b shows oxidation during discharge. Figure 1.10c shows an oxidation process when a cell is in open circuit.

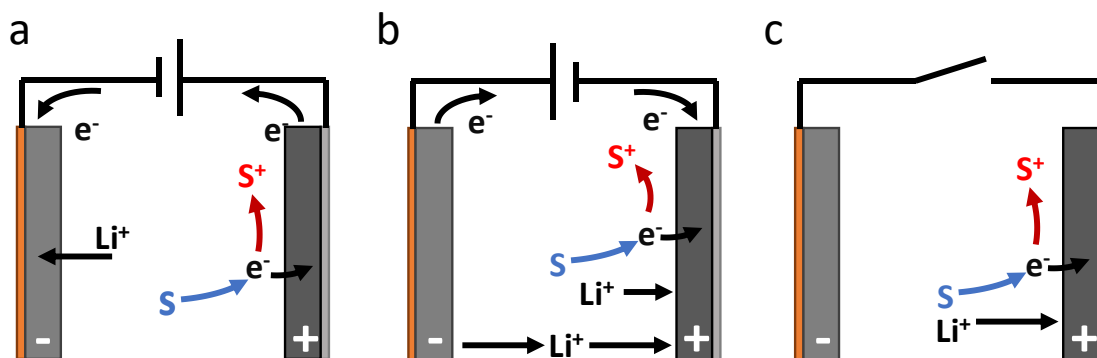


Figure 1.10: Electrolyte oxidation during a) charge, b) discharge, or c) open circuit.

During charge, oxidation causes electrons to be passed through the circuit and lithium is intercalated into the negative electrode. The current due to charge balance counts towards the cell charge capacity but is irreversible during discharge. During discharge oxidation causes lithium to intercalate into the positive electrode without passing current through the external circuit, decreasing the discharge capacity of the cell. In the scenario described by Figure 1.10, the Li^+ concentration in the electrolyte is decreased.

1.6.2 Charge Endpoint Capacity Slippage

The excess capacity during charge and lost capacity during discharge from oxidation reactions can be used as a performance metric. Figure 1.11 shows that when plotting cell voltage vs. cumulative capacity over many cycles, oxidation causes the voltage curve to shift, or slip, towards higher capacity. The difference in capacity between the upper cut-off voltage points of each cycle is called ‘charge endpoint capacity slippage’, labelled ΔQ_c in Figure 1.11. The discharge endpoint slippage, ΔQ_d , can be defined in a similar manner for the lower cut-off voltage.

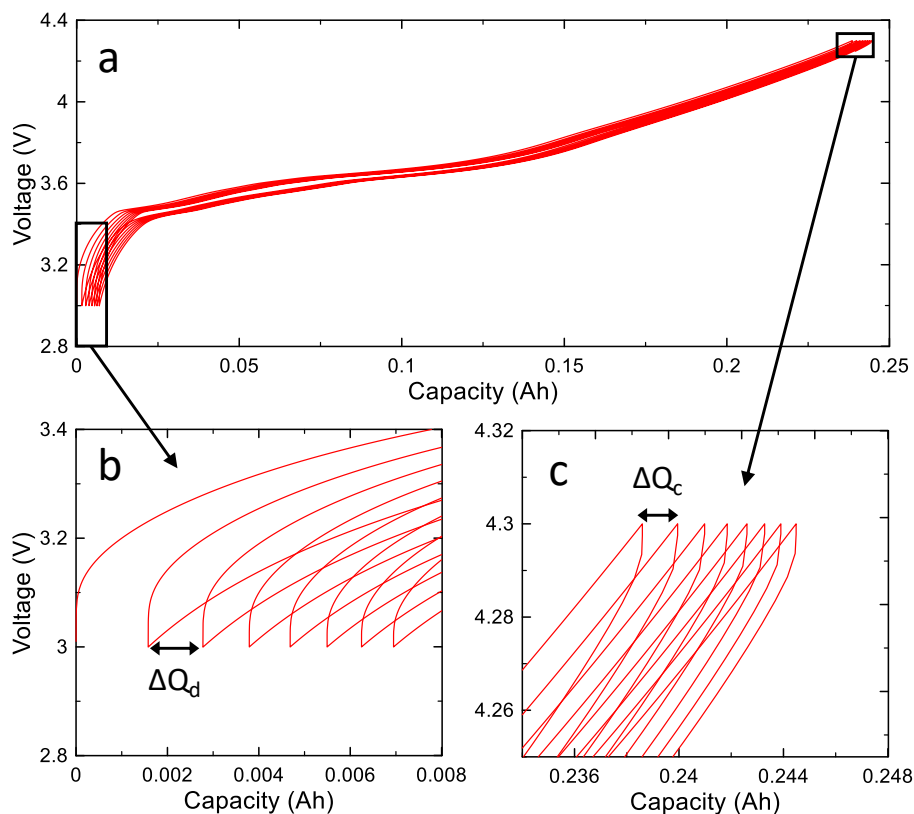


Figure 1.11: Voltage vs capacity of an NMC532/graphite cell during 8 cycles between 3.0 V and 4.3 V. a) shows the full voltage range, b) shows a blown-up view of the discharge endpoint slippage, and c) shows a blown-up view of the charge endpoint capacity slippage.

Typically, the charge endpoint capacity relative to the end of the first cycle is used as a diagnosis of the relative amount of electrolyte oxidation occurring when comparing different cells.¹²¹ Such a plot is shown in Figure 1.12, in which Cell A experiences less electrolyte oxidation than Cell B, and thus shows a slower increase in charge endpoint capacity.

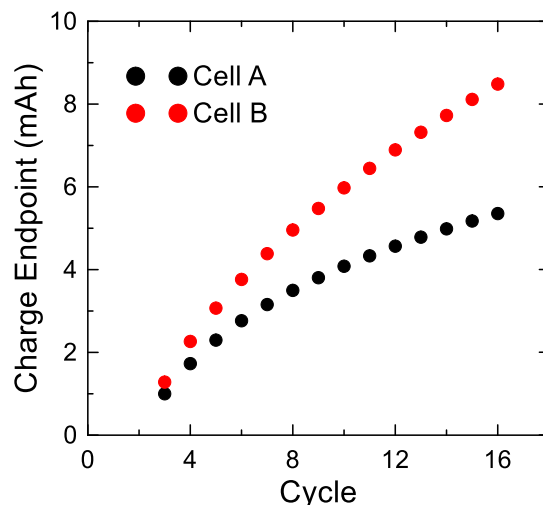


Figure 1.12: Charge endpoint capacity vs cycle number for two cells under identical cycling conditions. Cell A has less electrolyte oxidation.

1.6.3 Self-Discharge

Figure 1.10c shows that oxidation causes lithium intercalation into the positive electrode (self-discharge) in an open circuit condition. At the top of charge, graphite is typically in the stage-2 to stage-1 plateau, and positive electrode materials typically have a sloped voltage curve. Therefore, any change in the open circuit voltage (OCV) at the top of charge is due to self-discharge from oxidation processes.¹³⁰ A common comparative test is to measure the OCV of cells with different solvents or additives at various temperatures and voltages. These OCV tests are a very simple way to probe electrolyte oxidation and are referred to as ‘storage’ tests. Storage tests can also be done at low cell voltage to probe electrolyte reduction. At low cell voltages the positive electrode is not as oxidative, while negative electrodes can still react with electrolyte. Therefore, low-voltage storage tests are also useful to probe reduction reactions.

Figure 1.13 shows an example of a storage test at 60°C where Cell A (shown in black) experiences less electrolyte oxidation than Cell B (shown in red). Duplicates of each cell are shown to demonstrate the consistency of the measurements.

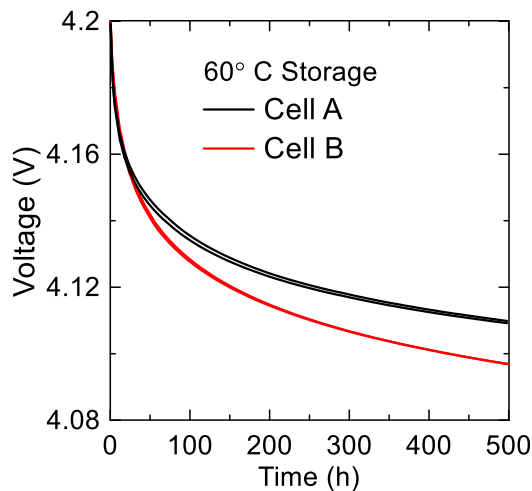


Figure 1.13: Open circuit storage test at 60°C and a starting voltage of 4.2 V. Cell A (black) experiences less electrolyte oxidation as Cell B (red). Results for identical pair cells are shown.

1.6.4 Electrolyte Reduction

When electrolyte species S is reduced at the negative electrode, gaining an electron, it can react with Li^+ from the salt, electrode, or SEI.^{4,47,121,131} Figure 1.14 shows a schematic of electrolyte reduction. Charge balance is maintained by lithium deintercalation from the negative electrode, so no additional current is passed through the circuit, unlike during electrolyte oxidation. Thus, the schematic is unchanged for reduction during charge, discharge, and OCV.

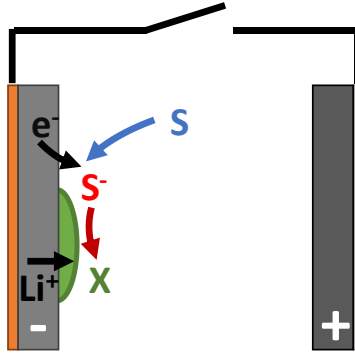


Figure 1.14: Electrolyte reduction at the negative electrode. Electrolyte species S reduces, gaining an electron from the negative electrode. A Li^+ ion then reacts irreversibly with S^- to form species X, shown as a solid product to demonstrate SEI growth.

1.6.5 Capacity Fade

Electrolyte reduction irreversibly consumes Li in a cell, which influences the achievable capacity. To illustrate the effect of electrolyte reduction on cell capacity, consider the following situation: N Li atoms are available in the positive electrode. $(N - n)$ are intercalated into the negative electrode during charge and n Li atoms are consumed in reduction reactions. Then the maximum reversible amount of lithium would be $(N - n)$ during discharge. After discharge when the graphite is empty of lithium, the positive electrode contains $(N - n)$ Li atoms and the cell has n fewer Li atoms in its ‘inventory’. The positive electrode can never be fully lithiated after any reduction occurs.

Capacity loss, usually called capacity fade (Q_{fade}) in the literature, can be quantified by the change in charge or discharge capacity (Q^d) between a cycle $(n-1)$ and subsequent cycle n :

$$Q_{fade} = Q_{n-1}^d - Q_n^d. \quad 1.4$$

Capacity fade can also be written as the difference between charge endpoint capacity slippage and subsequent discharge endpoint capacity slippage:

$$Q_{fade} = \Delta Q_d - \Delta Q_c . \quad 1.5$$

Capacity loss due to reduction can be visualized as the electrode voltage curves effectively shifting with respect to each other and is called ‘shift loss’. Figure 1.15 demonstrates the effect of electrolyte reduction on capacity loss and shift loss in an NMC/graphite cell using the example above.

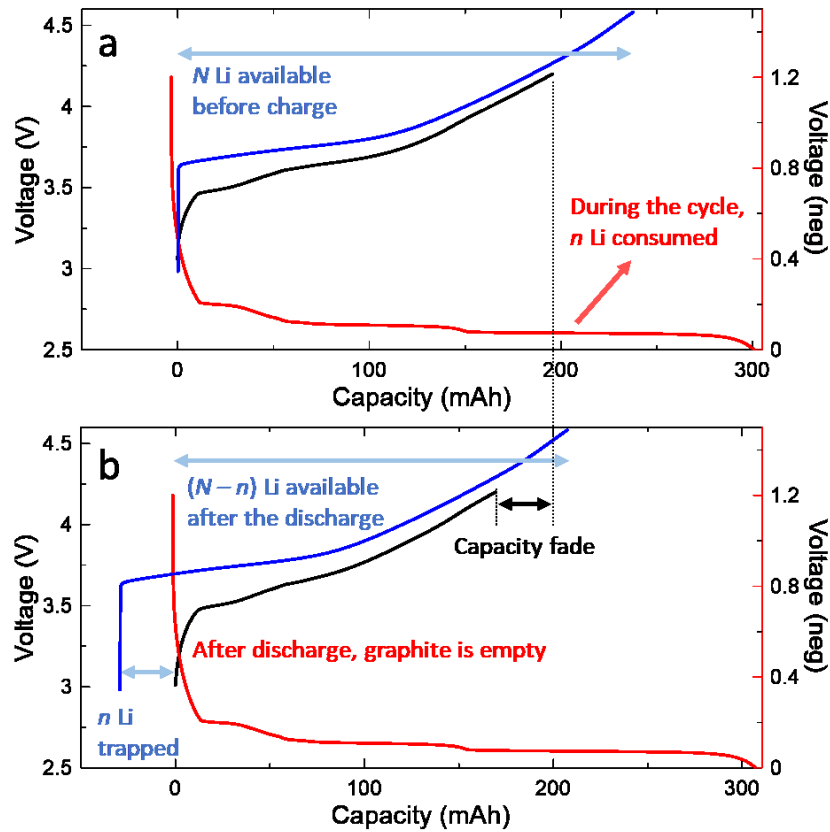


Figure 1.15: Relative electrode shift due to electrolyte reduction in an NMC/graphite cell cycled between 3.0 V and 4.2 V. The NMC positive electrode is shown as a blue curve, the graphite negative electrode is shown by a red curve, and the full cell is shown in black. a) Before cycling the electrode voltage curves align at 0 mAh and the positive electrode contains N Li atoms. b) After cycling, n Li atoms have been consumed in reduction processes. When graphite empties, the positive electrode contains $N - n$ Li atoms, and the available capacity of the cell is decreased.

The discharge capacity or fractional discharge capacity vs. cycle number or time can be used as a tool to probe electrolyte reduction. However, capacity loss can also be

caused by active material loss or an increasing rate of oxidation, which can cause difficulties when comparing results between cell chemistries.^{121,132,133} The fractional discharge capacity for two cells cycled under identical conditions is shown in Figure 1.16. Cell A (shown in black) experiences less fade than Cell B (shown in red) and might therefore have fewer reduction processes occurring.

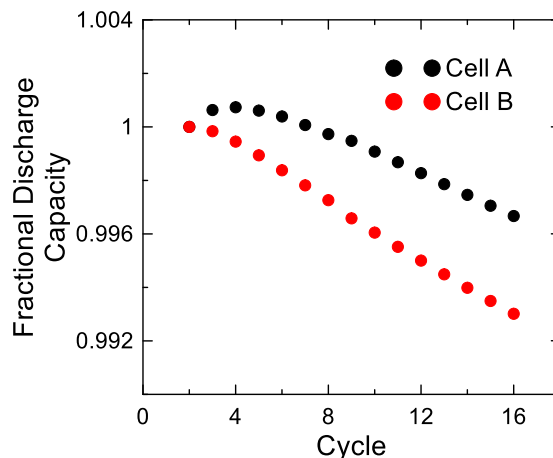


Figure 1.16: Fractional capacity fade for two cells under identical cycling conditions. Cell A may experience less electrolyte reduction causing capacity loss than Cell B.

A useful technique has been developed to fit full cell voltage curves to the constituent positive and negative electrode curves before and after cycling.^{132,134,135} This technique to measure electrode shift loss fits the derivatives of reference electrode voltage curves to the full cell voltage curve to determine the amount of shift loss that has occurred. Thus, this method is called ‘dV/dQ analysis’. Capacity fade due to active mass loss can be accounted for by shrinking the relative size of the voltage curves in addition to relative slippage. However, dV/dQ analysis requires low rate cycles and high precision to achieve clear features in the voltage curves.

1.6.6 Cross-talk and Shuttle Reactions

As mentioned previously, when an electrolyte species is oxidized or reduced products from the reactions can migrate to the other electrode and further react there. This interaction between electrodes is called cross-talk. Figure 1.17 shows a cross-talk reaction beginning with species S oxidizing at the positive electrode and migrating to the negative electrode to be reduced. Some cross-talk processes have the same effect on slippage, storage, and capacity fade as the combination of a single oxidation reaction and a single reduction reaction combined. However, the implications of cross-talk reactions mean that not only do the individual electrode materials play a role in the rate and type of reactions occurring in cells, but the combination of electrode materials can also affect the parasitic reactions that occur. Therefore, solvent or additive systems cannot be developed universally for all cells and must be tuned to each unique combination of chemistries.

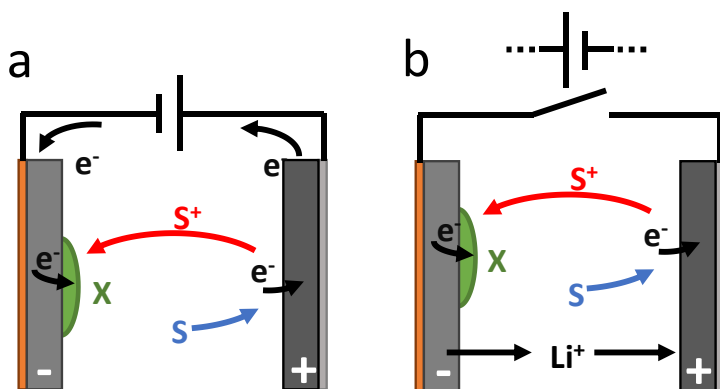


Figure 1.17: Cross-talk between electrodes. Electrolyte species S is oxidized at the positive electrode, and the product is reduced at the negative electrode into SEI species X. a) shows cross-talk during charge and b) shows cross-talk during discharge and OCV.

One special type of cross-talk reaction is a reversible ‘shuttle reaction’, demonstrated in Figure 1.18.^{136,137} After a species S is oxidized to S^+ at the positive electrode it can migrate to the negative electrode and reversibly reduce back to S. During

charge and discharge a shuttle reaction causes charge endpoint capacity slippage, but does not contribute to capacity fade, SEI growth (and thus impedance growth), or any other detrimental effects.

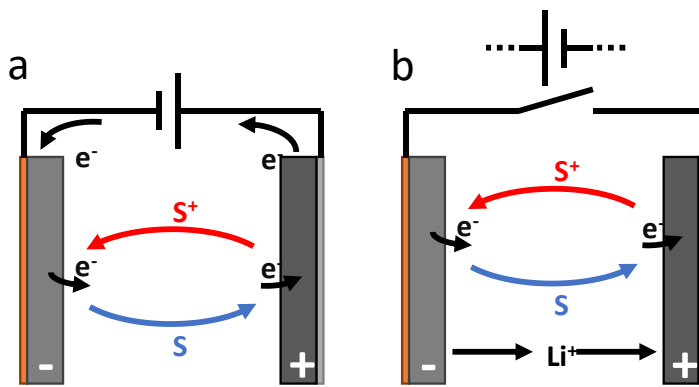


Figure 1.18: A reversible electrolyte shuttle reaction. Species S is oxidized at the positive electrode, migrates to the negative electrode, and reduces reversibly back to S. a) During charge a current supplies charge balance to the cell. b) During discharge or OCV a self-discharge mechanism provides charge balance.

Truly reversible redox shuttles can influence the measured capacity loss or charge endpoint capacity slippage without having an impact on the lifetime of a cell. However, it is likely rare that a shuttle reaction involving species from the electrolyte is truly reversible. It may be that multiple transits of a molecule occur between electrodes before the oxidized species reacts and cannot transfer charge anymore. Therefore, measurements of charge endpoint capacity slippage can overestimate the degree of electrolyte oxidation if a large number of transits can occur compared to a single transit. Some works have employed redox shuttle molecules with specific activation potentials to prevent cell overcharge in systems where individual cell voltages are not monitored.^{136,138–140}

1.6.7 Coulombic Efficiency

All failure mechanisms in a lithium-ion cell contribute to a discrepancy in the amount of capacity supplied to a cell during charge (Q_c) and the subsequent amount of capacity which can be recovered during discharge (Q_d).^{121,141} The ratio of discharge capacity to the previous charge capacity is called the coulombic efficiency, or CE:

$$CE = \frac{Q_d}{Q_c}. \quad 1.6$$

If the CE of a cell is exactly unity, a cell would last forever. The CE has contributions from the fractional charge endpoint capacity slippage (oxidation) per cycle and the fractional capacity fade (reduction and active material loss) per cycle, both with respect to the discharge capacity of the cycle:¹²¹

$$CE = 1 - \left(\frac{\Delta Q_c}{Q_d} + \frac{Q_{fade}}{Q_d} \right). \quad 1.7$$

The CE of a cell has been found to be a very good short-term predictor of cell failure if measured with enough accuracy.^{121,141,142} Figure 1.19 shows the CE of two cells tested under identical conditions. Cell A has a higher CE than Cell B, meaning Cell A has fewer parasitic reactions and/or less material degradation occurring. Thus, Cell A will very likely have a longer lifetime.

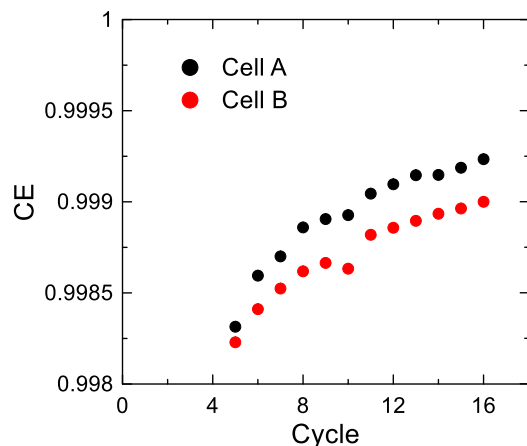


Figure 1.19: Coulombic efficiency vs cycle number for two cells under identical cycling conditions. Cell A has a higher CE than Cell B and will likely have a longer lifetime. Small changes in temperature (as seen in cycle 10) can have a noticeable impact on high-precision measurements.

If a cell is to last 100 cycles before it reaches 80% of its original capacity, a CE of ~ 0.998 is required. For a cell to last 10000 cycles to 80% capacity, a CE of ~ 0.99998 is required. The precision in CE measurements is therefore very important and must be on the order of 10^{-5} to predict cell lifetimes in the tens of thousands of cycles. The ultra-high precision charger at Dalhousie University is capable of these precision measurements, and has been used extensively as a tool to probe parasitic reactions and cell lifetimes with different electrode chemistries, solvent systems, and additives.^{108–113,121,135,141–143}

1.6.8 Impedance

Electrolyte oxidation and reduction consumes electrolyte species over time, which can ultimately lead to cell failure if too much electrolyte is decomposed or if thick, passivating layers form. The rate of these processes tends to slow over time as SEI growth occurs, as seen by the increase in CE in Figure 1.19. However, SEI growth increases the impedance of a cell over time, limiting Li^+ diffusion which can lead to Li plating on the negative electrode.^{116,144,145}

The impedance of a cell has contributions from the electrolyte, electrode materials, and SEI layers.^{2,146,147} The internal resistance of all the components of the cell (R_{cell}) contributes an overpotential (η), when a direct current I is applied. The overpotential also has contributions from the intrinsic voltage hysteresis of the electrode materials (V_{hyst}), diffusion effects, and lithium concentration gradients.^{148,149} The overpotential can be interpreted as the difference between the measured cell voltage (V_{cell}) and the thermodynamic equilibrium voltage of the electrodes. Ignoring the impact of diffusion effects, the overpotential can be written as

$$\eta = V_{cell} - V_{eq} = IR_{cell} + V_{hyst}. \quad 1.8$$

During charge the overpotential increases the measured cell voltage by η and decreases the cell voltage by η during discharge. The separation of charge and discharge voltage is often referred to as voltage polarization. Figure 1.20a shows voltage polarization during one cycle of an NMC532/graphite cell. The current applied to the cell was small and equal to the cell capacity over 20 hours (C/20), or 12 mA. A higher current would increase η as shown by Equation 1.8. Cell impedance is often monitored during cycling by observing the difference in average voltage (\bar{V}) between charge and discharge, called ΔV :

$$\Delta V = \bar{V}_{charge} - \bar{V}_{discharge}. \quad 1.9$$

Figure 1.20b shows ΔV vs. cycle number for two cells. Cell A, in black experiences less impedance growth than Cell B, in red.

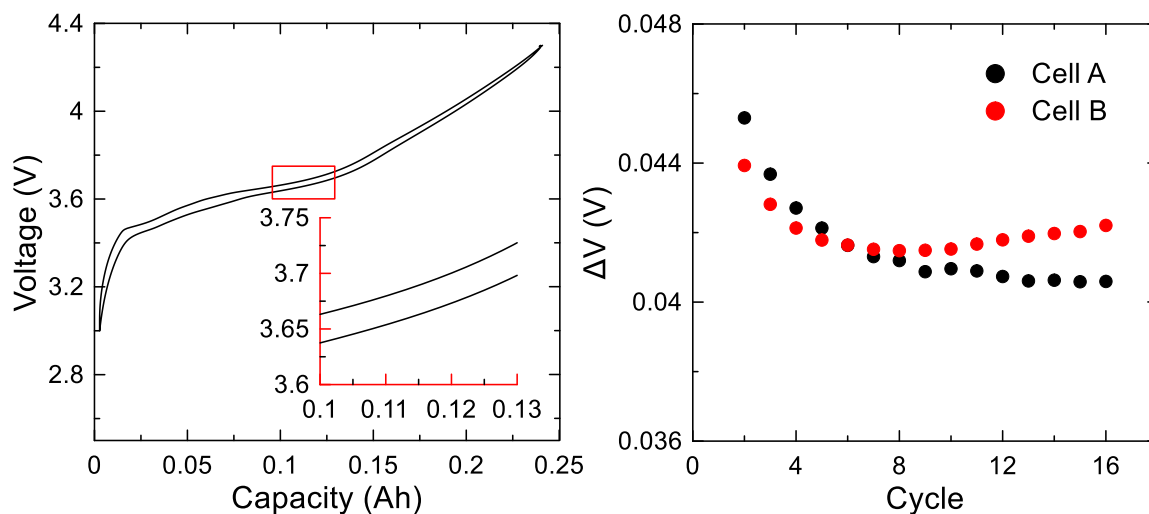


Figure 1.20: a) Voltage vs capacity of a charge discharge cycle of an NMC532/graphite cell at a C/20 rate from 3.0 V to 4.3 V. The inset shows a blown-up scale depicting voltage polarization, when η is the cell overpotential. b) ΔV vs. cycle for two cells cycled under identical conditions. Cell A (black) has less impedance growth than Cell B (red).

1.7 SCOPE OF THESIS

The previous sections introduced the components of lithium-ion cells, some of the major challenges in adapting high energy density cells while maintaining long lifetime, and some common methods to probe parasitic reactions. This aim of the work presented in this thesis is to develop new testing methods to investigate parasitic reactions in lithium-ion cells that are complementary to existing techniques. Desired methods are *in-situ* and non-destructive and can be made on machine-made pouch cells yielding consistent results.

This work aims to combine existing electrochemical techniques with isothermal microcalorimetry. Isothermal microcalorimetry is a method of measuring the thermal power, or heat flow, of a sample (in this case a lithium-ion cell). During normal operation a lithium-ion cell has multiple contributions to the heat flow, including a portion due to the energy absorbed and released in parasitic reactions. In theory it should be possible to use

the information from this ‘parasitic heat flow’ to learn more about parasitic reactions. Chapter 2 will discuss isothermal microcalorimetry and its application to lithium-ion research. Past works using isothermal calorimetry to study lithium-ion cells will be discussed and the current work will be motivated. Emphasis will be given towards works which used isothermal microcalorimetry to study parasitic reactions.^{150–154}

Chapter 3 will discuss the experimental techniques used in this thesis including the cells used in this work, electrolytes, ultra-high precision coulometry, long-term cycling, gas evolution measurements, electrochemical impedance spectroscopy, storage experiments, and isothermal microcalorimetry of cells. The treatment of uncertainty throughout this work will also be discussed briefly.

Chapter 4 will introduce the use of isothermal microcalorimetry to help determine SEI formation processes. The heat flow during SEI formation is compared with quantum chemistry calculations and electrochemical tests.

Chapter 5 will introduce a method to measure the average parasitic heat flow of a lithium-ion cell as a function of voltage during a slow charge-discharge process. The application of this charge-discharge technique will be discussed using two studies: the effect of voltage and electrolyte additives in electrolytes containing no EC in NMC442/graphite cells, and the effect of graphite type and additive content on parasitic reactions in NMC532/graphite cells.

Chapter 6 will discuss additional developments to the charge-discharge method. The treatment of the cell overpotential will be considered to increase the cycling rate of the experiments. Additionally, a technique will be introduced which approximates the heat flow due to the changes in entropy of the electrode materials, which can be used to

differentiate between the parasitic heat flow during charge and discharge. These developments are applied to two studies: the effect of MA on parasitic reactions in NMC532/graphite and NCA/SiO-graphite cells, and the effect of various NMC compositions and positive electrode coatings on the parasitic heat flow of NMC/graphite cells.

Chapter 7 will introduce a technique which aims to extract information about the net enthalpy reaction of parasitic reactions in lithium-ion cells. The heat flow of a cell was measured during voltage-hold conditions while the current is provided by precision current sources. The use of calorimetry to determine the enthalpy of reaction was validated in proof-of-concept studies using reversible shuttle molecules. The voltage-hold technique was then applied to study the effect of three solvent systems (organic carbonates, organic carbonates with MA, and fluorinated carbonates) and positive electrode coatings on parasitic reaction enthalpy.

Chapter 8 will discuss the impact and conclusions of this work and provide recommendations for future studies using isothermal microcalorimetry to study parasitic reactions in lithium-ion cells.

CHAPTER 2 LITHIUM-ION ISOTHERMAL MICROCALORIMETRY

Isothermal microcalorimetry is a method of measuring the thermal power, or heat flow, of a sample at constant temperature. This chapter will introduce the use of isothermal microcalorimetry for the study of lithium-ion cells. Section 2.1 will derive the model used in this work for the heat flow of a lithium-ion cell during operation and discuss each contribution to the heat flow. Past studies of lithium-ion cells using isothermal microcalorimetry will be discussed in Section 2.3, with a focus on studies probing parasitic reactions.

2.1 HEAT FLOW OF A LITHIUM-ION CELL

2.1.1 Derivation of Measured Heat Flow

The derivation below was adapted from Dr. Laura Downie's thesis.¹⁵⁵ The change in energy (U) of a lithium-ion cell at a constant temperature (T) is expressed as the sum of the change in heat (q') supplied to the cell and the change in work done on the cell (W):

$$dU = dq' + dW. \quad 2.1$$

The thermal power, or heat flow given off by the cell (q) as measured by the calorimeter can then be written as:

$$\frac{dq}{dt} = \frac{dW}{dt} - \frac{dU}{dt}. \quad 2.2$$

The change in internal energy can be rewritten in terms of the entropy (S) and Gibbs free energy (G) (at constant volume and pressure):

$$dU = TdS + dG. \quad 2.3$$

When a cell is charged by a current I , the time derivative of the electrochemical work done to the cell is equal to the supplied current multiplied by the cell voltage (V_{cell}). During discharge this work is done to the system. Therefore, the current supplied to a cell during charge is defined as positive, and the current supplied by the cell during discharge is negative. Work is also done to the system by the change in volume of the cell (v) multiplied by the pressure (P):

$$\frac{dW}{dt} = IV_{cell} - P \frac{dv}{dt}. \quad 2.4$$

The change in volume in pouch cells due to gas generation in this work is on the order of 0 mL to 0.5 mL. Volume growth of 0.5 mL at 1 atm over one day of testing would yield a heat flow of 0.59 μ W, which is at the detection limit ($\sim 1 \mu$ W) of the calorimeter used in this work. Additionally, the cell volume fluctuates due to reversible structural changes in the electrode materials. The reversible volume change from electrode materials has been found to be $\sim 30 \mu$ L.⁵⁹ Therefore, the change in volume is considered negligible and not considered in this work. Combining equations 2.2, 2.3, and 2.4, the heat flow measured by the calorimeter is given by:

$$\frac{dq}{dt} = IV_{cell} - T \frac{dS}{dt} - \frac{dG}{dt}. \quad 2.5$$

The entropy of mixing due to concentration gradients in the electrode materials and electrolyte are negligible in comparison to the change in configurational entropy and phase changes in the electrode materials.¹⁵⁶ Therefore, only changes in entropy related to the change in lithiation state of the electrode materials will be considered. The entropy contribution can be expressed as the change in entropy per lithium site (s) with the change

in lithium content in the material (x), where x is the ratio of filled lithium sites (n) to the total number of sites (N):

$$\frac{dS}{dx} = N \frac{ds}{dx}. \quad 2.6$$

The entropy and Gibbs free energy of each electrode must be considered independently, denoted by + and – subscripts for the positive and negative electrodes, respectively. Equation 2.5 may be combined with Equation 2.6 using the chain-rule for derivatives, to give:

$$\frac{dq}{dt} = IV_{cell} - TN \left(\frac{ds_+}{dx_+} \frac{dx_+}{dt} + \frac{ds_-}{dx_-} \frac{dx_-}{dt} \right) - \left(\frac{dG_+}{dx_+} \frac{dx_+}{dt} - \frac{dG_-}{dx_-} \frac{dx_-}{dt} \right). \quad 2.7$$

The change in fractional lithium content of each electrode can be expressed by:

$$\frac{dx_{\pm}}{dt} = \mp \frac{I}{Ne} \quad 2.8$$

where e is the electronic charge. During charge (positive I), the positive electrode is delithiated (negative change in x), and the negative electrode is lithiated (positive change in x).

The change in Gibb's free energy with lithium content can be written in terms of the chemical potential:

$$\frac{dG}{dx} = \frac{dG}{dn} N = N\mu. \quad 2.9$$

Substituting Equations 2.8 and 2.9 into 2.7 yields:

$$\frac{dq}{dt} = IV_{cell} + \frac{IT}{e} \left(\frac{ds_+}{dx_+} - \frac{ds_-}{dx_-} \right) - \frac{I}{e} (\mu_- - \mu_+). \quad 2.10$$

Equation 1.1 shows that the last term in 2.10 is equal to the thermodynamic equilibrium voltage between the electrodes, V_{eq} multiplied by I . The difference between the measured and equilibrium potentials is the cell overpotential (see Section 1.6.8).

$$V_{cell} - V_{eq} = \eta \quad 2.11$$

Equation 2.10 can then be written as

$$\dot{q} = \frac{dq}{dt} = I\eta + \frac{IT}{e} \left(\frac{ds_+}{dx_+} - \frac{ds_-}{dx_-} \right). \quad 2.12$$

Equation 2.12 describes the measured heat flow of an ideal cell. As discussed in Section 1.6, parasitic reactions occur in cells, which are not described by Equation 2.12. Every chemical process absorbs or emits energy, in this case in the form of heat. Therefore, a term to account for the parasitic heat flow must be added (\dot{q}_p):

$$\dot{q} = I\eta + \frac{IT}{e} \left(\frac{ds_+}{dx_+} - \frac{ds_-}{dx_-} \right) + \dot{q}_p. \quad 2.13$$

As will be seen, \dot{q}_p is highly dependent on the cell voltage, materials, and electrolyte used.

Equation 2.13 describes the heat flow of a lithium-ion cell with an applied current. This thesis uses various experimental protocols to isolate the parasitic heat flow using Equation 2.13. The first term in Equation 2.13, the overpotential heat flow, and the second term, the entropic heat flow, will be discussed in the next sections.

2.1.2 Overpotential

As discussed in Section 1.6.8, the overpotential of a cell is the difference between the measured cell voltage and the thermodynamic equilibrium voltage of the electrode materials. Using Equation 1.8, the heat flow due to overpotential can be expressed as

$$I\eta = I^2 R_{cell} + IV_{hyst}. \quad 2.14$$

The voltage hysteresis is positive during charge and negative during discharge. Therefore, the overpotential heat flow is always exothermic. Since the overpotential heat flow is current-dependent, the magnitude of this term can be adjusted with respect to the parasitic heat flow to increase the accuracy of measurements.

2.1.3 Entropy

As mentioned above, the only considerable contribution to entropic heat flow in lithium-ion cells is due to the changes in entropy of the electrode materials. Configurational entropy changes arise as lithium ions are inserted into or removed from the electrode material lattice structures. In some materials such as $\text{Li}_x\text{Mo}_6\text{Se}_8$ (from $0 < x < 1$) the entropy as a function of x can be modeled well by a mean-field lattice gas approximation, in which lithium randomly occupies sites during lithiation.^{157,158} However, in most materials such as graphite, NMC, NCA, and LCO, phase transitions take place yielding complicated entropy profiles.^{159–161}

Experimental methods have been developed to measure the change in entropy of materials as a function of lithiation using potentiometric studies^{159–162} and electrothermal impedance spectroscopy (ETIS).¹⁵⁹ Potentiometric techniques measure the change in OCV with the temperature of a cell at many states of charge (x') to obtain an entropy profile, given by

$$\frac{dS(x')}{dx} = e \frac{dV_{eq}(x')}{dT}. \quad 2.15$$

However, long relaxation times for the lithium concentration in the electrode materials when the cell potential is changed causes this technique to be very time consuming (>30 hours per state of charge) for use in this work. ETIS techniques measure a temperature differential between the cell and the ambient temperature ignoring contributions to heat due to parasitic reactions in cells. Therefore, such a treatment of measuring the change in entropy is also unsuitable for this work. Due to the limitations of the existing techniques outlined above, the present work aimed to develop techniques to

extract the parasitic heat flow that did not depend on a robust treatment of the entropic heat flow.

Equation 2.13 shows that the entropic heat flow is dependent on the current applied to the cell. This current dependence has two advantages: the entropic heat flow is reversible between charge and discharge, and, as for the overpotential heat flow, the magnitude of the entropic heat flow can be controlled by the current. Chapter 5 uses the reversibility and proportionality of the entropic heat flow of a cell to the applied current to calculate the parasitic heat flow. Chapter 6 introduces a new technique using the methods developed in Chapter 5 to obtain an approximation of the entropic heat flow.

2.1.4 Heat Flow of an NMC/graphite cell

Figure 2.1a shows the heat flow (in black) of one cycle of a machine-made NMC532/graphite cell at a rate of C/20 (10 mA) from 3.0 V to 4.2 V as a function of capacity. Section 3.1 will discuss the pouch cells used in this work in more detail. The measured cell voltage is shown on the right axis, in blue. The heat flow and voltage during charge and discharge are shown as solid and dashed lines, respectively. An orange line demonstrates the approximate level of irreversible heat flow. Irreversible heat flow is due to the overpotential heat flow and the parasitic heat flow. The reversible entropic heat flow causes an approximate mirror-like effect around the irreversible heat flow as a function of voltage. Figure 2.1b shows a blown-up scale of the high-voltage region of the cycle in which heat flow is plotted against cell voltage.

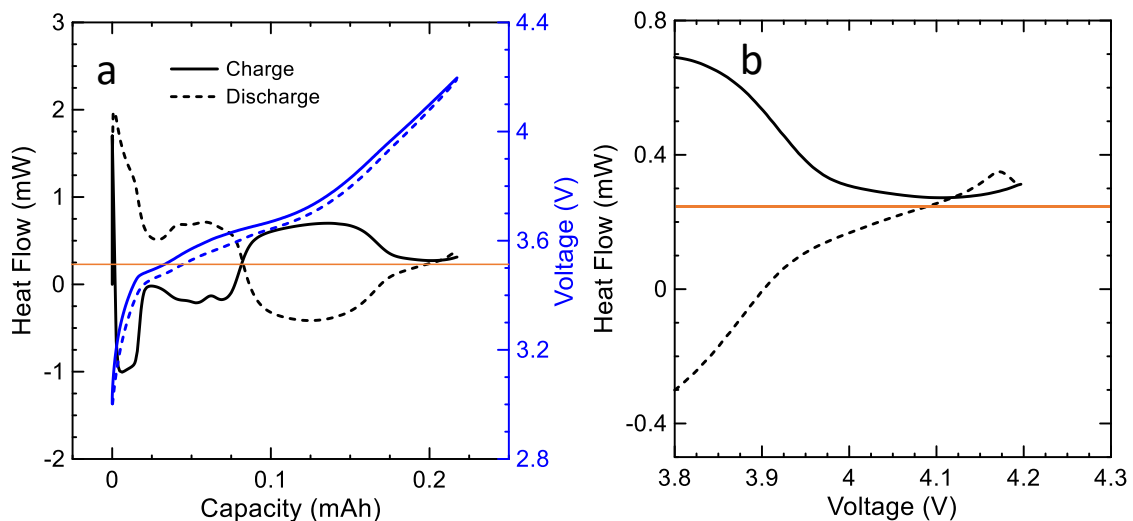


Figure 2.1: Heat flow profile of an NMC532/graphite cell during charge to 4.2 V (solid line) and discharge to 3.0 V (dashed line) at 10 mA and 40°C. Heat flow is shown in black and cell voltage is shown in blue. An orange line shows the approximate irreversible heat flow. a) Full cycle view. b) Blown up view of the high-voltage region, demonstrating an increase in parasitic heat flow, plotted against voltage.

In Figure 2.1b the heat flow appears to increase, deviating from the average heat flow above ~ 4.0 V. The sudden increase in heat flow was due to parasitic reactions occurring in the cell at high voltage. When the positive electrode voltage increased out of the stability window of the electrolyte, the rate of oxidation and likely reduction and cross-talk processes increased (see Section 1.6).

2.2 PARASITIC HEAT FLOW

Almost all past work using isothermal microcalorimetry has focused on measuring the magnitude of the parasitic heat flow. However, the effect of different types of parasitic reactions must be considered carefully when comparing the magnitude of parasitic heat flow between different cell chemistries. Section 1.6 introduced the mechanisms taking place inside a cell during electrolyte oxidation and reduction.

When an oxidation reaction occurs (with no cross-talk) in a cell with an applied current, an internal current forms inside the cell due to the transfer of positive charge from one electrode to the other (see Figure 1.10). This current will be referred to as the parasitic current, I_p . The parasitic current causes a heat flow of $I_p V$. Additionally, the enthalpy of reaction of the oxidation process ΔH_{ox} , occurring at a rate k_{ox} , causes a heat flow of $-k_{ox}\Delta H_{ox}$. The enthalpy of reaction is the difference between the enthalpies of the products and the reactants. Therefore, an exothermic reaction has a negative enthalpy of reaction. The parasitic heat flow of one type of oxidation process is therefore

$$\dot{q}_{p\ ox} = I_p V - k_{ox}\Delta H_{ox}. \quad 2.16$$

During a reduction reaction (with no cross-talk, shown in Figure 1.14), no internal transfer of charge occurs. Therefore, the parasitic heat flow due to one type of reduction process is simply

$$\dot{q}_{p\ red} = -k_{red}\Delta H_{red}. \quad 2.17$$

The total heat flow of all reactions occurring in a cell can be expressed as

$$\dot{q}_p = I_p V - \sum_i k_i \Delta H_i. \quad 2.18$$

Equations 2.16 to 2.18 demonstrate that different types of reactions can have a large impact on the parasitic heat flow of a cell. If a cell has a considerable rate of reduction reactions and no oxidation reactions, it may still have a lower parasitic heat flow compared to a cell with fewer oxidation reactions due to the $I_p V$ term present in the cell experiencing electrolyte oxidation. Cross-talk reactions, in which there would be a contribution from $I_p V$ and the net reaction enthalpies of chemical reactions at both electrodes must also be considered.

The effect of different reactions on parasitic heat flow must be considered throughout this work when comparing the magnitude of parasitic heat flow between cells. Chapter 7 will introduce some methods which aim to probe the reaction enthalpies of parasitic reactions.

The following section will introduce some isothermal microcalorimetry studies that have been done in the past, with an emphasis on studies which probed parasitic reactions in lithium-ion cells.

2.3 PAST STUDIES OF LITHIUM-ION ISOTHERMAL MICROCALORIMETRY

Isothermal calorimetry studies on lithium-ion cells began as early as 1985,¹⁵⁷ and until recently, largely focused on the overpotential and entropic terms, neglecting the heat flow due to parasitic reactions. Some of these studies aimed to probe structural changes in positive and negative electrode materials using the entropic heat flow.^{157,163–168} Kobayashi et al.¹⁶⁸ investigated the effect of cycling a commercial LCO/graphite cell over 700 times on the total heat flow of the cell. Separate coin cells which contained LCO/Li, graphite/Li, and LCO/graphite were measured. The cells with Li metal electrodes are called half-cells. By studying the entropy profiles of the full cells compared to half-cells it was found that the main degradation mechanism of the commercial cell over 700 cycles was due to active material mass loss of the graphite negative electrode. Lu and Prakesh¹⁶⁹ showed that graphite staging transitions in mesocarbon microbeads yield reversible entropic heat flow which agrees with graphite entropy profiles found by other techniques. Other studies have investigated the effect of charge and discharge rate on heat generation, with a focus on thermal management.^{165,170–172}

Of particular interest to the present work are studies which have used very high accuracy isothermal microcalorimeters to probe parasitic reactions in cells. Krause et al.¹⁵⁰ developed the first of such methods probing the parasitic reactions occurring in cells containing LTO and graphite negative electrode materials. Equation 2.13 showed that the entropic heat flow is reversible between charge and discharge, and the overpotential heat flow is always exothermic. The parasitic energy (E_p) of one cycle (of time t) was calculated using the difference between the integrated charge and discharge heat flow (\dot{q}_{ch} and \dot{q}_{dis}) (to remove the entropic contribution) minus the overpotential heat flow of the cycle calculated as the difference between the integrated IV power during charge (IV_{ch}) and discharge (IV_{dis}):

$$E_p = \int_0^t \dot{q}_p = \left(\int_0^t \dot{q}_{ch} dt - \int_0^t \dot{q}_{dis} dt \right) - \left(\int_0^t IV_{ch} dt - \int_0^t IV_{dis} dt \right) \quad 2.19$$

The method developed by Krause et al. enabled measurements of the parasitic energy of small coin cells (capacity ~2 mAh) with $\pm 5\%$ to 15% uncertainty. The magnitude of the parasitic heat flow agreed with the observed trend in measurements of CE and capacity fade. The method can be applied to voltage windows to explore the effects of average voltage on parasitic heat flow but cannot be used to measure the parasitic heat flow as a continuous function of voltage. The method was also used to calculate the enthalpy of reaction using the total parasitic energy divided by the moles of lithium lost per cycle, measured by capacity fade (see Section 1.6.5), assuming the only contribution to parasitic heat flow was due to reaction enthalpy.

A more recent publication by Krause et al.¹⁵¹ used the same method of extracting the parasitic energy and explored the effect of different rates and voltage windows. The study compared machine-made, wound LCO/graphite pouch cells with a capacity of ~250

mAh. The method proved to be consistent at rates of 10 mA and 20 mA. However, the method could still only determine coarse-grained effects of voltage on parasitic heat flow. Additionally, the consistency in the data may only be suitable for comparisons between cells with a substantial difference in performance.

A significant amount of work was done by Dr. Laura (Downie) McCalla to probe parasitic reactions using isothermal microcalorimetry. Many parts of this work are a continuation of Dr. Downie's work in the Dahn Lab.

Downie et al.¹⁵² studied the total measured heat flow of LCO/graphite pouch cells containing varying amounts of VC as an electrolyte additive. By cycling at a low rate of $<C/100$ (2 mA) from 3.9 V to 4.2 V, the contributions of entropic heat flow and overpotential heat flow were small enough to observe considerable differences due to parasitic heat flow. The results showed that in the voltage ranges studied, the addition of VC decreased the parasitic heat flow in cells, in agreement with measurements of CE. However, being qualitative, the technique did not account for differences in resistance due to thicker SEI layers in cells with more VC. Additionally, without accounting for the entropic heat flow, different cell chemistries are not comparable using this method.

Downie and Dahn¹⁵³ then developed a method to calculate the parasitic heat flow by modelling each contribution in Equation 2.13 by a linear or quadratic function f (eg. $f = Az + B$, where A and B are fitting parameters and z is the state of charge). The overpotential heat flow was assumed to be primarily due to internal resistance, so the voltage hysteresis was not included. Under this treatment, Equation 2.13 becomes

$$\dot{q} = f_{\text{overpotential}}(z) \cdot I^2 + f_{\text{entropy}}(z) \cdot I + f_{\text{parasitic}}(z). \quad 2.20$$

Pouch cells (LCO/graphite and NMC/graphite) with capacities of ~ 200 mAh were charged and discharged in small voltage windows of 0.1 V above 3.9 V at rates of 10 mA, 5 mA, 2 mA, and 1 mA. The fitting parameters for each term were then adjusted to provide a least squares fit over all four currents in each voltage window. Figure 2.2i shows an example of the fitted data for the four currents from 4.2 V to 4.3 V using quadratic entropic and parasitic terms and a linear overpotential term. The dashed magenta line represents the extracted parasitic heat flow using the fitting method. It should be noted that the parasitic heat flow appeared to be well represented by the average of the 1 mA charge-discharge data. Figure 2.2ii shows the fitted components for the highest current, 10 mA, in a) and the lowest current, 1 mA, in b). Figure 2.2iii demonstrates the results of this fitting method for two NMC442/graphite cells containing a control electrolyte (no additives) and the same electrolyte with 2% wt. VC as an additive.

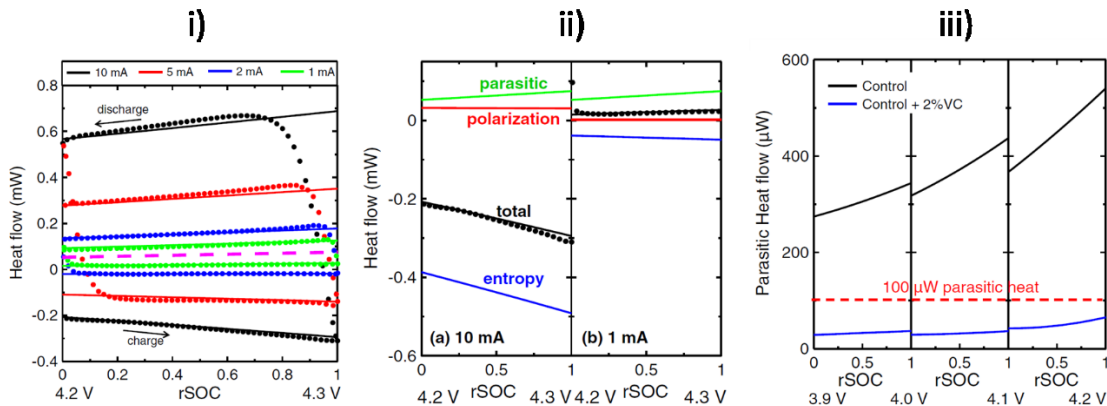


Figure 2.2: Figures from Downie and Dahn.¹⁵³ i) Fitted heat flow of an NMC/graphite pouch cell cycled at four rates between 4.2 V and 4.3 V using a quadratic entropic term and linear terms for overpotential and parasitic heat flow. The dashed magenta line represents the calculated parasitic heat flow ii) The resulting functions for entropic, overpotential (polarization), and parasitic heat flow at 10 mA and 1 mA. iii) Extracted parasitic heat flow for NMC/graphite cells with 2% wt. VC as an additive and a control (no additive) electrolyte. Figures used with permission from the Journal of the Electrochemical Society, **161**, A1782-A1787 (2014).¹⁵³

The above method developed by Downie and Dahn was capable of obtaining the parasitic heat flow as a function of voltage and extracting and comparing the parasitic heat flow of any cell type. However, the experiments had several drawbacks. Since each voltage range required multiple currents, the experiments took a substantial amount of time. As seen in Figure 2.2iii, the extracted parasitic heat flow was discontinuous at the voltage endpoints. Possible reasons for the discontinuities were:

1. Model functions: Heat flow components are not modelled realistically by linear or quadratic functions, even in small voltage ranges.

2. Overpotential: Heat flow contributions from voltage hysteresis needed to be considered, especially during cycles with higher currents. Additionally, overpotential caused by higher currents causes the measured cell potential to show anomalous behaviour near voltage endpoints when current changes, as seen in 10 mA and 5mA cycles in Figure 2.2i.

3. Time dependence: SEI growth due to parasitic reactions mitigates parasitic reactions and therefore parasitic heat flow. Fitting used in this method assumed the parasitic heat flow function was the same during each cycle.

To address point 3 above, Downie et al.¹⁵⁴ added a time dependence to the parasitic heat flow term in Equation 2.20. The results showed that the parasitic heat flow did change over time and the inclusion of a time dependent term could improve the model. However, the experiments still required a long time and yielded large discrepancies at voltage endpoints. Additionally, any heat flow caused by an impedance increase in the cell over the four cycles at each voltage range may be absorbed into the time-dependent parasitic term, contributing to additional uncertainty.

To explore the effect of voltage hysteresis, Downie et al.¹⁷³ explored the effect of current and cell materials on the cell overpotential. A voltage dependent overpotential term was included in the time dependent model based on the cell type used.

Downie's methods were the first reported techniques to provide accurate measurements of parasitic heat flow over large voltage ranges that were independent of the cell type used. However, the methods required lengthy data collection times and very careful treatment of data during the fitting process. Cells chemistries could be compared using this method provided the difference in heat flow was larger than the uncertainty in fits and the discrepancies between voltage window endpoints. It was one goal of this thesis to improve on the approach developed by Downie and coworkers.

CHAPTER 3 EXPERIMENTAL TECHNIQUES

3.1 POUCH CELLS

All electrochemical measurements used in this work were performed on small, machine-made, wound pouch cells ranging from 180 mAh to 370 mAh in capacity. Figure 3.1 (cell 1) shows the cell geometry used for NMC/graphite cells used in this work. All NMC/graphite cells used in this work were made by LiFUN Technology (Zhuzhou City, Hunan Province, PRC). Figure 3.1 (cell 2) shows the cell geometry used for NCA/SiO-graphite cells used in this work. All NCA/SiO-graphite cells used in this work were obtained from one of Tesla's suppliers. Figure 3.1a shows each of the exterior pouch cell geometries. The extra room above each jelly-roll allows for any gas generated to be moved out of the electrode stack. Figure 3.1b shows the jelly-rolls when removed from the cells. Figure 3.1c and d show the unwound jelly-rolls of the NMC/graphite and NCA/SiO-graphite geometries, respectively. In each case, the positive electrode is on top, the negative electrode is on the bottom, and the separator envelopes the negative electrode.

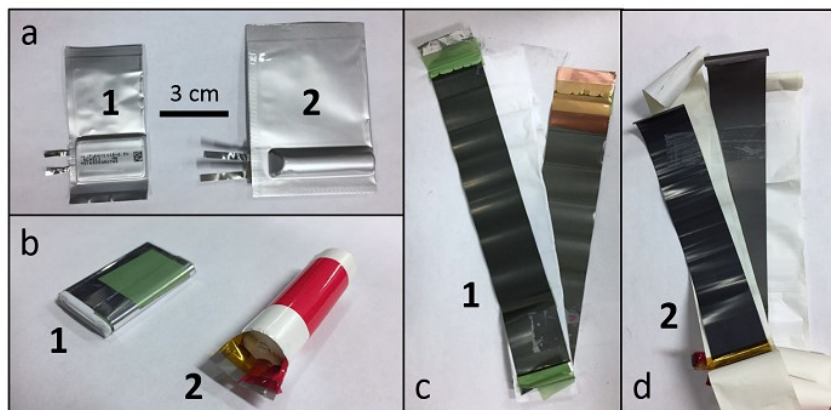


Figure 3.1: The two cell geometries used in this thesis. a) 1: LiFUN NMC/graphite pouch cell, 2: Panasonic NCA/SiO-graphite cylindrical pouch cell. b) Jelly-rolls of the two cell types. c) Unrolled NMC/graphite cell. d) Unrolled NCA/SiO-graphite cell.

Table 2 lists the specifications for all cells used in this work, where data were available. In each experiment throughout this work, the cells used will be indicated by the cell name provided in the first row of Table 2.

Table 2: Cell builds used in this work

Cell Name	NMC442/AG	NMC532A/NG	NMC532B/NG	NMC622A/NG	NMC622B/NG	SC NMC532/NG	SC NMC532/AG	Coated SCNMC532/	Uncoated SCNMC532/AG	NCA/SiO-graphite
Manufacturer	LiFUN	LiFUN	LiFUN	LiFUN	LiFUN	LiFUN	LiFUN	LiFUN	LiFUN	Tesla Supplier
Balance Voltage	4.7 V	4.5 V	4.5 V	4.5 V	4.5 V	4.5 V	4.5 V	4.4 V	4.4 V	4.2 V
Capacity to 4.2 V	160 mAh	260 mAh	260 mAh	245 mAh	245 mAh	225 mAh	225 mAh	225 mAh	225 mAh	360 mAh
Positive Electrode Material	NMC442	NMC532	NMC532	NMC622	NMC622	Single crystal NMC532	Single crystal NMC532	Single crystal NMC532	Single crystal NMC532	NCA
Coating	None	Al ₂ O ₃	Proprietary	Al ₂ O ₃	Proprietary	Proprietary	Proprietary	Proprietary	None	
Pos. Elect. conductive additives		CB	CB	CB	CB	CB+KS-6	CB+KS-6	CB+KS-6	CB+KS-6	
Pos. Elect. Binder		PVDF	PVDF	PVDF	PVDF	PVDF	PVDF	PVDF	PVDF	
Positive Electrode Composition Ratio		96:02:02	96:02:02	96:02:02	96:02:02	94:2:2:2	94:2:2:2	94:2:2:2	94:2:2:2	
Separator		PE	PE	PE	PE	PE	PE	PE	PE	
Negative Electrode Material	Artificial graphite	Natural graphite BTR918II	Natural graphite BTR918II	Natural graphite BTR918II	Natural graphite BTR918II	Natural graphite BTR918II	Artificial graphite Kaijin AML400	Artificial graphite Kaijin AML400	Artificial graphite Kaijin AML400	SiO-graphite blend
Negative Electrode conductive additive		CB+CMC+SBR	CB+CMC+SBR	CB+CMC+SBR	CB+CMC+SBR	CB+CMC+SBR	CB+CMC+SBR	CB+CMC+SBR	CB+CMC+SBR	
Negative Electrode Composition		95.4:1.3:1.1:2.2	95.4:1.3:1.1:2.2	95.4:1.3:1.1:2.2	95.4:1.3:1.1:2.2	95.4:1.3:1.1:2.2	95.4:1.3:1.1:2.2	95.4/1.3/2.2/1.1	95.4/1.3/2.2/1.1	
Positive Electrode Material Source	Umicore	Umicore	Umicore	Umicore	Umicore					N/A
Negative Electrode Material Source		BTR	BTR	BTR	BTR	BTR	Kaijin	Kaijin	Kaijin	N/A

CB = carbon black, KS-6 = artificial graphite, PVDF = polyvinylidene fluoride, PE = polyethylene, CMC = carboxymethyl cellulose, SBR = styrene butadiene rubber

3.2 ELECTROLYTES

All electrolytes used in pouch cells were made in an argon-filled glovebox. Table 3 lists the supplier and purity of each chemical used in this work. Each experiment will refer to chemicals used in this table.

Table 3: Electrolyte chemicals used in this work

Electrolyte Chemical	Common name	Company	Purity (%)	Water content (ppm)
LiPF ₆	lithium hexafluorophosphate	BASF	99.9	<20
EC	ethylene carbonate	BASF	99.95	<10
EMC	ethyl methyl carbonate	BASF	99.92	<20
EC:EMC:DMC (25:5:70 wt.)	blend of EC, EMC and dimethyl carbonate (DMC)	BASF or Capchem	99.92	<20
EC:EMC (3:7 vol.)	blend of EC and EMC	BASF or Capchem	99.92	<20
FEC	fluoroethylene carbonate	BASF	99.94	<20
TFEC	bis(2,2,2-trifluoroethyl) carbonate	HSC Corporation	99.8	
MA	methyl acetate	BASF	99.99	
VC	vinylene carbonate	BASF	99.5	<100
TAP	triallyl phosphate	TCI America	>94	
TTSPi	tris(trimethylsilyl)phosphite	TCI America	>95	
TTSP	tris(trimethylsilyl)phosphate	TCI America	>98	
PES	prop-1-ene-1,3-sultone	Lianchuang Medicinal Chemistry Co., Ltd	98.2	
PBF	pyridine boron trifluoride	3M	>97	
DTD	1,3,2-dioxathiolane-2,2-dioxide	Sigma Aldrich	98	
DDB	2,5-di-tert-butyl-1,4-dimethoxybenzene	Sigma Aldrich	98	
DBDB	3,5-di-tert-butyl-1,4-dimethoxybenzene	Odom Lab, University of Kentucky	NA	
DMB	2,5-dimethyl-1,4-dimethoxybenzene	Odom Lab, University of Kentucky	NA	

3.3 CELL FORMATION CYCLE

The formation cycle of a cell is the first cycle the cell undergoes after being filled with electrolyte. Ideally most of the SEI is formed during this cycle. This work used different rates and upper cut-off voltages during formation. Therefore, each experiment will specify the specifics of each formation process. However, some information is common to every formation protocol, and will be discussed below.

Before being filled with electrolyte, cells were cut open and heated in a vacuum oven for 14 hours at 80°C (NMC442/graphite) or 100°C (all other cells) to remove residual moisture. The cells were then transferred into an argon-filled glovebox without exposure to air. In the glovebox, cells were filled with a predetermined amount of electrolyte with an adjustable air-displacement pipette. The volume of electrolyte used will be noted in discussion of each experiment. Cells were sealed with a compact vacuum sealer (MSK-115A, MTI Corp.). NMC/graphite cells were sealed for 4 seconds at 165°C and -90 kPa. NCA/SiO-graphite cells were sealed for 5 seconds at 170°C and -90 kPa. All cells were then placed in cell holders and connected to a ‘wetting station’ which held cells at a constant voltage of 1.5 V for 24 hours to ensure complete electrode wetting by the electrolyte.

Cells were then connected to a Maccor 4000 series cycler (Maccor Inc.). Three formation protocols were used in this work, and will be referred to by Formation A, B, or C. The upper cut-off voltage (UCV) used in each protocol will be noted in the text where applicable as it varied by experiment. The term ‘degas’ below refers to moving cells into the glovebox, cutting open the pouch to release gas, and resealing the cell using the same vacuum sealing conditions as noted above.

The formation protocols are:

- A. NMC/graphite: Clamp cell between rubber spacers to displace gas formed during formation. Charge to UCV at a $C/20$ rate in a $40 \pm 0.1^\circ\text{C}$ temperature box. Hold at UCV for one hour. Discharge to 3.8 V at $C/20$. Hold at 3.8 V for one hour. Degas.
- B. NCA/SiO-graphite: Charge for one hour at a rate of $C/2$ in a $40 \pm 0.1^\circ\text{C}$ temperature box (50% SOC). Store at OCV in a $60 \pm 0.1^\circ\text{C}$ temperature box for 23 hours. Move back to $40 \pm 0.1^\circ\text{C}$ and charge to 4.2 V at $C/2$ and hold for one hour. Discharge to 3.8 V at $C/2$ and hold for one hour. Degas.
- C. Heat flow during formation: Charge at 2 mA ($\sim C/100$) at 40°C up to 3.5 V.

3.4 LONG-TERM CYCLING

One of the simplest ways to test the lifetime of a cell is to perform charge-discharge cycling. By varying the temperature, UCV, and rate, the lifetime of electrode materials, coatings, solvents, co-solvents, and additives can be tested head-to-head. Typically, these tests are done at moderate to high rates to accelerate degradation mechanisms. Due to the desired rates, long testing times, and high throughputs of long-term cycling experiments, the accuracy of measurements is typically not sufficient to compare charge-endpoint slippage or CE. Therefore, long-term cycling tests are typically used to track discharge capacity, normalized capacity, and ΔV over hundreds or thousands of cycles or hours.

Cells were clamped between rubber blocks in cell holders and placed in $40.0 \pm 0.1^\circ\text{C}$ or $20.0 \pm 0.1^\circ\text{C}$ temperature boxes or a temperature-controlled room at $20 \pm 1^\circ\text{C}$. Cells were connected to Neware battery testers (Neware, Shenzhen, China) and were

cycled between specified lower and upper voltage cut-offs at various rates. The rate, temperature, and voltage limits of each testing profile will be specified in each experiment.

Long-term cycling tests were done using constant-current-constant-voltage (CCCV) conditions during charge and a constant-current discharge. A CCCV charge means the cell is charged to the upper cut-off voltage at constant current. The cell is then held at the upper cut-off (constant-voltage) until the current drops below a specified value (typically $C/20$). The constant voltage portion ensures that all cells reach a more uniform state of charge regardless of the constant current rate.

3.5 ULTRA-HIGH PRECISION COULOMETRY

Ultra-high precision coulometry (UHPC) allows for accurate measurements of the CE, charge-endpoint slippage, capacity fade, and ΔV . The UHPC at Dalhousie has an accuracy of 5 ppm in measurements of CE, which is necessary to extrapolate lifetime on the order of many thousands of cycles (see Section 1.6.7).¹⁴¹ The high-precision primarily comes from the measurement of the supplied current. The current is supplied from a Keithley 2602B source-meter (0.002% of full scale setpoint accuracy) and measured externally by the voltage drop over a precision resistor as measured by a Keithley 2002.¹⁷⁴ The measurement accuracy of the current is 0.003% of full scale.¹⁴¹ For reference, the accuracy of the Maccor 4000 and Neware systems are 0.05% and 0.1% of full scale, respectively.^{175,176} Additional improvements in precision are due to the accuracy in voltage measurements (< 0.2 mV vs. 1 mV and 2.5 mV for the Maccor and Neware systems), and

time between measurements (<1 s due to linear interpolation vs. 10 ms and 1-5s¹ for the Maccor and Neware systems, respectively).^{175,176}

UHPC measurements reported in this work were performed at $40.0 \pm 0.1^\circ\text{C}$ in temperature-controlled boxes. UHPC measurements are typically made at low rates to reduce the uncertainty in CE. This work performed most tests using C/20 constant current cycling between two voltage set points for 16 cycles. Specifics of each protocol will be noted for each experiment.

3.6 GAS MEASUREMENTS

3.6.1 *Ex-situ* gas measurements

Ex-situ gas measurements were performed by measuring the weight of a cell submerged in water before and after various testing protocols. *Ex-situ* gas measurements are a quick and useful way to determine the overall gas production of any test such as formation or long-term cycling. When time-dependent or voltage-dependent effects on gas generation are desired, *in-situ* methods are more useful (next section). In this work, all cell volumes were measured before and after formation, calorimetry tests, and cycling. The results are shown when applicable.

For *ex-situ* gas measurements, cells were suspended by a hook connected to a precision balance and submerged in NanoPure water (Barnstead NanoPure, Thermo Scientific) with a resistivity of 18 M Ω cm and density of 0.9982 g cm⁻³ at 20°C. The density of water changes approximately 0.0002 g cm⁻³ per degree Celsius around 20°C.¹⁷⁷ The volumes of pouch cells used in this study were ~2.5 mL, and changes in volumes were

¹ Multiple versions of Neware systems were used during this thesis

considered significant over 0.1 mL. Therefore, a density of 1 g cm^{-3} was used for convenience, with negligible loss in accuracy.

Using Archimedes' principle, a cell of mass m_{cell} and volume v_{cell} suspended in a liquid with density ρ would yield a mass m_{meas} measured by the balance given by

$$m_{meas} = m_{cell} - \rho v_{cell}. \quad 3.1$$

When measured again after any given test, the difference in mass before and after the test yields

$$\Delta m_{meas} = \Delta m_{cell} - \rho \Delta v_{cell}. \quad 3.2$$

Considering the mass of the sealed cell cannot change, and assuming a density of 1 g cm^{-3} the magnitude of the change in volume is equal to the change in mass of the cell:

$$\Delta m_{meas} = -\rho \Delta v_{cell}. \quad 3.3$$

3.6.2 *In-situ* gas measurements

In-situ gas measurements can be made in tandem with electrochemical measurements to observe time, rate, and voltage dependent gas generation. For example, *in-situ* gas measurements can determine the onset voltage of gas production during the formation cycle or the onset of gas-producing parasitic reactions during high-voltage tests.

Measurements were performed by using the apparatus and procedure described by Aiken et al.¹⁷⁸ Cells were suspended in silicone vacuum pump oil and the change in weight was measured using sensitive load cells and converted to volume using Archimedes' principle. Cells were connected to a Neware cycler for electrochemical tests. The specifics of each protocol will be discussed for each experiment.

3.7 ELECTROCHEMICAL IMPEDANCE SPECTROSCOPY

Electrochemical impedance spectroscopy (EIS) is a very useful technique to probe the effects of different electrode materials, electrolytes, and testing conditions on the evolution of cell impedance. As mentioned in Section 1.6.8 parasitic reactions can form reaction products which thicken the SEI layers, increasing cell impedance. Additionally, mechanical damage to electrodes such as particle cracking or loss of electrical connection and salt or electrolyte loss can contribute to the cell impedance.^{146,147,179–181} EIS measurements are made by applying a small oscillating potential (V) typically on the order of millivolts to a cell and measuring the current response. The impedance of the cell (Z_{cell}) is then given by

$$Z_{cell} = \frac{V}{I}. \quad 3.4$$

A simple schematic of an electrode-electrolyte interface can be modelled as follows: a resistor (R_s) and capacitor (C) in parallel can be used to represent the electronic resistance and electrochemical double-layer capacitance formed by the SEI, and a resistor (R_{el}) can be used to represent the ionic resistance of the electrolyte. This circuit section is shown in Figure 3.2a. The equivalent impedance of this system can be written as

$$\begin{aligned} Z_{eq} &= R_{el} + \frac{1}{\frac{1}{R_s} + j\omega C} \\ &= R_{el} + \frac{R_s}{1 + \omega^2 C^2 R_s^2} - j \frac{\omega C R_s^2}{1 + \omega^2 C^2 R_s^2}. \end{aligned} \quad 3.5$$

The positive real vs. negative imaginary components of the impedance can be plotted to compare EIS ‘spectra’ between cells. This type of plot is referred to as a Nyquist plot. Figure 3.2b shows the Nyquist plot for the simple circuit section shown in Figure 3.2a, in

which the impedance components are typically multiplied by the electrode area. The high-frequency intercept in this case is due to the ionic resistance of the electrolyte. The diameter of the semi-circle is equal to the charge-transfer resistance (called R_{ct}) through the SEI.

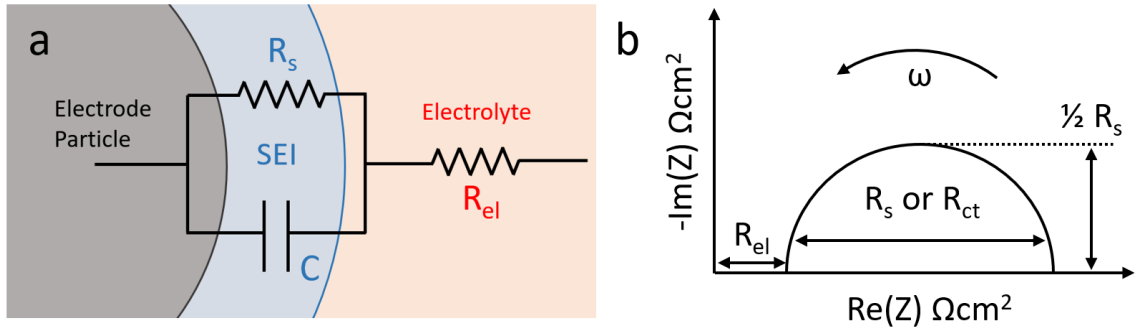


Figure 3.2: a) A simple circuit component model of an electrode-electrolyte interface. b) A Nyquist plot of the circuit section shown in a) when an AC response is measured, given by Equation 3.5. The signal frequency ω increases from right to left.

Figure 3.2 demonstrates the simplest case scenario for one ideal electrode. In a cell there are two electrodes, inhomogeneous SEI layers, connections between cell particles, different sizes and shapes of particles, connections between the electrode particles and current collectors, and the separator. Complex modelling and fitting of impedance spectra using many parameters cells have been reported in the literature.^{147,179,180,182} However, these treatments are quite intensive and are out of the scope of this thesis. Typically, the R_{ct} value of the diameter of the semi-circle in the Nyquist plot is used to compare impedance between cells, or before and after tests. Changes in R_{ct} value indicate the total increase in charge transfer resistance through both electrodes, SEI layers, and the electrolyte. This work primarily uses the R_{ct} value to make comparisons between cells.

EIS measurements before and after tests in this work were performed in a $10.0 \pm 0.1^\circ\text{C}$ temperature box. AC impedance spectra were collected at a cell voltage of 3.8 V

from 10 kHz to either 10 mHz, 30 mHz, or 100 mHz (ten points per decade) with a signal amplitude of 10 mV using a Biologic VMP-3.

One experiment in Chapter 6 used an automated EIS technique. Automated EIS measurements were made using an in-house frequency response analysis (FRA) system described by Nelson et al.¹⁴⁶ Cells were cycled at a rate of C/3 between 3.0 V and 4.2 V in a $40 \pm 0.1^\circ\text{C}$ temperature box with a constant voltage hold until the current reached C/20 at the top of charge. Every 20 cycles an FRA cycle was performed. In an FRA cycle the current was changed to C/20 and every 0.1 V during both charge and discharge the current was stopped and the impedance spectrum was collected.

3.8 STORAGE EXPERIMENTS

Storage experiments can probe the rate of reactions at the positive or negative electrode by measuring the OCV of a cell at high or low cell voltages, respectively (see Section 1.6.3). Storage experiments were performed after cycling a cell twice between two specified voltage endpoints at a rate of C/20. Cells were then charged or discharged to the desired storage voltage, held at a constant voltage for 24 hours, and immediately transferred to a $60^\circ\text{C} \pm 0.1^\circ\text{C}$ temperature box connected to high-precision Keithley voltage meters (Keithley Instruments) through a switching network. Cell voltages were recorded once every 15 minutes for the first 6 hours, then once every 6 hours for 494 hours.

3.9 ISOTHERMAL MICROCALORIMETRY

A significant amount of preliminary work was done by Dr. Laura (Downie) McCalla to establish isothermal microcalorimetry in the Dahn Lab at Dalhousie University.

The experimental setup described below was established during Downie's PhD work.¹⁵⁵ Changes to the setup by Downie were only made to repair broken cables or to connect cells to different charging systems. Section 3.9.1 will discuss the measurement of heat flow using an isothermal microcalorimeter. Section 3.9.2 will describe the experimental setup used in this work. Section 3.9.3 will describe the baseline and calibration method used before each experiment. Section 3.9.4 will discuss the treatment of uncertainty in measurements of heat flow.

3.9.1 Heat Flow Measurements

Isothermal microcalorimetry experiments were performed using a TAM III isothermal microcalorimeter (TA Instruments). The TAM III used in this work had twelve microcalorimeters with 20 mL sample holders (ampoules). The TAM III has an operational temperature range of 15°C to 150°C with a temperature stability of 10 μ K/24h and precision of 100 μ K.^{183,184} The temperature precision is achieved using a temperature monitoring system with 32 platinum resistance thermometer sensors and a proprietary heating and cooling system.¹⁸³ The calorimeters monitor the heat flow to an accuracy of 1 μ W, have a sensitivity of 100 nW, and a maximum detectable heat flow of 50 mW.^{183,184} The accuracy of the calorimeter is limited by the temperature stability of the oil-filled thermal bath, and the precision is limited by the detection limit of the thermocouple sensors. Figure 3.3 shows an expanded view of one calorimeter channel in the TAM III.

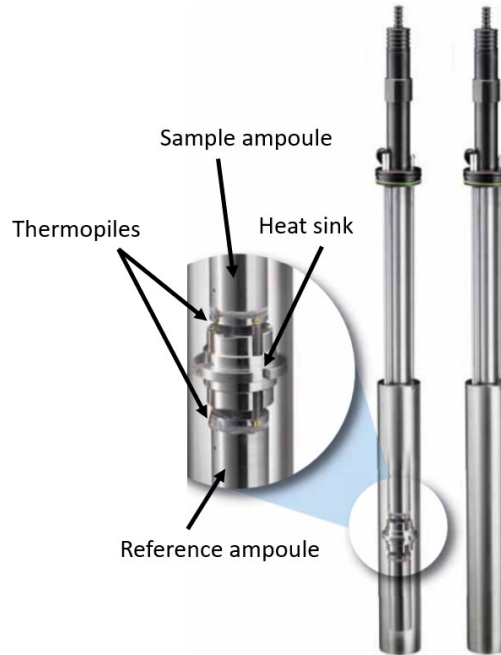


Figure 3.3: A labelled schematic of the interior of a TAM III calorimeter. Figure adapted from Reference 184.

The heat flow from the sample ampoule can be expressed in terms of the rate of heat exchange from the sample and the rate of heat accumulation in the sample. Given the heat conductance of the sample (k_s), the temperature difference between the surroundings and the sample (ΔT), and the heat capacity of the sample (C_s), the heat flow can be expressed by

$$\frac{dq}{dt} = k_s \Delta T - C_s \frac{dT_s}{dt}. \quad 3.6$$

A potential difference (V_s) is measured across the thermopile which is proportional to its Seebeck coefficient (S_b) and the temperature difference between the sample and heat sink. Assuming isothermal environmental conditions, Equation 3.6 can be written as

$$\frac{dq}{dt} = k_s \frac{V_s}{S_b} - \frac{C_s}{S_b} \frac{dV_s}{dt}. \quad 3.7$$

Assuming the heat transfer due to the temperature differential is distributed uniformly, a lumped thermal capacitance model can be used. The thermal conductance of the sample ampoule is then given by the heat capacitance of the ampoule divided by the time constant of the ampoule (τ_s). Equation 3.7 becomes

$$\frac{dq}{dt} = \frac{C_s}{S_b \tau_s} \left(V_s - \tau_s \frac{dV_s}{dt} \right) = \varepsilon_s \left(V_s - \tau_s \frac{dV_s}{dt} \right). \quad 3.8$$

The constant ε_s is the calibration constant of the calorimeter. The time constant is determined by the calorimeter and is defined as the time required for the sample ampoule, which does not generate heat, to reach approximately 63.2% of a target heat flow when a known heat is applied. The time constants for the calorimeters in the TAM III are 297 ± 3 s, or approximately five minutes.¹⁸³

To reduce uncertainty in measurements, the TAM III has a reference ampoule for each calorimeter channel. The heat capacity, Seebeck coefficients, and time constants are assumed to be equal between each sample and reference ampoule. The heat flow of the sample including a correction for the reference ampoule is given by

$$\frac{dq}{dt} = \varepsilon \left(V_s - V_r - \tau_s \frac{d(V_s - V_r)}{dt} \right). \quad 3.9$$

The last term in Equation 3.9 is used to correct the measured heat flow for the time response of the calorimeter. This work did not apply this time correction. Therefore, the heat flow measured by the calorimeter in this work is given by

$$\frac{dq}{dt} = \varepsilon (V_s - V_r). \quad 3.10$$

3.9.2 Experimental Setup

Figure 3.4a shows a photo of the TAM III. Each channel is seen with a black cap and a white cable. Each channel contains a lifter which lowers the ampoule into the calorimeter. The lifter assembly and labelled components are shown in Figure 3.4b. The lifter contains a series of thermal barriers ending with a rubber O-ring to limit heat transfer through the air out of the calorimeter. One thermal barrier (C in Figure 3.4b) is made of high-iron steel to act as a magnetic stop to allow for temperature equilibration when lowering a room temperature sample into the calorimeter. All cells were allowed to equilibrate for a minimum of 45 minutes before lowering into the calorimeter. The spring helps create firm contact between the ampoule and the bottom of the calorimeter.

Figure 3.4c shows the cell and connections inside the ampoule as well as the spring-seal on the ampoule cap. The ampoule contains the cell, which is connected to two pairs (voltage and current for each electrode) of 32 gauge dual-twist cryogenic polyimide coated phosphor bronze wires (LakeShore Cyrotronics Inc.). The wires have a thermal conductivity of $48 \text{ W/m}\cdot\text{K}$ at 300 K to minimize heat transfer out of the calorimeter.¹⁸⁵ Holes were drilled through each of the thermal barriers in the lifters to allow the wires to be fed into the ampoule. The holes were sealed with Torr Seal (Varian Inc.) epoxy resin once the wires were in place. Cell connections and wires were covered with Kapton[®] tape (to prevent short circuiting or wearing of the wire coating) due to its durability and high thermal stability. The small gauge wires were spliced onto CAT-5 ethernet cables outside of the lifter which allowed for lifters to be moved and connected easily.

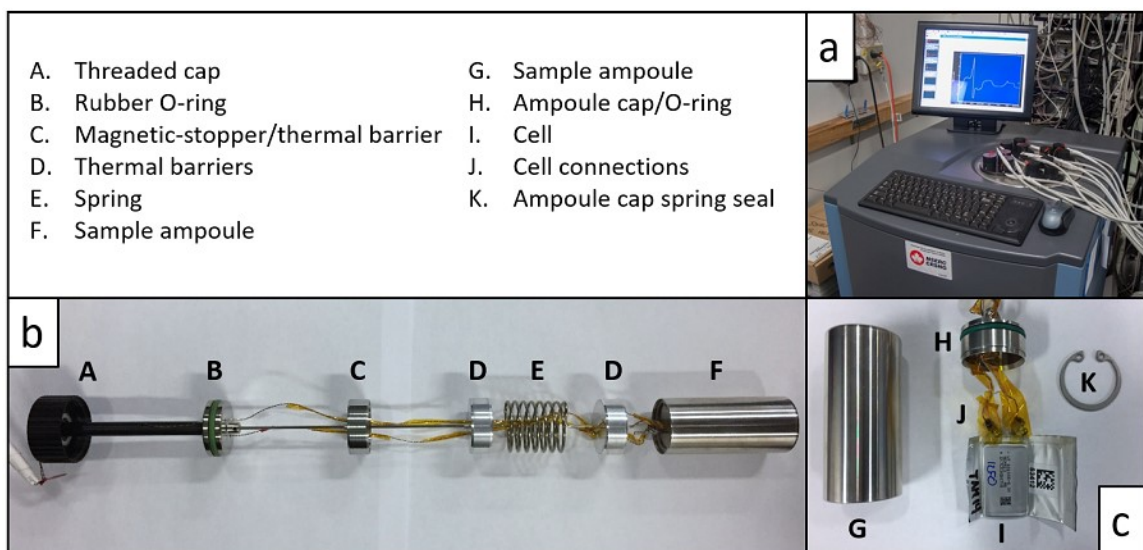


Figure 3.4: a) The TAM III isothermal microcalorimeter (TA Instruments) used in this work. b) One of 12 lifters (one for each channel) with labelled components. c) A close-up view of the cell connections inside the ampoule, and the ampoule components.

3.9.3 Baseline and Calibration

The TAM III has an internal calibration setting in which finely tuned heaters give a known heat flow which is measured by the calorimeter. However, an independent calibration was performed to remove any potential baseline offset due to a cell, wires, and tape within the ampoule. A dry pouch cell was cut open and a precision resistor ($10.00 \pm 0.01 \Omega$, TE Connectivity, Part: YR1B10RCC) was inserted into the cell. The wire leads were connected, and the calibration cell was sealed in the ampoule and lowered into the calorimeter after equilibrating at the magnetic stop for 45 minutes. Once in the calorimeter, the cells required at least 24 hours to reach a stable baseline. A 0.0 mW baseline was then set as the average heat flow over a stable, one-hour window. Each channel was connected to the Maccor 4000 cycling system and a current of 15 mA was applied to the calibration resistor for 3 hours to provide a heat flow of 2.25 mW. During the last 30 minutes the current was applied, the measured signal was calibrated to 2.25 mW. The cell was allowed

to rest for 24 hours to ensure the heat flow reached 0.0 ± 0.5 mW before removing the calibration cell and inserting test cells.

3.9.4 Experimental Notes and Uncertainty

All calorimetry experiments presented in this thesis were conducted at 40°C. Experimental protocols varied by experiment and the details of each will be discussed in the applicable section.

Downie found the reproducibility of heat flow measurements to be equivalent to the cell-to-cell variability in other electrochemical tests.¹⁵⁵ Therefore, the uncertainty in measurements is limited by the small differences due to cell construction. This work used machine-made pouch cells, so cell-to-cell variability was small. Ellis et al. found that the standard deviation in the capacity of cells similar to cells used in this thesis was 1 mAh for 26 cells with an average capacity of 196 mAh.¹⁸⁶ The measurements of CE and charge endpoint capacity slippage per cycle after 16 cycles at C/20 and 40°C were found to be 0.99835 ± 0.00002 and 0.179 ± 0.003 mAh cycle⁻¹, respectively.

Most experiments were performed using pair cells to ensure consistency, unless otherwise noted. Uncertainty is typically reported as the range of values between pair cells, which is a conservative estimate. Downie found that the standard deviation between seemingly identical pouch cells cycled at 1 mA was approximately ± 2 μ W (1-2% of signal). Approximately 2% is a good estimate of the uncertainty of a single pouch cell in this work as the currents used and magnitude of the measured heat flow were on the same orders of magnitude. Most pair cells reported in this work show similar variability, so in most cases data from one cell are shown to simplify comparisons.

3.10 GENERAL NOTES ON UNCERTAINTY

This thesis does not treat data with any robust error analysis. Identical pair cells were used for almost every experiment presented in this thesis. The dominating source of uncertainty was due to the cell-to-cell variability in the manufacturing process which will be seen to be very small. In some cases, the data from both pair cells are presented. The uncertainty in these measurements can be approximated by the range between pair cell data. In other cases the averaged data of pair cells are shown and the reported uncertainty is the range between pair cells.

Other sources of uncertainty include mixing electrolyte solutions, filling and degassing pouch cells, temperature fluctuations during testing, and power outages. When mixing electrolytes, care was taken to ensure chemicals were weighed to within 1% of the target value. The uncertainty in electrolyte volume during filling was assumed to be less than 1%. Some electrolyte can be lost during vacuum sealing after filling or degassing. The mass of cells before and after vacuum sealing was measured for 10 cells and was found to be the same within 3% on average. Multiple power interruptions occurred during this work which caused anomalous data points which will be noted in the text.

CHAPTER 4 USING HEAT FLOW TO PROBE SOLID ELECTROLYTE INTERPHASE FORMATION REACTIONS

The work in this chapter was a collaborative effort with Dr. David Hall. Some cells used in this chapter were made by Dr. Hall and some cells were made by the author. All calorimetry measurements and data processing were performed by the author of this thesis. Dr. Hall authored¹⁸⁷ and co-authored¹⁸⁸ the two works cited in this chapter from which density-functional theory (DFT) results are used.

As discussed in Section 1.5.4, electrolyte additives are used to form passivating SEI layers which protect electrodes from parasitic reactions. However, little is known about the exact pathways occurring during SEI formation. Although SEI-forming reactions from additives are desired, they are parasitic reactions by definition and as such may be useful to this body of work. Formation reactions will emit or absorb heat based on the reaction pathway(s). Therefore, isothermal microcalorimetry may be a useful tool to probe formation reactions. Results from the heat flow of formation can be compared to theoretical values in an attempt to understand the mechanisms and products present during and after SEI formation.

Unlike the rest of this thesis, this chapter does not contribute to the understanding of the *unwanted* parasitic reactions which affect cell lifetime during operation. However, this chapter demonstrates how isothermal microcalorimetry can be used to develop and understand the electrode-electrolyte interfaces responsible for most parasitic reactions. This technique is the first reported method to use isothermal microcalorimetry to probe formation reactions.

4.1 EXPERIMENTAL

This work used NMC442/AG cells (180 mAh balanced to 4.7 V). The control electrolyte was EC:EMC (3:7 wt.) with 1.0 M LiPF₆. The additives used in this study were VC, FEC, PES, and PBF. Additives were included in the specified weight percentages in each study (2% or 4%). Electrochemical tests were performed using the Maccor 4000 cycler. Formation protocol C was used for each experiment (see Section 3.3). Cells were not clamped between rubber blocks during formation due to the small size of the calorimeter ampoule.

4.2 HEAT FLOW OF FORMATION

Some results in this section are reprinted with permission from *Phys. Chem. Chem. Phys.*, **18**, 11383–11390 (2016).¹⁸⁹ Copyright 2017, the Royal Society of Chemistry. Dr. Hall prepared the manuscript.

During the start of a formation cycle the graphite negative electrode potential drops rapidly below the reduction potential of electrolyte species. When this occurs, the electrolyte preferentially reduces, reacting with lithium on the electrode surface instead of intercalating into the graphite. Since NMC has a relatively flat voltage curve at the beginning of charge, a plateau can be seen in the full cell voltage when reduction occurs at the negative electrode. As the SEI grows and begins to become passivating the rate of reaction slows, and the graphite begins to intercalate lithium, increasing the cell voltage.

Figure 4.1 shows the measured voltage of a cell with the control electrolyte in red during the first ~10% of charge. Blue lines mark the region where the majority of electrolyte reduction takes place. A green line marks the approximate time when the

negative electrode begins to intercalate lithium and the cell begins to charge. The measured heat flow is shown in black. Studies have found that electrolyte species which are more coordinated to Li^+ (EC especially) in electrolyte are preferentially consumed in reactions at the electrodes.^{131,190} Therefore, it is assumed that EC reduction dominates the SEI formation process here.

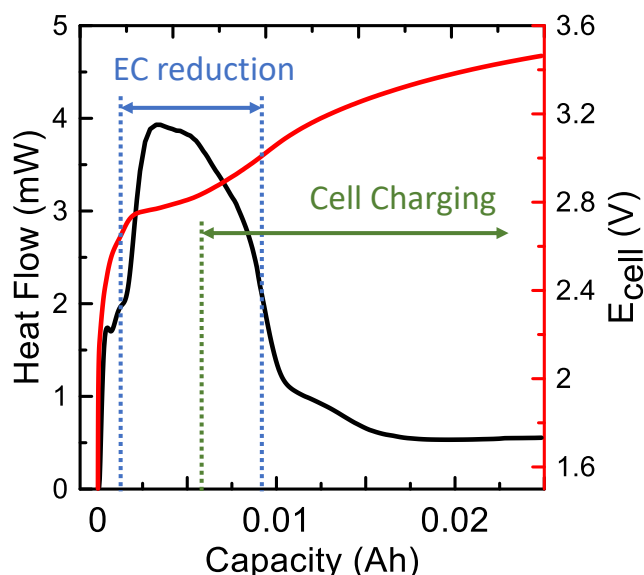


Figure 4.1: The heat flow (black) and voltage (red) of an NMC442/AG cell with control electrolyte containing EC during a formation cycle at 2 mA ($\sim C/100$). The onset of EC reduction produces a large heat flow. As the SEI forms, the rate of EC reduction decreases and the cell begins to charge.

The magnitude of the heat flow during the EC reduction plateau in Figure 4.1 (4 mW) is an order of magnitude higher than is measured with identical cells at the same rate during non-formation cycles (0.1 mW) (see Figure 2.2). When the rate of reaction slowed and the cell began charging, the heat flow decayed to the previously observed levels of heat flow during normal operation. The large, distinct features observed in Figure 4.1 were an indication the isothermal microcalorimetry was a good tool to probe formation processes.

Figure 4.2a shows a comparison between the voltage curves of cells containing the control electrolyte and the control electrolyte with 2% VC, 2% FEC, 2% PES, and 2% or 4% PBF. Figure 4.2b shows the heat flow during formation beneath each voltage curve. In each case the heat flow and voltage measurements of pair cells differed by only a few percent, so only one of each pair cells are shown. Figure 4.2 shows that each additive had a unique heat flow profile, and some additives mitigated the EC reduction plateau such as VC, FEC and PES, while PBF did not, indicated by the 2.8 V plateaus. The heat flow of the control cell exhibited small features at the beginning of charge. The exact reason for these features is not known but could be due to reactions with very small quantities of water in the cell, and a portion could be due to the entropic heat flow of the positive electrode. No such features appeared in the heat flow from cells containing additives since the additives reduced almost immediately, at higher negative electrode potentials than EC.

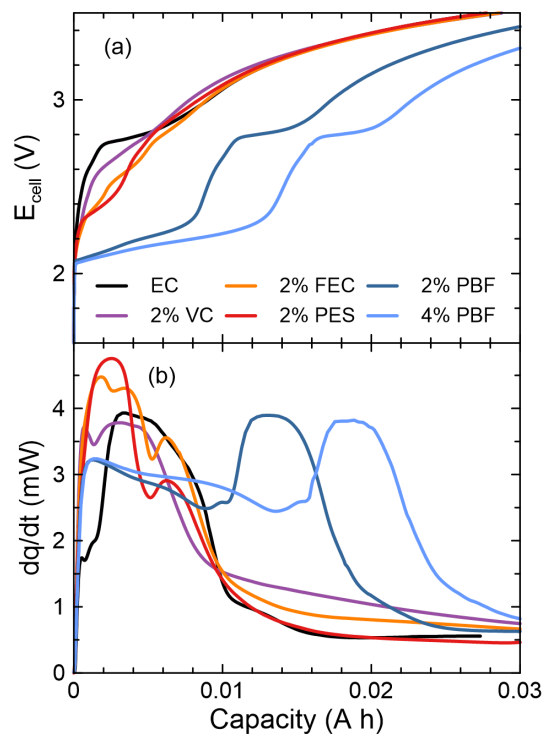


Figure 4.2: a) Measured cell voltage and b) heat flow during cell formation at 2 mA ($\sim C/100$) from NMC442/AG cells that contained either the control electrolyte with no additives (black, labelled EC to indicate EC reduction) or control electrolyte with additives as labelled.

Figure 4.2 shows that the amount of charge required to form the SEI ranged from 5 mAh to 10 mAh for each additive. For example, 2% wt. VC given a two-electron reduction process would consume about 11.2 mAh of charge. However, this is slightly more than the capacity used by VC formation in Figure 4.2. A one electron reduction would yield 5.6 mAh of capacity. The capacity of the formation of 4% PBF was approximately twice that of 2% PBF, and the heat flow profiles were very similar. A larger than expected charge capacity, and an increasing cell voltage during additive reduction could mean that other processes such as EC reduction and lithium intercalation into graphite take place alongside additive reduction. A smaller than expected capacity would indicate that all of the additive was not consumed during formation. However, there

was likely excess additive dissolved in electrolyte outside of the jelly-roll, so not all additive molecules in the electrolyte were expected to react at the graphite surface. GC experiments would be a useful way to probe excess electrolyte after formation.

The electrochemical features in the voltage curves in Figure 4.2a can be viewed more conveniently by plotting heat flow with the derivative of the capacity with respect to voltage (differential capacity, or dQ/dV). Each voltage plateau is seen as a peak in dQ/dV . Figure 4.3 shows that every electrochemical feature in the dQ/dV plot corresponds to a feature in the heat flow. Heat flow features are labelled by the possible species being reduced.

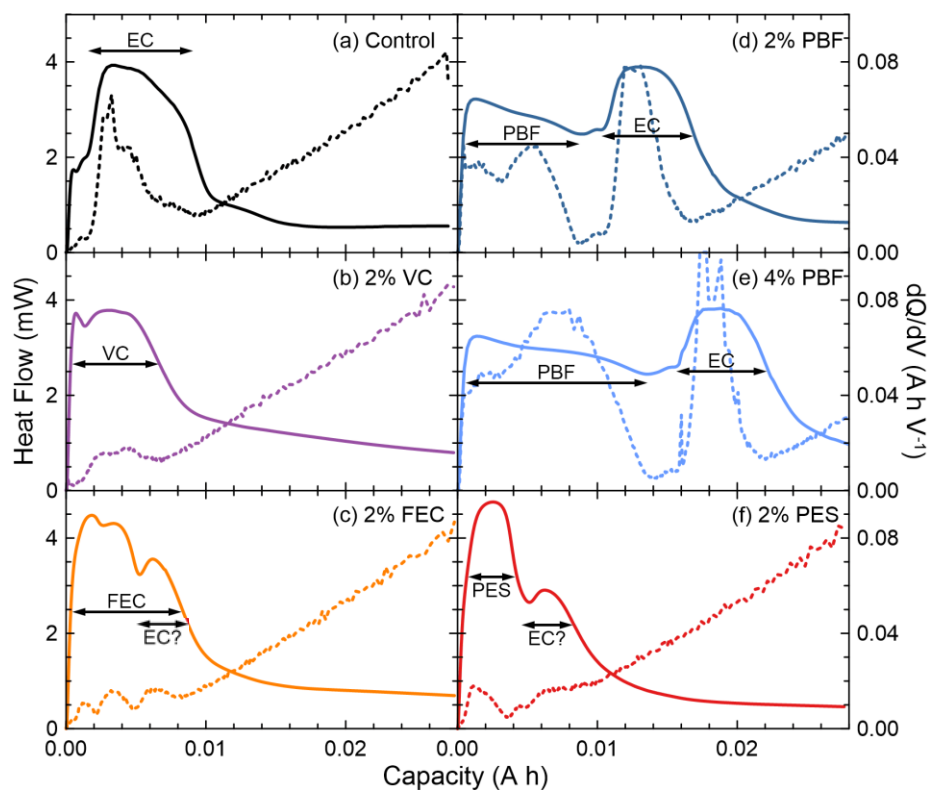


Figure 4.3: The heat flow and differential capacity of a) control electrolyte (EC reduction), b) 2% VC, c) 2% FEC, d) 2% PBF, e) 4% PBF, and f) 2% PES.

As mentioned previously, FEC may react to produce VC and LiF .^{83,101,191} Density functional theory (DFT) calculations have shown that radical anions formed by the

reduction of VC may initiate spontaneous VC polymerization.¹⁹² The two electrochemical features in Figure 4.3b for VC were not consistent with the reported reaction schemes of a one electron reduction followed by a spontaneous chemical step. The initial feature in VC may be due to the larger water impurity in the VC used here (100 ppm vs. 10-20 ppm). The initial electrochemical feature for FEC in Figure 4.3c occurred at a lower cell voltage than VC, and the second two features occurred at approximately the same voltages. The matching cell voltages and dual-peaks in both dQ/dV and heat flow suggest the second and third steps in FEC and VC may be similar. However, the final step in both VC and FEC occurred at the same cell voltage as EC reduction, so it is possible that a small amount of EC is reduction was present, and the one-electron reduction scheme for VC is valid. The SEI formation reactions of FEC and VC are of great interest to the lithium-ion field and future work could investigate these reaction pathways using the methods outlined in this chapter.

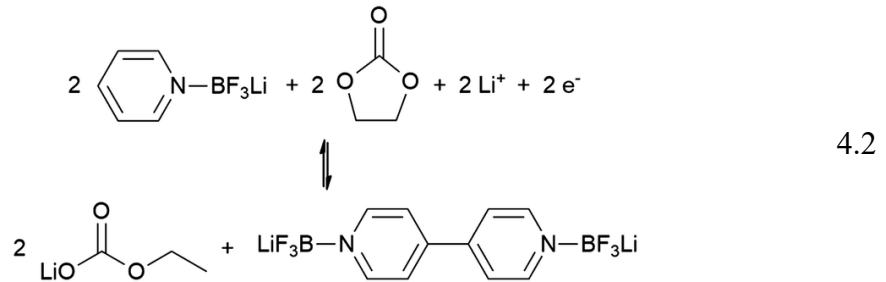
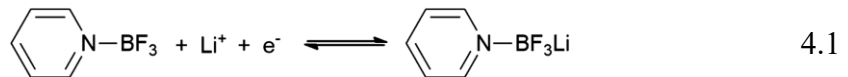
The heat flow and dQ/dV of PES had one electrochemical feature possibly followed by a small amount of EC reduction. The heat flow PBF showed one or two electrochemical features at very similar cell voltages followed by a large amount of EC reduction. The next sections will investigate the formation reactions of PBF and PES in more detail.

4.3 PYRIDINE BORON TRIFLUORIDE

Figure 4.2 showed that PBF exhibited a clear voltage plateau and a more consistent heat flow than other additives. The reduction of PBF was thus a good candidate to attempt to combine theoretical studies and experimental results probing formation reactions. Although PBF did not seem to passivate the negative electrode, PBF has been found to

decrease charge endpoint capacity slippage, increase CE, and lead to lower voltage fade during high voltage storage.^{193–195} Therefore, reactions which occur at the negative electrode during formation may contribute to a positive electrode SEI, and warrant investigation.

Hall et al. proposed a two-step electrochemical reaction for the reduction of PBF shown in Equations 4.1 and 4.2.¹⁸⁷ A one-electron reduction to form LiPBF is followed by another one-electron reaction with lithium and EC to form C₃H₅LiO₂ and Li₂(PBF)₂. The absence of gaseous products was supported by gas chromatography (GC) and *in-situ* gas measurements.¹⁸⁷



The standard potentials of each electrochemical step were calculated using DFT to be 1.27 V and 3.92 V vs. Li/Li⁺, respectively.¹⁸⁷ Assuming the positive electrode was at ~3.6 V at the beginning of charge the corresponding cell potential to initiate reduction would be approximately 2.3 V, in good agreement with Figure 4.2 (plateau at ~2.2 V). The second step would then occur at an overpotential of 3.92 V – 1.27 V = 2.65 V. Assuming the first reaction step occurred at the negative electrode potential, the heat flow due to the reaction overpotentials for the two-electron ($n = 2$) reduction would be given by

$$\dot{q}_{overp} = I \left(\frac{\eta_1 + \eta_2}{n} \right) = 2 \text{ mA} \left(\frac{0 \text{ V} + 2.65 \text{ V}}{2} \right) = 2.65 \text{ mW}. \quad 4.3$$

At the negative electrode, Li^+ preferentially reacts at the surface so there should be approximately no entropic heat flow from the graphite electrode. An approximation of the level of heat flow from the entropic changes in the positive electrode can be made assuming a simple mean field lattice gas model. The entropy (S) can be expressed using Stirling's approximation with the number of ways to arrange n lithium atoms in N sites using the ratio of lithiation ($x = n / N$) which starts at $x = 1.0$ for the fresh positive electrode:

$$S = -Nk_b [x\ln(x) + (1 - x) \ln(1 - x)]. \quad 4.4$$

The heat flow due to changes in entropy from Equation 4.4 is on the order of -0.5 to -0.15 mW for the duration of the PBF reduction plateau and is given by:¹⁵⁷

$$\dot{q}_{entropy} = \frac{IT}{e} \frac{ds_+}{dx_+} = \frac{IT}{Ne} \frac{dS_+}{dx_+} = -I \frac{k_b T}{e} \ln\left(\frac{x}{1-x}\right). \quad 4.5$$

The heat flow from the cell overpotential (not the reaction overpotential) is approximately $1\mu\text{W}$ at the currents used here, which is within the uncertainty of the calorimeter and three orders of magnitude less than measured heat flow. Additional heat flow comes from the enthalpy of reaction (ΔH) of any chemical step involved in the reaction pathway multiplied by the rate of reaction. The heat flow due to reaction enthalpy is then

$$\dot{q}_{enthalpy} = -\frac{I}{F} \left(\frac{\Delta H}{n}\right) \quad 4.6$$

where F is the Faraday constant, yielding a total heat flow during formation of:

$$\dot{q} = I \left(\frac{\eta_1 + \eta_2}{n}\right) - \frac{I}{F} \left(\frac{\Delta H}{n}\right) - I \frac{k_b T}{e} \ln\left(\frac{x}{1-x}\right). \quad 4.7$$

Hall et al. assumed the two-step reaction of PBF was purely faradaic, ignoring any chemical steps potentially involved with the second step (Equation 4.2). Although likely

an oversimplification, the heat flow due to the electrochemical overpotential can be used to make qualitative comparisons between the experimental and theoretical results.

Figure 4.4 shows the measured (black) and calculated values (orange) of the heat flow during formation of 2% PBF and 4% PBF excluding the enthalpy of reaction involved in the second step. The length of the calculated value ends at the amount of capacity available from PBF reduction assuming a constant rate of reaction (6.8 mAh for 2% PBF).

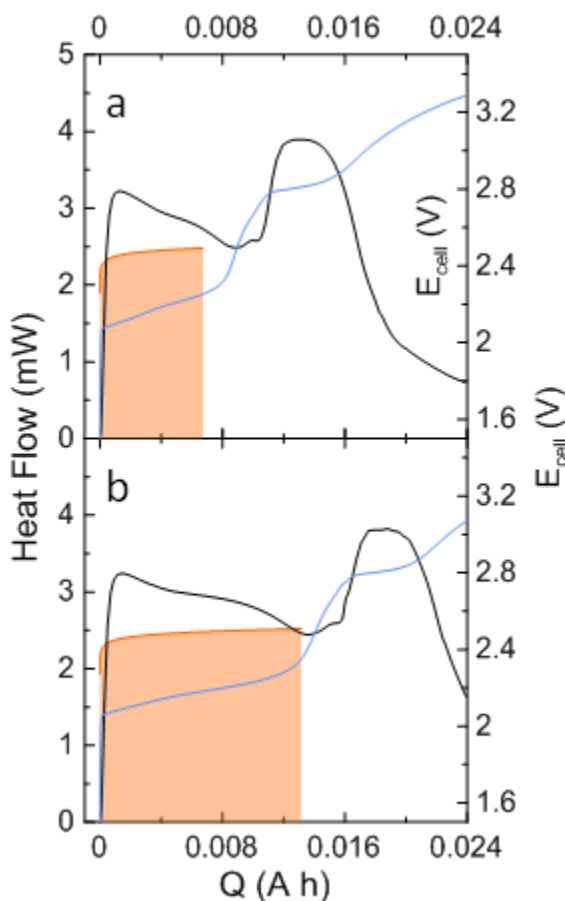


Figure 4.4: The measured heat flow of formation for a) 2% PBF and b) 4% PBF (black) and calculated values (orange). The cell voltage is shown in blue.

The calculated heat flow in Figure 4.4 appears to be an underestimate due to the exclusion of the reaction enthalpy for any chemical step resulting from the second reduction. However, the enthalpy of reaction term was likely exothermic in this case, as

the heat flow of formation decayed as the reaction rate slowed (indicated by an increase in cell voltage). Further work could focus on determining any contributions to reaction enthalpy involved in any chemical steps.

The values of experimental and theoretical heat flow obtained for PBF show that isothermal microcalorimetry could be a useful tool to probe formation reactions but is restricted by the uncertainty in DFT calculations and the complexity of the reaction mechanisms. The accuracy of calculated standard potentials is limited by the accuracy of the Li/Li⁺ reference value, the accuracy of solvation model used, surface interactions of the reduced species, the size of the basis set, and the accuracy of the density functional itself. An uncertainty in ~10% in the calculation of the standard potentials could lead to upwards of 0.5 mW of additional heat flow. Experiments on pouch cells are consistent; however, the exact potential of the negative electrode is difficult to determine. Future studies could use graphite/Li-metal reference coin cells (also called half-cells) to measure the reduction potential of PBF to compare with pouch cells and DFT-calculated values.

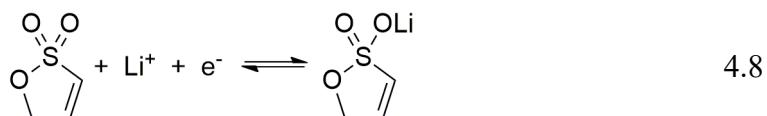
The next section will briefly look at a case where many possible reaction enthalpies of a chemical step after two electrochemical steps have been calculated.

4.4 PROP-1-ENE-1,3-SULTONE

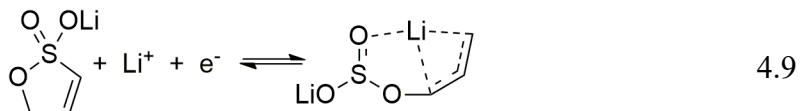
The heat flow of formation for 2% PES was shown in Figure 4.1 and Figure 4.2. The heat flow of PES was the highest of all additives tested (~4.8 mW) and showed a single reduction feature, likely followed by a small amount of EC reduction. Self et al.¹⁸⁸ proposed a formation pathway for PES beginning with two consecutive one-electron steps followed by a spontaneous chemical step. The two electrochemical steps yield an organo-

lithium compound Li₂PES which then may spontaneously react with EC, EMC, or PES.

The two electrochemical steps were given by



and



The standard potentials of the two electrochemical steps were 0.9 V and 4.3 V vs. Li/Li⁺, respectively. Similar to the methods above for PBF, assuming the positive electrode was at a cell voltage of 3.6 V, the cell voltage corresponding to a 0.9 V negative electrode potential would be 2.5 V. The observed voltage plateau occurred at cell voltage of ~2.4 V, in good agreement with the calculation. The overpotential for the second step would then be 4.3 V – 0.9 V = 3.4 V.

Self et al. proposed 18 chemical pathways for the reaction of Li₂PES with EC, EMC, or PES. Each reaction was found to be spontaneous ($\Delta G < 0$) and exothermic ($\Delta H < 0$). The purpose of this study was to develop a method to help support possible pathways of SEI formation. Therefore, the specifics and likelihood of each reaction, and the calculations are out of the scope of this thesis. For simplicity, the 18 pathways were split into four groups based on similarities in the magnitude of the reaction enthalpy and reaction products. i) reactions of Li₂PES with EC or EMC yielding lithium alkoxides ($\Delta H = -0.046$ eV, -0.051 eV, -0.185 eV, -0.195 eV, 0.550 eV, -0.63 eV), ii) reactions of Li₂PES with EMC which produce lithium semicarbonates ($\Delta H = -1.68$ eV, -1.857 eV, -1.858 eV, -1.976 eV), iii) reactions of Li₂PES with PES ($\Delta H = -2.214$ eV, -2.221 eV, -2.298 eV, -2.333 eV,

-2.357 eV, -2.575 eV), and iv) reactions of Li₂PES with EC which produce lithium semicarbonates ($\Delta H = -3.63$ eV, -3.67 eV). Figure 4.5 shows the average calculated heat flow of reaction groups i) to iv) compared to the measured heat flow using Equation 4.7.

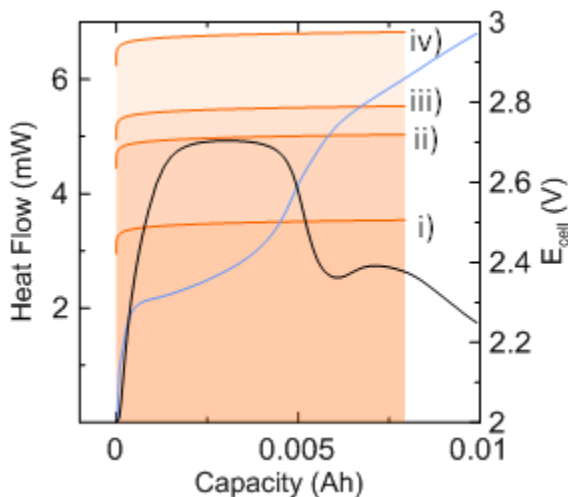


Figure 4.5: Heat flow of formation for 2% PES. Experimental data are shown in black and calculated heat flow of reaction groups i) to iv) is shown in orange. Cell voltage is shown in blue.

If the DFT calculations performed by Self et al. were assumed to be accurate, the heat flow data would suggest that reactions which produce lithium semicarbonates from Li₂PES and EMC (group ii), and reactions of Li₂PES with PES (group iii) were the most likely pathways. As discussed above the uncertainties involved in DFT calculations are difficult to quantify. However, in the present case the large differences between pathways ii) and iii) vs. i) and iv) may allow for slightly more confidence in the comparison with experimental results.

In the case of PES, isothermal microcalorimetry may be a useful tool to probe SEI formation reactions *in-situ* and non-invasively. Techniques which probe reaction products such as GC and surface characterization such as X-ray photoelectron spectroscopy (XPS) after formation are difficult to interpret due to air exposure, rinsing of the electrode surface,

and since *ex-situ* and post-mortem studies cannot probe the reactions in real time. The use of isothermal microcalorimetry may be useful to eliminate possible pathways when other techniques cannot differentiate between different reactions.

4.5 CONCLUSIONS

This chapter introduced a method to measure the heat flow during the formation cycle of a lithium-ion cell. Contributions to heat flow include the chemical overpotential of each electrochemical reduction step, the enthalpy change during any chemical reactions, and the changes in entropy of the positive electrode. Heat flow was measured for a control cell containing 1.2 M LiPF₆ in EC:EMC (3:7 wt.), and cells with the control electrolyte and 2% or 4% of VC, FEC, PES, and PBF. Each electrochemical feature in voltage curves had a corresponding feature in the heat flow data. Voltage plateaus and heat flow features at ~2.8 V were consistent between the control electrolyte and PBF, suggesting PBF does not passivate the negative electrode against EC reduction.

Experimental results for the reaction of PBF were compared to DFT calculations from the literature of the standard potentials of a proposed reaction pathway. Results underestimated the theoretical heat flow, but more work is needed to ensure the accuracy of DFT measurements and investigate the simplified second electrochemical step which may include a chemical step with reaction enthalpy.

A comparison of the heat flow of PES with theoretical results from the literature was made for a proposed reaction pathway composed of two electrochemical steps followed by a chemical step. Of 18 possible reactions, two categories of reactions were deemed most likely based on the comparison of theoretical to experimental heat flows.

The method developed here motivates further work in the investigation of electrolyte additive reaction pathways using isothermal microcalorimetry. Combining experimental data with calculations may be necessary to narrow down options when multiple reaction pathways are feasible. Isothermal microcalorimetry was proven to be a unique way of probing electrochemical reactions *in-situ*.

CHAPTER 5 CHARGE-DISCHARGE METHOD OF EXTRACTING PARASITIC HEAT FLOW

5.1 MOTIVATION

As discussed in Section 2.3, previous methods of extracting the parasitic heat flow of lithium-ion cells have certain limitations. Methods developed by Krause et al. utilized the reversibility of entropic heat flow to obtain the total parasitic energy over a voltage window but cannot be used to measure parasitic heat flow as a continuous function of voltage.^{150,151} Methods developed by Downie et al. could obtain the parasitic heat flow as a function of voltage.^{153,154} However, Downie's methods required very long experimental times and fitting of complicated heat flow profiles with linear or polynomial functions over small voltage windows. The work in this chapter uses ideas from the works of both Krause' and Downie's works. The aim of the work in this chapter was to develop a method to extract the parasitic heat flow of a cell as a continuous function of voltage, with no fitting required.

Downie et al. found that the parasitic heat flow obtained using time-dependent fitting methods was very similar to the average between the total charge and discharge heat flow at the lowest of four rates used (1 mA, $\sim C/200$).¹⁵⁴ Recalling Equation 2.13, the entropic heat flow is proportional to the applied current and is thus reversible between charge and discharge. Therefore, the entropic heat flow as a function of voltage is cancelled out when averaged, as used by Krause.¹⁵⁰ The overpotential heat flow was quite small at 1 mA in the cells used by Downie and as such did not contribute significantly to the average heat flow. By using a small current, effects from the cell overpotential near charge-discharge endpoints (when the current switches) were also avoided. Thus, charging

and discharging a cell using a small current can be an effective way to obtain the parasitic heat flow.

5.2 METHOD

5.2.1 General Derivation

Using equation 2.13 and substituting the direction of current (positive for charge, negative for discharge), the average heat flow between charge and discharge as a function of voltage yields

$$\begin{aligned}\dot{q}_{average} &= \frac{|I|\eta + |-I|\eta}{2} + \left(\frac{IT}{2e} + \frac{(-I)T}{2e} \right) \left(\frac{ds_+}{dx_+} - \frac{ds_-}{dx_-} \right) + \dot{q}_{p\ average} \\ &= |I|\eta + \dot{q}_{p\ average}\end{aligned}\tag{5.1}$$

or

$$\dot{q}_{p\ average} = \dot{q}_{average} - |I|\eta.\tag{5.2}$$

Equation 5.2 shows that the average parasitic heat flow as a function of voltage between the charge and discharge of a cycle can be found by subtracting the heat flow due to overpotential from the average of the total heat flow. This ‘charge-discharge method’ allows for the measurement of the magnitude of the parasitic heat flow and does not rely on any fitting methods or robust treatment of the entropy of the electrode materials. Additionally, since the parasitic heat flow is obtained over one cycle at one rate (compared to four cycles at four rates in Downie’s works) the effects of the time dependence of parasitic reactions from cycle to cycle do not need to be accounted for. However, the charge-discharge method presented here cannot differentiate between the parasitic heat flow during charge and the parasitic heat flow during discharge during the single cycle at one rate, whereas Downie’s fitting methods could.

Low currents must be used when using the charge-discharge method to maximize the magnitude of parasitic heat flow compared to entropic and overpotential components, and to minimize the effects of voltage drop or rise due to overpotential at current switch points. In this chapter, 1 mA ($\sim C/160$ to $C/200$) was used. Since just one full charge and discharge cycle at a rate of $C/200$ would take 400 hours to complete, only measurements in specific voltage ranges could be probed. Typically, the high voltage range (> 4.0 V) was of interest since most parasitic reactions occur above 4.0 V. When probing reactions at the negative electrode only, low voltage ranges could be used. Voltage ranges in this chapter ranged from 0.2 V to 0.7 V between endpoints, or ~ 60 hours to ~ 160 hours per cycle.

5.2.2 Overpotential Treatment

The cell voltage was measured during all calorimetry tests. The cell overpotential could be approximated to reasonable accuracy using the voltage measurements throughout the tests. Equation 1.8 showed that to calculate an overpotential the equilibrium voltage is needed, and can be rewritten as

$$\eta = |V_{meas} - V_{cell}|. \quad 5.3$$

Figure 5.1a shows the measured cell voltage *vs.* cumulative capacity for a 1 mA charge and discharge of a ~ 180 mAh NMC442/AG cell in a voltage window from 3.9 V to 4.4 V. The discharge voltage did not reach 0 Ah at the end of discharge due to charge endpoint slippage and capacity fade (Section 1.6). Figure 5.1b shows the measured cell voltage *vs.* SOC (treated here as the fractional charge or discharge capacity). The overpotential in this chapter was treated as half of the difference between the charge and discharge voltage curves as a function of SOC. Figure 5.2 shows the calculated

overpotential and the overpotential heat flow (current multiplied by overpotential) on the left and right axes, respectively. The calculated overpotential heat flow from 3.9 V to 4.4 V at 1 mA was found to be on the order of 10 μ W on average.

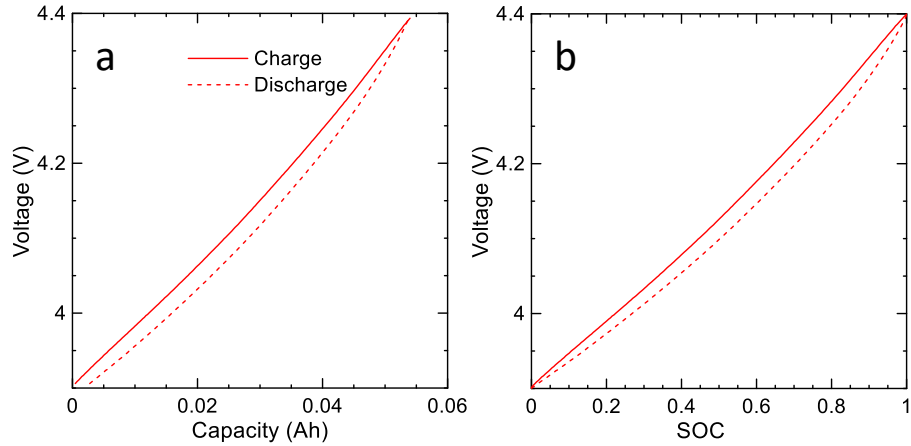


Figure 5.1: a) Cell voltage during charge (solid line) and discharge (dashed line) plotted vs. cumulative capacity for an NMC442/AG cell. b) Cell voltage vs. SOC (fractional capacity)

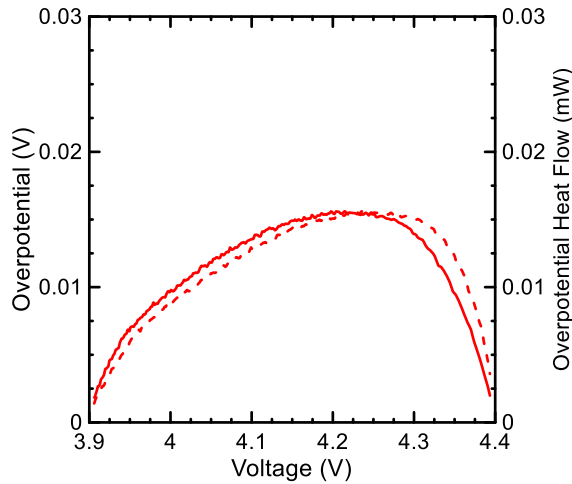


Figure 5.2: Calculated overpotential (left axis) and overpotential heat flow (right axis) during charge (solid line) and discharge (dashed line) of the cell in Figure 5.1 assuming a 1 mA current.

5.2.3 Parasitic Heat Flow and Consistency

Figure 5.3 shows the parasitic heat flow from the example above from 3.9 V to 4.4 V at 1 mA in red. The total measured charge and discharge heat flows are shown as solid and dashed black lines, respectively. The overpotential heat flow calculated above is shown in blue. The parasitic heat flow calculated using the charge-discharge method and the above treatment of the overpotential ranged from 25 μW to 200 μW . At the cycle endpoints the calculated overpotential heat flow approached 0 mW as a result of the calculation using the cell SOC. Although not a true representation of the heat flow near the cycle endpoints, the contribution to overpotential was small enough to consider the SOC treatment as a good approximation to the overpotential heat flow. Chapter 6 develops the treatment of overpotential further when larger currents than $C/200$ are used.

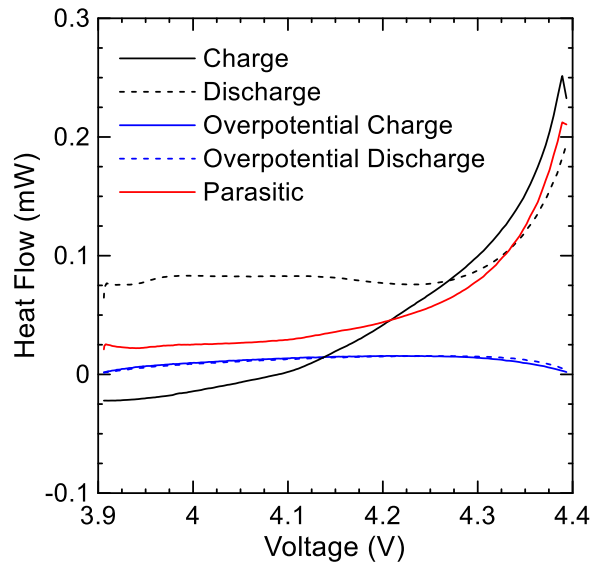


Figure 5.3: Parasitic heat flow (red) calculated as the average of the measured charge (solid black) and discharge (dashed black) heat flow minus the heat flow from the calculated overpotential (blue) during charge (solid) and discharge (dashed).

Figure 5.4 demonstrates the typical consistency between pair cells using the charge-discharge method. Three additive blends are shown in Figure 5.4 in SC-NMC532/AG cells

cycled from 4.0 V to 4.4 V at 1 mA. The data for each pair of cells were almost identical. Figure 5.4 shows that the charge-discharge method is a consistent technique. Therefore, slight differences in parasitic heat flow can be detected and correlated to cell performance.

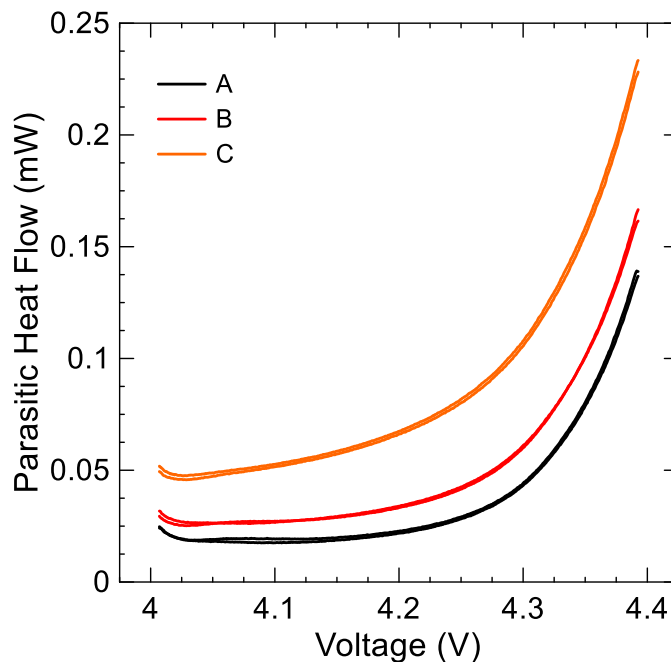


Figure 5.4: Parasitic heat flow of pair cells (SC-NMC532/AG) cycled from 4.0 V to 4.4 V at 1 mA found using the charge-discharge method with three different additive blends (A, B, and C). The data show excellent cell-to-cell consistency.

The charge-discharge method can be used to probe the effect of different voltage ranges on the magnitude of parasitic heat flow. The effectiveness of new additive or solvent systems can be investigated by comparing different additives in the same cell type, or by comparing different solvent systems. As mentioned previously, the differences between charge and discharge parasitic heat flows cannot be differentiated using the charge-discharge method, as only the average parasitic heat flow can be obtained. Chapter 6 will introduce a method which approximately separates the components of charge and discharge parasitic heat flow by estimating the entropic heat flow using the charge-discharge method.

Section 5.3 will demonstrate a study using the charge-discharge method to compare the parasitic heat flow of cells with EC-free electrolytes with various additives to a traditional EC-containing electrolyte. Section 5.4 will discuss a study in which the charge-discharge method was used to support various other electrochemical testing methods when comparing the effect of artificial graphite and natural graphite negative electrode materials and additive loadings on the parasitic heat flow.

5.3 STUDY: THE EFFECT OF ADDITIVES IN EC-FREE ELECTROLYTES

The work in this section is adapted with permission from *J. Electrochem. Soc.* **164** A567-A573 (2017), Copyright Journal of the Electrochemical Society, 2017.¹⁹⁶ Dr. Remi Petibon assisted in the design of the experiment and provided the cells used in calorimeter and UHPC experiments. The author performed all calorimetry measurements, data processing, and preparation of the manuscript.

5.3.1 Motivation

Blends of EC, EMC, and DMC have been ubiquitous in the lithium-ion field due to the passivating film-forming features of EC, and the transport properties and low temperature performance of EMC and DMC. However, a recent work by Petibon et al. found that electrolytes containing only EMC as a solvent were found to out-perform EC-containing electrolytes during high voltage tests (> 4.4 V).¹⁹⁷ By creating a simple electrolyte containing only EMC as a solvent and a small amount of VC as a passivating additive, cell cycle life and CE during 4.4 V cycling was greatly improved over electrolytes containing EC. Co-additives were found to further improve aspects of cycle performance and safety.

The study presented in this section aimed to investigate the effect of high voltage on the parasitic heat flow of EC-containing and EC-free electrolytes and to validate the charge-discharge method with UHPC studies. The effect of other film-forming additives combined with VC in EMC was also studied.

5.3.2 Experimental

The cells used in this work were NMC442/AG. The EC-containing electrolyte used in this work was 1.0 M LiPF₆ in EC:EMC (3:7 wt.) with 2% wt. PES, 1% wt. DTD, and 1% wt. TTSPi. The additive blend used is also known as PES211, and was discussed in Section 1.5.4. The EC-free electrolyte used in this work was 1.0 M LiPF₆ in EMC with 2% wt. VC. Co-additives to the EC-free electrolyte were also studied and included TTSP, PPF, and TAP added at 1% wt. Cells were filled with 0.9 g of electrolyte. The shorthand names used throughout this work are shown in Table 4.

Table 4: Electrolyte compositions (1.0 M LiPF₆)

Name	Solvent	Additives (wt. %)
Control	EC:EMC (3:7 wt.)	2% PES 1% DTD 1% TTSPi
EMC:VC	EMC	2% VC
EMC:VC + TTSP	EMC	2% VC 1% TTSP
EMC:VC + PPF	EMC	2% VC 1% PPF
EMC:VC + TAP	EMC	2% VC 1% TAP

Cells were formed using formation protocol A up to 4.2 V. Cells used for calorimetry studies underwent four cycles from 2.8 V to 4.2 V at 40°C to ensure a well formed SEI prior to measuring the parasitic heat flow. Cells were then cycled in the calorimeter at 1 mA between 3.9 V and the following sequence of upper cut off voltages: 4.2 V, 4.3 V, twice to 4.4 V, twice to 4.5 V, 4.6 V, and twice to 4.2 V. Some voltage ranges were repeated to investigate the effect of repeated exposure to the same voltage range. Cell volumes and EIS spectra were measured before and after calorimetry tests.

Cells for UHPC studies were connected to the UHPC at 40°C and cycled using a ‘barn’ cycling protocol for 16 cycles. Cells were charged at 15 mA from 2.8 V to 4.3 V, then at 5 mA up to 4.5 V. Cells were then discharged at 5 mA from 4.5 V to 4.3 V and 15 mA from 4.3 V to 2.8 V.

5.3.3 Results and Discussion

Figure 5.5 shows the UHPC results of the barn-cycle protocol, proposed by Xia et al. to enhance the effects of high-voltage operation for screening electrolyte additives.¹⁹⁸ Figure 5.5a shows the CE results for each pair of cells. The EC-free electrolytes all had higher CE than the control electrolyte – including EMC:VC – even though the additive combination PES211 has been found to perform better than 2VC in EC-containing electrolytes.^{113,199} Figure 5.5b shows the charge endpoint capacity slippage relative to the end of the first charge. As discussed in Section 1.6.2, higher charge endpoint capacity slippage indicates electrolyte oxidation at the positive electrode. The EC-free electrolytes had lower charge endpoint capacity slippage than the control, suggesting that EMC was less reactive at the positive electrode at high voltage, or that it made a better positive electrode SEI than EC-containing electrolytes. The capacity fade was also lower for EC-free electrolytes, shown in Figure 5.5c, likely indicating less electrolyte reduction consuming lithium at the negative electrode when EMC was used instead of EC. In each case, EMC:VC was found to have the worst performance of EC-free electrolytes. The UHPC performance of EC-free electrolytes at high voltage was enhanced by the addition of all co-additives in the study, particularly by PPF and TTSP.

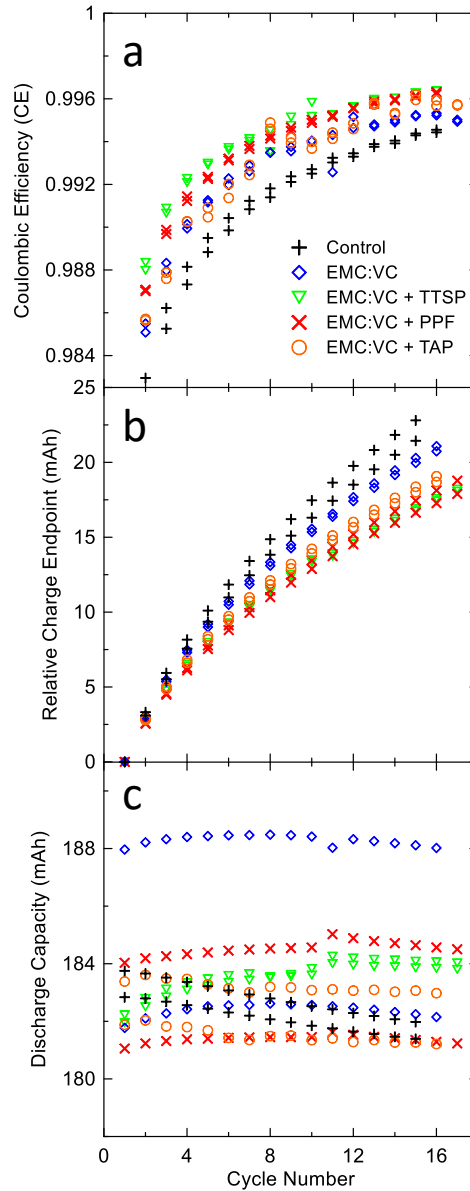


Figure 5.5: UHPC results for the barn cycling protocol from 2.8 V to 4.5 V at 40°C. a) Coulombic efficiency, b) relative charge endpoint, and c) discharge capacity.

Next, the effect of the above electrolytes on parasitic heat flow was studied to understand trends in heat flow compared to UHPC results. Figure 5.6a and Figure 5.6b show the calculated parasitic heat flow during cycles to 4.2 V and 4.3 V, respectively. The difference in parasitic heat flow from one control cell is shown in the bottom panel of each graph. Only one cell of each electrolyte type is shown for simplicity. Pair cell parasitic

heat flow values were within 1% for almost all cells in all cycles (a summary figure later in the text demonstrates the consistency between cells in this study). Figure 5.6 shows that EC-free electrolytes had higher parasitic heat flow than the control up to 4.3 V. EMC:VC+PPF had similar parasitic heat flow to the control. The observed differences in performance may have been due to the presence of quite protective SEI layers in the control cell due to the high loading additives. The difference plots in Figure 5.6 show that the relative performance of cells did not change significantly from 4.2 V to 4.3 V. The difference in scale should also be noted between cycles.

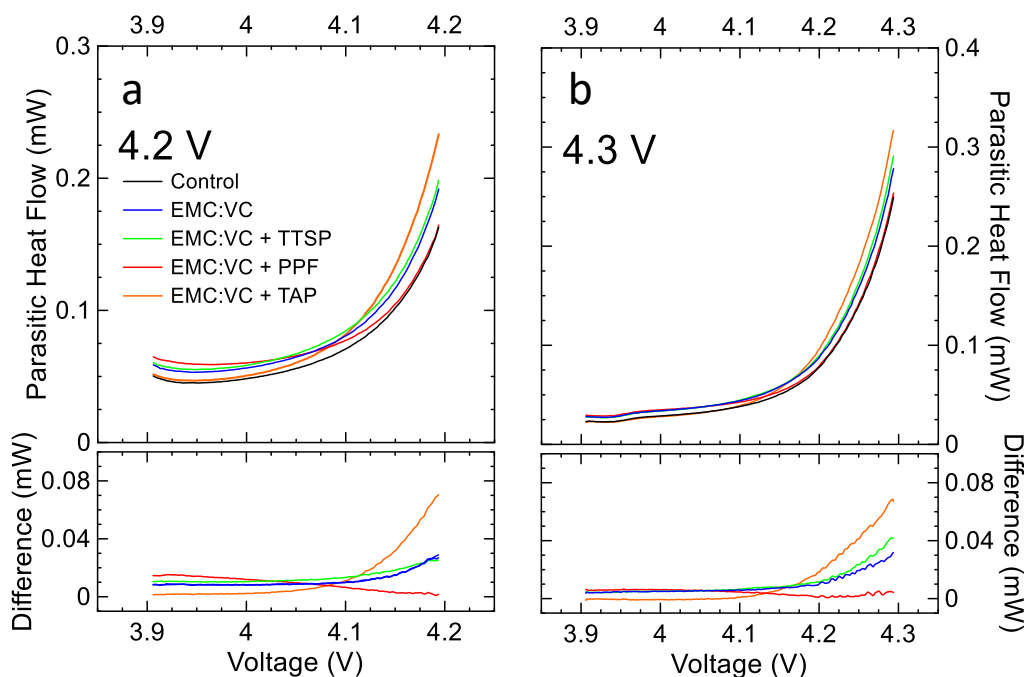


Figure 5.6: Calculated parasitic heat flow during cycles between 3.9 V and a) 4.2 V and b) 4.3 V at 1 mA and 40°C. The bottom panels show the difference between each cell and the control cell.

Figures 5.7a, b, c, and d show the parasitic heat flow during the two cycles to 4.4 V and two cycles to 4.5 V, respectively. All electrolytes had almost identical parasitic heat flow during the first cycle to 4.4 V. A large onset of parasitic heat flow occurred just above 4.3 V for all cells, suggesting all electrolytes had limited stability above a cell voltage of

4.3 V (corresponding to a positive electrode potential of ~ 4.4 V). However, during the second cycle to 4.4 V, the parasitic heat flow was less than half that of the first cycle. The lower parasitic heat flow suggested that oxidation products from parasitic reactions in the first cycle to 4.4 V might have created a passivating SEI on the positive electrodes in all cells.

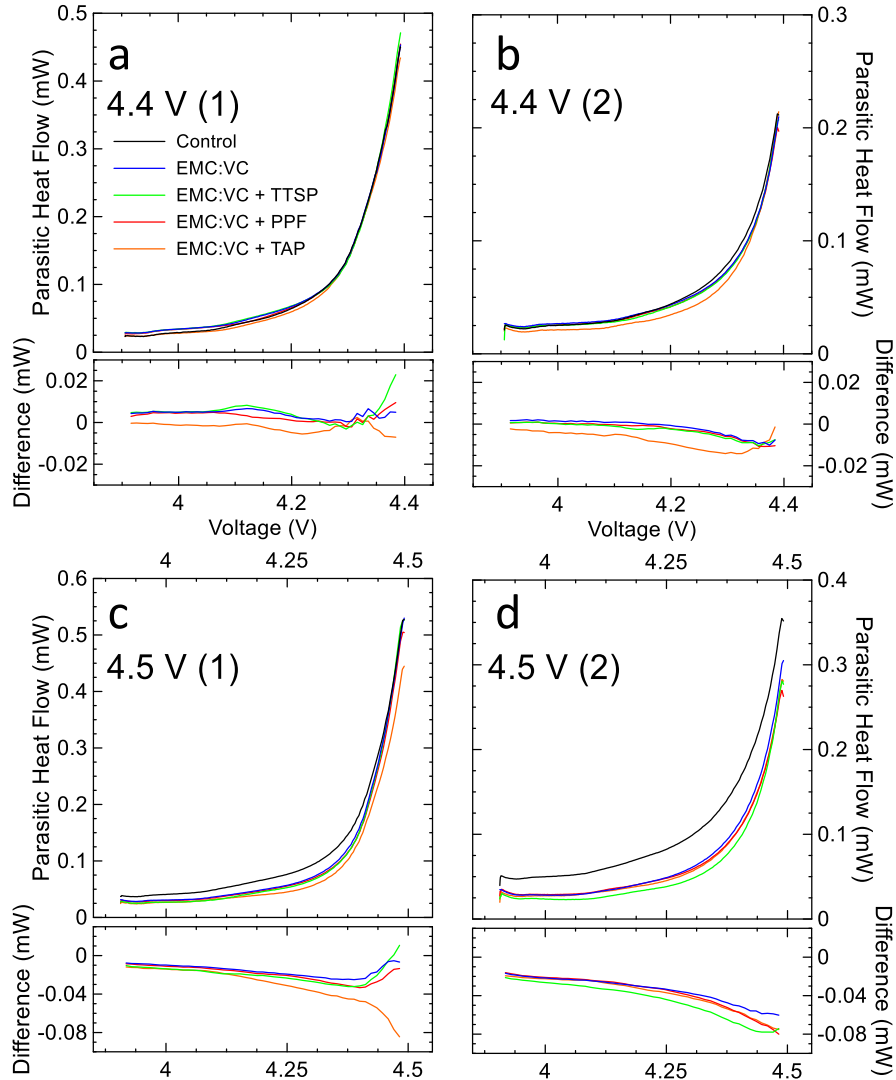


Figure 5.7: Calculated parasitic heat flow during cycles between 3.9 V and a,b) 4.4 V, c) 4.5 V, and d) 4.6V at 1 mA and 40°C. The bottom panels show the difference between each cell and the control cell.

Figure 5.7c and Figure 5.7d show that above 4.4 V EC-free electrolytes had lower parasitic heat flow than the control. During the two cycles to 4.5 V, the heat flow of the control cell increased at the bottom of charge. An increasing parasitic heat flow suggests SEI layers in the control cell were becoming less passivating or more cross-talk reactions from the oxidation products may have been occurring. In all cycles above 4.3 V, EMC:VC without co-additives performed worse than with co-additives.

Figure 5.8a shows the parasitic heat flow for the cycle from 3.9 V to 4.6 V. The same trend was observed as in cycles to 4.5 V: The parasitic heat flow of the control cell increased at low voltages and was higher than EC-free cells throughout the voltage range. Figure 5.8b shows the parasitic heat flow during the first and last cycles to 4.2 V. Ideally the parasitic heat flow would decrease between the first and last cycles due to the build-up of SEI. Figure 5.8b shows that EC-free electrolytes likely developed protective SEI layers over the cycles to high voltage, whereas the control cells had the same level of parasitic heat flow as the beginning of the protocol from 3.9 V to 4.1 V.

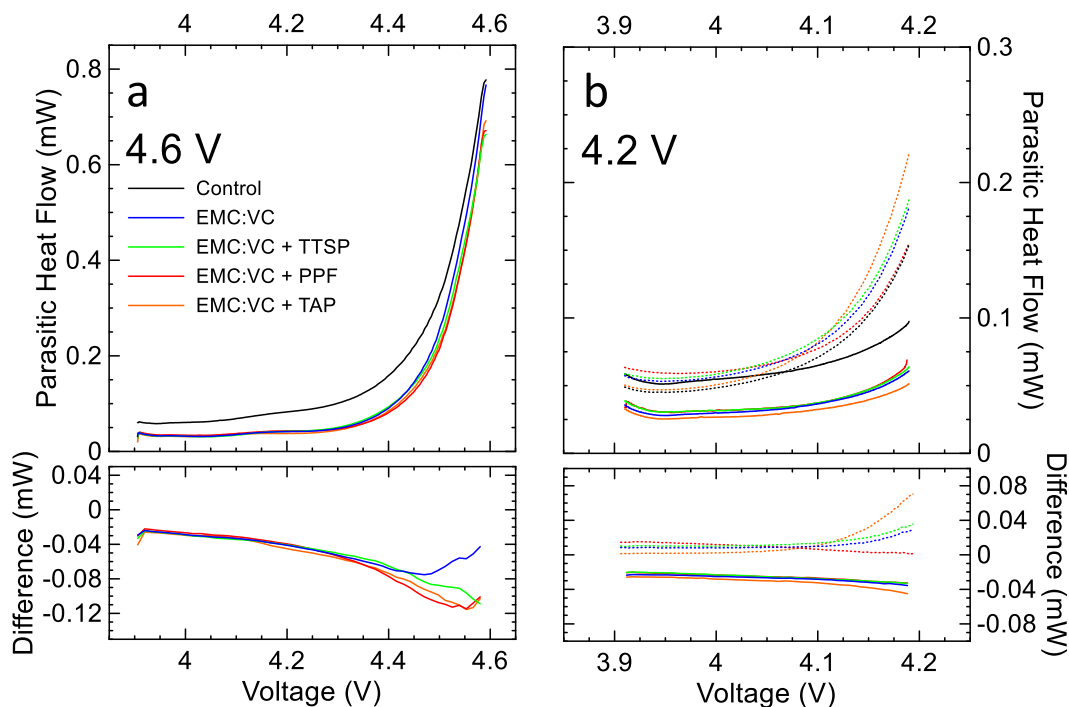


Figure 5.8: Calculated parasitic heat flow during cycles between 3.9 V and a) 4.6 V and b) the first (solid lines) and last (dashed lines) cycles to 4.2 V at 1 mA and 40°C. The bottom panels show the difference between each cell and the control cell.

Figure 5.9 shows a summary of all cycles in the calorimetry protocol. The mean parasitic heat flow per cycle was calculated for each cell. The average between each pair of cells is plotted, and the range between pair cells is shown by the error bars. The benefit of EC-free electrolytes is seen clearly when the ordering of cells changed during the two cycles to 4.4 V. The control cell then exhibited much higher parasitic heat flow over the 4.5 V and 4.6 V cycles. As found in Figure 5.6 to Figure 5.8, co-additives were beneficial compared to EMC:VC at high voltage. However, there was no co-additive which stood out compared to the others.

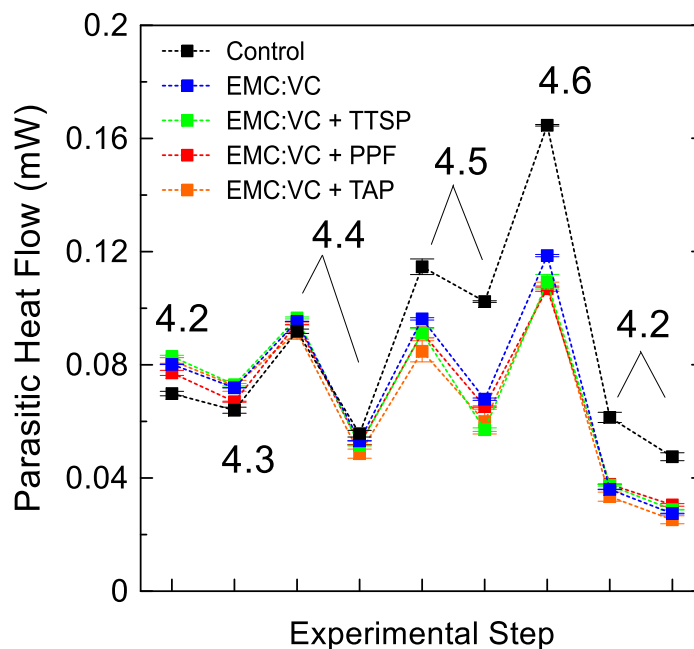


Figure 5.9: Average calculated parasitic heat flow over each cycle between 3.9 V and the labelled voltage limits 1 mA and 40°C. Each point represents the average of the pair cells used. The control cell data show the range between pair cells to demonstrate the measurement uncertainty.

Calorimetry experiments at high voltage agreed with UHPC results in this study. The charge-discharge method proved to be a consistent method to obtain the parasitic heat flow as a function of voltage, with little difference between pair cells. Parasitic heat flow at low voltages in each cycle and comparisons between parasitic heat flow at the beginning and end of the experiment yielded insight into the development of the SEI layers in each electrolyte. Obtaining parasitic heat flow as a continuous function of voltage allowed for important observations such as small differences between electrolytes, and the sudden onset of a large amount of parasitic heat flow above 4.3 V. However, the parasitic heat flow could not differentiate between co-additives, similar to UHPC results.

Figure 5.10 shows EIS results taken after formation at a cell voltage of 3.8 V. The R_{ct} (diameters of the semi-circular spectra, see Section 3.7) were quite large for EMC:VC

+ TAP compared to all other electrolytes. Otherwise, EC-free electrolytes had smaller R_{ct} values compared to the control. The average R_{ct} value between pair cells are shown in Figure 5.10b, where the error bars indicate the range between pair cells. A passivating SEI with low R_{ct} is desired when designing cells for high-rate applications. Figure 5.10c shows the gas produced during formation (grey) and after calorimetry experiments (red). Ideally a cell would produce minimal gas during high-voltage operation. Typical commercial cells do not feature gas pouches like the cells used here, so generated gas can induce cell failure. Figure 5.10b and Figure 5.10c show that the cells with the lowest R_{ct} exhibited the largest amount of gas production. Although the control cell had significantly more parasitic heat flow at high voltage, the gas volume of control cells was the lowest of all cells after calorimetry experiments. EMC:VC + PPF perhaps showed the best compromise of high CE, low R_{ct} , and moderate gas production. Figure 5.10d shows a photograph of the separator from each electrolyte. EC-free electrolytes contained lighter-colored separators than the control, which had large, dark deposits stuck to the surface. The color of the separator might represent a qualitative comparison of the number of side-reactions occurring in cells.

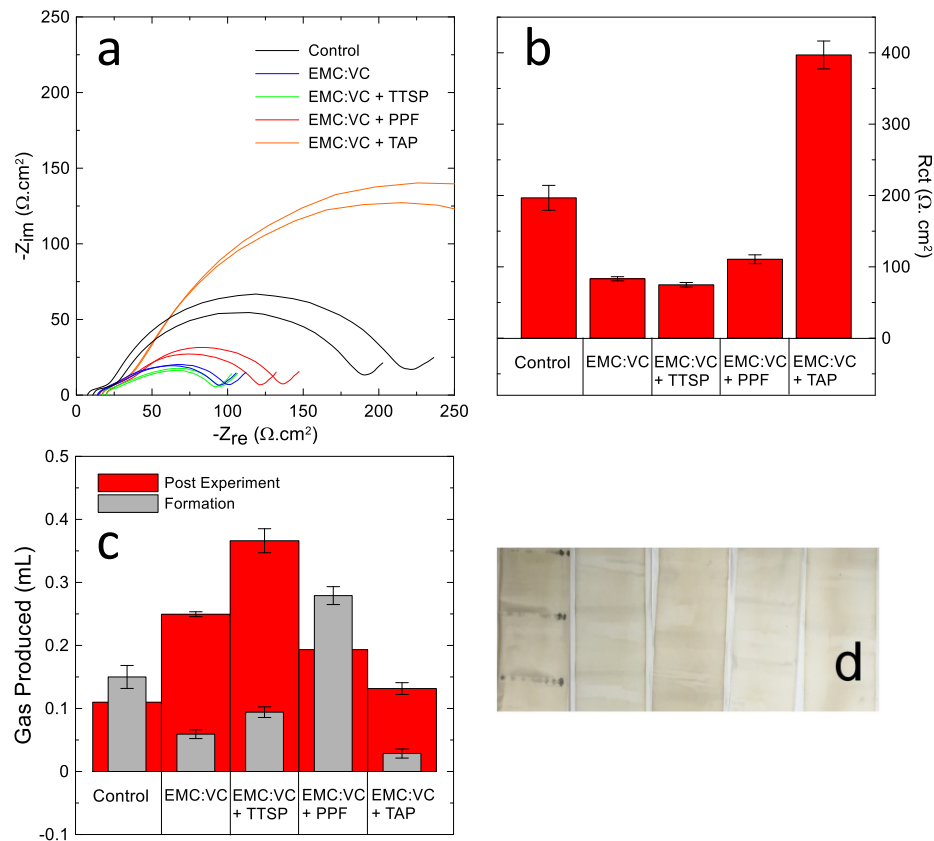


Figure 5.10: a) EIS spectra for each cell after cell formation. b) Average R_{ct} of pair cells after formation. c) Average gas volumes of pair cells after formation (grey) and after calorimetry experiments (red). Error bars demonstrate the range between pair cells. d) Photograph of the separators of each electrolyte after calorimeter experiments (same order as in the legend from left to right).

5.3.4 Conclusions

EC-free electrolytes with simple additive blends were shown to have superior performance above 4.4 V compared to a well-known high voltage additive blend in an EC-containing electrolyte. EC-free electrolytes produced more gas than the EC-containing control electrolyte, but typically had lower impedance. Results from UHPC experiments agreed with the parasitic heat flow calculated using the charge-discharge method. The charge-discharge method demonstrated the effect of upper cut off voltage on parasitic heat

flow on both types of electrolyte, clearly demonstrating a higher degree of parasitic reactions in EC-containing cells after exposure above 4.4 V.

Future studies on EC-free electrolytes should focus on maintaining high CE and low R_{ct} while also reducing the amount of gas generated in parasitic reactions. A study after the work in this section authored by Lin Ma et al. (and coauthored by the author of this thesis) focused on optimizing the additive content in EC-free electrolytes, and also used the charge-discharge method of obtaining parasitic heat flow.²⁰⁰ In the study by Ma et al. 3% wt. VC was found to be the optimal amount of VC in a 1.0 M LiPF_6 EMC electrolyte in the cells used (which were identical to the cells in this section). It was also found that 3% wt. FEC as an additive yielded less parasitic heat flow than when VC was used as the additive. However, another study investigated physical properties of EC-free electrolytes and found the absence of EC yielded lower electrolyte conductivities.²⁰¹ Therefore, only EMC as a solvent can negatively impact the high-rate properties of cells containing EC-free electrolytes.

5.4 STUDY: THE EFFECT OF ADDITIVE CONTENT AND GRAPHITE TYPES ON PARASITIC REACTIONS

The work in this section is adapted with permission from *J. Electrochem. Soc.* **164**, A3545-A3555, (2017), Copyright the Journal of the Electrochemical Society, 2017. The study was a collaborative effort and combined data from different authors. *In-situ* gas measurements were performed by Jenn Allen, an undergraduate summer student co-supervised by the author of this thesis. UHPC and long-term cycling results were obtained from Dr. Jing Li. Alex Louli performed *in-situ* pressure measurements on cells. All other

measurements, data processing, and preparation of the manuscript was performed by the author.

5.4.1 Motivation

As discussed throughout this thesis, electrolyte additives have been widely used to mitigate parasitic reactions that occur at both electrodes in lithium-ion cells. Improving the stability of electrode-electrolyte interfaces allows for cells to be operated at higher positive electrode potentials, thus increasing the available capacity and energy density of the cell while decreasing the cost per kWh.

Another way of addressing the issues of cost and energy density is to use materials with intrinsically higher energy density such as natural graphite (NG) as a negative electrode material instead of synthetic graphite, here called artificial graphite (AG). NG is known to perform poorly in some cells, which has in the past been attributed to surface exfoliation and cracking of particles.^{48,49,202,203} Park et al. found spherical natural graphite showed signs of particle swelling and cracking caused by mechanical strain during cycling, which could be suppressed using a carbon coating process.⁴⁸ Carbon coatings on natural graphite negative electrodes have been studied in the past to avoid exfoliation from propylene carbonate-containing electrolytes, but these coatings might decrease the energy density.^{202,203} AG performance reported in the literature appears to outperform natural graphite. However, few direct comparisons of artificial and natural graphite exist in the literature. Lee et al.²⁰⁴ found that plasma treated AG performed better in long term cycling and rate testing, and had a similar irreversible capacity compared to the treated NG, while the NG material had a higher specific capacity. The purpose of the present study was to

elucidate the differences in electrochemical performance of AG and NG using non-destructive techniques, in otherwise identical electrochemical systems.

The ternary electrolyte additive blend, PES211 (2% wt. PES, 1% wt. DTD, 1% wt. TTSPi) in 1.2 M LiPF₆ EC:EMC (3:7 wt.) was used in different loading amounts to provide different levels of SEI protection (i.e. $x = 0.5$ PES211 would use half of the weight percent of additive loading: 1% PES, 0.5% DTD, 0.5% TTSPi). Li et al. provided an in-depth study on the electrochemical properties of the materials studied in this work and found that AG containing cells performed better than NG cells in long term cycling experiments from 3.0 V to 4.2 V and 4.3 V at 20°C and 40°C, and showed better performance in UHPC testing.²⁰⁵ However, UHPC and long-term cycling experiments alone were not sufficient to explain the differences in performance between AG and NG cells.

This section expands on Li's work, providing results of *in-situ* measurements of parasitic heat flow using isothermal microcalorimetry, as well as *in-situ* gas and *in-situ* pressure measurements of pouch cells. The charge-discharge method was used as a way of probing parasitic reactions, but in conjunction with gas and pressure measurements aimed to make more specific conclusions about the failure mechanisms present in NG.

5.4.2 Experimental

The cells in this work were SC-NMC532/AG and SC-NMC532/NG. Single-crystal NMC532 has been found to have superior performance at high voltage to polycrystalline NMC which is typically used in cells.²⁰⁶ By using a positive electrode which performs well, differences in the performance of AG and NG negative electrode materials may be more apparent. Details of the electrochemical performance of single crystal NMC532 can

be found in Reference 206. The properties of the AG and NG graphite materials used in this work are summarized in Table 5.

Table 5: Physical properties of AG and NG used in this study (provided by suppliers)

Type	D50 (μm)	Tap Density (g/cm^3)	Specific Surface Area (m^2/g)	Press Density (g/cm^3)	Reversible capacity (mAh/g)	First Cycle Efficiency (%)	Pr*	Pt^
AG	16 (3)	1.1	1.2 (5)	N/A	~345	~92.1	0.13	0.02
NG	18 (2)	1.1 (1)	3.8 (8)	1.80(5)	~360	~94	0.06	0.07

*Probability of random stacking

^Probability of 3R (rhombohedral) stacking

The base electrolyte used in this work was 1.2 M LiPF_6 EC:EMC (3:7 wt.). The additive blend was a 100%, 50%, or 25% loading of PES211. Cells were filled with 0.84 mL of electrolyte. Shorthand cell names are used throughout the rest of this work and refer to the additive loading and graphite type. For example, 0.5 NG corresponds the 50% additive loading in an NG cell: 1% PES, 0.5% DTD, and 0.5% TTSPi in an SC-NMC532/NG cell.

Cells for isothermal microcalorimetry experiments were formed to 4.2 V using formation protocol A. Cells were then placed in the calorimeter at 40°C and cycled four times using a C/20 rate between 3.0 V and 4.2 V to ensure a well formed, stable SEI on the negative electrode. Cells were then cycled three times at 1 mA between 3.65 V and 3.85 V to investigate the effect of parasitic reactions at the negative electrode, to avoid large amounts of parasitic reactions associated with a high voltage positive electrode. Cells were then cycled between 4.0 V and different upper cut-off limits: 4.2 V, 4.3 V (twice), 4.4 V (twice) and again 4.2 V (twice) at 1 mA to investigate the performance and the parasitic heat flow in different high voltage ranges.

UHPC cycling was performed between 3.0 V and 4.1 V, 4.2 V, 4.3 V, and 4.4 V at C/20, 40°C for 16 cycles.

During *in-situ* gas measurements 0.25 AG, 0.25 NG, 1.0 AG, and 1.0 NG cells were cycled once between 3.0 and 4.3 V and then held at 4.4 V for 100 hours and 4.5 V for 100 hours at 40°C to investigate differences in gas production between AG and NG.

Scanning electron microscopy (SEM) was performed with a NanoScience Phenom Pro G2 Desktop SEM. Uncycled dry NMC532/AG and NMC532/NG pouch cells were disassembled, and small pieces of the negative electrodes were cut out and mounted on double-sided carbon tape and stuck to the SEM sample stubs.

In-situ stack pressure measurements were made in the apparatus described by Louli et al. in Reference 59. Pouch cells were volumetrically constrained in an aluminum enclosure such that any volume expansion of the cell would exert a force on the enclosure. The force was measured with subminiature load cells (LCKD - OMEGA Engineering), with capacities of 100 or 250 lbs (445 and 1112 N), connected to DP25B-S-A (OMEGA Engineering) strain gauge panel meters. The load cells were fastened in the enclosure with the pouch cell, separated by a force distributing plate. The measured force was converted to Pa using the pouch cell area of $\sim 6.0 \text{ cm}^2$. For *in-situ* measurements, the pouch cells were connected to an E-One Moli Energy Canada battery testing system at $40.0 \pm 0.1^\circ\text{C}$. The analog 0-10 V output of the strain gauge panel meter was connected to a ‘slave channel’, allowing for simultaneous voltage and pressure measurements.

Long-term cycling was performed at a C/3 rate with a CCCV protocol at 40°C. Every 50 cycles a C/20 cycle was performed to test low-rate capacity retention.

5.4.3 Results and Discussion

Figure 5.11 shows SEM images of the AG and NG electrodes used in this work. AG particles were much smaller than NG particles and were more varied in size and shape. NG particles were more spherical, with larger pores between particles.

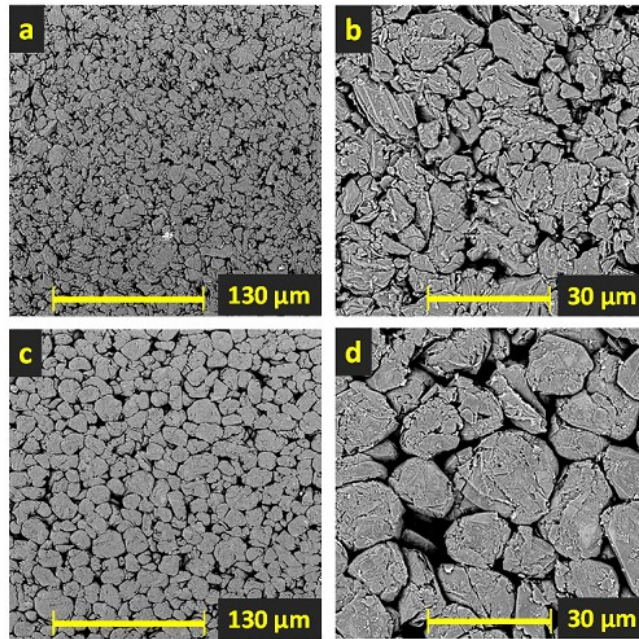


Figure 5.11: SEM images of a,b) AG electrode surface c,d) NG electrode surface

Figure 5.12 provides the summarized details of 16 UHPC cycles performed at 40°C at a C/20 rate from 3.0 V to 4.1 V, 4.2 V, 4.3 V and 4.4 V. Fractional charge endpoint capacity slippage per hour and fractional fade per hour are shown as the value at the end of the 16th cycle, and coulombic inefficiency ($CIE = 1 - CE$) per hour is shown as the linearly interpolated value at the 16th cycle using results of the previous five cycles, plotted as a function of upper cut-off voltage. Figures 5.12a, c, and e show the fractional fade per hour, fractional charge endpoint capacity slippage per hour, and coulombic inefficiency per hour, respectively, for 1.0 AG (black), 0.5 AG (red) and 0.25 AG (orange). Figures 5.12 b, d and f show the UHPC results for 1.0 NG (blue), 0.5 NG (magenta) and 0.25 NG

(light blue) cells. The color scheme is consistent throughout this work. In each plot for NG cells, 1.0 NG and 0.5 NG cells use the same y-axis as AG cells on the left, and the 0.25 NG cells use the light blue y-axis on the right. Points show the average value between pair cells and the error bars represent the range between pair cells.

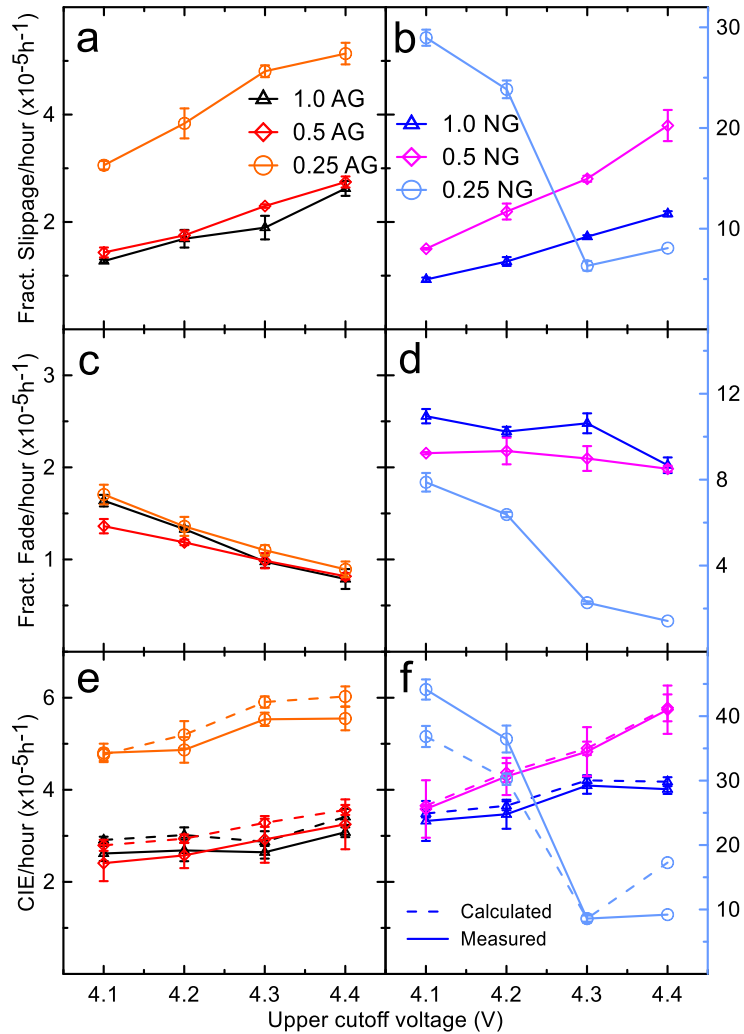


Figure 5.12: UHPC results of additive blend loadings of 0.25, 0.5, and 1.0 in AG cells (left column) and NG (right column – only 0.25 NG is represented on the right y-axis): a) Fractional charge endpoint slippage per hour, b) fractional discharge capacity fade per hour, and c) CIE per hour cycling between 3.0 V and 4.1 V, 4.2 V, 4.3 V, and 4.4 V at C/20 and 40°C. Points represent the value at the 16th cycle (slippage and fade) and the projected 16th cycle value based on a linear fit of the last 5 cycles (CIE), plotted as a function of upper cut-off voltage. Calculated CIE is shown as a dotted line and represents the sum of the fractional slippage and fade results.

Figures 5.12 a and b show 1.0 AG and 1.0 NG cells had comparable charge endpoint capacity slippage, which may suggest the magnitude of electrolyte oxidation at the positive electrode in these cells was similar. Figure 5.12c shows that the capacity fade in NG cells was always larger than in AG cells with the same additive loading. Table 5 shows that the surface area of NG was larger than AG, which could suggest more surface reactions occurred on NG due to a less protective SEI, leading to this higher fade, which would make the comparison between these graphite types difficult. However, the surface area was obtained using Brunauer–Emmett–Teller (BET) analysis and may not be a good indication of the electrochemically active surface area. Pore-size distribution analysis was not available at the time of the present study. A nitrogen molecule (used in the BET method) is much smaller in size than electrolyte solvent and additive molecules used in Li-ion cells. To be convinced the additive loadings were appropriate to compare, Figure 5.13 shows the normalized differential capacity (dQ/dV) vs. voltage during cell formation for 0.25, 0.5, and 1.0 AG and NG cells. In each case, the additive (2.5 V) and solvent (2.8 V – 3.0 V) reduction peaks were very similar between cells with the same additive loading which suggests that regardless of the BET surface area, the electrochemically active surface area between the graphite samples was effectively the same.

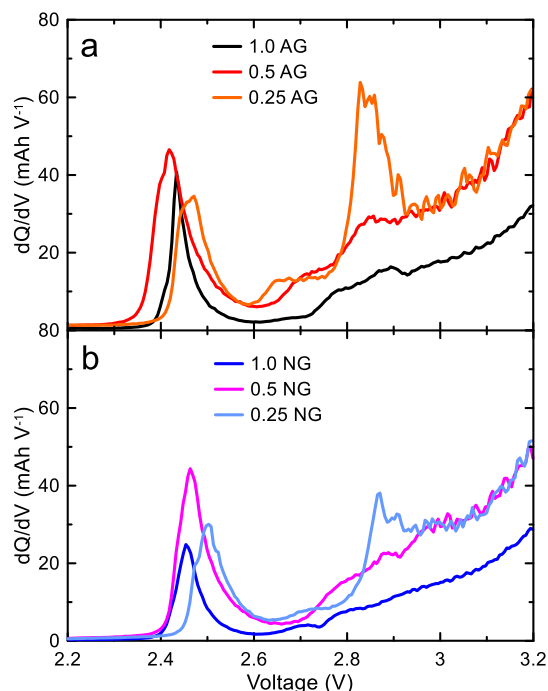


Figure 5.13: Differential capacity dQ/dV plotted against cell voltage for a) AG cells and b) NG cells.

In Figure 5.12, as the additive loading was decreased to 0.5, NG cells tended to have corresponding increases in charge endpoint capacity slippage. However, both AG and NG had relatively little change in fade. When the additive loading was further decreased to 0.25, fade more than doubled in NG cells and stayed about the same in AG cells. At the same time, charge endpoint capacity slippage increased slightly in AG cells while increasing by an order of magnitude in NG cells. In all cells other than 0.25 NG cells the slippage and fade increased with upper cut-off voltage. At 4.3 V, 0.25 NG cells showed a dramatic decrease in slippage and fade. However, not enough to remain competitive with 0.5 and 1.0 loading cells. This curious behaviour may be due to a large onset of reactions over 4.2 V, such as oxygen evolution from the NMC532 surface as recently reported by Xiong et al.²⁰⁷ and by Jung et al.⁸ which could result in a thickened, more protective SEI layer. This is purely speculation but is an interesting observation for future studies. Due

to the slightly higher fade in NG cells and the larger effect of decreased additive loading on NG cells, the CIE in NG cells was higher at all additive loadings and under all cycling conditions. A possible explanation for the observed performance may reside in the structural properties of the graphite types.

The typically low P_r -value (the probability of random stacking between layers of graphite, or turbostratic misalignment) of natural graphite (see Table 5) may suggest that there is less “pinning” between adjacent graphene layers and that more local exfoliation occurs during lithiation/delithiation, creating more surface to passivate and more electrolyte reduction products. Electrolyte reduction products such as lithium alkoxides can migrate to the positive electrode and be oxidized there creating charge endpoint capacity slippage in UHPC experiments. Low charge endpoint capacity slippage in 1.0 NG UHPC results could be explained by fewer parasitic reactions at the surface of graphite particles with a protective SEI, regardless of the possible internal particle strain and or expansion. When the additive content was decreased, the SEI layer was less protective and mechanical strain or expansion may have weakened the SEI, exposing new graphite surface where solvent was reduced to create new SEI and other reactants. Both 1.0 AG and 0.5 AG cells performed similarly in UHPC tests, suggesting a more stable SEI and a graphite structure less likely to exfoliate, probably because of the larger P_r -value of AG compared to NG. Following these assumptions, the large increase in slippage and fade in 0.25 NG cells may originate from continual formation of unstable SEI and associated reduction products, causing continual loss of lithium inventory resulting in significant capacity loss. The migration of reduction products such as alkoxides to the positive electrode could have increased the charge endpoint capacity slippage. The increase in charge endpoint capacity

slippage for both the 0.25 AG and 0.25 NG cells indicated an insufficient amount of additive in order to fully passivate the graphite electrodes. The lack of passivation was also observed in Figure 5.13, where solvent reduction occurred for both 0.25 AG and 0.25 NG but not for other additive loadings.

Isothermal microcalorimetry was then used to investigate how the parasitic heat flow (calculated using the charge-discharge method) compared with the results from UHPC studies. Low voltage cycles were performed when the graphite was in the stage-2L to stage-2 voltage plateau (cell voltage \sim 3.6 V to 3.9 V) and high-voltage cycles took place during the stage-2 to stage-1 plateau cell voltage $>$ 4.0 V. Measuring parasitic heat flow during voltage plateaus decreased any effects of slight mismatches in entropic changes as a function of voltage during charge and discharge.

The extracted parasitic heat flows from three consecutive low voltage cycles (3.65 V to 3.85 V) at 1 mA are shown in Figure 5.14. This low potential range was selected to try to minimize effects of electrolyte oxidation at the positive electrode and only probe reactions occurring at the negative side. It must be stressed, however, that species created by reduction reactions at the negative electrode could migrate to the positive side and still be oxidized at 3.65 V. Results for pair cells are not shown but were nearly identical in every case. A summary image later in this work (Figure 5.16) shows the differences between pair cell results. 1.0 AG, 1.0 NG and 0.5 AG cells yielded nearly identical heat flows through the voltage range in all three cycles, except between 3.8 V and 3.85 V, where 1.0 NG cells had slightly higher parasitic heat flow. 0.25 AG cells showed slightly higher parasitic heat flow throughout the voltage range in all cycles. However, the 0.25 NG cells had much higher parasitic heat flow than 0.25 AG: over five times higher at 3.65 V and

three times as high at 3.85 V. The similar levels of parasitic heat flow between 1.0 AG and 1.0 NG suggest the full additive loading was sufficient to provide an effective SEI on both negative electrodes. The 0.25 AG cells showed only a small increase in parasitic heat flow over 1.0 and 0.5 AG, while much higher parasitic heat flow in 0.25 NG indicated a much higher rate of parasitic reactions.

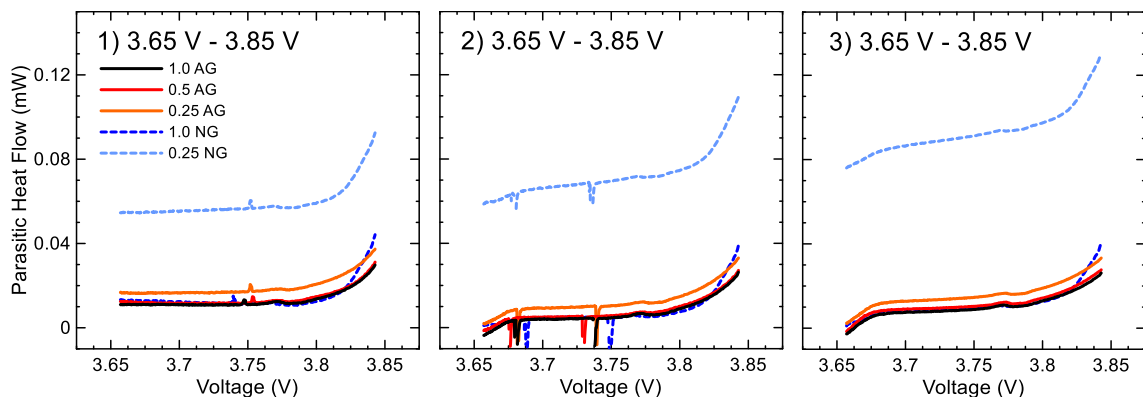


Figure 5.14: Extracted parasitic heat flow of each cell and electrolyte type during 3 cycles between 3.65 V and 3.85 V at 1 mA and 40°C. Noise seen during the first and second cycles were due to power interruptions. Numbers in the top left of each panel correspond to the 1 mA cycle number in the microcalorimetry protocol.

Parasitic heat flow measured during high voltage cycles between 4.0 V and 4.3 V (two cycles) and 4.0 and 4.4 V (two cycles) are shown in Figure 5.15. Numerical labels in each panel indicate the 1 mA cycle number, i.e. 4.3 V cycles occurred before 4.4 V cycles. At high voltage, the effects of additive loadings did not change significantly from low voltage results, suggesting that processes initiated at the negative electrode were being probed. The 1.0 AG and 1.0 NG cells still showed equivalent parasitic heat flows, which suggests the oxidized products from high voltage reactions at the positive electrode did not have different effects on the two negative electrode materials if a sufficient SEI was present. As the additive loading was decreased, AG cells showed a gradual increase in parasitic heat flow, indicating either more oxidation products were reducing at the less

protected negative electrode or more reduction products from the negative electrode were oxidizing at the positive electrode. Either option could explain the difference in parasitic heat flow of 1.0 AG and 0.5 AG when cells were exposed to high voltage. The 0.25 NG cells were not plotted in Figure 5.15 as to appropriately show differences between the AG cells and 1.0 NG cells. The 0.25 NG cells contained parasitic heat flow an order of magnitude larger than that of the 1.0 AG cells and are shown in a summary in Figure 5.16.

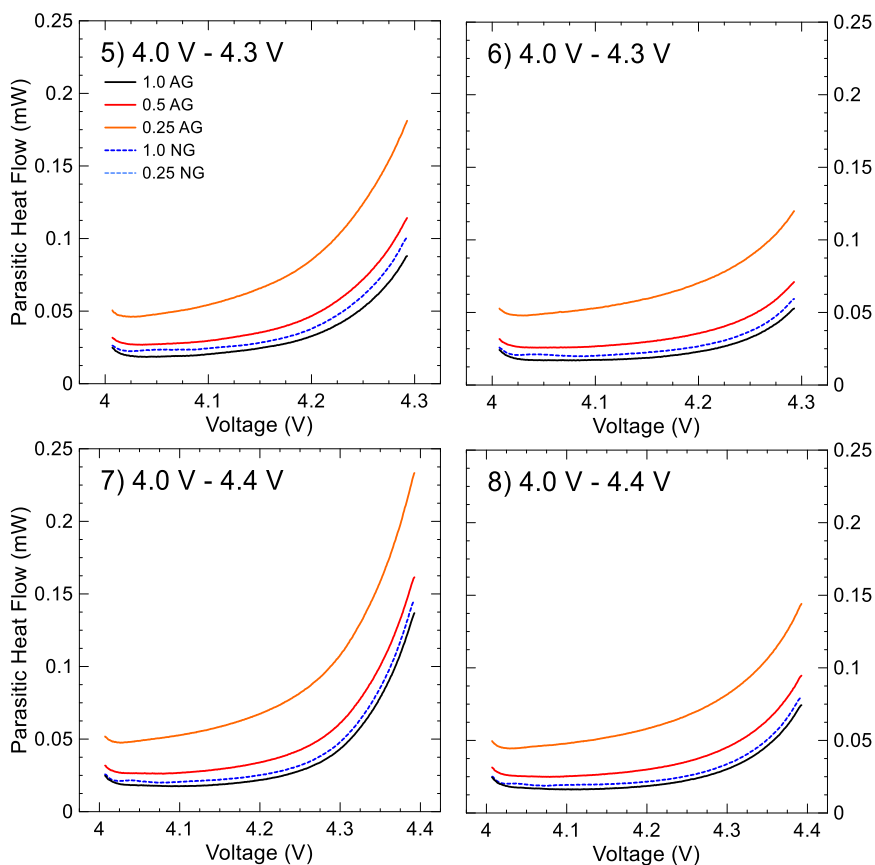


Figure 5.15: Extracted parasitic heat flow for two cycles from 4.0 V to 4.3 V and 4.0 V to 4.4 V at 40°C. Numbers in each panel correspond to the 1 mA cycle number in the microcalorimetry protocol.

In Figure 5.16, the heat flow was integrated over the entire voltage range for each cell and averaged to give the mean parasitic heat flow per cycle. Figure 5.16a shows the summarized results including the 0.25 NG cells and Figure 5.16b shows the results

excluding the 0.25 NG cells to compare the results clearly. Points in Figure 5.16 indicate the average between two pair cells and error bars show the range between pair cells. The parasitic heat flow of 0.25NG cells continued to deviate compared to other cells from the low voltage cycling, increasing significantly at high voltage. While all AG cells and 1.0 NG cells decreased in parasitic heat flow during the second cycle to 4.3 V and 4.4 V, 0.25 NG increased, suggesting the passivating qualities of the SEI were not improving. Due to the increase in parasitic heat flow even at low voltages and the large deviation from the performance of 0.25 AG cells, these parasitic reactions/processes were attributed to originating at the negative electrode.

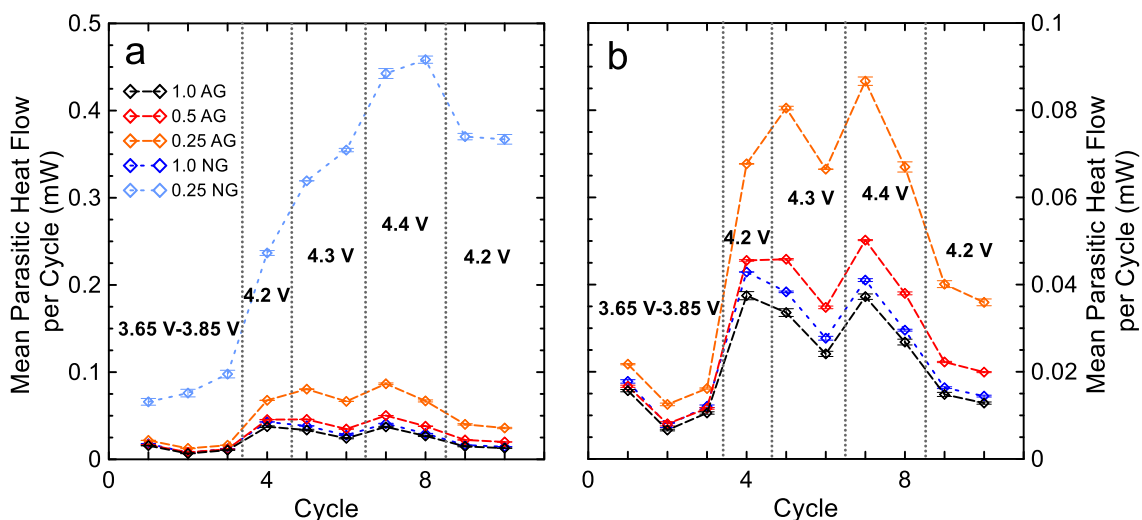


Figure 5.16: Summary of all microcalorimetry cycles. The mean parasitic heat flow over each cycle is shown for all cells in a), and b) shows a zoomed in view of cells excluding the 0.25 NG cells.

Figure 5.17 shows the *in-situ* volume measurements of 1.0 and 0.25 AG and NG cells during 2 cycles from 3.0 V to 4.3 V at 40°C measured at a C/20 rate followed by 100 hour voltage-holds at 4.4 V and 4.5 V. The 1.0 AG and 1.0 NG cells showed no gas evolution during either voltage-hold. The 0.25 AG cells show no gas evolution at 4.4 V and until approximately 30 and 50 hours into the 4.5 V hold. The 0.25 NG cells show a

small amount of gas production at 4.4 V and a steadily increasing amount of gas at 4.5 V. Increased gas production at high voltage suggested an increase in parasitic reactions. The cells had identical positive electrodes, so the increased gas production must have resulted from interactions between the negative and positive electrodes. Species created at the negative electrode must have moved to the positive and react there, generating at least some of the gas. These results suggest that a full additive loading was sufficient to protect the negative electrode from creating these species. The 0.25 loading was insufficient to protect NG from generating these species while AG cells did not produce gas until long after exposure to 4.5 V. *In-situ* gas results agreed with microcalorimetry results, which showed continually increasing parasitic reactions in 0.25 NG cells at high voltage while all other cells decreased in parasitic heat flow with time.

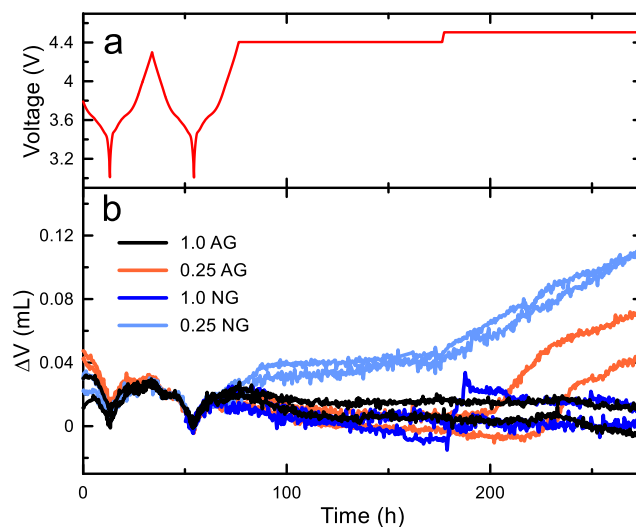


Figure 5.17: *In-situ* volume measurements during 4.4 V and 4.5 V holds at 40°C for 100 hours each. a) The voltage vs time for a 1.0 AG cell. b) cell volume change vs time, normalized to the bottom of discharge of the first cycle.

To investigate the effect of mechanical strain and particle swelling in NG cells, *in-situ* stack pressure measurements were performed. Cells were placed in aluminum cell holders between a metal plate and a pressure sensor. The cell thickness was therefore

constrained so that swelling would cause a stack pressure increase as compliant material in the cells compressed. Cells were cycled between 3.0 V and 4.2 V at a C/6 rate at 40°C. The method and apparatus are described in detail by Louli et al.⁵⁹ The raw voltage and pressure vs. time for one of each cell are shown in Figure 5.18a (1.0 AG and 1.0 NG) and in Figure 5.18b (0.25 AG and 0.25 NG). Figure 5.18c and Figure 5.18d summarize the pressure data by plotting the change in average pressure integrated over cycle time vs cycle number and the change in pressure at top of charge vs. cycle number, respectively. The 1.0 AG cells showed minimal change in average pressure and top of charge pressure over the course of over 1 month of cycling. The 0.25 AG cells showed a small increase over 1.0 AG cells during cycling. Conversely, 1.0 and 0.25 NG cells both showed large increases in average pressure and pressure at top and bottom of charge. The increase in stack pressure at top of charge could indicate the continual mechanical strain and swelling of graphite particles, as well as SEI growth. If the method was sensitive enough to measure SEI growth, the thickening of SEI layers may also be the reason behind the slightly higher pressure in 0.25 AG cells. The increase in pressure at bottom of charge suggested the expansion of NG and possibly the increase in SEI thickness was irreversible.

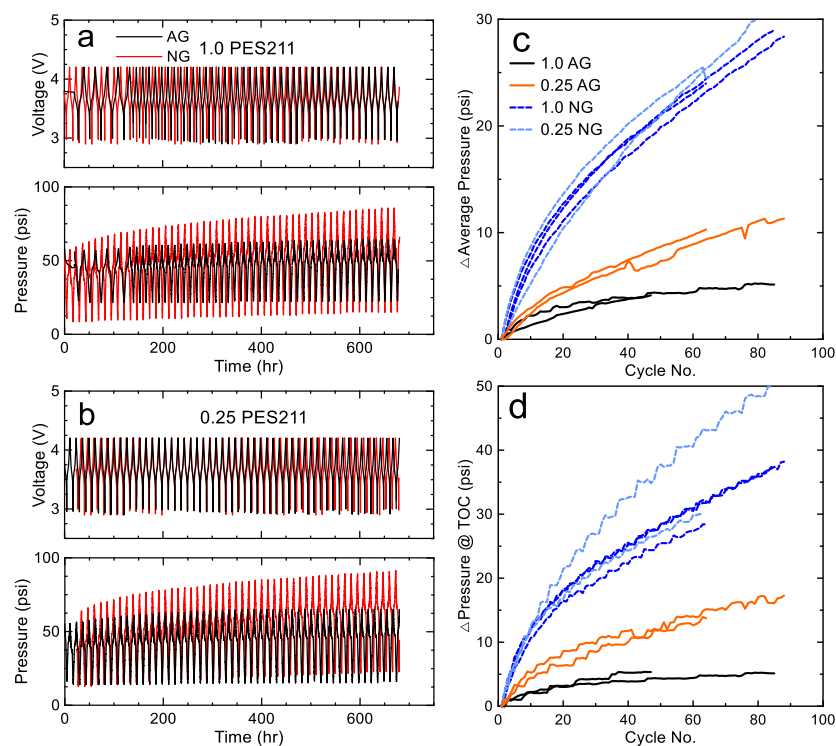


Figure 5.18: *In-situ* pressure measurements of a) 1.0 AG and 1.0 NG cells, b) 0.25 AG and 1.0 NG cells vs. time cycled from 3.0 V to 4.2 V at a rate of C/6 at 40°C. c) The averaged pressure over each cycle. d) The change in pressure at top of charge.

Although *in-situ* stack pressure measurements are not yet mature enough to elucidate all of the mechanisms behind the increases in pressure, the results shown here can be used to connect to the findings of both UHPC and calorimetry measurements.

To probe the mechanism responsible for the observed capacity loss in NG cells, 1.0 AG and 1.0 NG cells which underwent UHPC cycling to 4.2 V were tested using dV/dQ analysis.^{132,135} The full additive loading 4.2 V cells were chosen to minimize the influence of electrolyte oxidation and to observe the impact of graphite expansion on the full additive loading after many cycles at a high rate, which was not possible in calorimetry studies. After UHPC cycling, long-term cycling was performed on AG and NG at a C/3 rate with a constant voltage hold at top of charge until the current reached a value of C/20 for 558 and 586 cycles, respectively at 40°C. Cells were then cycled on the UHPC system once again

for two cycles at $C/20$. Figures 5.19a, b, and c show the discharge capacity, normalized discharge capacity, and ΔV , respectively, during the long-term cycling. Figure 5.19 shows that even with the full additive loading, 1.0 NG cells had higher capacity fade and impedance growth than 1.0 AG cells. The dV/dQ analysis results are shown in Table 6.

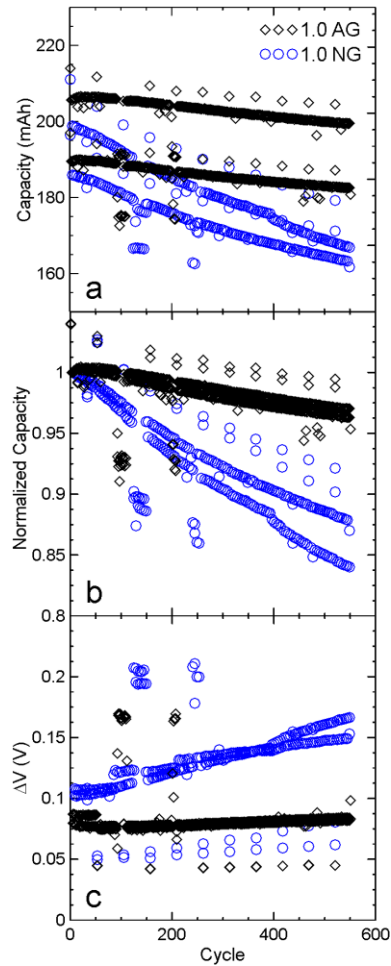


Figure 5.19: Long term cycling results for NMC532/AG and NMC532/NG cells from 3.0 V to 4.3 V during $C/3$ CCCV cycling at 40°C . a) discharge capacity, b) fractional discharge capacity, and c) ΔV . 1.0 AG cells (black diamonds) and 1.0 NG cells (blue circles) were used for dV/dQ analysis.

Table 6: dV/dQ fitting results for AG and NG cells

Cell	Cycle number	Normalized Capacity	Negative Shift (mAh)	Positive Shift (mAh)	Negative Mass (g)	Positive Mass (g)	Total Shift (mAh)
AG	2	1.00	-4.09997	0.25996	0.88	1.154	13.45
	559	0.946	-3.3	-13.39108	0.8863	1.158	
NG	2	1.00	-3.62	0.08	0.886	1.14	31.33
	587	0.866	-1.8	-29.43404	0.894	1.13971	

$$\text{Total Shift} = (\text{pos. at cycle 2}) - (\text{pos. at end}) + (\text{neg. at end}) - (\text{neg. at cycle 2})$$

Fits to the dV/dQ and dQ/dV data using the reference materials for AG cells, shown in Figure 5.20a and Figure 5.20b, and NG shown in Figure 5.20c and Figure 5.20d, demonstrated good fitting of all voltage curve features. The AG cells had approximately 95% capacity retention after 560 cycles while the NG cell had 87% capacity retention. The total relative electrode shift (both electrodes relative to cycle 2) for AG and NG cells was 13.45 mAh and 31.33 mAh respectively, and the electrode material mass loss was found to be negligible for both cells. Therefore, the observed capacity fade in NG cells was not due to mass loss caused by particle expansion and damage, but due to lithium inventory loss at the negative electrode, which was worse for the NG cells. The loss of lithium inventory can be supported by the impedance growth seen in NG cells, likely caused by a thickening SEI.

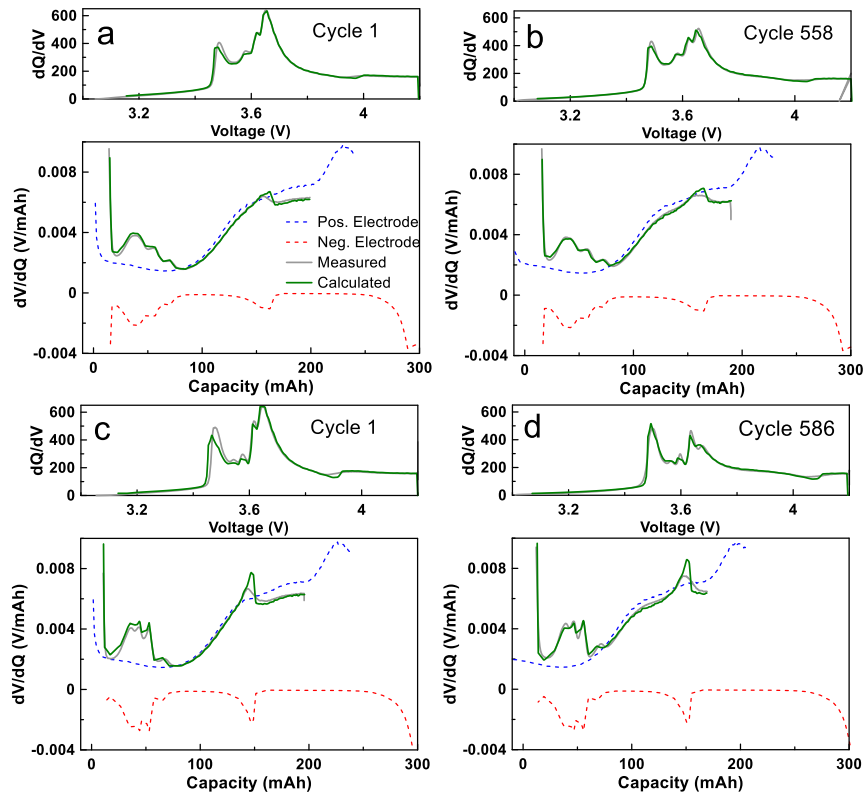


Figure 5.20: dV/dQ fitting results of 1.0 AG cells before (a) and after 550 cycles (b), and 1.0 NG cells before (c) and after (b) 586 cycles. The positive electrode reference curves are shown in blue, negative reference in red, fitted results in green, and experimental results in grey.

Figure 5.21a and Figure 5.21c demonstrate the fitted relative positions of the positive and negative electrode voltage curves of AG and NG cells, respectively, during the first full UHPC cycle. Figure 5.21b and Figure 5.21d show the results of post long-term cycling. The NG cells initially had slightly more negative electrode capacity than AG cells and contained a larger stage-2-stage-1 voltage plateau. The NG cells may therefore have spent a slightly longer amount of time in the two-phase plateau during high voltage cycling in early cycles. It is unknown if different times in graphite stages may have influenced the amount of particle swelling, and thus the parasitic heat flow or cycling performance, though the similar trends in AG and NG cells in microcalorimetry results

suggest that it did not. Additionally, due to the large amount of relative electrode shift caused by lithium inventory loss, the time spent in the stage-2-stage-1 plateau was smaller in NG than AG cells after cycling. Future work could investigate the effects of the amount of time spent in specific graphite stages in NG. Internal stress might impact the cell more when graphite is in the stage-1 phase.

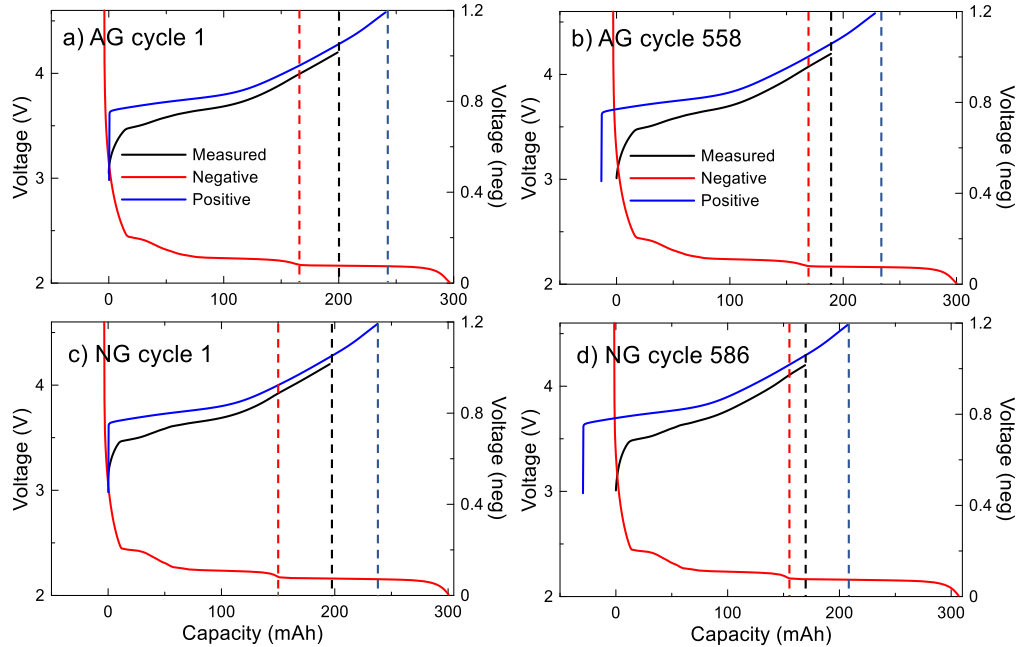


Figure 5.21: dV/dQ fitting of the first cycle of a) 1.0 AG and b) 1.0 NG cells. The full cell voltage curve is shown in black, the fitted positive electrode curve in blue, and the fitted negative electrode in red. The relative endpoint positions for the positive electrode and the full cell, and the position of the stage-2 graphite feature are shown as dotted lines.

Considering the results obtained from UHPC, microcalorimetry, *in-situ* pressure measurements, *in-situ* gas measurements, and dV/dQ fitting, the proposed mechanism for the observed performance of NG is shown in Figure 5.22. In Figure 5.22a, a graphite particle in a 0.25 NG cell has a thin SEI layer (red) after formation. During cycling the particle expands and contracts, breaking the SEI and reducing solvent or products of electrolyte oxidation from the positive electrode to form new SEI or other reaction

products, including gas. The mechanism was supported by the large parasitic heat flow and gas production of 0.25 NG cells, as well as the large relative electrode shift loss found in UHPC dV/dQ measurements. Over time the products of the continual SEI formation may have led to the increased impedance. Figure 5.22b proposes that a sufficiently thick SEI such as in 1.0 NG could sustain the strain of expansion and suppress surface area exposure, preventing reduction of solvent or other electrolyte species on the graphite surface. Low shift loss, no gas production, and low parasitic heat flow, all close to that of AG cells suggested that a sufficient SEI can help mitigate some unwanted performance characteristics of NG cells.

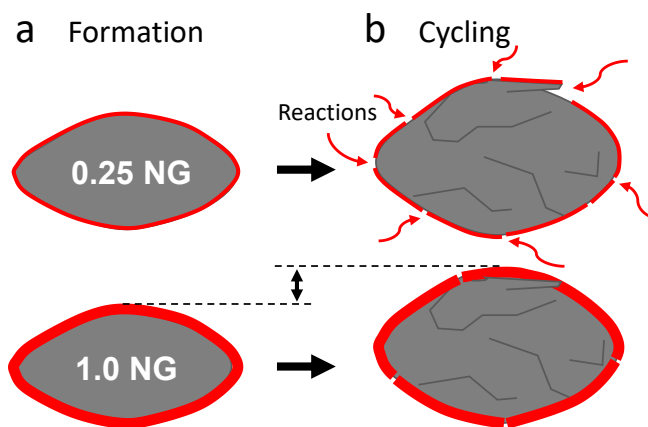


Figure 5.22: The proposed mechanism responsible for the observed UHPC performance of natural graphite. a) 0.25 NG cells with a thin or incomplete SEI film does not fully protect the electrode particles during expansion and contraction, causing electrolyte solvent or oxidized species to reduce at the exposed surface. b) 1.0 NG cells likely have a thick and fully formed SEI which is sufficient to withstand mechanical strain and does not expose new areas of electrode.

The above data in this section were all consistent with the model presented above. However, when the same graphite types were used in cells with different positive electrode materials, such as Al₂O₃-coated NMC622A and high-voltage coated NMC622B, major

differences could be seen. In 622A cells undergoing long-term cycling the two graphite types behaved similarly or even oppositely! Figures 5.23a, b, and c show the long-term cycling of 622A/AG and 622A/NG and Figures 5.23d, e, and f show data for 622B/AG and 622B/NG, all with the full loading 1.0 PES211 electrolyte at 40°C, C/3 CCCV, 3.0 to 4.2V. Figure 5.23 shows that just by changing the positive electrode coating, dramatic differences between the capacity retention and impedance growth of cells with the different graphite types were observed. The impedance growth for NMC622A cells with AG negative electrodes was worse compared to that of the cells with NG negative electrodes which was completely opposite to the behaviour observed in NMC532 cells. Interestingly, NMC622B/AG cells showed slightly worse impedance growth than NMC622B/NG cells, but the capacity retention and fade rate were much better in NMC622B/AG cells than NMC622B/NG cells. However, the effect of 0.25 PES211 was not tested, which would likely show much worse performance for cells with NG. The entire suite of experiments presented in this paper for the NMC532 cells have not yet been applied to the NMC622 cells. The purpose of Figure 5.23 is to alert readers that everything in a Li-ion cell matters and it is dangerous to create explanatory models for one cell chemistry and apply them, without verification, to other cell chemistries. Comparing Figure 5.19 and Figure 5.23 strongly suggests that inter-electrode interactions and electrode coatings play a strong role in determining the response of the graphite electrode.

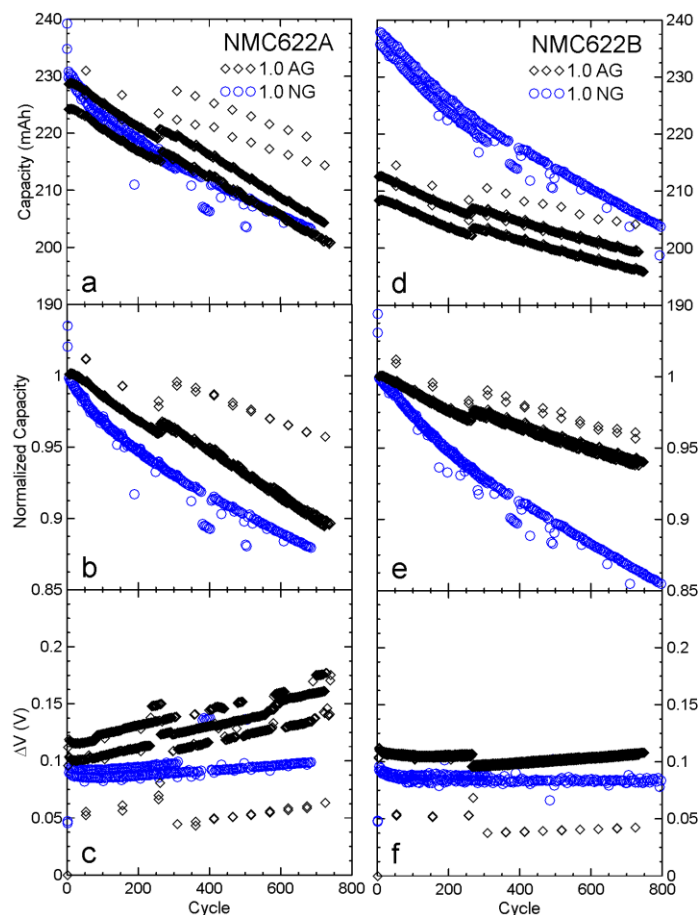


Figure 5.23: Long term cycling results for coated NMC622/AG and NMC622/NG cells with 1.0 PES211 electrolyte cycled at C/3 CCCV at 40°C. a,d) discharge capacity, b,e) fractional discharge capacity, and c,f) ΔV . NMC622A cells are shown in the left panels (a,b, and c) and NMC622B are shown in the right panels (d, e, and f). AG cells are shown as black diamonds and NG cells are shown as blue circles.

5.4.4 Conclusions

The electrochemical performance of SC-NMC532/AG and SC-NMC532/NG cells was studied using UHPC and *in-situ* measurements: isothermal microcalorimetry, gas volume, and pressure. Cells contained varying amounts of a 2% wt. PES, 1% wt. DTD, 1% wt. TTSPi additive blend to study the effect of the negative electrode material and the impact of the SEI. When additive loading was decreased in cells containing AG there was little increase in parasitic heat flow, minimal impact on UHPC metrics, very little

irreversible cell expansion measured by *in-situ* pressure measurements, no gas production during *in-situ* high voltage-holds, and little relative electrode shift loss in dV/dQ tests. In contrast, NG cells showed similar electrochemical performance and parasitic heat flow to AG when a full additive loading was used, but very large amounts of parasitic heat flow, poor electrochemical performance, gas production, and large shift loss when the additive loading was decreased. Pressure measurements showed irreversible expansion in all NG cells. The results suggest that NG undergoes irreversible particle strain and expansion, which does not increase the amount of parasitic reactions if a protective SEI film is present, as was the case in NG cells with a full additive loading. When the additive loading was decreased, the SEI layer was insufficient to protect newly created surface area on the expanding NG particles. Solvent and oxidation products from high voltage reactions at the positive electrode then continually reduced on the negative electrode, forming an unstable SEI, which caused the observed high parasitic heat flow, charge endpoint capacity slippage, capacity fade and low CIE.

The charge-discharge method of determining the parasitic heat flow was able to identify differences in the parasitic heat flow between cells with different types of graphite negative electrode, but otherwise identical cell chemistries. The results allowed for confidence in the proposed mechanisms for NG performance in SC-NMC532 cells and were consistent with all other measurements. Parasitic heat flow results confirmed that cross-talk reactions were prominent in cells with small additive loadings since cells with the same positive electrode materials had large differences in parasitic heat flow at high voltage.

5.5 CHAPTER CONCLUSIONS

The two studies presented in this chapter showed that the charge-discharge method is an effective way to obtain the parasitic heat flow of a lithium-ion cell during operation. The parasitic heat flow as a continuous function of voltage was useful when comparing cells with similar parasitic heat flow and was consistent between pair cells in both studies. The charge-discharge method introduced in this chapter was also used in studies to investigate the performance of single-crystal NMC532 compared to polycrystalline NMC532,²⁰⁶ and the optimization of additive content in EC-free electrolytes.²⁰⁰

The treatment of cell overpotential used in this chapter was only realistic when very low rates were used, such as $C/200$ (1 mA). Experimental protocols took approximately six weeks in the two studies in this chapter. Ideally, cells would take less time to test, so higher rates may be useful. Additionally, obtaining the difference between parasitic heat flow during charge and discharge of a cell would allow for more informative comparisons between cells. During the first exposure to high voltage, a large onset of parasitic reactions may form SEI products on the positive electrode, mitigating some reactions during discharge.

The next chapter introduces further developments to the charge-discharge method which aim to help shorten experiment times by charging at slightly higher rates, and to obtain differences between charge and discharge parasitic heat flow.

CHAPTER 6 IMPROVING THE CHARGE-DISCHARGE METHOD

The charge-discharge method of obtaining parasitic heat flow introduced in the previous chapter was found to be consistent between pair cells and supported existing methods of probing cell performance such as UHPC, long-term cycling, and gas measurements.

However, the difference in parasitic heat flow between charge and discharge could not be obtained due to the averaging of the entropic heat flow in the charge-discharge method. When cells were cycled slowly (1 mA in the previous chapter) the parasitic heat flow likely changed between a set voltage point during charge and the same voltage during discharge as reaction products thickened or stripped away the SEI. Obtaining the parasitic heat flow during charge and discharge may be a useful tool to observe the onset of parasitic reactions during the first exposure of a cell to a high voltage range. Section 6.1 of this chapter introduces a way to approximate the entropic heat flow of a cell to find the differences between the parasitic heat flow during charge and discharge. Section 6.2 presents a study in which the charge and discharge parasitic heat flows were calculated for different types of NMC/graphite cells with different coating types. The study also showed that the parasitic heat flow must be considered very carefully when cells with different materials and coatings were compared, motivating new methods of measuring the parasitic heat flow.

Additionally, the previous chapter showed that the treatment of overpotential was not realistic and required more attention if larger currents were to be used to speed up measurements. Section 6.3 aims to improve upon the accuracy and speed of the charge-discharge method by calculating a more realistic overpotential for cells during

measurements. Section 6.4 presents the results of two studies which explore the effect of methyl acetate (MA) in SC-NMC532/AG and NCA/SiO-graphite cells. The experiments further motivate the need for a more robust technique to differentiate between different reactions which may occur in cells.

6.1 CHARGE AND DISCHARGE PARASITIC HEAT FLOW

The charge-discharge method was used to show that parasitic heat flow changes with UCV, and also between cycles in the same voltage window. In the previous chapter, cells exhibited very high parasitic heat flow during the first cycle to a new UCV. During the charge portion of a cycle to a new voltage range, parasitic reaction products would typically begin to create more passivating SEI layers, decreasing the parasitic heat flow during the next cycle, but also during the discharge portion of the initial cycle. Therefore, the magnitude of the parasitic heat flows during charge and discharge in the initial high-voltage cycle were likely different. During the next cycle to the same UCV the parasitic heat flows between charge and discharge were likely much more similar than the previous cycle due to the initial build-up of SEI.

If the parasitic heat flow of a cell is assumed to be exactly the same between charge and discharge, the entropic heat flow can be found using the measured charge (*ch*) and discharge (*dis*) heat flow. The measured heat flow during each portion of a cycle as a function of voltage are given (using a simplified version of Equation 2.13) by

$$\dot{q}_{ch} = \dot{q}_{entropy\ ch} + \dot{q}_{overp\ ch} + \dot{q}_{p\ ch} \quad 6.1$$

and

$$\dot{q}_{dis} = \dot{q}_{entropy\ dis} + \dot{q}_{overp\ dis} + \dot{q}_{p\ dis}. \quad 6.2$$

where $\dot{q}_{entropy}$ is the entropic heat flow and \dot{q}_{overp} is the overpotential heat flow. If the assumption is made that the parasitic heat flows are the same between charge and discharge, and substituting the reversibility of entropic heat flow between charge and discharge, Equations 6.1 and 6.2 become

$$\dot{q}_{ch} = \dot{q}_{entropy} + \dot{q}_{overp\ ch} + \dot{q}_p \quad 6.3$$

and

$$\dot{q}_{dis} = -\dot{q}_{entropy} + \dot{q}_{overp\ dis} + \dot{q}_p. \quad 6.4$$

The entropic heat flow can then be calculated for a cycle with identical charge and discharge parasitic heat flow by

$$\dot{q}_{entropy} = \frac{(\dot{q}_{ch} - \dot{q}_{dis})}{2} + \frac{(\dot{q}_{overp\ ch} - \dot{q}_{overp\ dis})}{2}. \quad 6.5$$

The second term on the right hand side in Equation 6.5 is effectively zero since the overpotential heat flow during charge is almost identical to that of discharge using the methods outlined in Section 5.2.2.

Once the entropic heat flow is obtained for one cycle it may be used to calculate the parasitic heat flow during charge or discharge in any other cycle, since the entropic heat flow should not change between cycles. The charge and discharge parasitic heat flows can be expressed (using a simplified version of Equation 2.13) as

$$\dot{q}_{p\ ch} = \dot{q}_{ch} - \dot{q}_{overp\ ch} - \dot{q}_{entropy} \quad 6.6$$

and

$$\dot{q}_{p\ dis} = \dot{q}_{dis} - \dot{q}_{overp\ dis} + \dot{q}_{entropy}. \quad 6.7$$

Equations 6.5, 6.6, and 6.7 are only true if the parasitic heat flow during charge is exactly the same as during discharge as a function of voltage during the cycle in which the entropic heat flow was calculated. Therefore, in reality the method developed here is only

an approximate calculation and should be considered as a qualitative way to observe differences in parasitic heat flow between charge and discharge.

Figure 6.1a shows the measured heat flow during charge (solid lines) and discharge (dashed lines) of two cell types (NMC532B/NG and NMC622B/NG) with identical electrolytes during a 1 mA cycle between 3.9 V and 4.4 V following a previous cycle to 4.4 V (the details of the experiment will be discussed in the next section). The reversible nature of the entropic heat flow can be observed in Figure 6.1a, in which the parasitic heat flow is approximately the average between the measured charge and discharge heat flow. While likely not exactly the same, the parasitic heat flow could be assumed to be similar between charge and discharge since the cell had been cycled to 4.4 V previously. Equation 6.5 was then used to find the entropic heat flow during charge ($+\dot{q}_{entropy}$) and discharge ($-\dot{q}_{entropy}$) for each cell. The calculated charge and discharge entropic heat flows are shown in Figure 6.1b.

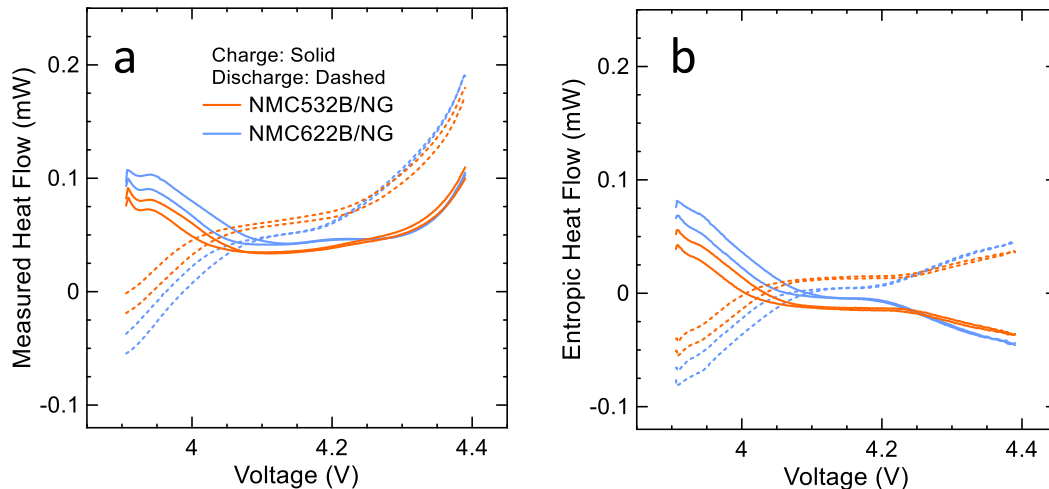


Figure 6.1: a) Heat flow during charge (solid lines) and discharge (dashed lines) NMC532B/NG (orange) and NMC622B/NG (blue) cells during a cycle between 3.9 V and 4.4 V at 1 mA after a previous cycle to 4.4 V at 40°C. b) The calculated entropic heat flow during charge (solid lines) and discharge (dashed lines).

The sharp features at the beginning of the charge portion of the cycle in Figure 6.1 were due to the initial change in current at the beginning of charge. The ‘crossover’ behaviour in the entropic heat flow seen in Figure 6.1b was likely due to the graphite stage-2 transition between two-phase regions. Figure 6.2 shows the typical cell balance in the cells used in Figure 6.1 (the cell shown in Figure 6.2 is NMC532B/NG). The full cell voltage is shown in black, the positive electrode in blue, and the negative electrode in red. Cells in Figure 6.1 were balanced for 4.5 V operation and transitioned through the graphite stage-2 region around 3.9 V to 4.0 V. It is possible that a significant amount of shift loss (see Section 1.6.5) could cause entropy features to shift as a function of voltage between cycles. Therefore, some anomalous features in charge and discharge parasitic heat flow using this method may appear in voltage ranges where large changes in entropy occur. Figure 6.1 also demonstrates the consistency of the entropic heat flow calculation between pair cells. Slight differences in electrode balancing between cells yielded slightly different entropic heat flow between pair cells at lower voltages. After the stage-2 feature, both pairs of cells had the same values of entropic heat flow, demonstrating excellent consistency.

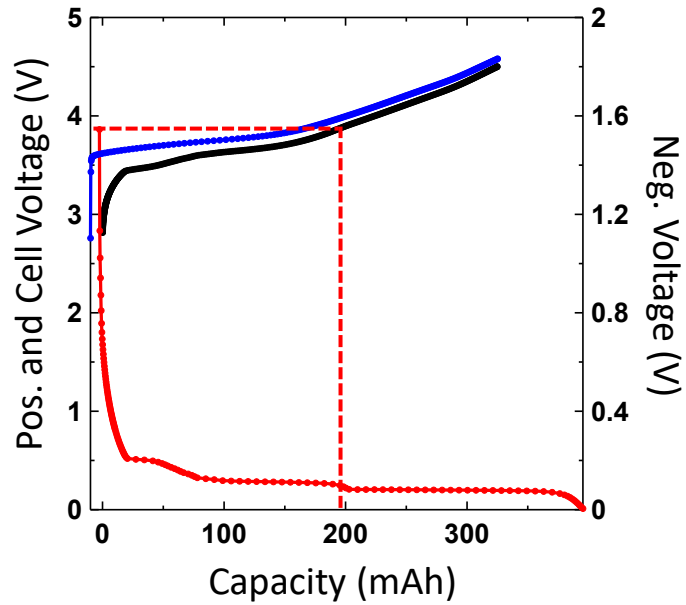


Figure 6.2: Voltage vs. capacity for an NMC532B/NG full cell (black), positive electrode (blue), and negative electrode (red). The dashed red lines show that the phase-2 graphite transition occurred at a cell voltage of approximately 3.9 V.

The parasitic heat flows during charge and discharge for each cell were calculated using Equations 6.6 and 6.7 and the entropic heat flow shown in Figure 6.1b. Figure 6.3 shows the charge and discharge parasitic heat flows of the cells above during the initial cycle to 4.4 V (prior to the cycle shown in Figure 6.1). The parasitic heat flow obtained using the charge-discharge method would be the average of the solid and dashed lines for each cell.

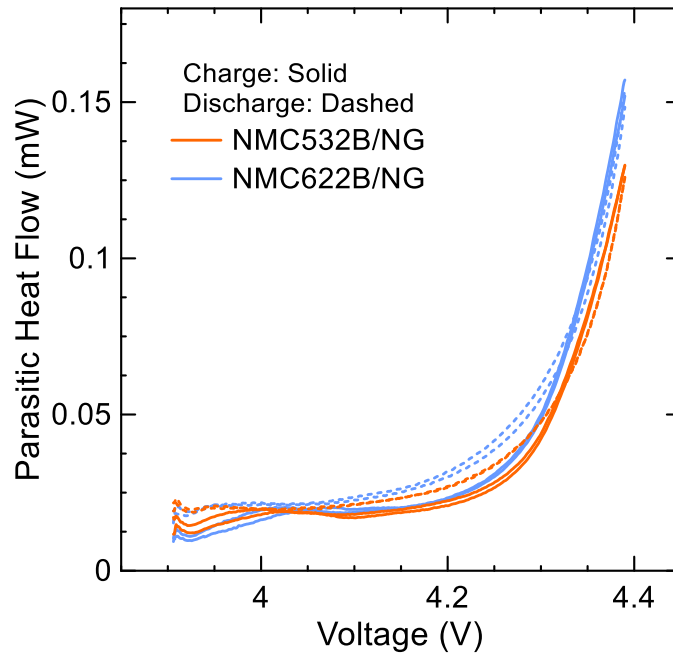


Figure 6.3: Charge (solid lines) and discharge (dashed lines) parasitic heat flow during a cycle between 3.9 V and 4.4 V at 1 mA and 40°C prior to the cycle in which the entropic heat flow was calculated. A pair of NMC532B/NG (orange) and NMC622B/NG (blue) are shown.

The parasitic heat flow during charge in Figure 6.3 was lower than the parasitic heat flow during discharge on average for each cell. The parasitic heat flow during charge increased sharply above 4.3 V for each cell and decreased smoothly during discharge as might intuitively be expected (the cycle shown was the first time the cell was exposed to a cell voltage over 4.3 V). Slight differences can be noted between cells, such as the faster increase in parasitic heat flow at a slightly lower voltage in NMC622B/NG cells compared to NMC532B/NG cells. The voltage region from 3.9 V to 4.0 V in Figure 6.3 was not consistent between cells, likely an artifact of the stage-2 features in entropic heat flow. Otherwise, pair cells showed good consistency.

The method developed in this section will be referred to as the ‘entropic method’ of calculating parasitic heat flow. The following section will describe a study which

utilized the charge-discharge method from Chapter 5 and the entropic method from this section.

6.2 STUDY: THE EFFECT OF DIFFERENT NMC COMPOSITIONS AND POSITIVE ELECTRODE COATINGS ON THE PARASITIC HEAT FLOW OF LITHIUM-ION POUCH CELLS

The work in this section is adapted with permission from *J. Electrochem. Soc.* **164**, A1203-A1212, (2017), Copyright the Journal of the Electrochemical Society, 2017.²⁰⁸ Jenn Allen, a summer student co-supervised by the author conducted *in-situ* gas measurements and made the cells used in this study. Dr. Kathlyne Nelson provided the UHPC and long-term cycling data. The author performed calorimetry experiments, EIS, *ex-situ* gas measurements, data processing, and manuscript preparation.

6.2.1 Motivation

Previous studies in this thesis have discussed the effects of electrolyte additives, solvents, and negative electrode materials on the parasitic heat flow of lithium-ion cells. This study investigates the impact of positive electrode composition and surface coating on parasitic heat flow.

As discussed in Section 1.3, different ratios of transition metals in NMC positive electrodes as well as surface coatings such as Al_2O_3 can impact the reactivity of the electrode surface with electrolyte at high electrode potentials.^{22,34,112} The presence of different interface chemistries may not only affect the degree of parasitic reactions which occur. The type of parasitic reactions occurring when surface coatings are present may differ from those which occur in an uncoated cell, or a cell with a different coating.

Similarly reactions which occur in NMC622 may be slightly different from those which occur in NMC532. Therefore, this study aimed to compare the relative performance of cells with different positive electrode materials using various established electrochemical methods with the results from parasitic heat flow measurements.

6.2.2 Experimental

Cells used in this study were NMC442/AG, NMC532A/NG, NMC532B/NG, NMC622A/NG, and NMC622B/NG. Coating A is Al₂O₃, and coating B is a proprietary high-voltage coating. Cells will be referred to by the positive electrode material and coating *i.e.*, 442, 532 A, 532 B, 622 A, and 622 B, respectively. Table 3 lists the nominal capacity of each cell charged to 4.2 V.

The electrolyte used in this work was 1.0 LiPF₆ in EC:EMC (3:7 wt.) with 2% wt. PES, 1% wt. DTD, and 1% wt. TTSPi as additives (PES211 additive blend). Cells were filled with 0.9 g (442 cells) and 0.84 g (all other cells) of electrolyte.

Cells for calorimetry studies were formed to 4.2 V using formation protocol A. Cells were then inserted in the calorimeter and cycled four times at a C/20 rate from 2.8 V to 4.2 V to ensure a well formed SEI before measurements of parasitic heat flow. Cells were then cycled at 1 mA (C/160 to C/260) from 3.9 V to a series of UCVs: 4.2 V, 4.3 V (twice), 4.4 V (twice) and then again at 4.2 V (twice). The parasitic heat flow of cells used in this work were scaled to the relative capacity of the 442 cells since cells did not have the same capacity (and thus electrode material responsible for parasitic reactions). Gas volume and EIS spectra were taken after formation and after calorimetry experiments.

Cells for *in-situ* gas measurements were formed to 4.2 V and then connected to the *in-situ* gas apparatus. Cells were cycled once from 3.0 V to 4.2 V then charged to 4.4 V

and held at a constant voltage for 100 hours at 4.4 V. Cells were then charge to 4.5 V and held at 4.5 V for 100 hours.

UHPC measurements were performed between 3.0 V and 4.1 V, 4.2 V, or 4.3 V at a C/20 rate at 40°C.

Long-term cycling measurements were performed using a C/3 CCCV protocol from 3.0 V to 4.1 V, 4.2 V, or 4.3 V at 40°C. Every 50 cycles a C/20 cycle was performed.

6.2.3 Results and Discussion

The parasitic heat flow from the charge-discharge method of each cell type during the two cycles to 4.3 V and 4.4 V are shown in Figure 6.4. The colour code used throughout this section is: 442 cells (black), 532 A cells (red), 532 B cells (orange), 622 A cells (blue), and 622B cells (light blue). Only one cell of each pair is shown for simplicity but all cells exhibited similar reproducibility to that shown in Figure 5.4.

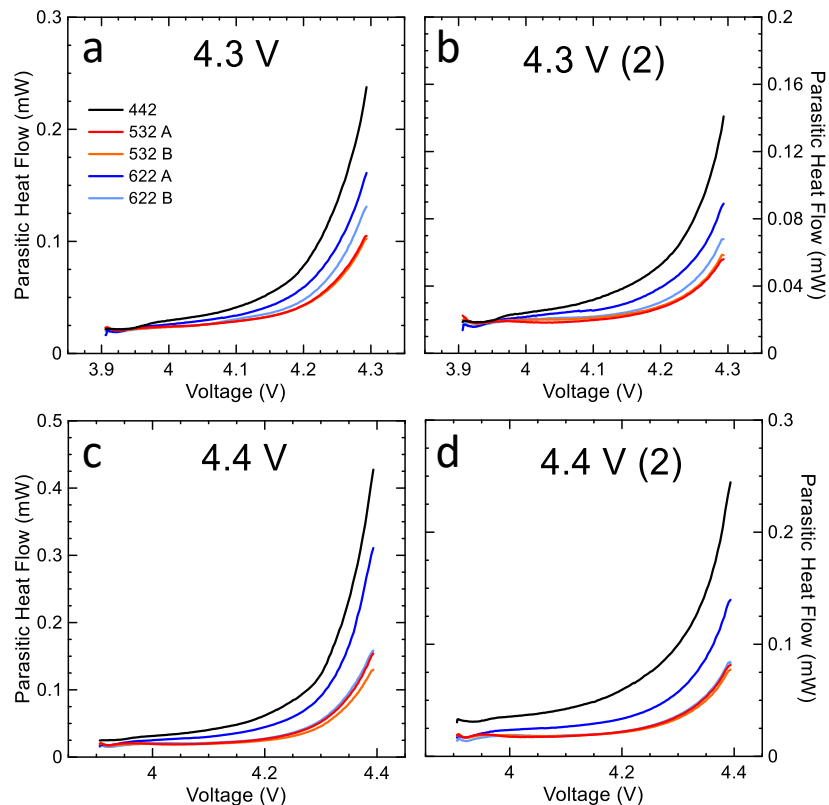


Figure 6.4: Parasitic heat flow of different cell types: 442 (black), 532 A (red), 532 B (orange), 622 A (blue), and 622 B (light blue) calculated using the charge-discharge method. Cycles were from 3.9 V to a) 4.3 V, b) second cycle to 4.3 V, c) 4.4 V, and d) second cycle to 4.4 V at 1 mA and 40°C.

Figure 6.4 shows that 442 cells (which did not have a coating) had similar parasitic heat flow to other cells around 4.0 V, but very high parasitic heat flow as voltage increased. During the low voltage portion of the last cycle to 4.4 V (Figure 6.4d) the parasitic heat flow of 442 cells had increased compared to the start of the first 4.3 V cycle in Figure 6.4a. All other cells had slightly decreasing parasitic heat flow at the bottom of charge during the cycles shown in Figure 6.4. The 622 A cells had the highest parasitic heat flow compared to other coated cells. The 532 B cells exhibited the lowest parasitic heat flow of all cell types tested. A sharper increase in the parasitic heat flow in some cells can be seen during the first cycles to 4.3 V and 4.4 V when the cells were exposed to new voltages for

the first time. This increase may have been due to a large onset of parasitic reactions during the charge portion. Due to the averaging of heat flows between charge and discharge, any major differences in parasitic heat flows were averaged out. Therefore, the large onset of parasitic heat flow may have been much more pronounced during each charge than observed in Figure 6.4.

Next, the entropic heat flow was calculated using the entropic method outlined in the previous section. Figure 6.5 shows the calculated entropic heat flow using each cycle in the protocol step to investigate whether or not an approximate entropic heat flow could be calculated from the data. In Figure 6.5, panels a) to f) represent each cycle in the protocol with the UCV labelled in the top of each panel. The second cycle to each UCV is denoted with '(2)' and the first cycle to 4.2 V after high voltage cycles is denoted '(post)'. Only one cell of each pair is shown for simplicity.

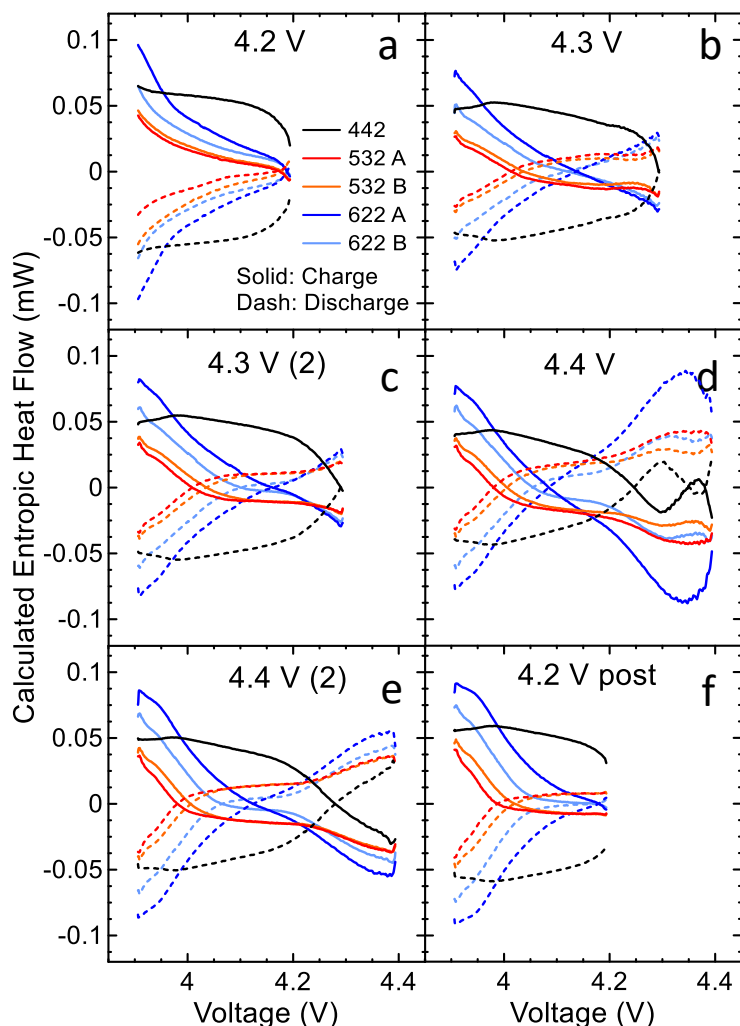


Figure 6.5: Extracted theoretical entropic heat flow during each protocol step using the entropic method.

Cycles in which cells are charged to a voltage range for the first time (a, b, and d in Figure 6.5) showed inconsistent behavior compared to cycles which contain no new voltage exposure (c, e, and f in Figure 6.5). The calculated entropic heat flows during both cycles to 4.3 V were very similar except for small features around 4.2 V which appeared during the first cycle to 4.3 V in Figure 6.5b. These similarities suggest that the parasitic heat flows during charge and discharge were likely similar during the first cycle to 4.3 V and no dramatic onset of parasitic heat flow or SEI formation occurred. In contrast, the entropic

heat flow calculated using the first cycle to 4.4 V (d in Figure 6.5) was dramatically different compared to the second cycle to 4.4 V. A large, noisy feature occurred for each cell in Figure 6.5d just above 4.3 V, when a large amount of parasitic heat flow was observed from each cell in Figure 6.4. A large onset of parasitic heat flow likely occurred during the first charge to 4.4 V, creating differences in the charge and discharge parasitic heat flows. Since the parasitic heat flow was not the same between charge and discharge, the entropic method calculation introduced the features. Calculated entropic heat flow shown in Figure 6.5 was smooth and relatively consistent between cycles in which cells were not exposed to any new voltage ranges (c, e, and f). Therefore, it was assumed that the entropic heat flow of the cells could be modelled using the entropic heat flow from the second cycle to 4.4 V in Figure 6.5e.

The charge and discharge parasitic heat flows for some cycles were calculated from Equations 6.6 and 6.7 and are shown in Figure 6.6. The first cycles to 4.2 V (black), 4.3 V (blue) and 4.4 V (red) are shown for each cell type. The parasitic heat flows during charge and discharge during the second cycle to 4.4 V were equal by definition, and during the second cycle to 4.3 V were almost identical, as indicated by the similar entropic heat flows in Figure 6.5c and Figure 6.5e. Parasitic heat flow during charge is shown as solid lines, and during discharge as dashed lines. Parasitic heat flow calculated using the charge-discharge method is shown as a light coloured line and was the average between charge and discharge parasitic heat flows. The scale is the same for all coated cells, and much higher for 442 cells (Figure 6.6a).

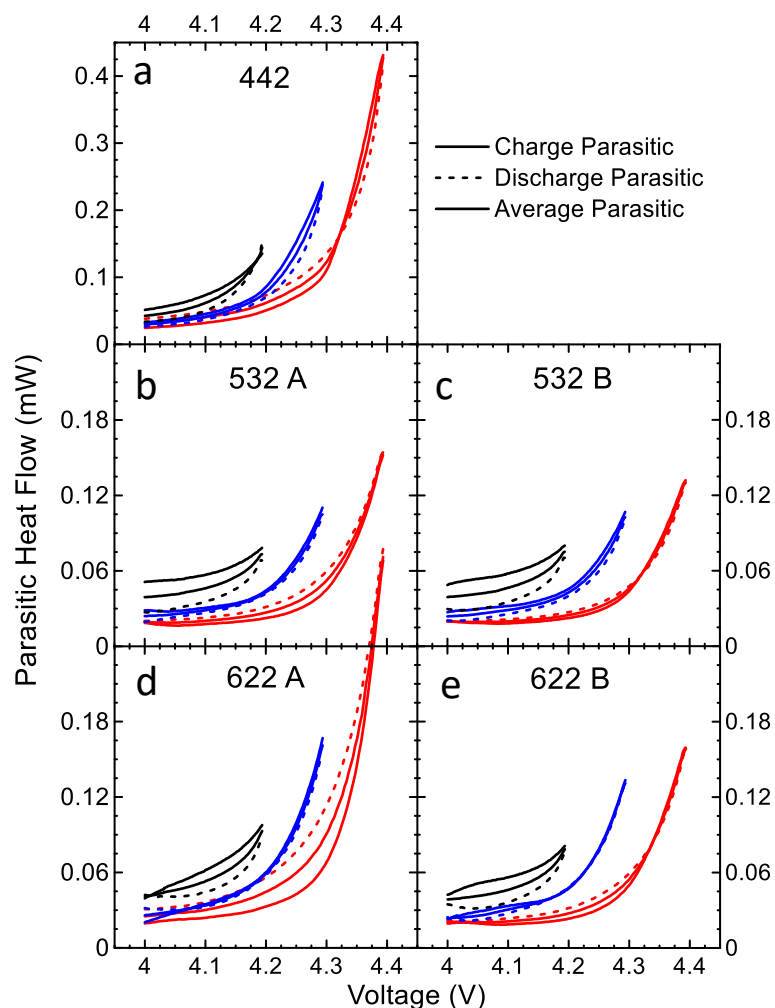


Figure 6.6: The calculated charge (solid lines) and discharge (dashed lines) parasitic heat flows of each cell type during the first cycle to each voltage range *i.e.*, cycle one to 4.2 V (black), cycle three to 4.3 V (blue), and cycle five to 4.4 V (red) at 40°C. The parasitic heat flow calculated using the charge-discharge method is shown as a light line for each cycle. Cell types are shown separately in each panel: a) 442, b) 532 A, c) 532 B, d) 622 A, and e) 622 B.

Figure 6.6 shows that there were not very significant differences between charge and discharge parasitic heat flows in cycles to 4.3 V. Significant differences were observed in cycles to 4.2 V. These differences may have been due to the cells being cycled at a very low current for the first time at 4.2 V and forming SEI products. The differences may have also occurred partially as an artifact of the change in charging rate from C/20 to 1 mA. The concentration gradient of Li in the electrodes may have relaxed slightly when cells changed

from C/20 to 1 mA. However, this is purely speculation and could be investigated by beginning 1 mA cycles at a lower voltage than 3.9 V to give time for Li gradients to equilibrate before parasitic heat flow calculations.

Different positive electrode coatings seemed to affect the differences between charge and discharge during cycles to 4.4 V in Figure 6.6. Cells with coating A had higher parasitic heat flow during discharge than charge throughout the cycle. Parasitic heat flow in cells with coating B decreased more quickly during discharge. The rate of increase of parasitic heat flow was also higher for cells with coating A. The results in Figure 6.6 suggested that coating B may mitigate parasitic reactions (particularly electrolyte oxidation) more than coating A. The results from parasitic heat flow measurements suggested that cells with coating B should have a longer lifetime compared to cells with coating A. Particularly, 622 A should have much shorter lifetime than other coated cells according to the magnitude of parasitic heat flow.

Figure 6.7a shows the summary of the mean parasitic heat flow during each cycle to the labelled UCV for all cells including pair cells (622 A did not have a pair cell in calorimetry experiments due to an internal short in the second cell). Figure 6.7b shows the *in-situ* gas results for pair cells of each cell type. Figure 6.7c shows the gas produced during formation (grey) and during calorimeter experiments (red) for each cell type. Figure 6.7d shows the R_{ct} results from EIS measurements on cells after formation (grey) and after calorimeter experiments (red). The average value of R_{ct} and gas produced in pair cells is shown in Figure 6.7c and Figure 6.7d and the error bars represent the range between pair cells (except for 622 A).

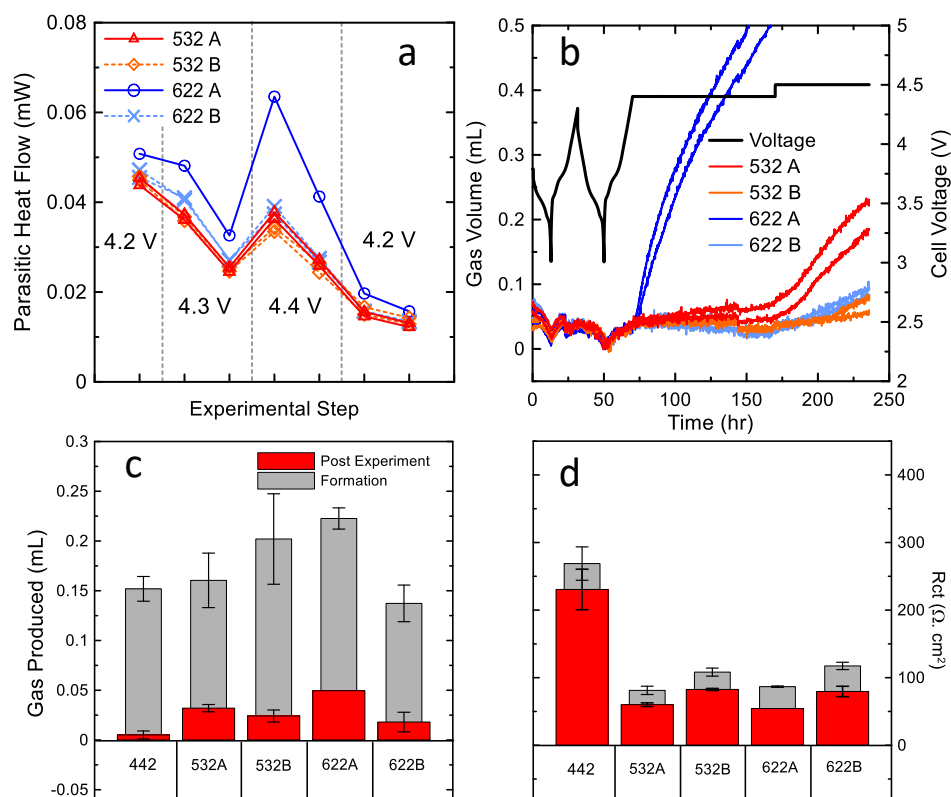


Figure 6.7: a) The mean parasitic heat flow during each cycle using the charge-discharge method for coated NMC grades between 3.9 V and the labelled UCV. b) *In-situ* gas measurements of cells during voltage-holds at 4.4 V and 4.5 V at 40°C. c) *Ex-situ* gas measurements and d) charge transfer resistance (R_{ct}) values from EIS measurements for each cell type after formation (grey) and after cells were removed for the calorimeter (red).

The *in-situ* gas results in Figure 6.7b show that cells with coating B produced no gas during 4.4 V voltage-holds and a very small amount at 4.5 V. The 532 A cells may have produced a very small amount of gas at 4.4 V and a significant amount of gas at 4.5 V (the cell volume was ~ 2 mL). The 622 A cells produced a very large amount of gas during the 4.4 V hold. The *in-situ* gas results suggested that coating B mitigated high voltage, gas-producing reactions from electrolyte oxidation or the reduction of species created during electrolyte oxidation (cross-talk). Although 622 B cells and 532 B cells had similar parasitic heat flow and gas production at high voltage, 622 A and 532 A had dramatically different performances in each test. The results from calorimetry and *in-situ*

gas measurements suggested that not only do the electrolyte, electrode material composition, and coating effect the performance of cells, but the synergy between a composition and the coating of the electrode material can have a dramatic effect on the reactions that occur. It is unknown as to why an Al₂O₃ coating on NMC622 yielded such high parasitic heat flow and gas production.

Figure 6.7c shows that during calorimetry studies, 622 A and 532 A cells produced more gas than the other cells. However, the 622 A cell did not produce a large amount of gas (< 0.05 mL). Figure 6.7d shows that the R_{ct} did not change considerably for all cells, decreasing slightly during calorimeter studies. One could have expected 622 A or 442 cells to have much higher impedance if the parasitic reactions formed solid products which thickened the SEI layer over time. The parasitic reactions in the cells used in this study likely formed gaseous products and consumed electrolyte without increasing the impedance significantly. Another possibility was that some reactions – especially in 622 A cells – acted as reversible shuttles, artificially increasing the parasitic heat flow.

Next, the cycling performance of the cells was investigated using long-term cycling and UHPC measurements. Only results for coated cells are shown, as the 442 cells were not deemed competitive with the coated cells. Figures 6.8 a, b and c show the results from UHPC studies from 3.0 V to 4.1 V, 4.2 V, and 4.3 V, respectively. The CIE is shown in the top row, fractional charge endpoint capacity slippage in the second row, and fractional discharge capacity fade in the third row.

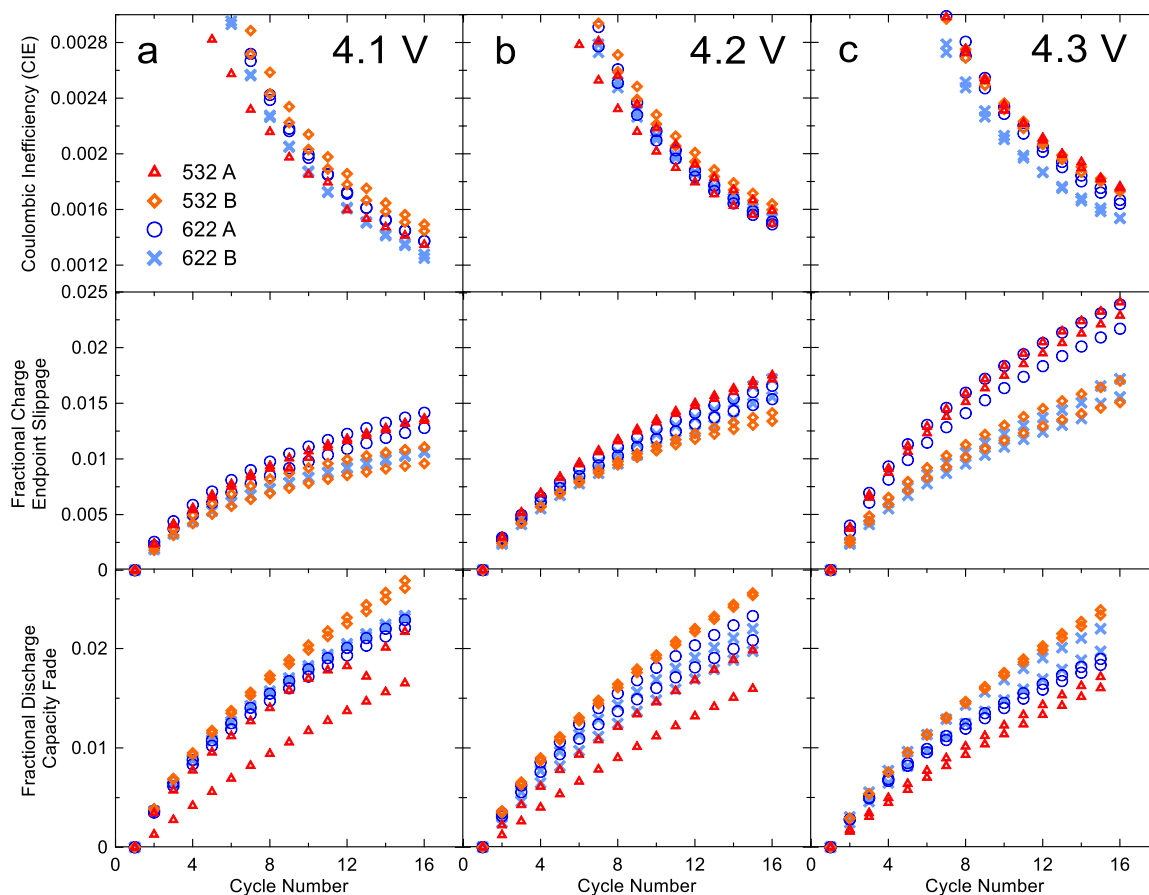


Figure 6.8: UHPC results for each cell type cycled from 3.0 V to a) 4.1 V, b) 4.2 V, and c) 4.3 V at C/20 and 40°C. The top row shows CIE, the middle row shows the fractional charge endpoint capacity slippage per cycle, and the bottom row shows the fractional discharge capacity fade per cycle.

In almost all cases in Figure 6.8 622 A and 532 A cells had the highest charge endpoint capacity slippage, indicating a larger degree of electrolyte oxidation was present in these cells. However, 622 A and 532 A cells also had the lowest fractional capacity fade, suggesting less electrolyte reduction and lithium loss was occurring in these cells. Again, these results may suggest that some reaction products in the cells in this study acted as somewhat reversible shuttles, artificially raising the slippage and parasitic heat flow but not decreasing the cell capacity. Alternatively, these cells may have just experienced a large degree of electrolyte oxidation reactions which did not produce products which

reduced at the negative electrode. Unfortunately, the magnitude of the parasitic heat flow alone cannot discern if different types of reactions are happening in different cells.

To further investigate the performance of cell types, long-term cycling was performed. Long-term results of cells cycled at 40°C at a rate of C/3 (CCCV) from 3.0 V to 4.1 V, 4.2 V, and 4.3 V are shown in Figure 6.9. Discharge capacity is shown in Figure 6.9a, fractional discharge capacity normalized to the third cycle in Figure 6.9b, and ΔV is shown in Figure 6.9c.

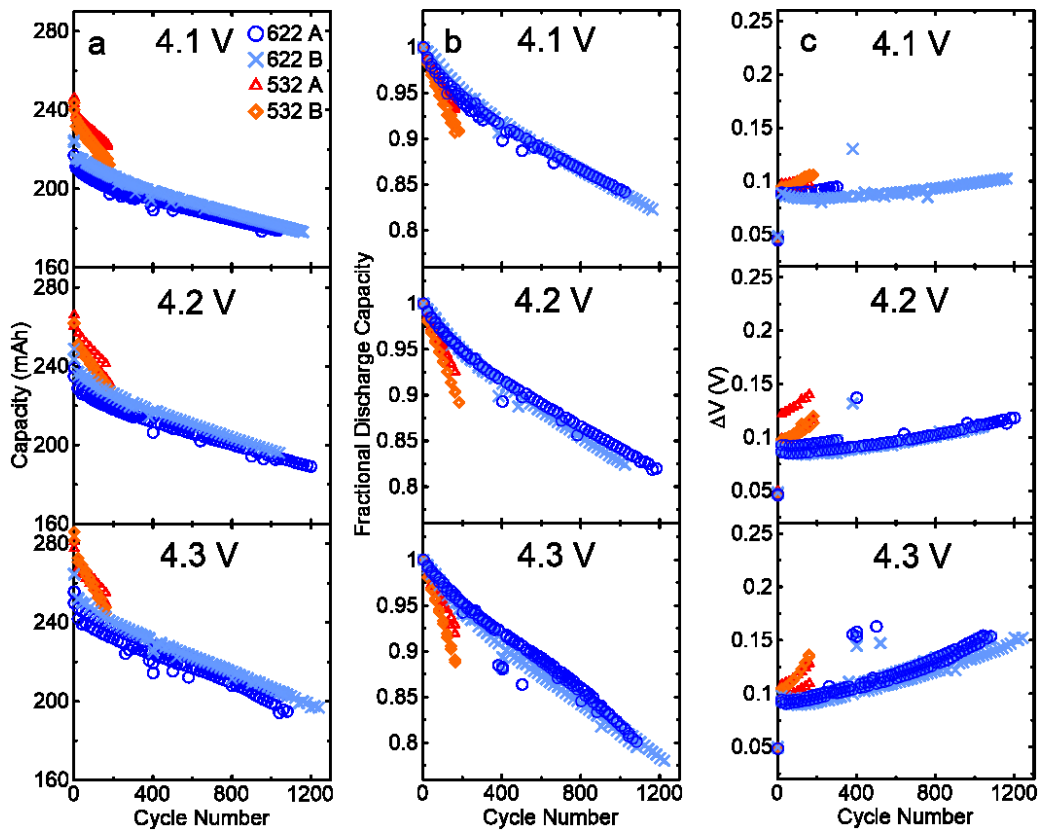


Figure 6.9: Long term cycling (C/3 CCCV at 40°C) from 3.0 V to 4.1 V, 4.2 V, and 4.3 V. Discharge capacity is shown in a), fractional discharge capacity in b), and ΔV in c).

Figure 6.9 shows that 532 A and 532 B had very poor cycling compared to 622 A and 622 B cells. The performance was deemed non-competitive at the time and the cells were removed after 200 cycles. The impedance of 532 A and 532 B increased very quickly

compared to 622 A and 622 B cells. 622 A and 622 B cells cycled very well, reaching 80% of the original capacity at about 1200 cycles at each voltage. The cycling data shown in Figure 6.9 did not agree with results for parasitic heat flow or UHPC studies, particularly in the case of 622 A. Therefore, it may be difficult to use short-term techniques such as UHPC and isothermal calorimetry when comparing different positive electrode materials and coatings between cells. The reasons for the disagreements in the data shown here are not known, but motivate new methods to differentiate between different types of parasitic reactions occurring in cells.

6.2.4 Conclusions

The parasitic heat flow of cells with identical electrolytes, different transition metal ratios of NMC and two different coatings were found using the charge-discharge method and the entropic method. The entropic method of calculating the parasitic heat flow demonstrated that coating B (proprietary high-voltage) mitigated parasitic heat flow during discharge compared to coating A (Al_2O_3). 622 A cells were found to exhibit much higher parasitic heat flow than other coated cells and produced a large amount of gas during 4.4 V operation in *in-situ* gas measurements.

UHPC testing and long-term cycling results did not agree with the parasitic heat flow. 532 A and 532 B cells showed very poor cycling but had low parasitic heat flow. 622 A and 622 B cells had equivalent cycling performance, losing 20% of the initial capacity in 1200 cycles during cycling up to 4.3 V. However, 622 A and 622 B cells had very different parasitic heat flow, gas production and UHPC results. The data suggested that the parasitic reactions occurring in cells with different coatings and compositions were different, even though the electrolyte was the same in each cell. One conclusion which

was consistent between all tests was that 622 B had the best performance in all tests: low parasitic heat flow, no gas under 4.4 V, low CIE, and long lifetime in long-term tests.

The results of this study demonstrate the need for a method to probe the reaction mechanisms in cells to determine if the parasitic processes occurring are the same. It is difficult to determine the relative long-term performance without using time-consuming methods if parasitic reaction mechanisms and products are not similar between cells. It will be the focus of Chapter 7 to introduce a method to probe the net enthalpy of reaction for parasitic reactions occurring in cells.

6.3 FURTHER TREATMENT OF OVERPOTENTIAL

The treatment of cell overpotential in Chapter 5 was slightly unrealistic due to the converging endpoints of cell voltage *vs.* SOC plots. However, the levels of overpotential heat flow were an order of magnitude smaller than the parasitic heat flow at high voltage when small (1 mA) currents were used. Since experimental protocols which take less than one month were desired, slightly higher currents were necessary.

Downie et al. found that in small voltage windows (0.1 V) the overpotential could be approximated well by an average value.¹⁷³ The study measured the overpotential as half the voltage polarization at 50% SOC in 0.1 V windows at multiple currents. The contribution from hysteresis was found as the intercept of the plot of overpotential *vs.* current, and the internal resistance of the cell was the slope (see the Equation 1.8 for overpotential). This measurement was performed in many 0.1 V ranges to find the overpotential as a function of cell voltage at the rate used in calorimetry experiments. The overpotential was found to increase as a function of voltage. Although the method was

accurate, the internal resistance of a cell can change over time as the cell degrades and/or SEI layers thicken. Additionally, the measurements took extra resources (cells, time, channels, and data processing).

The treatment of overpotential in Chapter 5 also showed increasing overpotential in the middle of the voltage ranges, but not near the endpoints. Therefore, a more accurate representation of the overpotential – particularly near the endpoints – would be a linear fit through the middle portion of the overpotential calculated using the SOC method. Figure 6.10 shows the overpotential heat flow calculated using the voltage vs. SOC as in Chapter 5 is shown in black. A linear fit to the overpotential heat flow at 33% and 67% SOC is shown in red. The cell shown was SC-NMC532/AG cycled from 4.0 V to 4.4 V at 1 mA at 40°C.

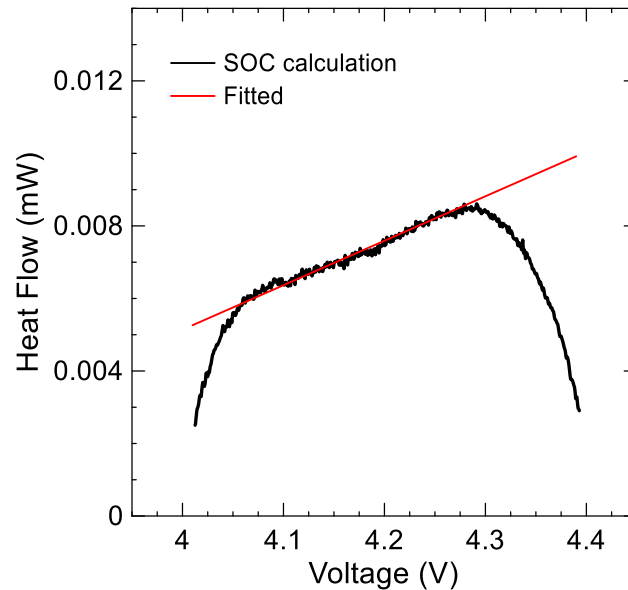


Figure 6.10: The overpotential heat flow calculated using the voltage vs. SOC (black). A linear fit to the overpotential heat flow at 33% and 67% SOC (red).

Figure 6.10 shows that the original method to obtain the overpotential heat flow underestimated the overpotential heat flow by $\sim 10 \mu\text{W}$ at the top of charge in the cells used

in this example. The underestimates at the beginning and end of the voltage window would carry through and artificially increase the calculated parasitic heat flow.

As discussed previously, the cell overpotential is the difference between the measured cell potential and the equilibrium voltage of the cell. Therefore, the heat flow is not recorded as a function of equilibrium voltage, but of the equilibrium voltage plus the overpotential (which is positive during charge and negative during discharge). Calculating the parasitic heat flow as a function of measured voltage (rather than equilibrium voltage) could theoretically introduce artifacts from ‘mismatches’ in entropic signatures. An entropic feature would be shifted to higher voltage during charge and lower voltage during discharge. Therefore, in this chapter all measurements had an ‘equilibrium correction’ back to the equilibrium voltage once the overpotential was calculated.

Figure 6.11 demonstrates the effects of the linear overpotential fitting and the overpotential equilibrium correction compared to the charge-discharge method in Chapter 5 using the same cell and cycle as Figure 6.10. The measured, uncorrected heat flow is shown in grey and the parasitic heat flow is shown in dashed blue. The corrected heat flow is shown in black, with the direction of the voltage correction indicated with an arrow. The corrected parasitic heat flow is shown in red. The fitted overpotential heat flow is shown in green.

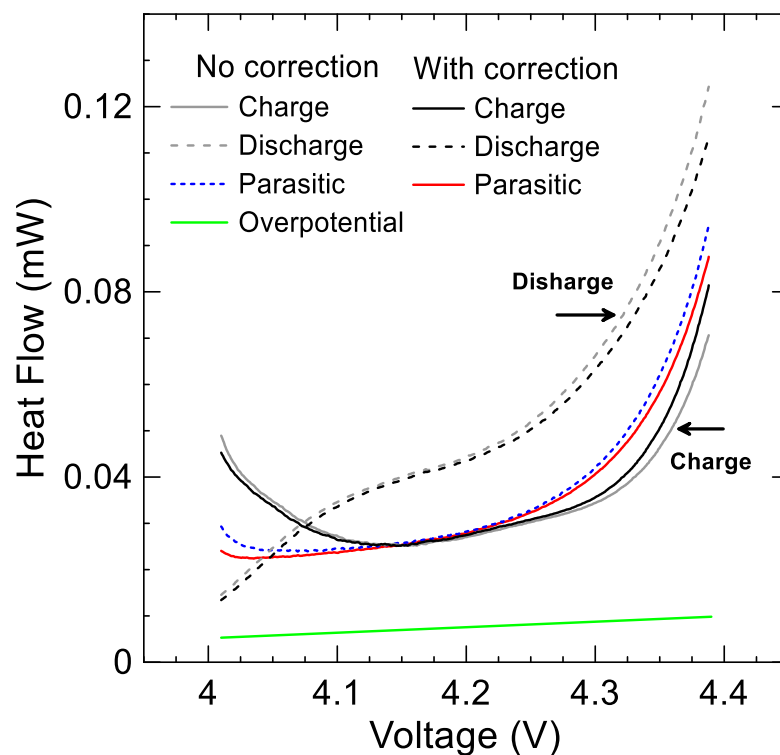


Figure 6.11: A demonstration of the fitted overpotential and equilibrium correction in an SC-NMC532/AG cell during a cycle from 4.0 V to 4.4 V at 1 mA. The uncorrected measured heat flow during charge (solid grey) and discharge (dashed grey). The parasitic heat flow calculated using the original charge-discharge method is shown in dashed blue. The corrected measured heat flow is shown in black, and the corrected parasitic heat flow is shown in red. The fitted overpotential heat flow is shown in green.

Figure 6.11 shows that the equilibrium correction and fitted overpotential changed the parasitic heat flow near the cycle endpoints. The upwards-curving 4.0 V feature in the uncorrected parasitic heat flow was not as pronounced when the fitted overpotential was used and the equilibrium correction shifted the stage-2 entropy features.

Figure 6.12 demonstrates the typical consistency between pair cells using the treatment of overpotential developed in this section. Each type of line indicates a different electrolyte. Some data in Figure 6.12 do not appear to have pair cells plotted. However, the pair cell data are almost directly overlapping.

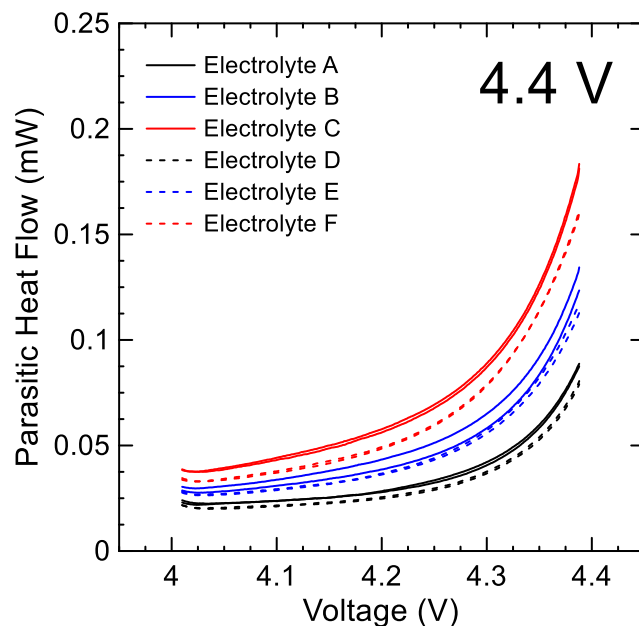


Figure 6.12: Parasitic heat flow of six pairs of cells with different electrolytes (called electrolytes A to F) calculated using the fitted overpotential and equilibrium correction demonstrate excellent consistency between pair cells.

The difference in parasitic heat flows using each method in Figure 6.11 was not very dramatic. However, the calculated parasitic heat flow using the fitted overpotential and equilibrium correction was more realistic. Additionally, the advantages to methods developed in this section are more noticeable when higher rates are used, and in cell types with entropic features in voltage ranges of interest.

Figure 6.13 shows the measured and parasitic heat flows with and without overpotential fitting and equilibrium correction for an NCA/SiO-graphite cell cycled at 3.7 mA ($\sim C/100$) from 3.9 V to 4.2 V at 40°C. NCA exhibits a small voltage plateau around 4.17 V vs. Li/Li⁺ (or ~ 4.09 V vs. graphite) which would correspond to a phase transition or structural change in the material.²⁰⁹ Li et al. recently found the feature to be due to a large lattice contraction during charge and expansion during discharge.²¹⁰ A ‘wiggle’ can be seen in the charge and discharge heat flow due to changes in entropy corresponding to the

lattice changes. A corresponding anomalous feature can be seen in the parasitic heat flow when the overpotential correction was not used (blue line in Figure 6.13). When the overpotential correction was used, the feature was much less noticeable (red line in Figure 6.13).

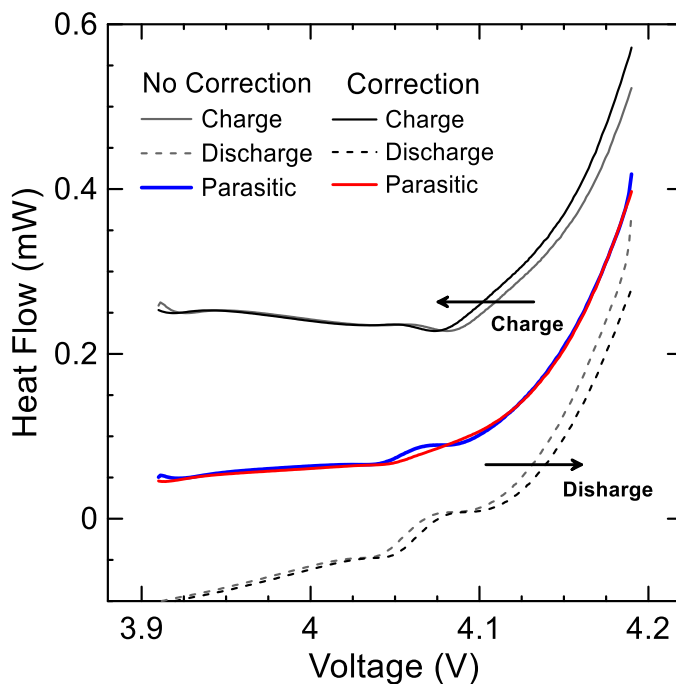


Figure 6.13: The uncorrected measured heat flow during charge (solid grey) and discharge (dashed grey) of an NCA/SiO-graphite cell cycled from 3.9 V to 4.2 V at 3.7 mA at 40°C. The parasitic heat flow calculated using the original charge-discharge method is shown in blue. The corrected measured heat flow is shown in black, and the corrected parasitic heat flow is shown in red.

This section introduced a more realistic treatment of the cell overpotential which did not rely on any external measurements, therefore accounting for increases in cell impedance during calorimetry studies. The next section will show two studies which utilize the charge-discharge method with fitted overpotential and equilibrium correction to investigate the effect of methyl acetate (MA, see Section 1.5.2) and the additives FEC and DTD on parasitic heat flow.

6.4 STUDY: THE EFFECT OF METHYL ACETATE IN NCA/SiO-GRAPHITE AND NMC/GRAPHITE POUCH CELLS

Some of the work in this section using SC-NMC532/AG cells is adapted with permission from *J. Electrochem. Soc.* **165**, A867-A875, (2018), Copyright the Journal of the Electrochemical Society, 2017.⁷⁶ Parts of this work containing NCA/SiO-graphite cells have been submitted to Tesla for approval as part of a manuscript.²¹¹ Works in this section involved many cells and was a collaborative effort: NMC cells in this section were made by Dr. Xiaowei Ma and Jenn Allen. UHPC measurements were performed by the author, Dr. Ma, and Dr. Jing Li. NCA cells used in this study were made by the author and Dr. Ma. *In-situ* gas measurements were performed by the author. Long-term cycling experiments and UHPC experiments were performed by Dr. Li, Dr. Ma, and the author. Calorimetry experiments, data processing, and manuscript preparation was performed by the author.

6.4.1 Motivation and Background

As a co-solvent, MA has been found to significantly increase the rate capabilities and low temperature performance of lithium-ion cells, but decrease the lifetime and can limit the film-forming properties of electrolytes.^{67,68,73-75} In addition, MA has a boiling point of 58 °C, meaning quantities of MA in cells need to be optimized to allow for good performance while also being safe.

Li et al. recently showed a desirable combination of MA in a solvent blend of 20:4:56:20 (EC:EMC:DMC:MA) with additives 2% wt. VC or FEC and 1% wt. DTD for high rate cycling (up to 2C –a full cell charge in 30 minutes) up to 4.3 V.⁷⁵ MA was found

to increase the conductivity and decrease the viscosity of electrolytes containing EC, EMC, and DMC. However, MA still decreased the cycle life of cells compared to when no MA was used in long-term cycling. The work in the first part of this section investigated the effect of MA on parasitic heat flow and *in-situ* gas measurements of SC-NMC532/AG pouch cells using similar electrolytes and cells as Li et al.⁷⁵ The previous section showed that different electrode materials can play a large role in the types of reactions which occur, and that electrolyte performance may vary between cell types. Therefore, the second part of this section investigated the effect of MA on parasitic reactions in NCA/SiO-graphite cells to see if the reaction mechanisms and changes in performance caused by MA applied to a completely different cell chemistry.

6.4.2 Experimental

Cells used in this section were SC-NMC532/AG and NCA/SiO-graphite.

Electrolytes used in NMC cells for UHPC studies were 1.2 M LiPF₆ in EC:EMC:DMC (25:5:70 wt.) with 0%, 20%, or 40% of the total electrolyte weight of MA. Either 2% wt. FEC alone or with 1% wt. DTD were added to each electrolyte as additives. In calorimetry studies EC:EMC (3:7 wt.) was used as the base solvent with the same ratios of MA and additives. It was found that the use of EMC *vs.* DMC did not significantly impact the parasitic heat flow or performance of cells so comparisons between solvents could be made.⁷⁶ Short-hand names for electrolytes in the text correspond to the amount of MA in cells and the additive(s). For example, 0MA FEC contains no MA in the base solvent and 2% FEC, while 20 MA 2FEC + 1DTD contains 20% MA in the base solvent, 2% FEC, and 1% DTD. 0.84 mL of electrolyte was used in each cell.

Electrolytes used in NCA cells were 1.2 M LiPF₆ in EC:EMC:DMC (25:5:70 wt.) with 0%, 20%, or 40% of the total electrolyte weight of MA. 2% wt. VC was used as an additive. Some cells substituted some EC and EMC for DMC to maintain a 25% weight ratio of EC and 5% ratio of EMC when MA was added to the electrolyte. Short-hand names for NCA cells in graphs correspond to the ratio of EC:EMC:DMC:MA, where the MA content is bolded. For example, 20:4:56:**20** corresponds to 20% MA in the base solvent. 25:5:30:**40** corresponds to 40% MA in a modified base solvent to maintain 25% EC and 5% EMC. In the text the amount of MA will be used to describe cells, *i.e.*, 40 MA corresponds to 40% wt. MA in the base electrolyte, 40 MA with 25 EC corresponds to 40% wt. MA in the modified base solvent. 1.0 mL of electrolyte was used in each cell.

Cells for calorimetry experiments on NMC cells were formed to 4.2 V using protocol A and cycled four times at C/20 from 3.0 V and 4.2 V at 40°C to ensure a well-formed SEI. In the calorimeter, cells were cycled at 1 mA (~C/200) from 4.0 V to 4.2 V, 4.3 V (twice), 4.4 V (twice), and again to 4.2 V. NCA cells for calorimetry experiments were formed to 4.2 V using protocol B and cycled four times at C/20 from 3.0 V and 4.0 V at 40°C to ensure a well-formed SEI. In the calorimeter, cells were cycled at 3.7 mA (~C/100) from 3.9 V to 4.0 V, 4.1 V (twice), 4.2 V (twice), and again to 4.0 V.

Cells used for UHPC measurements were formed to 4.3 V using protocol A (NMC cells) and 4.2 V using protocol B (NCA cells). UHPC measurements were performed by cycling cells at a C/20 rate at 40°C from 3.0 V to 4.3 V (NMC cells) and 3.0 V to 4.2 V (NCA cells) for 16 cycles.

In-situ gas measurements were made at 40°C. Cells were formed to 4.2 V. NMC cells were cycled twice from 3.0 V to 4.1 V, then held at 4.2 V, 4.3 V, and 4.4 V for 100

hours at each voltage. NCA cells were cycled twice from 3.0 V to 4.0 V and then held at 4.0 V, 4.1 V, and 4.2 V for 100 hours each.

Long-term cycling measurements were performed on NCA cells using C/3 or 1C (full charge in one hour) rates with a CCCV protocol at 40°C. During 1C cycling, every 50 cycles a ‘rate-map’ occurred in which cells performed a cycle at C/20, then three cycles with a C/2 charge and discharge rates of C/2, 1C, 2C, and 3C. Every 50 cycles during C/3 cycling a C/20 cycle was performed to test low-rate capacity retention.

6.4.3 Results and Discussion

MA in SC-NMC532/AG Cells:

Figure 6.14 shows the summarized details of 16 UHPC cycles performed at 40°C at a rate of C/20 from 3.0 V to 4.3 V plotted vs. MA content. Fractional charge endpoint capacity slippage per hour and fractional fade per hour are shown as the value at the end of the 16th cycle, and coulombic inefficiency (CIE = 1 – CE) per hour is shown as the linearly interpolated value at the 16th cycle using results of the previous five cycles, plotted as a function of upper cut-off voltage. Each of the UHPC metrics represent the value per cycle divided by the total time of the discharge (~20 hours). Figures 6.14a, b, and c show the coulombic inefficiency per hour, fractional charge endpoint capacity slippage per hour, and fractional fade per hour, respectively, for cells with 2FEC only (black) and 2FEC + 1DTD (red). The addition of DTD had almost no impact on charge endpoint capacity slippage in cells without MA. However, the impact of DTD on charge endpoint capacity slippage increased as the amount of MA increased, suggesting the positive electrode SEI formed by the addition of DTD significantly mitigated electrolyte oxidation compared to 2FEC cells. DTD and other sulfur-containing additives are well-known to form

passivating, stable SEI layers,^{103,104,106,108,212} and may therefore be particularly useful for MA containing electrolytes. Figure 6.14c shows that the addition of DTD lowered the capacity fade of cells regardless of MA content, which also suggested an improved negative electrode SEI. Figure 6.14c also shows that MA did not significantly affect capacity fade. The data shown in Figure 6.14 suggested that the largest contribution to the decreased performance of MA came from electrolyte oxidation at the positive electrode. One would suspect that due to the larger impact of DTD on CIE observed when cells contain MA, that the addition of DTD created SEI layers capable of mitigating the oxidation and reduction of electrolyte species, or subsequent cross-talk, decreasing the rate of parasitic reactions present in the cells compared to that of FEC alone.

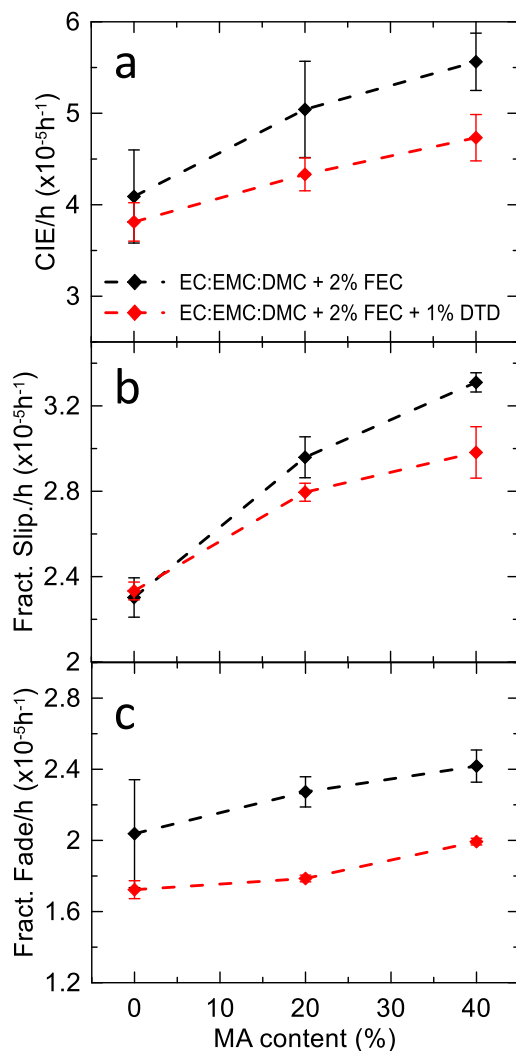


Figure 6.14: Summarized UHPC results plotted vs. MA content a) Fractional charge endpoint slippage per hour, b) fractional discharge capacity fade per hour, and c) CIE per hour cycling between 3.0 V and 4.3 V at C/20 and 40°C. Points represent the value at the 16th cycle (slippage and fade) and the projected 16th cycle value based on a linear fit of the last 5 cycles (CIE), plotted as a function of upper cut-off voltage.

Figures 6.15a, b, c, and d show the parasitic heat flow of cells during two cycles to 4.3 V and two cycles to 4.4 V, respectively. The 0 MA cells are shown in black, 20 MA cells in blue, and 40 MA cells in red. The small feature during the first cycle to 4.4 V was due to a power interruption. The 2FEC + 1DTD cells (dashed lines) had less parasitic heat flow than FEC cells (solid lines) in all cases. At 4.3 V the addition of DTD to 2FEC 20 MA cells almost compensated for the increased parasitic heat flow when MA was added

compared to 2FEC + 0 MA cells. The increase in parasitic heat flow with the addition of MA correlated well with the increase in charge endpoint capacity slippage from UHPC results. Additionally, cells with DTD also showed less parasitic heat flow and less charge endpoint capacity slippage. At 4.4 V the effect of DTD on mitigating parasitic heat flow was less pronounced, suggesting that DTD was only useful to significantly prevent oxidation reactions from MA up to 4.3 V. Higher parasitic heat flow throughout the voltage windows in cells with MA suggested that MA not only introduced oxidation reactions at a higher rate, but at much lower potentials compared to cells with the base solvent.

Measuring the rate of reactions as a function of voltage during cell operation is very useful. However, as discussed in Section 2.2, if the type of reactions which occur in a cell change with electrolyte content, cell materials, or voltage, the magnitude of the parasitic heat flow may not always correlate with the rate of parasitic reactions. Therefore, it is important to consider whether MA may change the types of reactions which occur in cells.

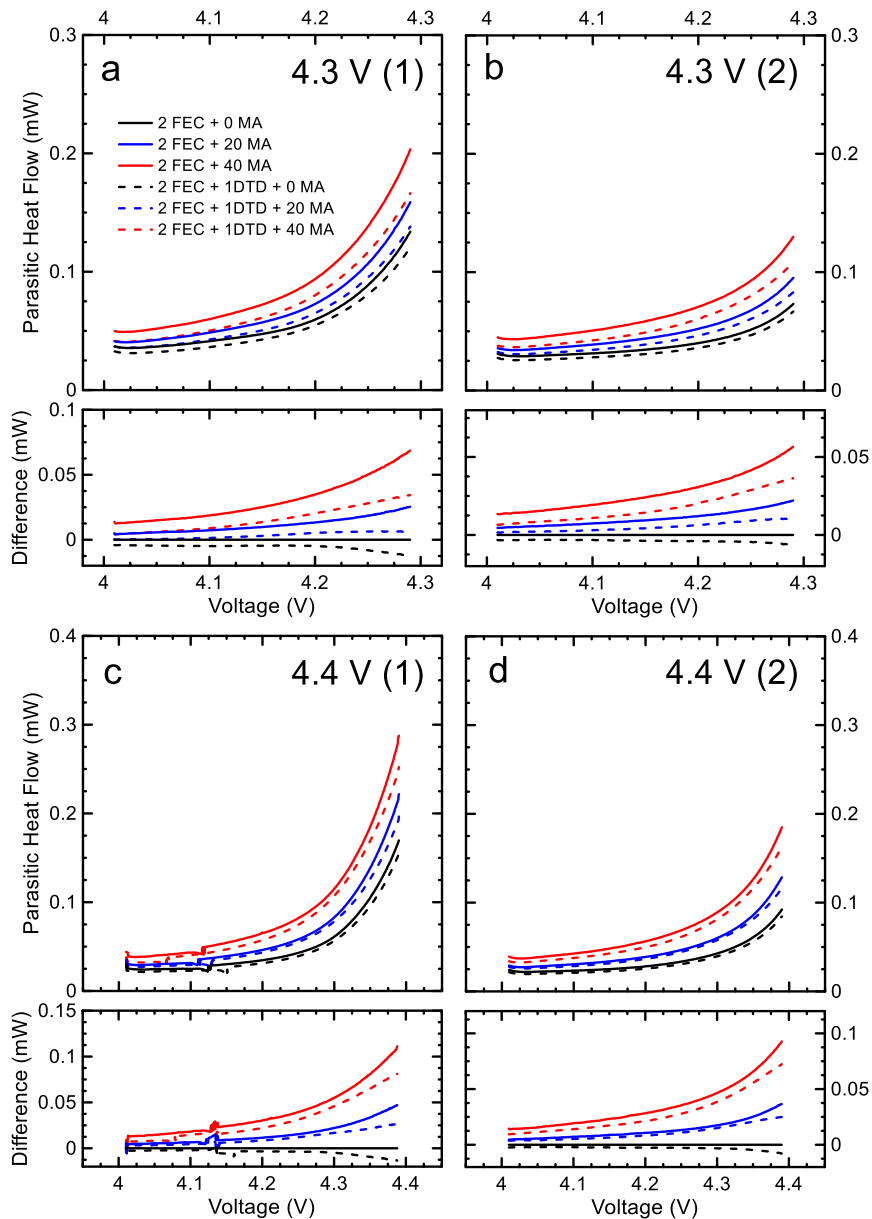


Figure 6.15: Parasitic heat flow calculated using the charge discharge method with the equilibrium correction and fitted overpotential at 1 mA and 40°C for cells with 0, 20 and 40 MA (black, blue, and red, respectively) with 2FEC alone (solid lines) and 2FEC + 1DTD (dashed lines). a) and b) show two cycles to 4.3 V. c) and d) show two cycles to 4.4 V. The bottom panel in each plot shows the difference in parasitic heat flow from a 2FEC 0 MA cell.

Figure 6.16 shows the mean parasitic heat flow per cycle to the indicated UCV for all cells used in this study. The points indicate the average value between pair cells and the error bars represent the range between pair cell values. All cells experienced similar

decreases in parasitic heat flow between the first cycle to each UCV and the second cycle to the same UCV. The similar decreases suggested that all cells were forming more protective SEI layers due to parasitic reaction products. Figure 6.16 shows that at all voltages MA caused more parasitic heat flow, and DTD mitigated parasitic heat flow.

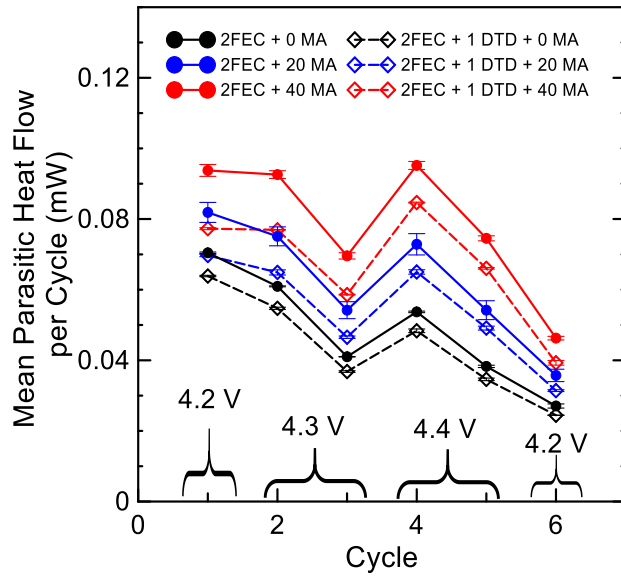


Figure 6.16: The mean parasitic heat flow per cycle to the labelled UCV. The average value between pair cells is plotted and the error bars represent the range between pair cells.

Figure 6.17 shows the results from *in-situ* gas measurements. Figure 6.17a shows the cell voltage vs. time and Figure 6.17b shows the gas volumes of pairs of cells. Cells with 0 MA hardly produced any gas, even at 4.4 V. Cells with 2FEC 20 MA and 2FEC 40 MA produced gas at all voltages, and 40 MA cells produced more gas than 20 MA cells. At 4.2 V, DTD prevented gas production with 20 MA and at 4.3 V reduced gas production in 40 MA cells significantly. At 4.4 V, cells with and without DTD produced similar amounts of gas by the end of the voltage-hold. All the trends seen in *in-situ* gas measurements agreed with the trends in parasitic heat flow at each voltage range if gas production is assumed to be correlated to parasitic heat flow. Additionally, an increase in gas at high voltage may be correlated with increased charge endpoint capacity slippage

indicating electrolyte oxidation. Therefore, the increased parasitic heat flow in cells with MA was likely due to gas-producing reactions which originated at the positive electrode.

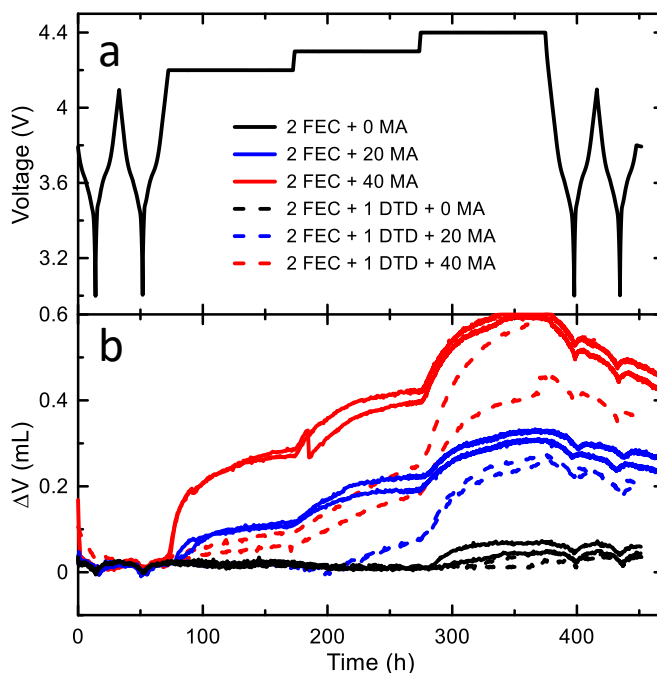


Figure 6.17: a) Cell voltage vs. time and b) Gas volume vs. time during *in-situ* gas measurements with voltage-holds to 4.2 V, 4.3 V, and 4.4 V for 100 hours each at 40°C. Cells were cycled to 4.1 V at C/20 before and after the protocol.

The results from UHPC, parasitic heat flow, and gas measurements showed that MA introduced parasitic reactions which produced gas. These reactions were most likely dominated by electrolyte oxidation, as indicated by higher charge endpoint capacity slippage, increased parasitic heat flow, and no significant increase in capacity fade compared to cells without MA. Although the results for parasitic heat flow agreed with other metrics, it was apparent that MA may have introduced different types of reactions compared to cells with no MA due to differences in gas generation. If the new reactions did not have the same reaction enthalpy as in cells with no MA, the magnitude of the parasitic heat flow must be considered carefully. A more endothermic reaction would lower the parasitic heat flow compared to other cells with the same rate of reaction, and a

more exothermic process would increase the parasitic heat flow. Additionally, a different reaction process could be either more harmful to the cell, or less harmful, *i.e.*, in the case of reversible shuttles, there is more parasitic heat flow without causing any unwanted products. Clearly, the latter is not the case here, as MA produced gaseous products and Li et al. found MA to have a negative impact during long-term cycling.⁷⁵ Nevertheless, a method to determine if parasitic reaction processes are the same between cells is further motivated by the results in this section, as it was in section 6.2 when different coatings and NMC compositions changed reaction processes.

MA in NCA/SiO-graphite Cells:

As mentioned previously, Li et al. found that MA increased the high-rate performance of SC-NMC532/AG cells. If MA could increase the high-rate performance of cells with an SiO-graphite negative electrode and an NCA positive electrode, one could achieve fast charging, high energy density cells. However, neither the effect of MA on high rates or lifetime for these materials have yet been reported in the literature.

Figure 6.18 shows the long-term cycling of 0 MA (black), 20 MA (blue), and 40 MA cells (red) from 3.0 V to 4.2 V at a rate of 1C (360 mA). Cells cycled at 20°C are shown in the left panels and cells cycled at 40°C are shown on the right. Figure 6.18a and b, c and d, and e and f show the discharge capacity, normalized discharge capacity to the third cycle, and ΔV , respectively. Cells with 0, 20, and 40 MA are shown in black, blue, and red, respectively. MA had a large impact on high-rate cycling at 20°C and no significant benefit at 40°C. All cells had significant capacity fade during 1C cycling. Continual rapid expansion and contraction of SiO in the negative electrode causing particle cracking, SEI growth, and mass loss were likely responsible for the quick capacity loss

(350 cycles was only ~1 month of cycling). Cycling at 1C quickly probed the rate-capabilities of the electrolytes but may not be useful to show the effects of parasitic reactions due to MA at high voltage in these cells due to the dominating effects of high-rate.

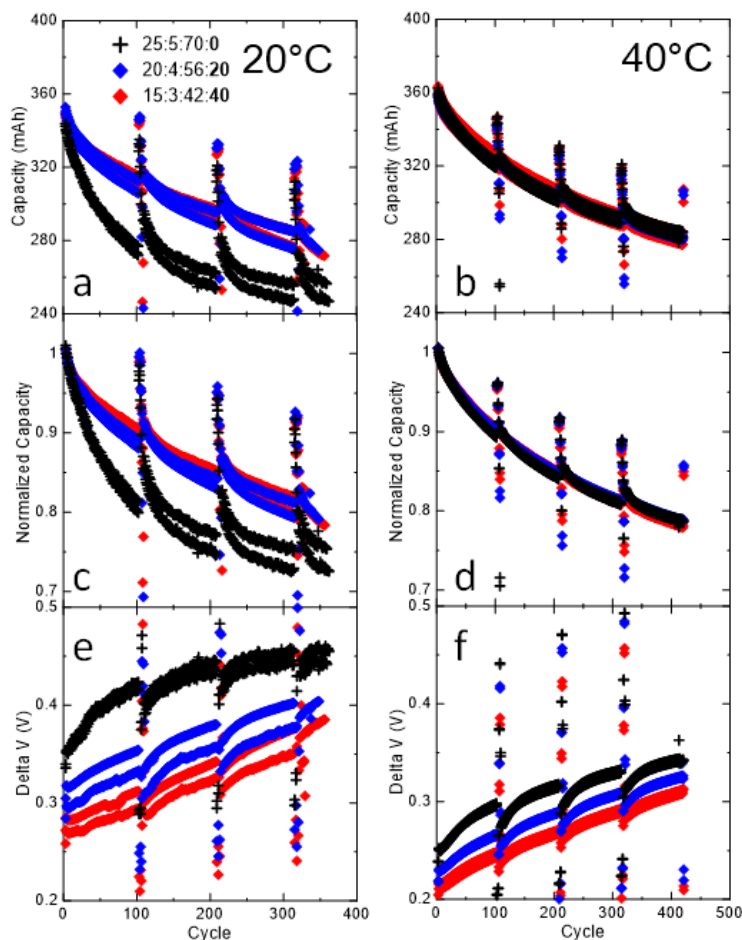


Figure 6.18: High rate (1C) CCCV cycling of cells from 3.0 V to 4.2 V at 20°C (left) and 40°C (right). a,b) capacity, c,d) normalized capacity, and e,f) ΔV . Cells containing 0 MA are shown in black, 20 MA in blue, and 40 MA in red. The ratios in the legend correspond to the weight ratio of EC:EMC:DMC:MA.

Although MA did not significantly affect the rate capabilities of 1C cycling at 40°C, Figure 6.19 shows MA significantly increased the rate capabilities at both temperatures at 2C and 3C cycles during the first rate-map after 100 cycles. Figure 6.18 and Figure 6.19 show that 40 MA cells did not have considerably higher rate performance compared to 20

MA cells. If MA also caused parasitic reactions in these cells compared to cells with 0 MA, 20 MA may offer a significant improvement in rate capability without influencing lifetime considerably.

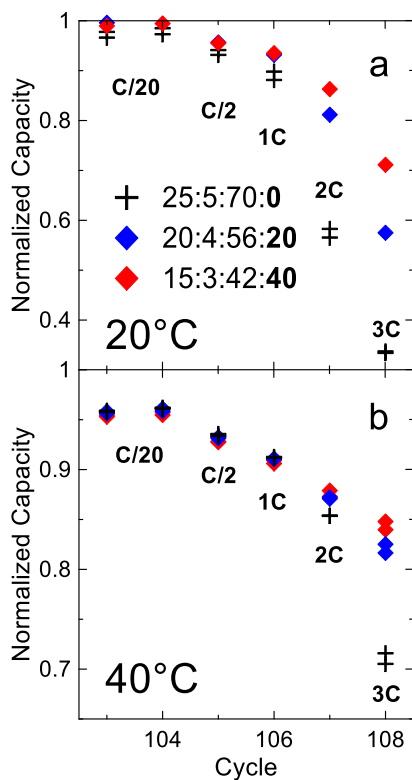


Figure 6.19: Normalized capacity during the first rate map after 100 1C cycles at a) 20°C and b) 40°C (from Figure 6.18). The ratios in the legend correspond to the weight ratio of EC:EMC:DMC:MA.

To investigate the effect of MA on lifetime, UHPC cycling was performed from 3.0 V to 4.2 V at 40°C for 16 cycles at C/20. Figures 6.20a, b and c show the results for CE, charge endpoint capacity slippage, and fractional discharge capacity, respectively. Pair cell data are shown for 0 MA cells (black) and 20 MA (blue). Figure 6.20 shows that 20 MA cells had lower CE, only due to the much higher charge endpoint capacity slippage compared to 0 MA cells. The capacity fade was the same for both electrolytes, suggesting that MA caused electrolyte oxidation at the positive electrode, but may not have caused an

increased amount of electrolyte reduction at the negative electrode. Similar results were shown for NMC cells earlier in this section.

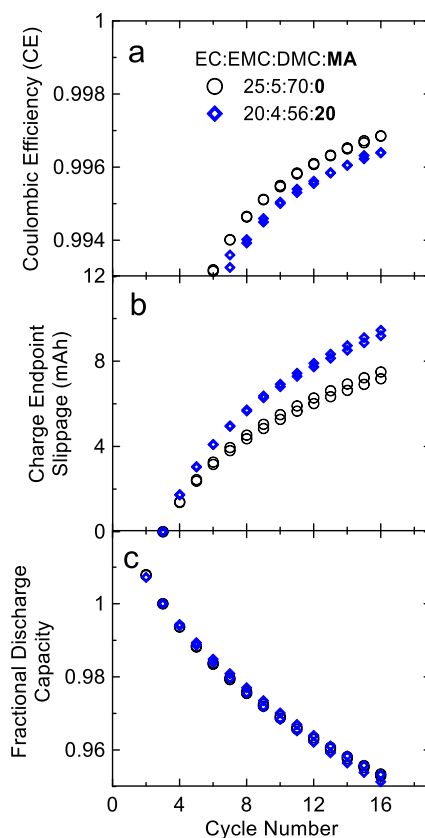


Figure 6.20: Ultra high precision results for a) coulombic efficiency, b) charge endpoint capacity slippage, and c) fractional discharge capacity of cells with 0 MA (black) and 20 MA (blue) cycled at C/20 from 3.0 V to 4.2 V at 40°C.

Figures 6.21a and b show cell voltage and gas volumes *vs.* time, respectively, during *in-situ* gas measurements. The 20 MA cells are shown in dashed blue and 0 MA cells are shown in solid black. The 20 MA cells created a significant amount of gas and began to produce gas at lower voltages compared to 0 MA cells, consistent with results using NMC cells. Figures 6.21c and d show the results from 60°C storage experiments at 4.2 V and 2.5 V, respectively. The 20 MA cells had faster voltage fade at 4.2 V, consistent with a larger degree of electrolyte oxidation compared to 0 MA cells. At 2.5 V, cells with

0 MA and 20 MA had similar rates of voltage drop, indicative of similar rates of reduction reactions. The results from storage experiments were in agreement with UHPC and gas measurements, suggesting MA did not contribute significantly to the amount of electrolyte reduction but increased the amount of electrolyte oxidation, particularly at increased voltage.

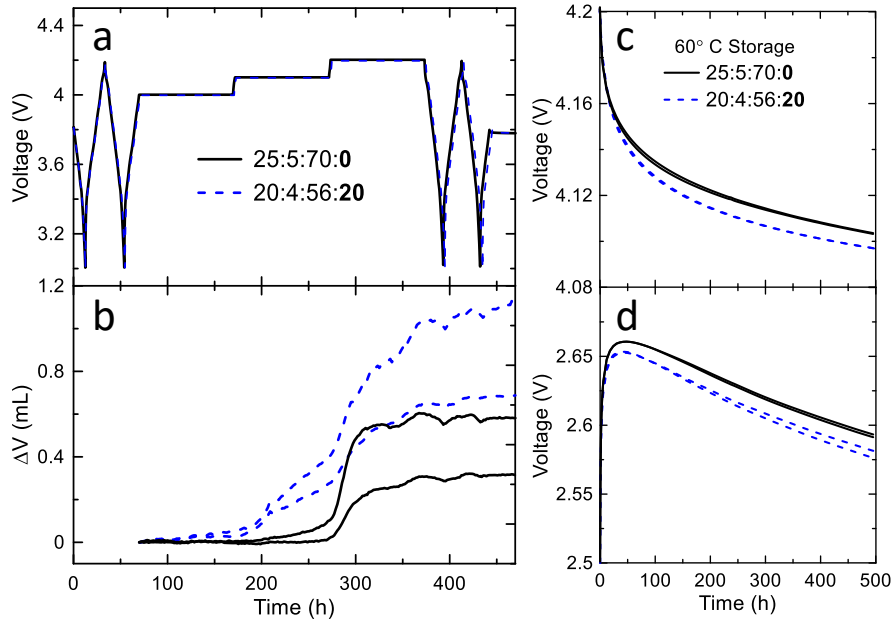


Figure 6.21: a) Voltage and b) gas volume from in-situ gas measurements of cells with 0 MA (solid black) and 20 MA (blue dashed) at 40°C during voltage-holds at 4.0 V, 4.1 V, and 4.2 V for 100 hours.

Figure 6.22 shows the parasitic heat flow of cells with 0 MA (black), 20 MA (blue), 20 MA with 25% EC (dashed blue), 30 MA (teal), 40 MA (red), and 40 MA with 25 EC (dashed red) during two cycles from 3.9 V to 4.1 V at 3.7 mA (C/100). The cells with 20 MA with 25 EC, 40 MA with 25 EC, and 30 MA did not have pair cells. The pair cells for other electrolytes are shown to demonstrate the approximate uncertainty in cells without pairs. Noise in the data was due to power failures over multiple days on which experiments were restarted immediately after the power failures occurred. The difference in parasitic

heat flow between each cell and one of the 0 MA cells for each cycle is shown in Figures 6.22b and d.

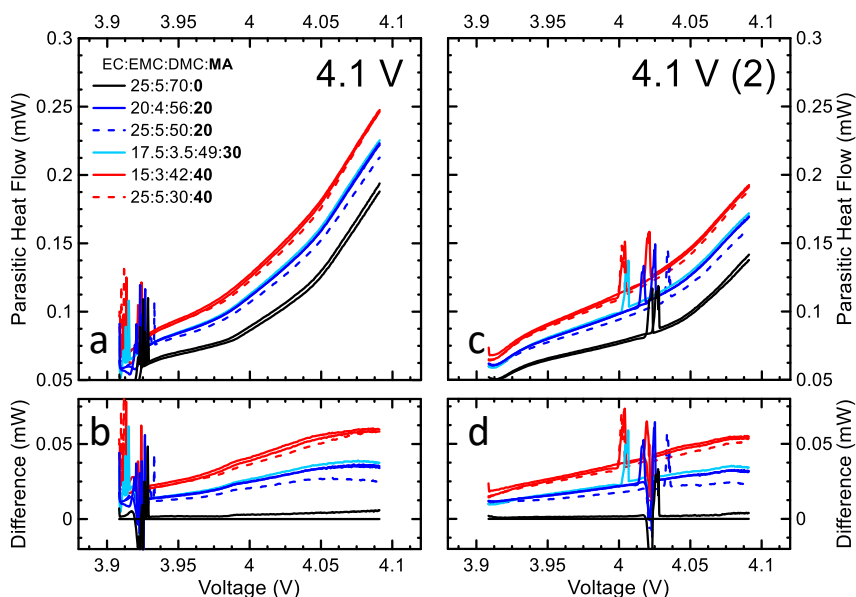


Figure 6.22: Parasitic heat flow of pouch cells cycled at C/100 between 3.9 V and 4.1 V at 40°C. The first and second cycles are shown in a) and c), while the difference in heat flow of each cell from a 0 MA cell is shown in b) and d), respectively.

Figure 6.22 shows that MA increased the parasitic heat flow in these cells, consistent with NMC cells. Changing the base solvent to contain 25% EC in the presence of 20 MA and 40 MA slightly lowered the parasitic heat flow in each case. A decreased EC concentration may have contributed to a less passivating SEI when large amounts of a co-solvent were added. The slight ‘kinks’ in the parasitic heat flow at ~3.98 V and ~4.05 V may have been due to entropy features from the NCA lattice contraction, or perhaps the slight increases were real and due to increased parasitic reactions if lattice contraction led to any strain and cracking of particles. However, this is purely speculative, and more work could be done to investigate the effects of NCA lattice contractions on parasitic heat flow.

Figure 6.23 shows the parasitic heat flow of cells during two cycles from 3.9 V to 4.2 V at 3.7 mA (C/100). From 3.9 V to 4.15 V the parasitic heat flow of cells containing

MA was higher than cells with 0 MA. However, above 4.15 V the parasitic heat flow of MA containing cells decreased below that of 0 MA cells. This behaviour was very curious, considering the large voltage fade seen at 4.2 V during storage experiments in cells with 20 MA compared to 0 MA and the higher charge endpoint capacity slippage in UHPC experiments. Additionally, the parasitic heat flows of cells with MA were higher than 0 MA cells during the subsequent cycle to 4.2 V, so the behavior only occurred above a certain voltage and was reversible. It is possible that MA introduced a different type of reaction above 4.15 V which was very endothermic compared to reactions in 0 MA cells. The behavior of MA in the NCA cells here was very different than MA in NMC cells, which showed more parasitic heat flow above 4.4 V.

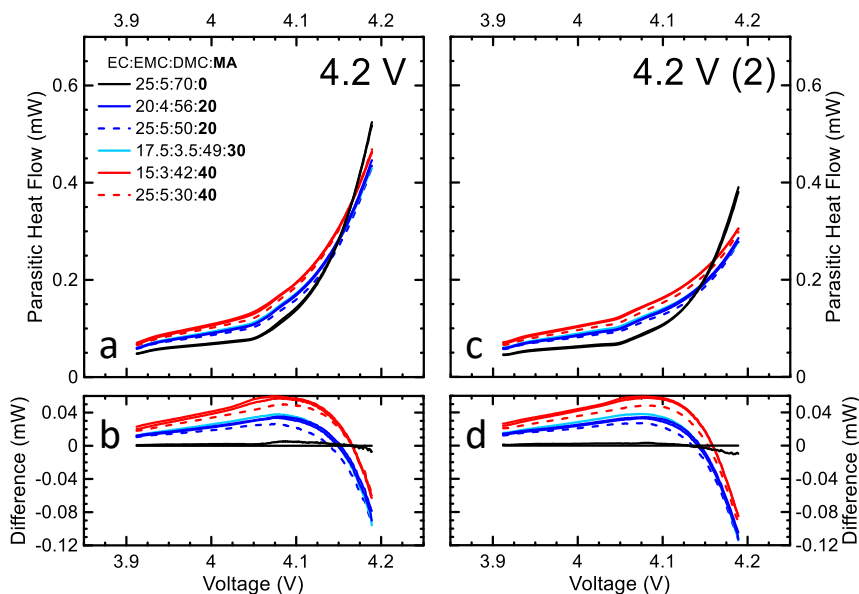


Figure 6.23: Parasitic heat flow of pouch cells cycled at $C/100$ between 3.9 V and 4.2 V at 40°C . The first and second cycles are shown in a) and c), while the difference in heat flow of each cell from a 0 MA cell is shown in b) and d), respectively.

Figure 6.24 shows the mean parasitic heat flow per cycle of each electrolyte type in this study. Plotted points show the average value between pair cells, and error bars represent the range between pair cells (when applicable). Figure 6.24 shows that regardless

of the strange behaviour above 4.15 V, 0 MA cells had lower parasitic heat flow on average in every voltage range studied.

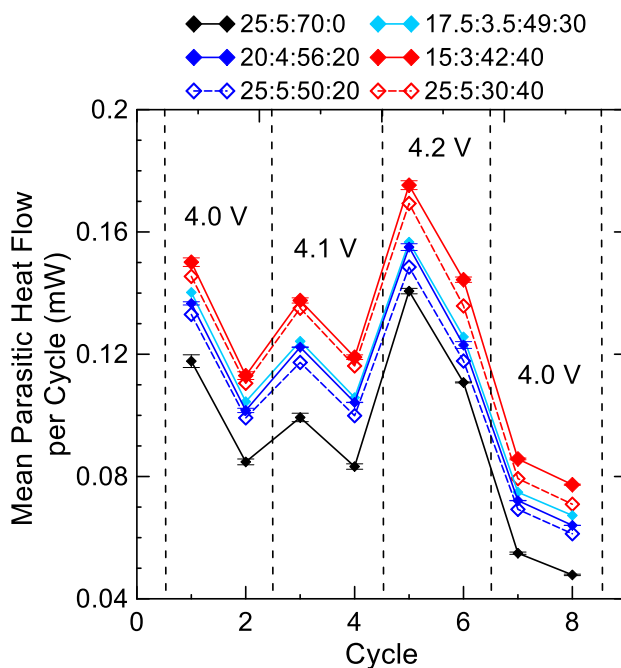


Figure 6.24: Mean parasitic heat flow per cycle of all cells cycled at C/100 between 3.9 V and the labeled upper cut off voltages at 40°C. The average value between pair cells is plotted and the error bars indicate the range between pair cells (when pair cells were used).

Cells used in calorimeter studies then underwent long-term cycling to ensure that the magnitude of parasitic heat flow could be correlated to lifetime in these cells when MA was present. Figure 6.25 shows the C/3 CCCV long-term cycling data for cells at 40°C. Figures 6.25a, b, and c show the discharge capacity, normalized discharge capacity, and ΔV , respectively. All cells with MA lost had more capacity loss and impedance growth than cells with 0 MA. Products from oxidation due to MA could have increased the positive electrode impedance, accounting for the larger impedance growth in MA-containing cells.

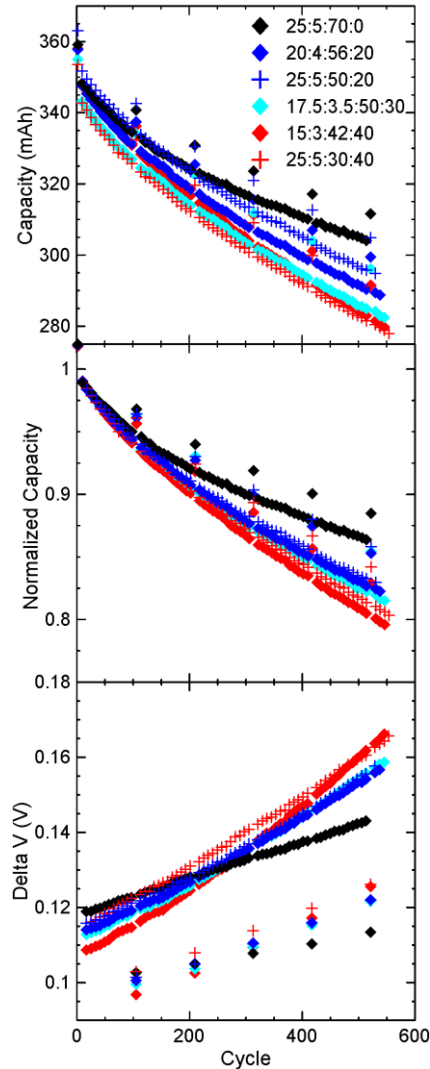


Figure 6.25: Long term cycling of cells after calorimetry experiments. Cells were cycled at 40°C at a rate of C/3 with a CCCV protocol. a) discharge capacity, b) normalized discharge capacity, c) ΔV .

Though UHPC studies found MA did not contribute to increased capacity fade, products from continual electrolyte oxidation may have eventually contributed to reduction at the negative, consuming lithium inventory and leading to the capacity loss seen in long-term cycling. Alternatively, electrolyte oxidation or reduction of species from MA may have exacerbated particle cracking at the positive electrode or negative electrode, leading to capacity fade from electrode mass loss. A detailed study on the failure mechanisms in

NCA/SiO-graphite cells such as the study on AG and NG discussed in Section 5.4 has not been completed and should be a focus of future work.

Mean parasitic heat flow in Figure 6.25 and long term cycling results in Figure 6.24 suggested that the results of parasitic heat flow in NCA/SiO-graphite cells can be used to predict cell lifetime. However, the behavior of the parasitic heat flow from cells with MA as well as *in-situ* gas measurements suggested that very different reactions may be present in cells containing MA in both NCA/SiO-graphite cells and SC-NMC532/AG cells. Additionally, the results from parasitic heat flow in NCA/SiO-graphite cells showed that the cell voltage may even play a role in the types of reactions which occur. Therefore, a method to differentiate between the reactions which occur at different voltages, cells types, and electrolytes is needed to ensure short-term studies can be predictive of long-term behaviour. This is the subject of the next chapter.

6.4.4 Conclusions

The effect of MA in SC-NMC532/AG and NCA/SiO-graphite cells on parasitic heat flow was studied. In each cell type it was found that the mean parasitic heat flow could be correlated with cycle life. However, *in-situ* gas measurements and parasitic heat flow results suggested that MA introduced different reactions compared to the base electrolytes in each cell type. Parasitic heat flow was higher in both cell types when MA was present except for above 4.15 V in NCA/SiO-graphite cells – suggesting endothermic reactions may take place in these specific cells with MA over 4.15 V.

The addition of 1% wt. DTD in SC-NMC532/AG cells was found to significantly decrease the negative impact of MA compared to when just 2% FEC was used as an additive. The effect of different additives and MA on parasitic heat flow was not studied

in NCA/SiO-graphite cells and should be the focus of future work, with care taken when comparing parasitic heat flow above 4.15 V.

In both cell types it was hypothesized that MA caused a significant increase in electrolyte oxidation at the positive electrode compared when no MA was used. However, MA was not found to significantly impact reactions at the negative electrodes, even when SiO was present in the negative electrode. If oxidation due to MA can be mitigated, very high-rate, low temperature, long-lifetime cells with high energy density could be achieved by using MA.

The overpotential correction and equilibrium correction were used in this study to provide a more realistic representation of the overpotential in cells, especially when C/100 was used in experiments on NCA/SiO-graphite cells.

6.5 CHAPTER CONCLUSIONS

In this chapter, the charge-discharge method was used to compare the trends in parasitic heat flow of different cell types. In Chapter 5 solvents and cell chemistries did not change significantly, and additives were varied between cells leading to excellent agreement between parasitic heat flow, UHPC, and cycling studies. Only changing the additives between cells may have only affected the relative stabilities of the SEI layers, without significantly affecting the reactants and products of different parasitic reactions between cells. Thus, the charge-discharge method was found to be a very reliable, predictive technique for electrolyte additive screening.

This chapter investigated different NMC compositions, positive electrode coatings, NCA as a positive electrode, SiO in the negative electrode, and MA as a co-solvent. Types

of parasitic reactions that occurred in cells seemed to change when changing the compositions of the electrolyte solvents and electrode surfaces in this chapter. Additionally, the voltage of a cell appeared to influence the types of reactions occurring in cells when MA was present. Therefore, methods that can not only detect the magnitude of parasitic heat flow in cells, but also determine if parasitic reactions are changing between cell types, electrolytes, or even voltages, are necessary.

The next chapter will outline a method to probe differences in parasitic reaction enthalpies between different cell types, coatings, solvents, and voltage ranges which was motivated by the results in this chapter.

CHAPTER 7 MEASURING PARASITIC REACTION ENTHALPY WITH ISOTHERMAL MICROCALORIMETRY AND HIGH-PRECISION COULOMETRY

This work has been submitted to Tesla for approval as part of a manuscript.²¹³

7.1 MOTIVATION

The previous chapters outlined methods of obtaining the parasitic heat flow as a continuous function of voltage over a variety of voltage ranges. Methods were developed to measure and account for the cell overpotential, and to differentiate between the parasitic heat flow during charge and the parasitic heat flow during discharge. The methods were consistent between pair cells and were found to be a good prediction of cell lifetime when comparing between cells with different additives. However, when different solvents were used in cells, or different electrode materials and coatings were used, the trends in parasitic heat flow did not always correlate with the performance in long-term tests. The previous chapters motivated a method which can measure the parasitic heat flow of a cell, but also probe any differences in types of reactions between cells.

The aim of this work is to introduce a method which is capable of both determining the magnitude of parasitic reactions as well as the net enthalpy of parasitic reactions in cells. This kind of technique allows for the same information to be collected as previous cycling methods in addition to information about the types of chemical processes occurring in cells. A proof-of-concept study is presented first using reversible redox shuttle molecules to show that isothermal microcalorimetry was capable of accurately measuring the expected net enthalpy of reaction of 0 kJ mol^{-1} for the redox shuttle, within uncertainty

($10 \pm 10 \text{ kJ mol}^{-1}$). The technique is then used to probe parasitic reaction enthalpies in cells with different positive electrode coatings and electrolytes at a variety of voltages.

7.2 EXPERIMENTAL

Coated and uncoated SC-NMC532/AG cells were used in this study. Experiments with shuttle molecules used cells without a coating on the positive electrode. Voltage-hold experiments used cells with a coating and cells without a coating on the positive electrode.

Electrolytes contained 1.2 M LiPF_6 in various solvents. Cells used in shuttle experiments either contained 0.1 M 2,5-di-*tert*-butyl-1,4-dimethoxybenzene (DDB), 3,5-di-*tert*-butyl-1,4-dimethoxybenzene (DBDB), or 2,5-dimethyl-1,4-dimethoxybenzene (DMB) in EC:EMC:DMC (25:5:70 wt.). Cells used for voltage-holds contained either EC:EMC:DMC 25:5:70 wt., (EC:EMC:DMC):MA 60(25:5:70):40 wt. or FEC:TFEC 3:7 wt.. Cells containing EC:EMC:DMC with and without MA contained 2% wt. VC and 1% wt. DTD. Cells containing FEC:TFEC contained 2% wt. PES and 1% wt. DTD.

Cells were cycled 4 times from 3.0 V to 4.2 V to ensure a well-formed SEI was present. Cells were then cycled between 4.0 V and different upper cut-off limits: 4.2 V (twice), 4.4 V (twice) and again to 4.2 V at 1.5 mA to compare previous cycling methods to voltage-holds. Cells were then connected to Keithley 2602B source meters (Keithley Instruments Inc.) and underwent voltage-holds at 3.8 V, 4.2 V, 4.3V, and 4.4 V for 100 hours while in the microcalorimeter. After the series of holds, some cells were connected to a Novonix 5V, 2A High Precision Cycler (Novonix, 177 Bluewater Road, Bedford, NS, Canada) and held at 4.4 V for 95 hours while in the calorimeter.

Cells used for shuttle experiments were inserted into the calorimeter and connected to the Maccor cycler, charged to 3.7 V at 10 mA, then charged at 2 mA until the end of the experiment.

7.3 REVERSIBLE REDOX SHUTTLES

To investigate whether isothermal calorimetry could be used to accurately measure reaction enthalpies in a real cell, stable, reversible redox shuttle molecules were used (see Section 1.6.6). DDB was found by Moshurchak et al. to have a lifetime of more than 200 full-capacity overcharge cycles when added to electrolyte at a concentration of 0.1 M in LiFePO₄/graphite coin cells.^{139,214} DBDB was found by Zhang et al. to have a limited lifetime of ~24 overcharge cycles under the same conditions.¹⁴⁰ DMB was found by Moshurchak to have very poor shuttle stability, lasting only 13 overcharge cycles.¹³⁷

Figure 7.1a shows a schematic of an activated redox shuttle operating in a cell under open circuit conditions. When the positive electrode of a cell is at a high enough potential to oxidize a shuttle molecule, S, to S⁺, the oxidized molecule can then migrate to the negative electrode and reduce back to S. This process yields a net reaction enthalpy change of 0 kJ mol⁻¹ since no net chemical reaction occurred. In OCV, this electron transfer causes an internal charge balance of Li⁺ ions from the negative electrode to the positive electrode (self-discharge). The internal current formed by the charge transfer is called the parasitic current, I_p (in these cases the redox shuttle does not ‘harm’ the cell but is considered a parasitic process here). In closed circuit conditions, such as in a voltage-hold, the charge balance due to the redox shuttle is supplied through the external circuit. Figure 7.1b shows a shuttle reaction during a voltage-hold.

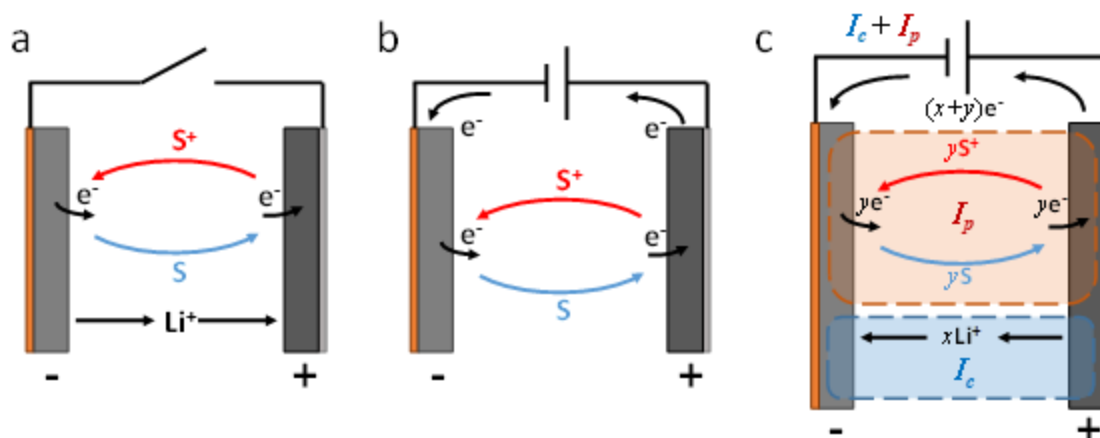


Figure 7.1: A redox shuttle process in a) open circuit voltage conditions b) closed circuit with electrode equilibrium, and c) closed circuit charge. I_c and I_p correspond to cell charging current and shuttle current, respectively.

Equation 2.18 shows that the parasitic heat flow has contributions from I_p multiplied by the cell voltage (V) and the rates and enthalpies of reaction for all parasitic reactions occurring in cells. Therefore, since the enthalpy change for a reversible redox shuttle is 0 kJ mol^{-1} , the parasitic heat flow from cells in Figures 7.1 a and b should be $I_p V$.

The shuttle molecules used in this study had reported oxidation potentials of 3.85 V to 4.1 V vs Li/Li⁺, or approximately 3.6V to 4.0 V vs graphite, depending on the state of charge of the graphite electrode.¹³⁷ Cells were charged using a constant current (CC) rate of 10 mA ($C/20$) to 3.7 V, at which time a CC rate of $C/100$ (2 mA) was applied. If all 2 mA of supplied current went into the redox shuttle above 3.7 V, the heat flow would be approximately 7.4 mW. If a portion x of the current acted to further charge the cell, while the remainder y was used by the shuttle, a situation shown in Figure 7.1c would arise, where I_c is the cell charging current, and I_p is the shuttle current, and the measured heat flow would be $I_p V < 7.4 \text{ mW}$.

Figures 7.2a, b, and c show the results from cells with DDB, DBDB, and DMB, respectively in the columns. Voltage vs. time is shown in row i) of Figure 7.2 for each cell after the shuttle was activated (black). The voltage of the cells increased slowly, indicating a portion of the supplied current was charging the cell, while the majority of the current was being used in the redox shuttle. Cells with DDB and DBDB had less voltage increase than DMB, indicating DMB was less stable compared to DDB and DBDB. A dashed green line in each panel in row i) indicates the voltage vs. time for a cell without shuttle molecules for comparison. The charging current, I_c does not contribute to the shuttle heat flow (I_pV) and is calculated using the differential capacity ($dQ\ dV^{-1}$) of a control cell (same cell and electrolyte without DDB) charged at a rate of $C/20$, and the differential voltage ($dV\ dt^{-1}$) of the DDB-containing cell by

$$I_c = \left(\frac{dQ}{dt}\right)_c = \left(\frac{dQ}{dV}\right)_{control} \left(\frac{dV}{dt}\right)_{shuttle} . \quad 7.1$$

I_c was then subtracted from the total current of 2 mA to calculate I_pV . Row ii) in Figure 7.2 shows the theoretical IV in blue, corrected I_pV in black, and the measured heat flow in red. I_c was approximately 5% of the charge current, or 0.1 mA for DDB and DBDB and ~20% (0.4 mA) for DMB. At this rate, the entropic heat flow of electrode materials and overpotential heat flow due to charging the cell would be on the order of 1 μ W, which is within the calorimeter uncertainty, and three orders of magnitude smaller than the measured heat flow.^{208,215} The net enthalpy change per mole of electrons transferred by I_p will be referred to as ΔH_e and is a measure of the net enthalpy of reaction for all reactions occurring in the cell per mole of electrons in the parasitic current. ΔH_e was then calculated as the difference between the measured heat flow and I_pV divided by the rate of electron transfer (I_p is proportional to the rate of reaction, k , by the one-electron redox process).

$$\Delta H_e = \frac{(I_p V - \dot{q})}{I_p} F \quad 7.2$$

where \dot{q} is the total heat flow and F is Faraday's constant. The calculated net enthalpy change per mole of electrons is shown in row iii) of Figure 7.2.

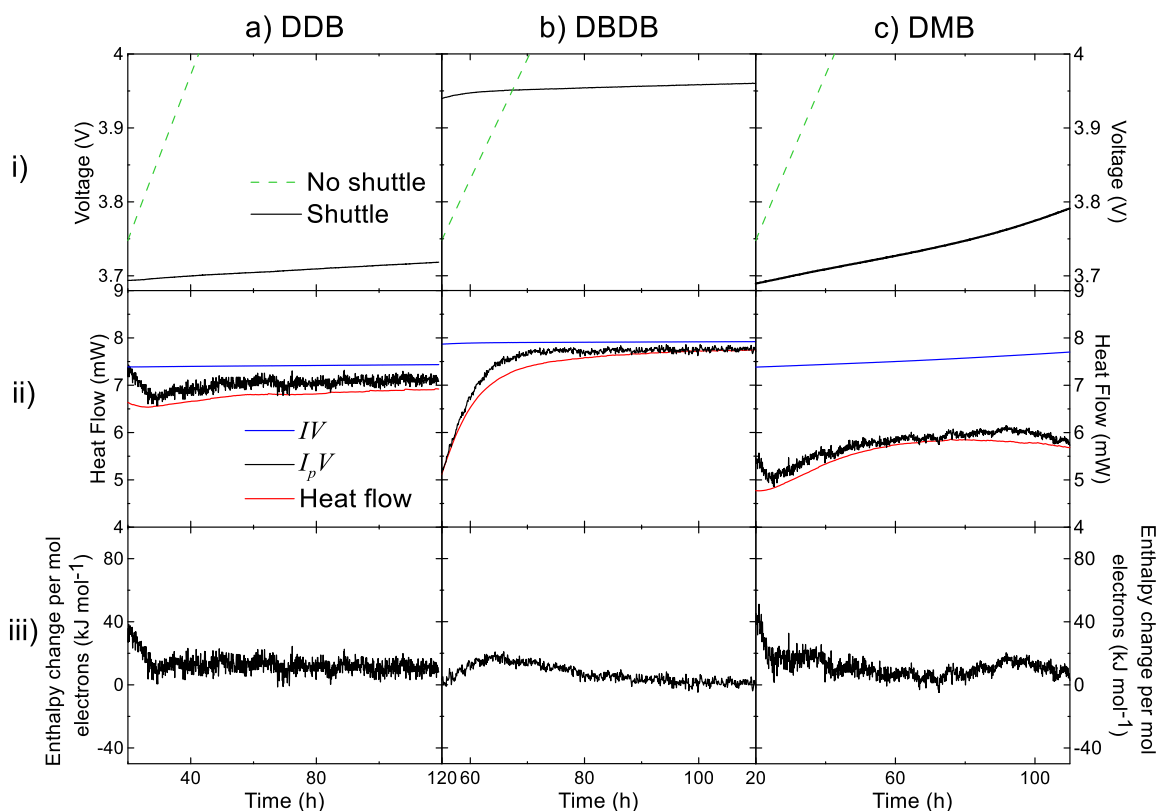


Figure 7.2: i) Voltage versus time during a 2 mA ($C/200$) charge for cells containing a) DDB, b) DBDB, c) DMB redox shuttle molecules (black) and a cell without shuttles (dashed green) ii) Calculated IV (blue), measured heat flow (red), and $I_{sh}V$ (black). iii) Calculated reaction enthalpy change per mole of electrons supplied to the shuttle.

DDB and DBDB had a very close ΔH_e to 0 kJ mol⁻¹ (10 ± 10 kJ mol⁻¹ and 1 ± 3 kJ mol⁻¹), while DMB had a ΔH_e of $\sim 30 \pm 10$ kJ mol⁻¹. In this case, a non-zero enthalpy change does not yield the enthalpy of reaction for a shuttle molecule decomposition. To calculate ΔH for a single decomposition one would need to know the number of transits a single molecule made on average before decomposition. Therefore, the smaller the ΔH_e , the more

stable the shuttle molecule likely was. No electrolyte additives were used in these cells, meaning there could be a small number of parasitic reactions occurring (especially in DBDB with a higher redox potential) in addition to the redox shuttles, which would contribute to heat flow and further offset the net enthalpy of reaction. Shuttles which were more stable as reported in the literature had closer to the expected enthalpy of reaction of 0 kJ mol^{-1} , while DMB had slightly higher than the expected value. The observed value of $\sim 10 \pm 10 \text{ kJ mol}^{-1}$ for the more stable shuttle molecules was assumed to be reasonable for this proof-of-concept experiment. The uncertainty in the shuttle reaction net enthalpy change can be considered when evaluating cells when parasitic reactions with non-zero enthalpy of reaction are being measured.

7.4 CHARGE-DISCHARGE METHOD

To investigate the enthalpy of reaction of parasitic reactions in different lithium-ion electrolyte systems at different voltages, three electrolyte solvent mixtures and two cell types were used. In Section 6.2 it was found that changing the positive electrode cell chemistry or positive electrode coatings had a substantial effect on parasitic heat flow in cells, but capacity retention in long-term cycling did not always follow the observed trend in parasitic heat flow.²⁰⁸ It was hypothesized that positive electrode coatings may have been contributing to different parasitic chemical pathways. Therefore, this study investigates both coated and uncoated SC-NMC532/AG cells. The effects of different coatings, compositions, and morphologies may be evaluated in future studies.

The solvent blends of EC:EMC:DMC (25:5:70 wt.) and EC:EMC:DMC:MA (15:3:42:40 wt.) were chosen to explore differences in enthalpy change when adding a co-

solvent to a known system, particularly with increased voltage. In Section 6.4 MA was shown to cause a small reduction in capacity retention during long-term cycling compared to cells with EC:EMC:DMC electrolytes.^{75,76} The studies suggested that MA led to increased electrolyte oxidation and gas production at the positive electrode at lower voltages than cells without MA, indicating a difference in parasitic reaction processes.

It was hypothesized that a solvent system with completely different chemistry would yield different enthalpies of reaction. Thus, FEC:TFEC was studied to observe any differences from the organic carbonate system. Fluorinated carbonates have been shown to improve capacity retention and lower parasitic heat flow at high voltage, but perform poorly in lower voltage ranges.^{80,215–217} The additive combinations of 2% VC and 1% DTD (for EC:EMC:DMC with and without MA) and 2% PES and 1% DTD (for FEC:TFEC) were chosen with the aim of creating robust SEI layers and simplifying or reducing the number of possible reaction pathways present in cells. The effect of different additives can be studied in future works.

Before exploring the enthalpies of reactions, cells underwent slow charge-discharge cycles (1.5 mA, $\sim C/130$) from 4.0 V to 4.2 V and 4.4 V. The charge-discharge method with a fitted overpotential and equilibrium correction was used. As found in previous chapters, the charge-discharge method may be unreliable when comparing cells in this work when many chemical parameters change at once. Different chemical reactions could change the contribution of reaction enthalpy to the parasitic heat flow in Equation 2.18.

Figure 7.3 shows the parasitic heat flow during two cycles to 4.2 V and two cycles to 4.4 V (Figures 7.3a, b and Figures 7.3c, d, respectively). Parasitic heat flows from cells with coated NMC532 are shown as solid lines and from cells with uncoated NMC532 are

shown as dashed lines. Parasitic heat flows from cells with EC:EMC:DMC are shown in black, EC:EMC:DMC:MA in blue, and FEC:TFEC in red. This colour scheme will be repeated through the rest of this work. Cells with MA showed significantly more parasitic heat flow than cells with EC:EMC:DMC, as expected from previous studies.^{75,76} Cells with FEC:TFEC demonstrated no clear trend between coated and uncoated cells during the two cycles at 4.4 V, and showed higher parasitic heat flow at lower voltages, consistent with previous findings.^{80,215} However, only qualitative comparisons can be made between organic carbonates and fluorinated carbonates using the charge-discharge method without knowing if the parasitic reaction enthalpies were different. In cells with EC:EMC:DMC with and without MA, the cells with coated NMC532 showed lower parasitic heat flow than cells with uncoated NMC532.

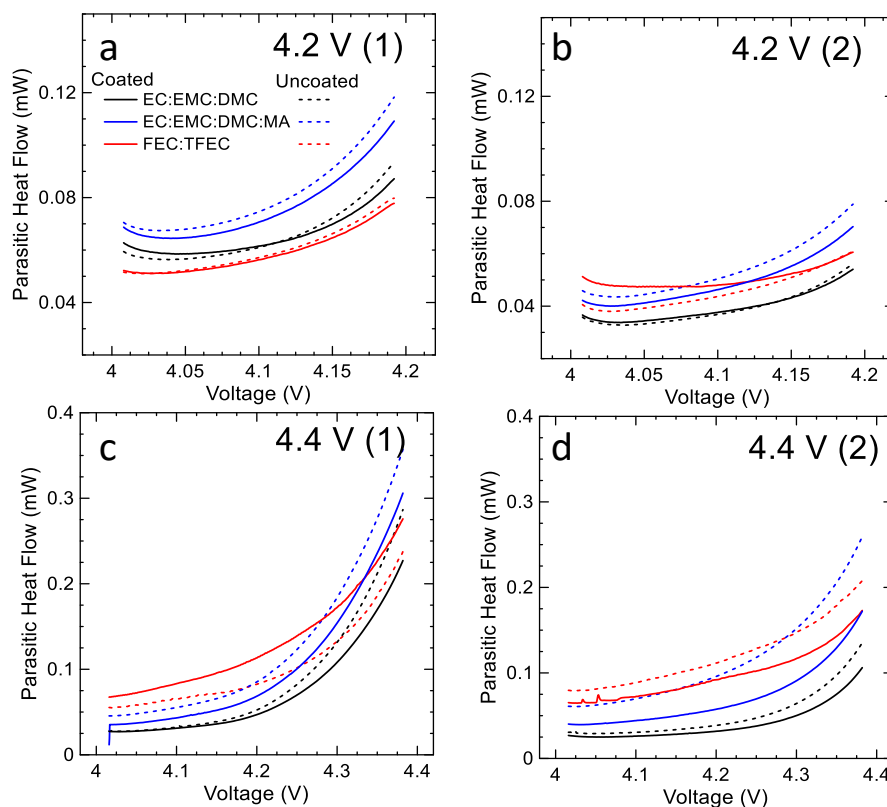


Figure 7.3: Calculated parasitic heat flow of cells with EC:EMC:DMC-based electrolytes (black), EC:EMC:DMC:MA-based electrolytes (red), and FEC:TFEC-based electrolytes (blue) cells during two cycles at 4.2 V (a,b) and 4.4 V (c,d). Results for cells with coated NMC532 are shown as a solid line and cells with uncoated NMC532 are shown as a dashed line.

Figure 7.4 shows a summary of the mean parasitic heat flow per cycle for all of the voltage windows studied. Parasitic heat flow often decreases over the course of an experiment due to a build-up of SEI products from parasitic reaction products, decreasing the rate of reactions over time, but increasing cell impedance. However, this does not always occur. Cells without coatings containing MA and both coated and uncoated cells with FEC:TFEC-based electrolytes had higher parasitic heat flow during the last cycle to 4.2 V than during the second cycle to 4.2 V, indicating less passivating SEI layers at the end of the experiment. Additionally, parasitic heat flow increased between subsequent cycles to 4.4 V in uncoated cells with FEC:TFEC electrolytes, but decreased in coated

cells. Therefore, it was apparent there were differences in types of reactions occurring in cells with different coatings but otherwise identical chemistries.

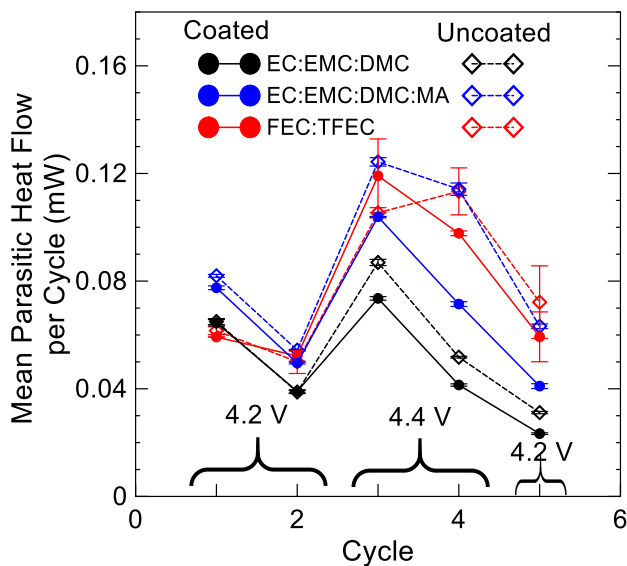


Figure 7.4: Mean parasitic heat flow per cycle for cells containing EC:EMC:DMC-based electrolytes (black), EC:EMC:DMC:MA-based electrolytes (red), and FEC:TfEC-based electrolytes (blue). Results for cells with coated NMC532 are shown as a solid line and cells with uncoated NMC532 are shown as a dashed line.

7.5 PARASITIC REACTION ENTHALPY

Consider Figure 7.5a, in which electrolyte species S oxidizes at the positive electrode and reduces at the negative electrode into species X in an irreversible fashion (an example of a cross-talk reaction). The net enthalpy of reaction for this process could be non-zero. The process leads to an internal current I_p , and a self-discharge process maintains charge balance in the cell.

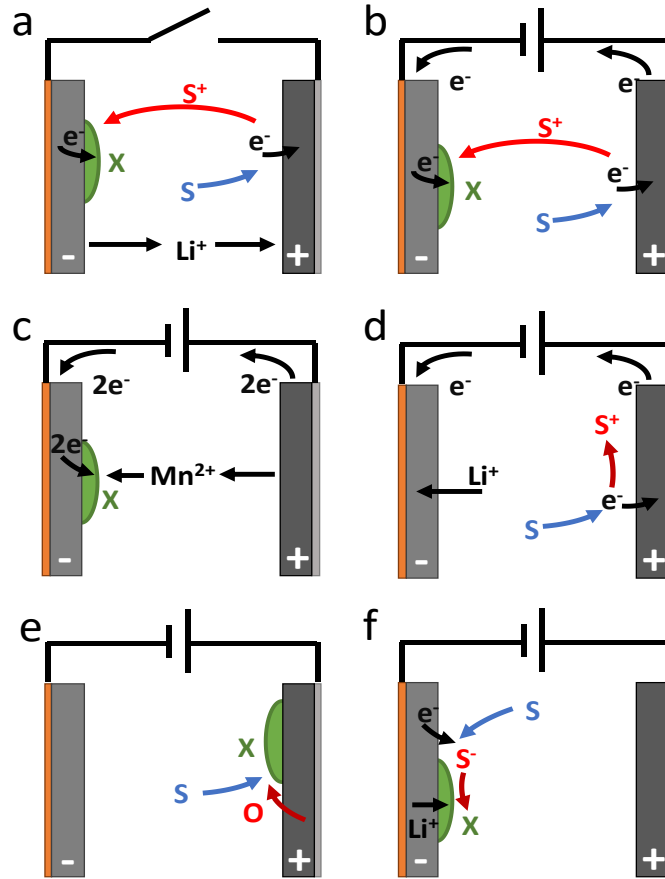


Figure 7.5: Simplified parasitic reaction schemes: a) open-circuit oxidation/reduction cross-talk. Diagrams b) to d) are shown in voltage-hold conditions: b) oxidation/reduction cross-talk, c) transition metal dissolution, d) solvent oxidation at the positive electrode. Diagrams e) and f) involve no internal current in voltage-hold (self-discharge in OCV): e) solvent-oxygen reaction, f) solvent reduction at the negative electrode.

Assuming only the cross-talk process from Figure 7.5a is present in a cell, the parasitic heat flow would be given by:

$$q_p = I_p V + k \Delta H \quad 7.3$$

where I_p is the parasitic current, k is the rate of the cross-talk reaction, and ΔH is the reaction enthalpy. When in closed circuit (such as during a voltage-hold shown in Figure 7.5b) the result is the same, but the charge balance can be applied to the cell through the external

circuit. I_p is then known and the parasitic reaction enthalpy per mole of electrons in the parasitic current (ΔH_e) can be calculated as

$$\Delta H_e = \frac{(I_p V - \dot{q}_p)}{I_p} F. \quad 7.4$$

Equation 7.4 is obviously not realistic, as real cells could contain any unknown number of reaction processes, and not all parasitic reactions produce a parasitic current. For example, Figures 7.5c and d demonstrate examples of parasitic reactions which produce a parasitic current; c) transition metal dissolution and d) solvent oxidation at the positive electrode. Figures 7.5e and f demonstrate examples of reactions which do not produce a parasitic current: e) a solvent-oxygen reaction and f) solvent reduction. The case in Figure 7.5f will lead to no parasitic current even under closed circuit conditions if the graphite electrode is in a two-phase plateau (eg. stage-1 LiC_6 and stage-2 LiC_{12}) where the potential is constant with lithium content.

Equation 7.4 does not directly account for reactions which do not produce a parasitic current, *i.e.* the proposed reduction of EC with lithium-ions and electrons to make lithium ethylene dicarbonate and ethylene at the negative electrode.^{77,84,86} The treatment of Equation 7.4 must be considered carefully, and the effects of the different reactions in Figure 7.5 investigated in future work. Therefore, in this work, the measurable quantity is defined as the net enthalpy change from *all* reactions occurring in the cell per mole of electrons in the parasitic current, called ΔH_e . Therefore, changes in the calculated net enthalpy change can either be due to different reaction pathways or to changes in the ratio of different reactions (*i.e.* if the rate of some endothermic solvent reduction reaction as pictured in Figure 7.5f increases more than a solvent oxidation reaction in Figure 7.5d in a cell, the magnitude of the net enthalpy change per mole of electrons will increase

disproportionately due to the increase in rate of reduction without a change in parasitic current).

7.6 VOLTAGE-HOLD EXPERIMENTS

Cells in the calorimeter were connected to Keithley source-meters controlled with in-house software. Cells were charged to 3.8 V and held for 100 hours. Then cells were charged to 4.22 V, held for 24 hours and then held at 4.2 V for 100 hours. Before each subsequent 100-hour hold to 4.3 V and 4.4 V cells were also charged to 20 mV higher than the hold voltage and held for 24 hours. This 24-hour charge-hold aimed to ensure the lithium concentration in the electrodes would reach equilibrium early in the 100 hour hold.

Figure 7.6 shows the measured heat flow (red) and IV (black) for each voltage-hold in cells having EC:EMC:DMC-based electrolytes with and without MA. IV had a high noise level due to large fluctuations in the current supplied to cells. Each data point represents data taken every five seconds and averaged over three-minute intervals by the software. Without this averaging of 36 points the noise level in the current was 75 μA , leading to a noise in I_pV of approximately 300 μW . No optimization of data point collection was investigated. Cells with MA had higher parasitic heat flow and a larger parasitic current than cells without MA, especially at high voltage. Figure 7.6 shows that majority of the measured heat flow was due to the IV term. This could help justify the use of the charge-discharge method if the difference in parasitic heat flow between cells is significant, as observed in the case of adding MA.

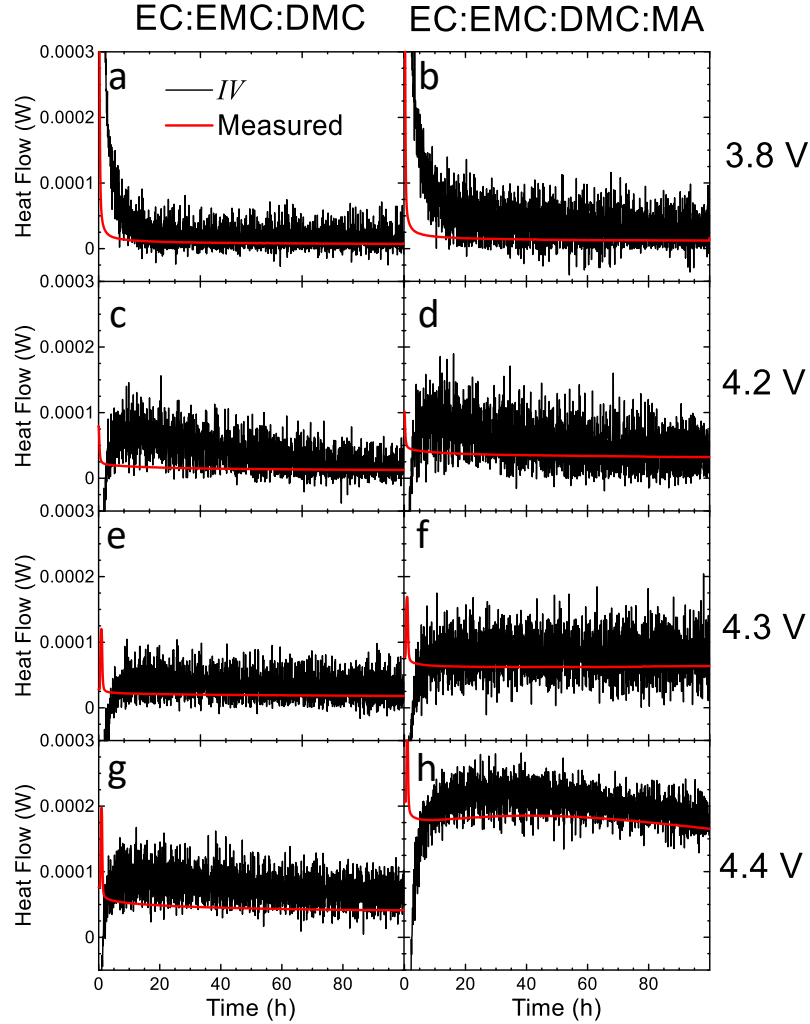


Figure 7.6: IV (black) and measured heat flow (red) in cells with coated NMC532 with EC:EMC:DMC-based electrolytes (left column) and cells with EC:EMC:DMC:MA-based electrolytes (right column) cells at different upper cutoff voltages: 3.8 V (a,b), 4.2 V (c,d), 4.3 V (e,f), and 4.4 V (g,h).

Approximately 50 hours into each hold the current appeared to reach a decay rate comparable to the decay rate of the heat flow (when IV decays faster than heat flow some current is still charging the cell to reach a homogeneous Li concentration in the electrodes). After 50 hours it was assumed all current was used in parasitic reaction charge balance such that $I = I_p$ and therefore $\dot{q} = \dot{q}_p$. In each case $I_p V$ was larger than the measured heat flow. Since less heat flow was measured than produced by $I_p V$, the parasitic reaction

enthalpies must have been net endothermic (positive ΔH_e). The noise level shown in Figure 7.6 was too large to deduce any quantitative information from this representation of the data. However, since the accuracy of a Keithley current source is better than 0.1%, integrating $I_p V$ over the final 50 hours of each hold was used to accurately represent the parasitic energy produced by maintaining charge balance at each voltage.¹⁷⁴ The integrated $I_p V$ over time, which will be termed cumulative IV energy (E_{IV}) and the integrated \dot{q} , here called cumulative parasitic energy (E_p), was used to reduce the noise over the length of the hold and obtain quantities with reliable units to ΔH_e . The total charge supplied during the voltage-hold is the parasitic capacity (Q_p). Equation 7.4 can then be rewritten to obtain the net enthalpy change per mole of electrons using the described energies:

$$\begin{aligned} \Delta H_e &= \frac{\int I_p V dt - \int \dot{q} dt}{\int I_p dt} F \\ &= \frac{E_{IV} - E_p}{Q_p} F. \end{aligned} \tag{7.5}$$

Figure 7.7 shows the integrated results starting after 50 hours during each voltage-hold. Figures 7.7a, b, c and d show E_p , E_{IV} , the difference between these energies, termed the cumulative reaction energy (E_r), and ΔH_e , respectively. Results are plotted after the 60 hour point since the noise introduced in ΔH_e was large during the first ten hours of the integration when fewer data points were used. Columns i, ii, iii, and iv correspond to voltage-holds at 3.8 V, 4.2 V, 4.3 V, and 4.4 V, respectively. In almost every case cells with coated NMC532 showed lower E_p than cells with uncoated NMC532, largely due to the smaller parasitic current present in these cells, observed in row b of Figure 7.7. In the case of cells with MA, at 4.4 V the pair cells with coated NMC532 yielded inconsistent results for E_p and E_{IV} , otherwise there was very good agreement between pair cells. Results

for ΔH_e became more consistent between pair cells as the hold voltage increased, due to the higher signal to noise ratio in I_p . Regardless, good qualitative agreement existed between ΔH_e for pair cells at each voltage.

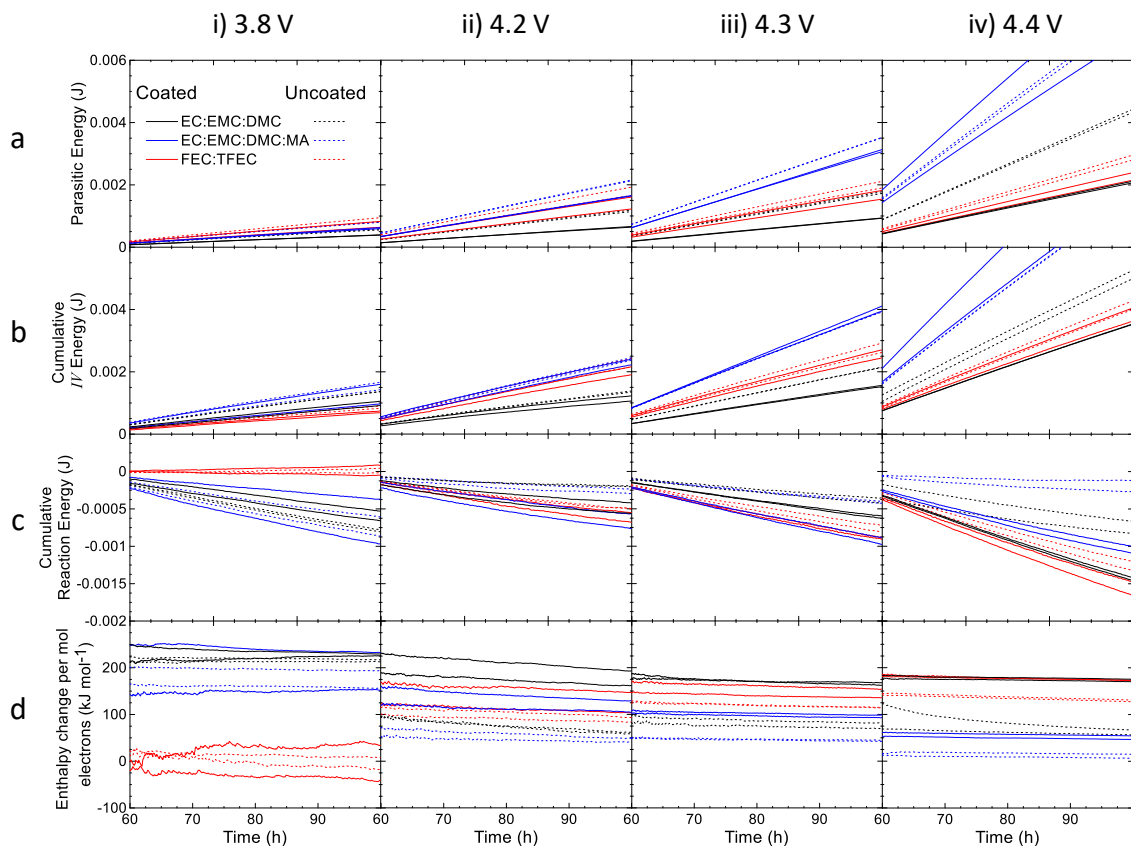


Figure 7.7: Integrated a) cumulative parasitic energy, b) cumulative IV energy, c) cumulative reaction energy, d) net enthalpy change per mole of electrons at different upper cutoff voltages: i) 3.8 V, ii) 4.2 V, iii) 4.3 V, iv) 4.4 V. Results for cells with coated NMC532 are shown as solid lines and results for cells with uncoated NMC532 as dashed lines. Black lines correspond to cells with EC:EMC:DMC-based electrolytes, blue to cells with EC:EMC:DMC:MA-based electrolytes, and red to cells with FEC:TFEC-based electrolytes.

Although MA-containing cells with coated NMC532 at 4.4 V yielded inconsistent results for E_p and E_{IV} , the calculated ΔH_e was the same. This suggested that the rate of reactions in one MA cell increased significantly over the other, but the reaction processes were the same in both cells. MA has been found to produce significant amounts of gas in

cells, so this may have been due to gas in part of the electrode stack, decreasing the active surface area of the cell.⁷⁶ The agreement in ΔH_e between pair cells at high voltage, and consistent ΔH_e between pair cells with different rates of reactions was quite encouraging, considering the noise level in I_p . Another notable observation was the large difference in ΔH_e at 3.8 V between organic carbonate cells and fluorinated carbonate cells. As voltage increased some chemistries exhibited a change in ΔH_e , others appeared to stay the same. To make more quantitative trends at low voltages, a higher precision measurement of I_p is needed.

To investigate whether trends could be found in the integrated data and ΔH_e , Figure 8 shows a summarized view of the curves in Figure 7.7. Figure 7.8a shows the cumulative E_p between 50 and 100 hours. Figure 7.8b shows the cumulative E_{IV} and the cumulative E_r over the same time interval (which total to E_p) and Figure 7.8c shows ΔH_e . Cells with coated NMC532 are shown as dark, narrow bars and cells with uncoated NMC532 are wide, lighter bars behind the data for the cells with coated NMC532. Values for the energies represent the total integration over the final 50 hours of each hold, and values for ΔH_e in Figure 7.8c are representative of the average value of ΔH_e during the final 40 hours of each voltage-hold. The first 10 hours were not included in this average due to the noise level at the beginning of the integration. Error bars represent the range of values between pair cells, and again show consistent results.

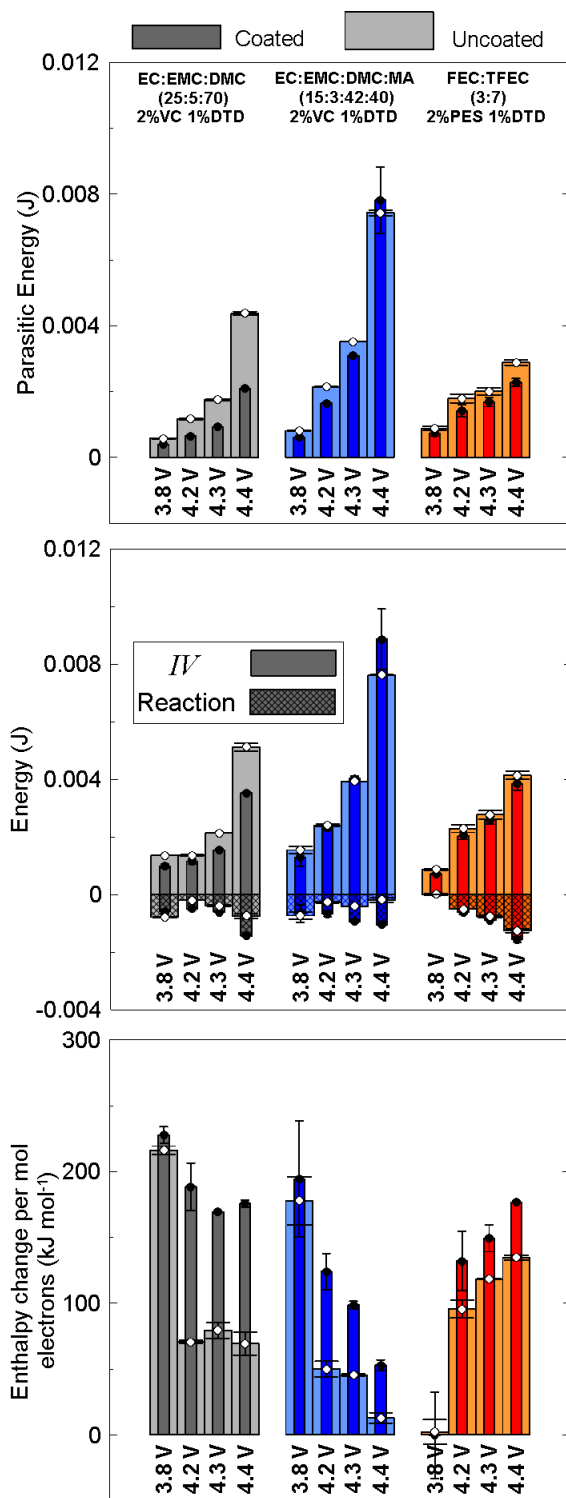


Figure 7.8: Total integrated results from the final 50 hours of voltage-holds. a) final cumulative parasitic energy, b) final cumulative IV and final cumulative reaction energy, and c) the enthalpy change per mole of electrons (average of the final 40 hours of voltage-hold). Results for cells with coated NMC532 are shown as thin, dark bars, and results for cells with uncoated NMC532 are thick, light bars.

In every case in Figure 7.8c, ΔH_e was lower for cells with uncoated NMC532 than for cells with coated NMC532. This may give cells with uncoated NMC532 a disadvantage when comparing charge-discharge parasitic heat flow results, as any reactions that occurred in cells with uncoated NMC532 were less endothermic. At 3.8 V, cells with coated and uncoated NMC532 had very similar ΔH_e around 225 kJ mol⁻¹. Above 4.2 V cells with uncoated NMC532 showed a much less endothermic ΔH_e than coated cells by about 100 kJ mol⁻¹. The coating on the positive electrode may have suppressed oxidation processes responsible for the more endothermic ΔH_e seen in the cells with coated NMC532. In both cells with coated and uncoated NMC532 having EC:EMC:DMC-based electrolytes, ΔH_e was approximately the same from 4.2 V to 4.4 V (175 kJ mol⁻¹ in cells with coated NMC532, and 75 kJ mol⁻¹ in cells with uncoated NMC532), suggesting that although the rate of reactions increased with increased voltage, the reaction processes in each cell type stayed the same.

However, in cells with MA, ΔH_e was similar to that of cells with EC:EMC:DMC-based electrolytes at 3.8 V, then as the hold voltage increased, ΔH_e decreased. Therefore, the addition of MA must have changed the net parasitic reaction processes to be less endothermic, or one or more exothermic process(es). The change could have been due to the introduction of least one additional, less endothermic process, the rate of this process increased with high voltage faster than the rate of reactions in cells with EC:EMC:DMC-based electrolyte alone. Section 6.4 suggested that MA was responsible for a significant increase in electrolyte oxidation at high voltage which produced gas and increased cell impedance over time, but did not significantly affect the negative electrode.^{76,211} The results here suggested this gas-producing oxidation process in SC-NMC532/AG cells was

likely exothermic. Conversely, ΔH_e increased in FEC:TFEC cells as the voltage is increased, suggesting multiple reaction pathways were present, the rates of which also varied differently with voltage. At 3.8 V ΔH_e was 0 ± 30 kJ mol⁻¹ in FEC:TFEC cells, suggesting either a shuttle-like reaction was occurring, or multiple reaction pathways with coincidentally net zero ΔH_e were occurring. Due to the reductive nature of FEC and reported performance in the literature the latter is more probable.

Cresce et al.¹³¹, Xu et al.^{190,218}, and Islam et al.¹⁹ have suggested that species coordinated to Li⁺ (typically EC in the EC:EMC:DMC-based electrolyte) preferentially react at the electrodes. In the cells with EC:EMC:DMC-based electrolyte here it could be that EC is preferentially oxidized or reduced in the same way, (just at different rates) with increased voltage, explaining the similar ΔH_e over an extended voltage range. MA has been found to reduce the binding energy of solvent to PF₆⁻ molecules⁷⁶, which is in turn correlated with increased rates of electrolyte oxidation.⁶³ This may explain how MA could introduce additional reaction pathways with rapidly increasing rates at higher voltages.

Figure 7.8 has shown that in some cell chemistries the rates of different reaction pathways may change independently with voltage. This adds an additional level of uncertainty when only comparing the magnitude of parasitic heat flow between cells with different coatings on the electrodes or different electrolytes. Interestingly, all values of ΔH_e measured show net endothermic parasitic processes. However, this does not suggest every reaction is net endothermic. It is possible a large, endothermic contribution comes from the origin of lithium involved in parasitic reactions, either from de-solvation of Li⁺ from solvent or from deintercalation from electrodes.^{190,218} In cells with MA the sharply decreasing ΔH_e suggested exothermic processes with increasing rates occurred at high

voltages. Therefore, it is highly possible that a hold at 4.5 V may have shown a net exothermic ΔH_e , or a cell containing more MA may yield net exothermic reactions. Due to cell balance (4.4 V) and concerns about exposing the expensive microcalorimeter to cells generating large volumes of gas, neither of these options was explored.

Future works will further explore trends with voltage and may also benefit from exploring how rates and enthalpies of reaction depend on cell temperature. The technique shown here would benefit from measurements such as GC-MS to study electrolyte content, XPS to analyze differences in electrode surfaces, and chemical simulations to investigate preferential chemical pathways in different systems. Future works will also utilize higher precision instruments to measure I_p . For example, after the sequence of voltage-holds summarized in Figure 7.8, some cells were connected to a Novonix high precision charger and were held at 4.4 V for 90 hours.

Figures 7.9a and b show the differences between the measurements done in this work using a Keithley source-meter (data taken every five seconds and points averaged over three minute intervals) and the Novonix system collecting a single data point without averaging every 30 seconds. Without the 36 point averaging, the noise in the Keithley data was $\sim 300 \mu\text{W}$. The Novonix system showed much higher accuracy with a noise level of $< 25 \mu\text{W}$ for single measurements. The voltage-hold on the Novonix system was not preceded by a voltage-hold to 4.42 V like the first voltage-hold, so the cell took longer to reach lithium equilibration in the cell.

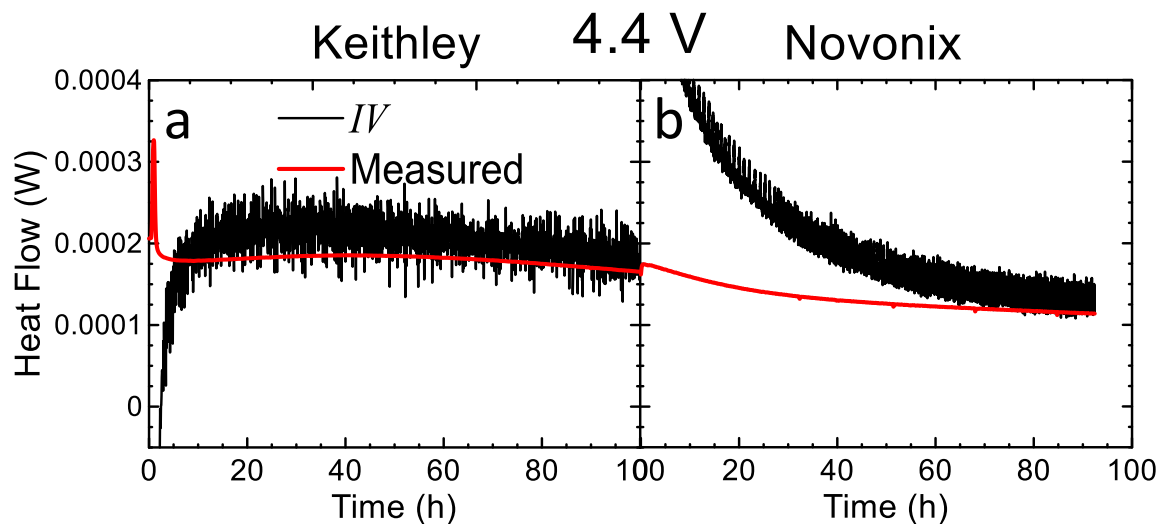


Figure 7.9: IV (black) and measured heat flow (red) from cells with coated NMC532 with an EC:EMC:DMC:MA-based electrolyte during a 4.4 V voltage-hold at 40°C on a) a Keithley 2602B source-meter and b) a Novonix charger.

Figure 7.10 shows a comparison between the cumulative parasitic energy, cumulative IV energy, and ΔH_e integrated in the same way as in Figure 7.7 for cells tested on both systems. The Novonix data was integrated after 70 hours into the hold when the decay in parasitic heat flow was closer to the decay in $I_p V$. Figures 7.10g and h show that the results for ΔH_e were consistent between cycling systems. The Novonix system could be used to increase the accuracy of data collected during low voltage-holds. As a side note, the cumulative E_{IV} and the cumulative E_p of cells with EC:EMC:DMC-based electrolytes decreased significantly less than other cells between the two ~100 hour 4.4 V holds, suggesting a thickening SEI caused by parasitic reaction products in MA-containing and FEC:TFEC-containing cells.

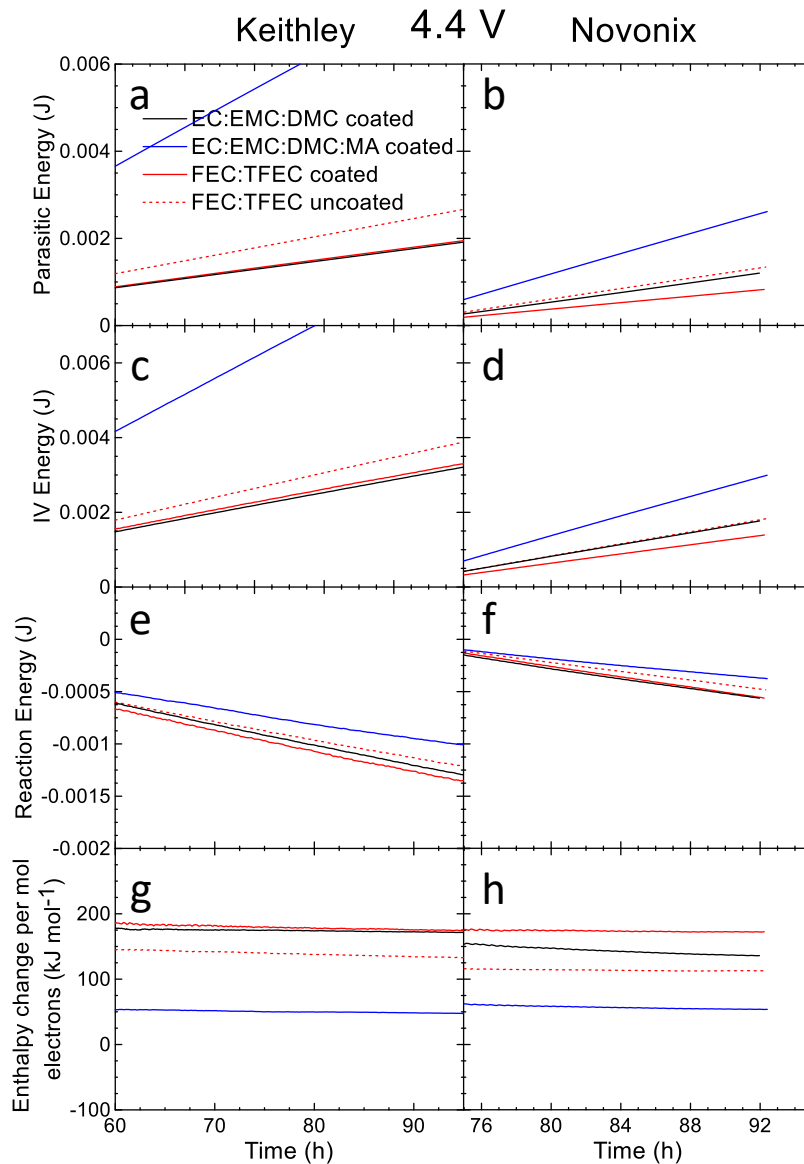


Figure 7.10: Integrated total parasitic energy (a,b), IV energy (c,d), reaction energy (e,f), and enthalpy change per mole of electrons (g,h) during 4.4 V holds on a Keithley 2602B source-meter (left column), and a Novonix system (right column) for some of the cell types used in this study.

This work aimed to act as a stepping stone into more quantitative, physical understandings of parasitic reactions in lithium-ion cells. Future studies using high precision current sources and combining computational and analytical techniques may be able to help elucidate the fate of electrolyte components in cells, and aid in diagnosing the

mechanisms behind cell death, impedance growth, and lithium loss. Additionally, combining experimental techniques with computational studies will further the understanding of how surface chemistry and electrode/coating-electrolyte interfaces affect parasitic reaction pathways.

7.7 CONCLUSIONS

A new technique to measure the rate and net enthalpy changes due to parasitic reactions in lithium-ion pouch cells was introduced. The technique employed high precision current sources to obtain the parasitic current during voltage-hold conditions, and isothermal microcalorimetry to measure the heat flow of the cell. The technique was capable of measuring the net enthalpy change per mole of electrons in the parasitic current (ΔH_e). Proof of concept experiments using stable, reversible shuttle molecules in uncoated SC-NMC532/AG pouch cells yielded net reaction enthalpies of $10 \pm 10 \text{ kJ mol}^{-1}$, close to the expected value of 0 kJ mol^{-1} .

Coated and uncoated SC-NMC532/AG pouch cells were filled with different solvent systems with 1.2 M LiPF_6 and were studied at 3.8 V, 4.2 V, 4.3 V, and 4.4 V. Most of the parasitic heat flow at all voltages was found to be due to Joule heating caused by the parasitic current. Cells with an EC:EMC:DMC (25:5:70 wt.) solvent showed an approximately constant ΔH_e from 4.2 V to 4.4 V in each cell type but an increase in reaction rate, suggesting the parasitic reaction pathways were unchanged, but the number of reactions increased with voltage. Cells containing EC:EMC:DMC:MA (15:3:42:40 wt.) as a solvent showed a decreasing ΔH_e as voltage increased, suggesting higher rates of reaction included additional reaction pathways influenced by the addition of MA. Cells with

FEC:TFEC as a solvent showed increasing ΔH_e with voltage, again suggesting different reaction pathways were present, with different rate dependencies on voltage. All reactions measured were net endothermic. Cells with coated NMC532 showed higher ΔH_e in each case, which suggest coated electrodes were preventing certain reactions. Results for ΔH_e were consistent between pair cells.

This novel study showed the importance of understanding the types of reactions in cells, as typical measurements of parasitic heat flow cannot account for differences in reaction enthalpies. This study also directly showed that different reactions in cells can have rates which change independently with voltage. Further studies combining this technique with simulations and compositional analysis of electrolyte, gas, and surface products are suggested.

CHAPTER 8 CONCLUSIONS

8.1 CONCLUSIONS

This thesis built on previous methods developed by Downie et al. and Krause et al. to measure the heat flow due to parasitic reactions in lithium-ion cells using isothermal microcalorimetry.^{150,155} The methods were capable of measuring the parasitic heat flow of machine-made pouch cells with high precision, *in-situ*, and non-destructively. The methods were used to probe reactions involved in the negative electrode SEI formation, and the effect of various additives, electrode materials, and electrolyte solvents on parasitic reactions. The methods for measuring parasitic heat flow were capable of predicting the relative long-term performance of cells in short experiments (~one month) when the same cell type was used with different electrolytes and yielded consistent values between duplicate cells. Compared to UHPC, *in-situ* gas, long-term cycling, EIS, and other common electrochemical testing methods, isothermal microcalorimetry measures the heat flow due to all types of parasitic reactions in a cell as they occur, instead of only some reactions (*in-situ* gas) or only measuring the averaged effects over time (UHPC, long-term cycling, EIS). However, more work is needed to determine what the exact reaction mechanisms are.

Chapter 4 introduced a new technique to probe the formation of the SEI due to additive and solvent reduction. The heat flow during formation was found to have unique features which corresponded to the reduction plateaus of EC and various additives (VC, FEC, PES, PBF) in voltage vs. capacity graphs. An expression for the magnitude of the heat flow during formation was developed and contained contributions from the entropy of the delithiating positive electrode during charge, the electrochemical overpotential of

reduction steps, and the enthalpy of reaction of any chemical steps in the reaction pathways. The measured heat flow was compared to a collaborator's DFT-proposed reaction pathways for PBF and PES. The method was found to underestimate the heat flow during formation of PBF by 20%. However, the proposed reaction pathway had an oversimplified second reduction step which likely contained an unaccounted for chemical reaction enthalpy. The heat flow of PES was found for four types of proposed pathways and was in agreement with two of the reaction types. The methods developed in Chapter 4 may be able to aid in the prediction of SEI formation pathways when coupled with DFT methods. However, the reliability of the technique relied heavily on the accuracy of DFT calculations.

Chapter 5 introduced the charge-discharge method of measuring the parasitic heat flow of lithium-ion cells during slow ($C/150$ to $C/200$) charge-discharge cycles. Averaging the measured heat flow between charge and discharge removed the reversible heat flow due to changes in the entropy of electrode materials. The approximate overpotential heat flow of the cell as a function of voltage was then determined and subtracted from the averaged heat flow. The resulting heat flow was due to parasitic reactions and could be compared between different cells. Chapter 6 showed further developments of the method by obtaining a more realistic overpotential using a linear fit, and then correcting the measured heat flow to the equilibrium voltage of the cell. Chapter 6 also introduced a method of approximating the entropic contribution to the heat flow. The entropic method of measuring the parasitic heat flow was used to differentiate the parasitic heat flows during charge and discharge. Unlike previous methods of measuring the parasitic heat flow, the methods developed here used minimal fitting of heat flow components and obtained the

parasitic heat flow as a continuous function of voltage. The methods were extremely consistent between pair cells.

In Chapter 5 the charge-discharge method was applied to study the effect of EC-free electrolytes with different additive combinations compared to EC-containing electrolytes. The parasitic heat flow was found to correlate well with UHPC results. EC-free electrolytes had lower parasitic heat flow than EC-containing electrolytes above 4.4 V, and showed significantly more protective SEI behavior above 4.4 V. Also presented in Chapter 5 was the effect of additive loadings on AG and NG negative electrodes. Parasitic heat flow was used in conjunction with *in-situ* gas and pressure measurements, UHPC results, and dV/dQ fitting to propose a mechanism for the observed poor performance of NG in the cells used.

In Chapter 6 the charge-discharge method was applied to cells with different NMC compositions (442, 532, 622) with different coatings (coating A: Al_2O_3 and coating B: a proprietary high-voltage coating). The results for parasitic heat flow suggested that 532 A, 532 B, and 622 B cells would have the longest lifetime if the magnitude of parasitic heat flow was an indicator of lifetime. However, 532 A and 532 B cells had the shortest lifetime in long-term studies. 622 A cells had high parasitic heat flow, large amounts of gas production, but similar cycling performance to 622 B cells which showed the least amount of gas and the lowest parasitic heat flow. The results of the study suggested that the magnitude of parasitic heat flow must be considered carefully and may not be an indicator of lifetime when different parasitic reactions occur between cells. Similarly, UHPC results may be misleading in cases where different parasitic reactions occur between cells. For example, shuttle reactions can increase charge endpoint capacity slippage, lower the CE,

and increase parasitic heat flow compared to other cells without having any negative impact on a cell.

Also discussed in Chapter 6 was a study investigating the impact of MA on the parasitic heat flow of different cells types (SC-NMC532/AG and NCA/SiO-graphite). MA was found to increase the charge endpoint capacity slippage, parasitic heat flow, and gas production in both cell types without significantly increasing the capacity fade. The results suggested that MA increased the amount electrolyte oxidation at the positive electrode, and at a lower voltage than in cells without MA. The effect of MA was mitigated slightly in UHPC, parasitic heat flow, and *in-situ* gas measurements by the addition of DTD in SC-NMC532/AG cells. Co-additives were not investigated in NCA/SiO-graphite cells. In NCA/SiO-graphite cells MA may have introduced different reaction mechanisms above 4.15 V which decreased the parasitic heat flow compared to cells without MA. The behaviour did not agree with *in-situ* gas or storage measurements, which suggested a higher rate of reactions in cells with MA above 4.1 V. The results suggested that when co-solvents are added into electrolytes the type of reactions can change, significantly influencing the parasitic heat flow. However, in both cell types the averaged parasitic heat flow of each cycle agreed with long-term performance and UHPC results.

Chapter 7 introduced a method which was motivated by the results of the studies in Chapter 6: A method of measuring parasitic heat flow that could obtain both the magnitude of parasitic heat flow and information about whether the parasitic reaction processes were changing between cell materials, electrolytes, or voltage ranges. By measuring the heat flow during a voltage-hold, the parasitic heat flow could be measured directly, along with the parasitic current. A proof-of-concept experiment using reversible shuttle molecules

found that the expected net enthalpy of reaction of 0 kJ mol^{-1} ($10 \pm 10 \text{ kJ mol}^{-1}$ and $0 \pm 3 \text{ kJ mol}^{-1}$ using two different stable reversible redox shuttle molecules) could be achieved using the theories outlined in this thesis. The net enthalpy change of all reactions in a cell per mole of electrons in the parasitic current (ΔH_e) was then found for coated and uncoated SC-NMC532/AG cells with different solvent systems. The method yielded consistent results for ΔH_e between pair cells. It was found that cells with coated positive electrodes yielded different net enthalpy changes than cells without coated electrodes. The results suggested that different reaction pathways occur in different cell types and could be influenced by the positive electrode chemistry, supporting the results of the studies in Chapter 6. Cells with an organic carbonate electrolyte had similar net enthalpy changes at all voltages, whereas cells with MA as a co-solvent or with fluorinated electrolytes had significantly different net enthalpy changes as the voltage changed. The study demonstrated that electrode surface composition, electrolyte, and cell voltage all play a role in determining what reactions occur in cells.

The methods developed in this thesis can be used to explore all aspects of cell chemistry on reactions occurring in lithium-ion cells (as well as other electrochemical storage devices). The methods rely on no external measurements or treatments of cell overpotential or entropy and yield very high precision, reliable results for the parasitic heat flow. The methods have been shown to be useful when combined with UHPC, gas measurements, pressure measurements, storage tests, EIS, and long-term cycling to elucidate failure mechanisms in certain cell types and electrolytes. Isothermal microcalorimetry is a unique, useful way to probe the parasitic reactions and should be

adapted broadly in the lithium-ion field as a short-term, predictive technique to achieve high energy density, long-lasting cells.

8.2 FUTURE WORK

The work in this thesis focused on developing methods to rank long-term lithium-ion cell performance (on the order of thousands of charge-discharge cycles or many years of operation) in a short experiment (~one month). When developing these methods, practical studies were done with the goal of developing insights into various materials and electrolytes and the effects of these cell components on parasitic reactions in cells. Therefore, two types of studies for future works will be discussed: studies focused on improving the performance and lifetime of lithium-ion cells, and studies to further develop the methods introduced in this thesis.

8.2.1 Future Studies to Improve Lithium-ion Cells

In Chapter 5, NG was found to have equivalent parasitic heat flow to AG when a sufficiently passivating SEI was present, but poor performance when smaller additive loadings were used. Although the full additive loading of PES211 was sufficient to prevent additional parasitic heat flow, cells showed increased impedance during long-term cycling. Additionally, PES211 was found by Liu et al. to have poor high-rate performance due to the thick SEI layers.¹¹⁶ The higher specific capacity of NG compared to AG could lead to higher energy density cells if additive combinations can be developed specifically for NG with different positive electrode materials. The properties of the SEI layers would ideally be flexible to allow for particle expansion of NG, passivating enough to prevent further reduction of solvent and shift loss, and low impedance to allow for high-rate operation.

Some studies have found that VC and FEC are useful for Si-based negative electrodes due to the seemingly flexible SEI formed by polymerization of VC.^{54,55,219,220} The effects of VC or FEC along with other co-additives in cells with NG negative electrodes should be investigated. Studies in this thesis found that the synergy between the electrolyte, both electrodes materials, and coatings play important roles in determining the performance of cells. Therefore, the studies should be expanded to explore pairing different positive electrodes with NG and various electrolyte combinations.

Chapter 6 investigated the impact of MA on cells. MA was found to increase the high-rate performance of cells but decrease the lifetime primarily due to electrolyte oxidation. Future studies should investigate additives which allow for low impedance SEI layers but are capable of mitigating electrolyte oxidation. Sulphur containing additives such as DTD used in Chapter 6, as well as fluorine-containing additives have been found to produce positive electrode SEI layers which may help in preventing electrolyte oxidation.^{90,101,107,114} Recently, LiPO_2F_2 has been reported as an additive in cells yielding lower impedance, higher rate capability and better lifetime while showing comparable UHPC performance at only 1% wt. compared to 2% VC.²²¹ However, the study showed that LiPO_2F_2 alone was not effective at mitigating negative impact of MA. Combining MA with an additive system containing LiPO_2F_2 and other co-additives (FEC, VC, DTD for example) should be studied in different cell types.

The combined optimization of lifetime, rate, and energy density using additives, electrode materials, coatings, solvents, salts, etc. poses a challenge: the number of combinations of materials and tests one can perform becomes unreasonable using only experimental methods. Therefore, computational methods should be used in conjunction

with experimental methods. Predicting the relative stability of bulk electrolytes, as well as the interfacial dynamics between electrolytes and various electrode, coating, or SEI surfaces could be studied and compared to experimental results. However, these studies would rely considerably on the current state of computational accuracy when dealing with large, complex systems. Computational studies are also limited by the current state of knowledge about these systems and the mechanisms/pathways occurring in parasitic reactions.

8.2.2 Development of parasitic heat flow methods

The charge-discharge method of measuring the parasitic heat flow was found to be a very informative, relatively short-term method of determining the degree of parasitic reactions occurring in cells. However, the method was only reliable when comparing the same cell type with small differences between additives or solvents. Future works utilizing the charge-discharge method should consider the differences between cells carefully. If different reactions may occur between cells, voltage-hold or other methods may be more useful.

As shown in Chapter 7, some types of reactions such as electrolyte oxidation, cross-talk, and transition metal dissolution can create a parasitic current. However, some reactions such as some reduction reactions and electrolyte-oxygen reactions, as well as non-electrochemical reactions occurring in the cell (thermal decomposition of salt), do not. Downie found that pouch cells with and without salt yielded identical heat flows at 40°C in open circuit, so the thermal decomposition of salt is assumed to be negligible here.¹⁵⁵ Most of the positive electrodes studied here should display little oxygen loss and transition metal dissolution from the positive electrode compared to other parasitic reactions.

Therefore, one may be able to further develop the voltage-hold method to differentiate between oxidation and reduction reactions using the mechanisms shown in Figures 7.5d and f, respectively. The following method is proposed and can be investigated and developed further in future studies.

If only oxidation (*ox*) and reduction (*red*) reactions are considered (and thus also cross-talk), the parasitic heat flow could be expressed by modifying Equation 2.18 to give:

$$\dot{q}_p = I_p V - k_{ox} \Delta H_{ox} - k_{red} \Delta H_{red}. \quad 8.1$$

The rate of oxidation reactions (k_{ox}) could be considered as proportional to the parasitic current during a voltage-hold, and the rate of reduction reactions (k_{red}) could be approximated using the amount of charge lost during the length of a voltage-hold (assuming one lithium atom is lost with each reduction reaction). A C/10 or C/20 cycle before and after each hold could be used to determine the capacity loss during the hold (Q_h) during the time of the hold (t_h) (and thus amount of lithium consumed by reduction reactions). Equation 8.1 could be expressed as

$$\dot{q}_p = I_p V - \frac{I_p}{F} \Delta H_{ox} - \frac{Q_h}{F t_h} \Delta H_{red}. \quad 8.2$$

Applying the integration techniques in Chapter 7, Equation 8.2 would become

$$E_p = Q_p V - \frac{Q_p}{F} \Delta H_{ox} - \frac{Q_h}{F} \Delta H_{red}. \quad 8.3$$

In the proposed experiment, Equation 8.3 would contain two unknowns, ΔH_{ox} and ΔH_{red} . However, over time the rates (and thus the capacities) of parasitic reactions would decrease. A subsequent hold at the same voltage would obtain different values of I_p , Q_p and Q_h , but should yield the same net enthalpy changes. The two different forms of Equation 8.3 from subsequent voltage-holds could be used to solve for the net enthalpies

changes. Additionally, multiple holds at the same voltage could be used to track trends in Q_p and Q_h to gain insight into which processes are changing at different rates. For example, if oxidation and reduction rates decay similarly, cross-talk processes may be dominant. If Q_p decays faster than Q_h , the positive electrode SEI may be thickening. The results could be used to understand at which electrodes different additives form SEI layers, or where different solvents and coatings have an impact.

Future studies using voltage-hold techniques should investigate the curious behaviour seen in NMC622A/NG cells in Chapter 5. Large amounts of parasitic heat flow and gas were observed, but performance did not correlate with the magnitude of parasitic heat flow compared to other cells. The cell types used in the study should be tested using the voltage-hold method at various voltages to determine the trends in parasitic reaction enthalpy with voltage, coating, and NMC composition. It may be that NMC622A/NG cells contained shuttle reactions which artificially raised the charge endpoint capacity slippage and parasitic heat flow. A net enthalpy change closer to 0 kJ mol^{-1} than other cells could indicate the existence of shuttle reactions in these cells.

Voltage-hold techniques would also benefit from studies using simplified electrolyte systems such as EC-free electrolytes. A study could be done to compare the parasitic reaction enthalpy of solvents containing only EMC with those containing EC and EMC, or blends of EC, EMC, and DMC. Experiments could compare reaction enthalpies between control cells (no additives) and cells with different types of additives (carbonates, fluorinated carbonates, phosphorous-containing, sulphur-containing, etc.) to investigate whether the SEI composition can affect the types of reactions happening in cells.

The work in this thesis showed that different parasitic reactions occurred in cells and depended on every component of the cells, as well as the cell voltage. The temperature dependence of reactions could also be studied. However, the methods developed here cannot elucidate the exact mechanisms behind the parasitic processes measured. Computational techniques such as DFT could be used to propose reaction pathways to compare theoretical reaction enthalpies with measured values. However, DFT methods are not exact and require careful consideration when comparing with experimental values. Compositional analysis techniques such as gas chromatography or x-ray photoelectron spectroscopy could be used to probe the gas, electrolyte, and SEI compositions of cells before and after voltage-holds to probe the products of the parasitic reactions measured. Trends in reaction products, SEI compositions, and SEI thicknesses could be compared to trends in reaction enthalpies to investigate changes in parasitic reactions between solvents, coatings, voltages, etc.

Isothermal microcalorimetry has been found throughout this work to provide insight into the failure mechanisms occurring inside lithium-ion cells. This section provided suggested future works that would allow for a better understanding of parasitic reactions in lithium-ion cells, and the possibility of decoupling reactions occurring at each electrode. The methods in this thesis should be developed further and would benefit from collaborative efforts to correlate electrochemical tests, chemical analyses, parasitic heat flow, and measurements of parasitic reaction enthalpies.

APPENDIX A: COPYRIGHT PERMISSIONS



Account Info

Help



Title: Journal of the Electrochemical Society
Article ID: 1945-7111
Publication: Publication 1
Publisher: CCC Reproduction
Date: Jan 1, 1948
 Copyright © 1948, CCC Reproduction

Logged in as:
 Stephen Glazier
 Account #:
 3000945447

LOGOUT

Order Completed

Thank you for your order.

This Agreement between Stephen Glazier ("You") and Electrochemical Society, Inc ("Electrochemical Society, Inc") consists of your order details and the terms and conditions provided by Electrochemical Society, Inc and Copyright Clearance Center.

License number	Reference confirmation email for license number
License date	Apr, 25 2018
Licensed content publisher	Electrochemical Society, Inc
Licensed content title	Journal of the Electrochemical Society
Licensed content date	Jan 1, 1948
Type of use	Thesis/Dissertation
Requestor type	Academic institution
Format	Print, Electronic
Portion	chart/graph/table/figure
Number of charts/graphs /tables/figures	3
The requesting person/organization	Stephen Glazier
Title or numeric reference of the portion(s)	Figure 2, Figure 3, Figure 7.
Title of the article or chapter the portion is from	Determination of the Voltage Dependence of Parasitic Heat Flow in Lithium Ion Cells Using Isothermal Microcalorimetry
Editor of portion(s)	N/A
Author of portion(s)	Downie, Laura
Volume of serial or monograph	12
Issue, if republishing an article from a serial	161
Page range of portion	A1782-A1787
Publication date of portion	August 19, 2014
Rights for	Main product
Duration of use	Life of current and all future editions
Creation of copies for the disabled	no
With minor editing privileges	no
For distribution to	Worldwide
In the following language(s)	Original language of publication
With incidental promotional use	no
Lifetime unit quantity of new product	Up to 499

Title	ISOTHERMAL MICROCALORIMETRY AS A TOOL TO PROBE PARASITIC REACTIONS IN LITHIUM-ION CELLS
Instructor name	Dr. Jeff Dahn
Institution name	Dalhousie University
Expected presentation date	Jul 2018
Requestor Location	Stephen Glazier 6310 Coburg Rd. Halifax, ON B3H 4R2 Canada Attn: Stephen Glazier
Billing Type	Invoice
Billing address	Stephen Glazier 6310 Coburg Rd. Halifax, ON B3H 4R2 Canada Attn: Stephen Glazier
Total (may include CCC user fee)	0.00 USD
Total	0.00 USD

CLOSE WINDOW

Copyright © 2018 [Copyright Clearance Center, Inc.](#) All Rights Reserved. [Privacy statement](#). [Terms and Conditions](#).
Comments? We would like to hear from you. E-mail us at customecare@copyright.com

BIBLIOGRAPHY

1. W. Li, B. Song, and A. Manthiram, *Chem. Soc. Rev.*, **46**, 3006–3059 (2017).
2. T. B. Reddy, *Linden's Handbook of Batteries, 4th Edition*, 4th ed., McGraw-Hill Education, New York, (2011).
3. K. Xu, *Chem. Rev.*, **104**, 4303–4418 (2004).
4. K. Xu, *Chem. Rev.*, **114**, 11503–11618 (2014).
5. D. P. Abraham, T. Spila, M. M. Furczon, and E. Sammann, *Electrochem. Solid-State Lett.*, **11**, A226–A228 (2008).
6. J. A. Gilbert, I. A. Shkrob, and D. P. Abraham, *J. Electrochem. Soc.*, **164**, A389–A399 (2017).
7. D. J. Xiong, L. D. Ellis, J. Li, H. Li, T. Hynes, J. P. Allen, J. Xia, D. S. Hall, I. G. Hill, and J. R. Dahn, *J. Electrochem. Soc.*, **164**, A3025–A3037 (2017).
8. R. Jung, M. Metzger, F. Maglia, C. Stinner, and H. A. Gasteiger, *J. Electrochem. Soc.*, **164**, A1361–A1377 (2017).
9. C. L. Campion, W. Li, and B. L. Lucht, *J. Electrochem. Soc.*, **152**, A2327–A2334 (2005).
10. Y. Talyosef, B. Markovsky, G. Salitra, D. Aurbach, H.-J. Kim, and S. Choi, *J. Power Sources*, **146**, 664–669 (2005).
11. D. Aurbach, B. Markovsky, Y. Talyossef, G. Salitra, H.-J. Kim, and S. Choi, *J. Power Sources*, **162**, 780–789 (2006).
12. K.J. Hyun, N. P. W. Pieczonka, and Y. Li, *ChemPhysChem*, **15**, 1940–1954 (2014).
13. L. Yang, B. Ravdel, and B. L. Lucht, *Electrochem. Solid-State Lett.*, **13**, A95–A97 (2010).
14. N. Nitta, F. Wu, J. T. Lee, and G. Yushin, *Mater. Today*, **18**, 252–264 (2015).
15. K. Mizushima, P. C. Jones, P. J. Wiseman, and J. B. Goodenough, *Mater. Res. Bull.*, **15**, 783–789 (1980).
16. Y. Wang, J. Jiang, and J. R. Dahn, *Electrochem. Commun.*, **9**, 2534–2540 (2007).
17. H. Wang, Y.-I. Jang, B. Huang, D. R. Sadoway, and Y.-M. Chiang, *J. Electrochem. Soc.*, **146**, 473–480 (1999).
18. N. Yabuuchi and T. Ohzuku, *J. Power Sources*, **119**, 171–174 (2003).
19. J. N. Reimers and J. R. Dahn, *J. Electrochem. Soc.*, **139**, 2091–2097 (1992).

20. H. Arai, S. Okada, Y. Sakurai, and J. Yamaki, *Solid State Ion.*, **109**, 295–302 (1998).
21. L. Ma, M. Nie, J. Xia, and J. R. Dahn, *J. Power Sources*, **327**, 145–150 (2016).
22. S.-M. Bak, E. Hu, Y. Zhou, X. Yu, S. D. Senanayake, S.-J. Cho, K.-B. Kim, K. Y. Chung, X.-Q. Yang, and K.-W. Nam, *ACS Appl. Mater. Interfaces*, **6**, 22594–22601 (2014).
23. A. Rougier, P. Gravereau, and C. Delmas, *J. Electrochem. Soc.*, **143**, 1168–1175 (1996).
24. X. Zeng, C. Zhan, J. Lu, and K. Amine, *Chem*, **In Press** (2018).
25. H.-J. Noh, S. Youn, C. S. Yoon, and Y.-K. Sun, *J. Power Sources*, **233**, 121–130 (2013).
26. P. Kalyani and N. Kalaiselvi, *Sci. Technol. Adv. Mater.*, **6**, 689–703 (2005).
27. M. Gu, I. Belharouak, J. Zheng, H. Wu, J. Xiao, A. Genc, K. Amine, S. Thevuthasan, D. R. Baer, J.-G. Zhang, N. D. Browning, J. Liu, and C. Wang, *ACS Nano*, **7**, 760–767 (2013).
28. H. Zheng, Q. Sun, G. Liu, X. Song, and V. S. Battaglia, *J. Power Sources*, **207**, 134–140 (2012).
29. Exciting Developments In NMC 811 Lithium Battery Technology, <https://cleantechnica.com/2018/03/04/exciting-developments-nmc-811-lithium-battery-technology/> (accessed April 18, 2018)
30. C. H. Chen, J. Liu, M. E. Stoll, G. Henriksen, D. R. Vissers, and K. Amine, *J. Power Sources*, **128**, 278–285 (2004).
31. J. Duan, G. Hu, Y. Cao, C. Tan, C. Wu, K. Du, and Z. Peng, *J. Power Sources*, **326**, 322–330 (2016).
32. K. Meng, Z. Wang, H. Guo, and X. Li, *Electrochimica Acta*, **234**, 99–107 (2017).
33. I. Bloom, S. A. Jones, V. S. Battaglia, G. L. Henriksen, J. P. Christophersen, R. B. Wright, C. D. Ho, J. R. Belt, and C. G. Motloch, *J. Power Sources*, **124**, 538–550 (2003).
34. S.-T. Myung, K. Izumi, S. Komaba, Y.-K. Sun, H. Yashiro, and N. Kumagai, *Chem. Mater.*, **17**, 3695–3704 (2005).
35. R. S. Arumugam, L. Ma, J. Li, X. Xia, J. M. Paulsen, and J. R. Dahn, *J. Electrochem. Soc.*, **163**, A2531–A2538 (2016).
36. A. Zhou, Y. Lu, Q. Wang, J. Xu, W. Wang, X. Dai, and J. Li, *J. Power Sources*, **346**, 24–30 (2017).

37. P. Mohan and G. Paruthimal Kalaignan, *Ceram. Int.*, **40**, 1415–1421 (2014).
38. K. J. Nelson, D. W. Abarbanel, J. Xia, Z. Lu, and J. R. Dahn, *J. Electrochem. Soc.*, **163**, A272–A280 (2016).
39. W. Xu, J. Wang, F. Ding, X. Chen, E. Nasybulin, Y. Zhang, and J.-G. Zhang, *Energy Environ. Sci.*, **7**, 513–537 (2014).
40. D. Wang, W. Zhang, W. Zheng, X. Cui, T. Rojo, and Q. Zhang, *Adv. Sci.*, **4**, n/a-n/a (2017).
41. G.-N. Zhu, Y.-G. Wang, and Y.-Y. Xia, *Energy Environ. Sci.*, **5**, 6652–6667 (2012).
42. N. A. Kaskhedikar and J. Maier, *Adv. Mater.*, **21**, 2664–2680 (2009).
43. J. R. Dahn, R. Fong, and M. J. Spoon, *Phys. Rev. B*, **42**, 6424–6432 (1990).
44. K. G. Gallagher, D. W. Dees, A. N. Jansen, D. P. Abraham, and S.-H. Kang, *J. Electrochem. Soc.*, **159**, A2029–A2037 (2012).
45. R. Fong, U. von Sacken, and J. R. Dahn, *J. Electrochem. Soc.*, **137**, 2009–2013 (1990).
46. D. Aurbach, Y. Ein-Eli, B. Markovsky, A. Zaban, S. Luski, Y. Carmeli, and H. Yamin, *J. Electrochem. Soc.*, **142**, 2882–2890 (1995).
47. P. Ganesh, P. R. C. Kent, and D. Jiang, *J. Phys. Chem. C*, **116**, 24476–24481 (2012).
48. Y.-S. Park, T.-W. Lee, M.-S. Shin, S.-H. Lim, and S.-M. Lee, *J. Electrochem. Soc.*, **163**, A3078–A3086 (2016).
49. H. Nakamura, H. Komatsu, and M. Yoshio, *J. Power Sources*, **62**, 219–222 (1996).
50. W. . Weydanz, M. Wohlfahrt-Mehrens, and R. . Huggins, *J. Power Sources*, **81–82**, 237–242 (1999).
51. J. P. Maranchi, A. F. Hepp, and P. N. Kumta, *Electrochem. Solid-State Lett.*, **6**, A198–A201 (2003).
52. M. N. Obrovac and L. Christensen, *Electrochem. Solid-State Lett.*, **7**, A93–A96 (2004).
53. A. Casimir, H. Zhang, O. Ogoke, J. C. Amine, J. Lu, and G. Wu, *Nano Energy*, **27**, 359–376 (2016).
54. T. Jaumann, J. Balach, U. Langklotz, V. Sauchuk, M. Fritsch, A. Michaelis, V. Teltevsij, D. Mikhailova, S. Oswald, M. Klose, G. Stephani, R. Hauser, J. Eckert, and L. Giebeler, *Energy Storage Mater.*, **6**, 26–35 (2017).
55. L. J. Krause, T. Brandt, V. L. Chevrier, and L. D. Jensen, *J. Electrochem. Soc.*, **164**, A2277–A2282 (2017).

56. Y.-S. Hu, R. Demir-Cakan, M.-M. Titirici, J.-O. Müller, R. Schlögl, M. Antonietti, and J. Maier, *Angew. Chem. Int. Ed.*, **47**, 1645–1649 (2008).
57. M. Miyachi, H. Yamamoto, H. Kawai, T. Ohta, and M. Shirakata, *J. Electrochem. Soc.*, **152**, A2089–A2091 (2005).
58. T. Zhang, J. Gao, H. P. Zhang, L. C. Yang, Y. P. Wu, and H. Q. Wu, *Electrochem. Commun.*, **9**, 886–890 (2007).
59. A. J. Louli, J. Li, S. Trussler, C. R. Fell, and J. R. Dahn, *J. Electrochem. Soc.*, **164**, A2689–A2696 (2017).
60. B. Ravdel, K. M. Abraham, R. Gitzendanner, J. DiCarlo, B. Lucht, and C. Campion, *J. Power Sources*, **119–121**, 805–810 (2003).
61. A. Guéguen, D. Streich, M. He, M. Mendez, F. F. Chesneau, P. Novák, and E. J. Berg, *J. Electrochem. Soc.*, **163**, A1095–A1100 (2016).
62. T. Doi, Y. Shimizu, M. Hashinokuchi, and M. Inaba, *J. Electrochem. Soc.*, **163**, A2211–A2215 (2016).
63. L. D. Ellis, I. G. Hill, K. L. Gering, and J. R. Dahn, *J. Electrochem. Soc.*, **164**, A2426–A2433 (2017).
64. C. Täubert, M. Fleischhammer, M. Wohlfahrt-Mehrens, U. Wietelmann, and T. Buhrmester, *J. Electrochem. Soc.*, **157**, A721–A728 (2010).
65. K. Xu, S. S. Zhang, U. Lee, J. L. Allen, and T. R. Jow, *J. Power Sources*, **146**, 79–85 (2005).
66. Z. Chen, W. Q. Lu, J. Liu, and K. Amine, *Electrochimica Acta*, **51**, 3322–3326 (2006).
67. M. C. Smart, B. V. Ratnakumar, and S. Surampudi, *J. Electrochem. Soc.*, **149**, A361–A370 (2002).
68. E. R. Logan, E. M. Tonita, K. L. Gering, J. Li, X. Ma, L. Y. Beaulieu, and J. R. Dahn, *J. Electrochem. Soc.*, **165**, A21–A30 (2018).
69. M. Ohtake, N. Nanbu, M. Takehara, M. Ue, and Y. Sasaki, *Meet. Abstr.*, **MA2008-02**, 175–175 (2008).
70. Fluoroethylene carbonate - FEC - H61502 - Alfa Aesar, <https://www.alfa.com/en/catalog/H61502/>. (accessed March 20, 2018)
71. Bis(2,2,2-trifluoroethyl) Carbonate 1513-87-7 | Tokyo Chemical Industry Co., Ltd., <http://www.tcichemicals.com/eshop/en/au/commodity/B4703/>. (accessed March 20, 2018)
72. D. Aurbach, M. L. Daroux, P. W. Faguy, and E. Yeager, *J. Electrochem. Soc.*, **134**, 1611–1620 (1987).

73. M. C. Smart, B. V. Ratnakumar, and S. Surampudi, *J. Electrochem. Soc.*, **146**, 486–492 (1999).
74. X. Ma, J. Li, S. L. Glazier, L. Ma, K. L. Gering, and J. R. Dahn, *Electrochimica Acta*, **270**, 215–223 (2018).
75. J. Li, H. Li, X. Ma, W. Stone, S. Glazier, E. Logan, E. M. Tonita, K. L. Gering, and J. R. Dahn, *J. Electrochem. Soc.*, **165**, A1027–A1037 (2018).
76. S. L. Glazier, J. Li, X. Ma, L. D. Ellis, J. P. Allen, K. L. Gering, and J. R. Dahn, *J. Electrochem. Soc.*, **165**, A867–A875 (2018).
77. D. Aurbach, Y. Ein-Ely, and A. Zaban, *J. Electrochem. Soc.*, **141**, L1–L3 (1994).
78. M. Egashira, H. Takahashi, S. Okada, and J. Yamaki, *J. Power Sources*, **92**, 267–271 (2001).
79. K. Xu and C. A. Angell, *J. Electrochem. Soc.*, **145**, L70–L72 (1998).
80. L. Hu, Z. Zhang, and K. Amine, *Electrochem. Commun.*, **35**, 76–79 (2013).
81. Z. Zhang, L. Hu, H. Wu, W. Weng, M. Koh, P. C. Redfern, L. A. Curtiss, and K. Amine, *Energy Environ. Sci.*, **6**, 1806–1810 (2013).
82. S. Komaba, T. Ishikawa, N. Yabuuchi, W. Murata, A. Ito, and Y. Ohsawa, *ACS Appl. Mater. Interfaces*, **3**, 4165–4168 (2011).
83. A. L. Michan, B. S. Parimalam, M. Leskes, R. N. Kerber, T. Yoon, C. P. Grey, and B. L. Lucht, *Chem. Mater.*, **28**, 8149–8159 (2016).
84. M. M. Islam and A. C. T. van Duin, *J. Phys. Chem. C*, **120**, 27128–27134 (2016).
85. J. L. Tebbe, T. F. Fuerst, and C. B. Musgrave, *ACS Appl. Mater. Interfaces*, **8**, 26664–26674 (2016).
86. G. V. Zhuang, K. Xu, H. Yang, T. R. Jow, and P. N. Ross, *J. Phys. Chem. B*, **109**, 17567–17573 (2005).
87. D. Aurbach, K. Gamolsky, B. Markovsky, Y. Gofer, M. Schmidt, and U. Heider, *Electrochimica Acta*, **47**, 1423–1439 (2002).
88. A. Chagnes and J. Swiatowska, (2012) <http://www.intechopen.com/books/lithium-ion-batteries-new-developments/electrolyte-and-solid-electrolyte-interphase-layer-in-lithium-ion-batteries>.
89. D. Aurbach, K. Gamolsky, B. Markovsky, G. Salitra, Y. Gofer, U. Heider, R. Oesten, and M. Schmidt, *J. Electrochem. Soc.*, **147**, 1322–1331 (2000).

90. D. Aurbach, B. Markovsky, G. Salitra, E. Markevich, Y. Talyossef, M. Koltypin, L. Nazar, B. Ellis, and D. Kovacheva, *J. Power Sources*, **165**, 491–499 (2007).
91. D. Aurbach, B. Markovsky, A. Rodkin, M. Cojocar, E. Levi, and H.-J. Kim, *Electrochimica Acta*, **47**, 1899–1911 (2002).
92. M. Nie and B. L. Lucht, *J. Electrochem. Soc.*, **161**, A1001–A1006 (2014).
93. T. Joshi, K. Eom, G. Yushin, and T. F. Fuller, *J. Electrochem. Soc.*, **161**, A1915–A1921 (2014).
94. S. Fang, D. Jackson, M. L. Dreibelbis, T. F. Kuech, and R. J. Hamers, *J. Power Sources*, **373**, 184–192 (2018).
95. N. N. Sinha, J. C. Burns, and J. R. Dahn, *J. Electrochem. Soc.*, **160**, A709–A714 (2013).
96. S. S. Zhang, *J. Power Sources*, **162**, 1379–1394 (2006).
97. L. Yang and B. L. Lucht, *Electrochem. Solid-State Lett.*, **12**, A229–A231 (2009).
98. J. Xia, L. Ma, C. P. Aiken, K. J. Nelson, L. P. Chen, and J. R. Dahn, *J. Electrochem. Soc.*, **161**, A1634–A1641 (2014).
99. D. Xiong, J. C. Burns, A. J. Smith, N. Sinha, and J. R. Dahn, *J. Electrochem. Soc.*, **158**, A1431–A1435 (2011).
100. J. C. Burns, N. N. Sinha, D. J. Coyle, G. Jain, C. M. VanElzen, W. M. Lamanna, A. Xiao, E. Scott, J. P. Gardner, and J. R. Dahn, *J. Electrochem. Soc.*, **159**, A85–A90 (2011).
101. E. Markevich, G. Salitra, and D. Aurbach, *ACS Energy Lett.*, **2**, 1337–1345 (2017).
102. E. Markevich, G. Salitra, K. Fridman, R. Sharabi, G. Gershinsky, A. Garsuch, G. Semrau, M. A. Schmidt, and D. Aurbach, *Langmuir*, **30**, 7414–7424 (2014).
103. A. Abouimrane, I. Belharouak, and K. Amine, *Electrochem. Commun.*, **11**, 1073–1076 (2009).
104. Z. Ding, X. Li, T. Wei, Z. Yin, and X. Li, *Electrochimica Acta*, **196**, 622–628 (2016).
105. T. Huang, M. Wu, W. Wang, Y. Pan, and G. Fang, *J. Power Sources*, **262**, 303–309 (2014).
106. X. Li, Z. Yin, X. Li, and C. Wang, *Ionics*, **20**, 795–801 (2013).
107. L. Madec, J. Xia, R. Petibon, K. J. Nelson, J.-P. Sun, I. G. Hill, and J. R. Dahn, *J. Phys. Chem. C*, **118**, 29608–29622 (2014).
108. J. Xia, N. N. Sinha, L. P. Chen, and J. R. Dahn, *J. Electrochem. Soc.*, **161**, A264–A274 (2014).

109. J. Xia, K. J. Nelson, Z. Lu, and J. R. Dahn, *J. Power Sources*, **329**, 387–397 (2016).
110. D. Y. Wang, N. N. Sinha, R. Petibon, J. C. Burns, and J. R. Dahn, *J. Power Sources*, **251**, 311–318 (2014).
111. D. Y. Wang, J. Xia, L. Ma, K. J. Nelson, J. E. Harlow, D. Xiong, L. E. Downie, R. Petibon, J. C. Burns, A. Xiao, W. M. Lamanna, and J. R. Dahn, *J. Electrochem. Soc.*, **161**, A1818–A1827 (2014).
112. L. Ma, J. Self, M. Nie, S. Glazier, D. Y. Wang, Y.-S. Lin, and J. R. Dahn, *J. Power Sources*, **299**, 130–138 (2015).
113. L. Ma, J. Xia, and J. R. Dahn, *J. Electrochem. Soc.*, **162**, A1170–A1174 (2015).
114. L. Madec, L. Ma, K. J. Nelson, R. Petibon, J.-P. Sun, I. G. Hill, and J. R. Dahn, *J. Electrochem. Soc.*, **163**, A1001–A1009 (2016).
115. K. J. Nelson, J. Xia, and J. R. Dahn, *J. Electrochem. Soc.*, **161**, A1884–A1889 (2014).
116. Q. Q. Liu, R. Petibon, C. Y. Du, and J. R. Dahn, *J. Electrochem. Soc.*, **164**, A1173–A1183 (2017).
117. T. Achiha, T. Nakajima, Y. Ohzawa, M. Koh, A. Yamauchi, M. Kagawa, and H. Aoyama, *J. Electrochem. Soc.*, **157**, A707–A712 (2010).
118. T. Kawamura, A. Kimura, M. Egashira, S. Okada, and J.-I. Yamaki, *J. Power Sources*, **104**, 260–264 (2002).
119. D. Rehnlund, F. Lindgren, S. Böhme, T. Nordh, Y. Zou, J. Pettersson, U. Bexell, M. Boman, K. Edström, and L. Nyholm, *Energy Environ. Sci.*, **10**, 1350–1357 (2017).
120. J. Xia, Z. Liu, D. Li, Z. Lu, and S. Zhou, *Rare Met.*, **30**, 48–51 (2011).
121. A. J. Smith, J. C. Burns, D. Xiong, and J. R. Dahn, *J. Electrochem. Soc.*, **158**, A1136–A1142 (2011).
122. A. Jarry, S. Gottis, Y.-S. Yu, J. Roque-Rosell, C. Kim, J. Cabana, J. Kerr, and R. Kostecki, *J. Am. Chem. Soc.*, **137**, 3533–3539 (2015).
123. M. He, L. Boulet-Roblin, P. Borel, C. Tessier, P. Novák, C. Villevieille, and E. J. Berg, *J. Electrochem. Soc.*, **163**, A83–A89 (2016).
124. A. Urban, D.-H. Seo, and G. Ceder, *Npj Comput. Mater.*, **2**, 16002 (2016).
125. E. Jonsson and P. Johansson, *Phys. Chem. Chem. Phys.*, **17**, 3697–3703 (2015).
126. N. Shao, X.-G. Sun, S. Dai, and D. Jiang, *J. Phys. Chem. B*, **115**, 12120–12125 (2011).
127. O. Borodin, W. Behl, and T. R. Jow, *J. Phys. Chem. C*, **117**, 8661–8682 (2013).

128. L. Cheng, R. S. Assary, X. Qu, A. Jain, S. P. Ong, N. N. Rajput, K. Persson, and L. A. Curtiss, *J. Phys. Chem. Lett.*, **6**, 283–291 (2015).
129. S. P. Ong, O. Andreussi, Y. Wu, N. Marzari, and G. Ceder, *Chem. Mater.*, **23**, 2979–2986 (2011).
130. N. N. Sinha, A. J. Smith, J. C. Burns, G. Jain, K. W. Eberman, E. Scott, J. P. Gardner, and J. R. Dahn, *J. Electrochem. Soc.*, **158**, A1194–A1201 (2011).
131. A. von Cresce and K. Xu, *Electrochem. Solid-State Lett.*, **14**, A154–A156 (2011).
132. H. M. Dahn, A. J. Smith, J. C. Burns, D. A. Stevens, and J. R. Dahn, *J. Electrochem. Soc.*, **159**, A1405–A1409 (2012).
133. J. Xu, R. D. Deshpande, J. Pan, Y.-T. Cheng, and V. S. Battaglia, *J. Electrochem. Soc.*, **162**, A2026–A2035 (2015).
134. A. J. Smith and J. R. Dahn, *J. Electrochem. Soc.*, **159**, A290–A293 (2012).
135. A. J. Smith, H. M. Dahn, J. C. Burns, and J. R. Dahn, *J. Electrochem. Soc.*, **159**, A705–A710 (2012).
136. C. Buhrmester, J. Chen, L. Moshurchak, J. Jiang, R. L. Wang, and J. R. Dahn, *J. Electrochem. Soc.*, **152**, A2390–A2399 (2005).
137. L. Moshurchak, PhD thesis, Dalhousie University (Canada), Canada (2009) <https://search.proquest.com/pqdtglobal/docview/305071554/abstract/13A13D4E03024BECPQ/1>.
138. C. Buhrmester, L. Moshurchak, R. L. Wang, and J. R. Dahn, *J. Electrochem. Soc.*, **153**, A288–A294 (2006).
139. L. M. Moshuchak, M. Bulinski, W. M. Lamanna, R. L. Wang, and J. R. Dahn, *Electrochem. Commun.*, **9**, 1497–1501 (2007).
140. Z. Zhang, L. Zhang, J. A. Schlueter, P. C. Redfern, L. Curtiss, and K. Amine, *J. Power Sources*, **195**, 4957–4962 (2010).
141. A. J. Smith, J. C. Burns, S. Trussler, and J. R. Dahn, *J. Electrochem. Soc.*, **157**, A196–A202 (2010).
142. J. C. Burns, A. Kassam, N. N. Sinha, L. E. Downie, L. Solnickova, B. M. Way, and J. R. Dahn, *J. Electrochem. Soc.*, **160**, A1451–A1456 (2013).
143. J. E. Harlow, D. A. Stevens, J. C. Burns, J. N. Reimers, and J. R. Dahn, *J. Electrochem. Soc.*, **160**, A2306–A2310 (2013).
144. T. C. Bach, S. F. Schuster, E. Fleder, J. Müller, M. J. Brand, H. Lorrman, A. Jossen, and G. Sxntl, *J. Energy Storage*, **5**, 212–223 (2016).

145. M. Broussely, P. Biensan, F. Bonhomme, P. Blanchard, S. Herreyre, K. Nechev, and R. J. Staniewicz, *J. Power Sources*, **146**, 90–96 (2005).
146. K. J. Nelson, G. L. d'Eon, A. T. B. Wright, L. Ma, J. Xia, and J. R. Dahn, *J. Electrochem. Soc.*, **162**, A1046–A1054 (2015).
147. D. W. Abarbanel, K. J. Nelson, and J. R. Dahn, *J. Electrochem. Soc.*, **163**, A522–A529 (2016).
148. W. Dreyer, J. Jamnik, C. Guhlke, R. Huth, J. Moškon, and M. Gabersček, *Nat. Mater.*, **9**, 448–453 (2010).
149. R. Chandrasekaran, *J. Power Sources*, **262**, 501–513 (2014).
150. L. J. Krause, L. D. Jensen, and J. R. Dahn, *J. Electrochem. Soc.*, **159**, A937–A943 (2012).
151. L. J. Krause, L. D. Jensen, and V. L. Chevrier, *J. Electrochem. Soc.*, **164**, A889–A896 (2017).
152. L. E. Downie, K. J. Nelson, R. Petibon, V. L. Chevrier, and J. R. Dahn, *ECS Electrochem. Lett.*, **2**, A106–A109 (2013).
153. L. E. Downie and J. R. Dahn, *J. Electrochem. Soc.*, **161**, A1782–A1787 (2014).
154. L. E. Downie, S. R. Hyatt, A. T. B. Wright, and J. R. Dahn, *J. Phys. Chem. C*, **118**, 29533–29541 (2014).
155. L. Downie, PhD thesis, Dalhousie University (2015) <http://DalSpace.library.dal.ca/handle/10222/58734>.
156. K. E. Thomas and J. Newman, *J. Electrochem. Soc.*, **150**, A176–A192 (2003).
157. J. R. Dahn, W. R. McKinnon, J. J. Murray, R. R. Haering, R. S. McMillan, and A. H. Rivers-Bowerman, *Phys. Rev. B*, **32**, 3316–3318 (1985).
158. J. R. Dahn, W. R. McKinnon, and S. T. Coleman, *Phys. Rev. B*, **31**, 484–489 (1985).
159. J. P. Schmidt, A. Weber, and E. Ivers-Tiffée, *Electrochimica Acta*, **137**, 311–319 (2014).
160. S. A. Hallaj, R. Venkatachalapathy, J. Prakash, and J. R. Selman, *J. Electrochem. Soc.*, **147**, 2432–2436 (2000).
161. Y. Reynier, R. Yazami, and B. Fultz, *J. Power Sources*, **119–121**, 850–855 (2003).
162. Y. F. Reynier, R. Yazami, and B. Fultz, *J. Electrochem. Soc.*, **151**, A422–A426 (2004).

163. W. Lu, I. Belharouak, S. H. Park, Y. K. Sun, and K. Amine, *Electrochimica Acta*, **52**, 5837–5842 (2007).
164. H. Bang, H. Yang, Y. K. Sun, and J. Prakash, *J. Electrochem. Soc.*, **152**, A421–A428 (2005).
165. H. Yang and J. Prakash, *J. Electrochem. Soc.*, **151**, A1222–A1229 (2004).
166. Y. Saito, K. Kanari, and K. Takano, *J. Power Sources*, **68**, 451–454 (1997).
167. W. Lu, I. Belharouak, J. Liu, and K. Amine, *J. Electrochem. Soc.*, **154**, A114–A118 (2007).
168. Y. Kobayashi, H. Miyashiro, K. Kumai, K. Takei, T. Iwahori, and I. Uchida, *J. Electrochem. Soc.*, **149**, A978–A982 (2002).
169. W. Lu and J. Prakash, *J. Electrochem. Soc.*, **150**, A262–A266 (2003).
170. A. Q. Yasir, L. Tomi, K. Juha, J. Kirsi, V. Kai, S. Lasse, and P. K. Mervi, *Int. J. Energy Res.*, **38**, 1424–1437 (2014).
171. Y. Saito, M. Shikano, and H. Kobayashi, *16th Int. Meet. Lithium Batter. IMLB*, **244**, 294–299 (2013).
172. S. J. Bazinski and X. Wang, *J. Electrochem. Soc.*, **161**, A168–A175 (2014).
173. L. E. Downie, S. R. Hyatt, and J. R. Dahn, *J. Electrochem. Soc.*, **163**, A35–A42 (2016).
174. Keithley 2600B Sourcemeter, <http://www.tek.com/keithley-source-measure-units/smu-2600b-series-sourcemeter>. (accessed April 6, 2018)
175. Maccor 4000 Series, <http://www.maccor.com/Products/Series4000.aspx>. (accessed April 6, 2018)
176. Battery Grading Operation in BTS 3000, <http://newarebattery.com/index.php/battery-grading-operation-in-bts3000>. (accessed April 6, 2018)
177. Mass, Weight, Density or Specific Gravity of Water at Various Temperatures, https://www.simetric.co.uk/si_water.htm. (accessed June 5, 2018)
178. C. P. Aiken, J. Xia, D. Y. Wang, D. A. Stevens, S. Trussler, and J. R. Dahn, *J. Electrochem. Soc.*, **161**, A1548–A1554 (2014).
179. C. H. Chen, J. Liu, and K. Amine, *J. Power Sources*, **96**, 321–328 (2001).
180. M. Kerlau, M. Marcinek, V. Srinivasan, and R. M. Kostecki, *Electrochimica Acta*, **52**, 5422–5429 (2007).

181. W. Uwe, K. Kerstin, L. Frank, and K. Michael, *Energy Technol.*, **4**, 1620–1630 (2016).
182. K. Nelson, PhD thesis, Dalhousie University (2017) <https://DalSpace.library.dal.ca/handle/10222/73493>.
183. TA Instruments, TAM Basic Theory And Applications Training Course, (2007).
184. TA Instruments, Microcalorimetry Brochure (2007).
185. Cryogenic Wire Specifications Lake Shore Cryotronics Inc, <https://www.lakeshore.com/products/cryogenic-accessories/wire/pages/Specifications.aspx>. (accessed April 6, 2018)
186. L. D. Ellis, J. P. Allen, L. M. Thompson, J. E. Harlow, W. J. Stone, I. G. Hill, and J. R. Dahn, *J. Electrochem. Soc.*, **164**, A3518–A3528 (2017).
187. D. S. Hall, M. Nie, L. D. Ellis, S. L. Glazier, S. Hyatt, R. Petibon, A. Xiao, W. M. Lamanna, K. Smith, I. G. Hill, and J. R. Dahn, *J. Electrochem. Soc.*, **163**, A773–A780 (2016).
188. J. Self, D. S. Hall, L. Madec, and J. R. Dahn, *J. Power Sources*, **298**, 369–378 (2015).
189. D. S. Hall, S. L. Glazier, and J. R. Dahn, *Phys. Chem. Chem. Phys.*, **18**, 11383–11390 (2016).
190. K. Xu, Y. Lam, S. S. Zhang, T. R. Jow, and T. B. Curtis, *J. Phys. Chem. C*, **111**, 7411–7421 (2007).
191. X. Zhao, Q.-C. Zhuang, S.-D. Xu, Y.-X. Xu, Y.-L. Shi, and X.-X. Zhang, *Int J Electrochem Sci*, **10**, 2515–2534 (2015).
192. J. Self, MSc thesis, Dalhousie University, Halifax, NS, Canada (2015) <http://dalspace.library.dal.ca/handle/10222/60315>.
193. M. Nie, J. Xia, and J. R. Dahn, *J. Electrochem. Soc.*, **162**, A1186–A1195 (2015).
194. M. Nie, J. Xia, L. Ma, and J. R. Dahn, *J. Electrochem. Soc.*, **162**, A2066–A2074 (2015).
195. J. Xia, L. Ma, K. J. Nelson, M. Nie, Z. Lu, and J. R. Dahn, *J. Electrochem. Soc.*, **163**, A2399–A2406 (2016).
196. S. L. Glazier, R. Petibon, J. Xia, and J. R. Dahn, *J. Electrochem. Soc.*, **164**, A567–A573 (2017).
197. R. Petibon, J. Xia, L. Ma, M. K. G. Bauer, K. J. Nelson, and J. R. Dahn, *J. Electrochem. Soc.*, **163**, A2571–A2578 (2016).

198. J. Xia, M. Nie, L. Ma, and J. R. Dahn, *J. Power Sources*, **306**, 233–240 (2016).
199. L. Ma, D. Y. Wang, L. E. Downie, J. Xia, K. J. Nelson, N. N. Sinha, and J. R. Dahn, *J. Electrochem. Soc.*, **161**, A1261–A1265 (2014).
200. L. Ma, S. L. Glazier, R. Petibon, J. Xia, J. M. Peters, Q. Liu, J. Allen, R. N. C. Doig, and J. R. Dahn, *J. Electrochem. Soc.*, **164**, A5008–A5018 (2017).
201. E. R. Logan, E. M. Tonita, K. L. Gering, L. Ma, M. K. G. Bauer, J. Li, L. Y. Beaulieu, and J. R. Dahn, *J. Electrochem. Soc.*, **165**, A705–A716 (2018).
202. M. Yoshio, H. Wang, and K. Fukuda, *Angew. Chem. Int. Ed.*, **42**, 4203–4206 (2003).
203. M. Yoshio, H. Wang, K. Fukuda, Y. Hara, and Y. Adachi, *J. Electrochem. Soc.*, **147**, 1245–1250 (2000).
204. C. Lee, Y.-J. Han, Y. D. Seo, K. Nakabayashi, J. Miyawaki, R. Santamaría, R. Menéndez, S.-H. Yoon, and J. Jang, *Carbon*, **103**, 28–35 (2016).
205. J. Li, H. Li, A. Cameron, S. Glazier, Q. Liu, and J. R. Dahn, *J. Electrochem. Soc.*, **164**, A2756–A2766 (2017).
206. J. Li, A. R. Cameron, H. Li, S. Glazier, D. Xiong, M. Chatzidakis, J. Allen, G. A. Botton, and J. R. Dahn, *J. Electrochem. Soc.*, **164**, A1534–A1544 (2017).
207. D. J. Xiong, L. D. Ellis, J. Li, H. Li, T. Hynes, J. P. Allen, J. Xia, D. S. Hall, I. G. Hill, and J. R. Dahn, *Submitted to J. Electrochem. Soc.* (2017).
208. S. L. Glazier, K. J. Nelson, J. P. Allen, J. Li, and J. R. Dahn, *J. Electrochem. Soc.*, **164**, A1203–A1212 (2017).
209. K. Kleiner, J. Melke, M. Merz, P. Jakes, P. Nagel, S. Schuppler, V. Liebau, and H. Ehrenberg, *ACS Appl. Mater. Interfaces*, **7**, 19589–19600 (2015).
210. Jing Li, J. E. Harlow, N. Stakhieko, N. Zhang, and J. R. Dahn, *Submitted to Tesla for approval* (2018).
211. S. L. Glazier, X. Ma, D. S. Hall, and J. R. Dahn, *Submitted to Tesla for approval* (2018).
212. K. Xu and C. A. Angell, *J. Electrochem. Soc.*, **149**, A920–A926 (2002).
213. S. L. Glazier, S. A. Odom, and J. R. Dahn, *Submitted to Tesla for approval* (2018).
214. J. Chen, C. Buhrmester, and J. R. Dahn, *Electrochem. Solid-State Lett.*, **8**, A59–A62 (2005).
215. S. L. Glazier, L. E. Downie, J. Xia, A. J. Louli, and J. R. Dahn, *J. Electrochem. Soc.*, **163**, A2131–A2138 (2016).

216. M. He, L. Hu, Z. Xue, C. C. Su, P. Redfern, L. A. Curtiss, B. Polzin, A. von Cresce, K. Xu, and Z. Zhang, *J. Electrochem. Soc.*, **162**, A1725–A1729 (2015).
217. K.-C. Möller, T. Hodal, W. K. Appel, M. Winter, and J. O. Besenhard, *J. Power Sources*, **97–98**, 595–597 (2001).
218. K. Xu, A. von Cresce, and U. Lee, *Langmuir*, **26**, 11538–11543 (2010).
219. R. Jung, M. Metzger, D. Haering, S. Solchenbach, C. Marino, N. Tsiouvaras, C. Stinner, and H. A. Gasteiger, *J. Electrochem. Soc.*, **163**, A1705–A1716 (2016).
220. G. M. Veith, M. Doucet, R. L. Sacci, B. Vacaliuc, J. K. Baldwin, and J. F. Browning, *Sci. Rep.*, **7**, 6326 (2017).
221. L. Ma, L. Ellis, S. L. Glazier, X. Ma, Q. Liu, J. Li, and J. R. Dahn, *J. Electrochem. Soc.*, **165**, A891–A899 (2018).